Optical Propagation Effects on Wavefront Sensing and Deformable Mirror Control in Solar Multi-Conjugated Adaptive Optics

PUTTIWAT KONGKAEW

How to cite:

KONGKAEW, PUTTIWAT (2025) Optical Propagation Effects on Wavefront Sensing and Deformable Mirror Control in Solar Multi-Conjugated Adaptive Optics. Doctoral thesis, Durham University.

Optical Propagation Effects on Wavefront Sensing and Deformable Mirror Control in Solar Multi-Conjugated Adaptive Optics

Puttiwat Kongkaew

A thesis presented for the degree of
Doctor of Philosophy

Centre for Advanced Instrumentation
Department of Physics
Durham University
United Kingdom
October 2025

Optical Propagation Effects on Wavefront Sensing and Deformable Mirror Control in Solar Multi-Conjugated Adaptive Optics

Puttiwat Kongkaew

Abstract

As global infrastructure depends more on technology, vulnerability to solar activity grows. Ground-based observations provide high-resolution solar observations needed for further understanding of the Sun. However, they are hindered by atmospheric turbulence. Multi-Conjugate Adaptive Optics (MCAO) mitigates these distortions, enabling sharp imaging across wide fields. Yet implementing solar MCAO is difficult due to strong daytime turbulence and short wavelengths, which heighten scintillation and complicate control.

Firstly, this thesis proposes a method to reduce the required high altitude turbulence size with 10 nm intensity-weighted mean wavefront error, capable of reducing 55% simulation time to generate a new turbulence layer in optical communications and up to 27% for solar MCAO.

After that, this thesis seeks to enhance solar MCAO simulation speed by accelerating the Shack-Hartmann Wavefront Sensor (SH-WFS) model. The intensity-weighted gradient (IG) method is introduced as a more efficient alternative to the conventional Fourier transform (FT) method. The IG method uses simulation time only 35–60% and memory usage by 30-40% of the FT method while preserving the accuracy of 3 nm RMS error. The error of the noise equivalent angle of SH-WFS in scintillation is less than 10% of the scintillation-free.

Additionally, this thesis investigates pupil distortion in MCAO systems, identifying DM-induced scintillation and RMS actuator shifts as significant contributors to control errors. Results show system performance degrades when scintillation exceeds 0.1 or actuator shifts surpass 10% of the actuator pitch. These insights are critical for optimising MCAO systems in solar observation and other high-turbulence applications.

Supervisors: Tim Morris and James Osborn 29th October 2025

Dedication

My grandparents, who cared for my future but never had a chance to see this milestone.

Acknowledgements

This PhD is funded by the National Astronomical Research Institute of Thailand (NARIT) through the Royal Thai Government scholarships for science and technology graduates, aligned with the priorities of the Ministry of Higher Education, Science, Research and Innovation (MHESI) in 2020.

Thanks to all my advisors, Prof. Tim Morris and Prof. James Osborn, who have given me invaluable opportunities and guidance throughout my academic journey.

Thank you, Matthew Townson, et al. and Andrew Reeves, for implementing and publishing AOtools and Soapy simulation for me to use and build on.

Though I have never attended the AO class at UCSC in my undergraduate studies, Claire Max's ASTR 289 lecture is always my first to go to for more AO knowledge. In addition, I also visited Andrey Tokovinin's CTIO for further gateway.

I also deeply appreciate the Australian Astronomical Observatory (AAO) for hosting me for their winter studentship in 2015. With the opportunity, I was exposed to Adaptive Optics for the first time with supervision from Michael Goodwin and Jessica Zheng.

Thank you, National Astronomical Research Institute of Thailand (NARIT), Christophe Buisset, Anthony Berdeu, and Angelie Alagao, for exposing me to professional research in optics.

Thanks to my experience as a demonstrator in the advanced laboratory in optics at Durham University and the students attending it, I had the opportunity to strengthen my optics laboratory knowledge and science communication skills.

I sincerely thank the Centre for Advanced Instrumentation (CfAI) team at Durham University for their patience and support during my many long visits to their offices. These people include Tim Morris, James Osborn, Aurelie Magniez, Beni Hoffmann, Benjamin Shaw, James Gill-Fleming, Amrit Nayak, Chris Graham, Kathryn Hartley, Lily Beesley, Lai Zhang, Polly Gill, Ryan Griffith, Josh Hughes, Duncan Mackenzie, Ian Dolby, Cyril Bourgenot, Kieran O'Brien, Lisa Bardou, Oliver Farley, Lazar Staykov, Nazim Ali Bharmal, Tim Butterley, Marc Dubbeldam, Emily Ronson, Craig Maclean, Jeremi Grabas, Meryem Dag, Jaya Chand, Ieva Jankute, Deborah Malone, Perrine Lognone, Robert Harris, Rose Blyth, Sajjad Mahdizadeh, Kathryn Barret, Phineas Whitlock, Isabelle Crossley, Daniel Martin, James Carpenter, John Connolly, Jitsupa Paenoi, Ram Sharman, Alejandro Buendia, Peter Wizinowich, Ashina Sadaf, Laureen Pradel, and Alice Bellec.

I also owe my gratitude to other friends I made in Durham: Surasing Phukae, Harit Mahaton, Sukrit Best, Hussaya Nookaew, Suttikoon Koonkor, and Toonyawat Angkhanawin.

I deeply appreciate my family for their love, forgiveness, and unwavering support through thick and thin, even when I might not have always deserved it. Poonsook Boonyanate, Sikaret Kongkaew, Jirawath Kongkaew, Sakul Boonyanate, Sujitra Boonyanate, Sirmsree Chaisorn, Panita Chaisorn, Saneh Boonyanate, Wachira Boonyanate, Jew Boonyanate, Oai Boonyanate, Rev. Woorawut Boonyanate, Thammawat Kongkaew, Worrapong Kongkaew, Worrapot Kongkaew, Thunyawit Sriradon, Phatcharadol Sriradon, and Jakkrit Kongkaew. This also extends to friends of the family, Saowapa Sakyaphan, Mayuree Chompoo-ngam, Sirichan Upala, Chintana Phanchanda, Satis Inpakdee, Pattaya Yamano, Thongchai Pahoosee, Treetossapon Sanitjai, Mae Noi, Kru Prim, Phimon Thong-indam and Phitsamai Pudphrom. Without them I would have not survived the mental depression.

I hold my respect toward Banleng Sumano, Ponsit Thammataro, Woorawut Boonyanate, Arithat Tanmetha, Treetossapon Sanitjai, P'First, and Harit Mahaton for the chaplain support throughout my life.

I am grateful to all those who trusted and encouraged me before my PhD journey, who helped me through my depression.

Friends in Thailand: Panupong Yordwong, Jang Khamchan, Rev. Arithat Tanmetha, Sthaporn Chanayai, Panward Panyasrilert, Cheewapon Chookiat, Sukit Saowapanee, Sasiporn Chinakat, Teerachart Soratana, Ekapob Kulchoakrungsun, Roongthiva Thavon, Laksika Tuekdee, Pawichaya Poonsawadkitikul, and many more.

NARIT, where I worked before the PhD study: Christophe Buisset, Anthony Berdeu, Angelie Alagao, Chanthira Boonsri, Chanisa Kanchanasakul, Supachai Awiphan, Nawapon Nakharutai, Somsawat Rattanasoon, Sujeeporn Tantipong, Jitsupa Paenoi, Pimnipa Pho-ngam, Pornapa Artsang, Peerachart, Weerapot Wanacharoen, Adipol Phosrisom, Piramon Kumnurdmanee, and Marcus Halson.

Chiang Mai University (CMU), who advised and encouraged me for my study path: Siramas Komoljinda, Suwicha Wannawichien, Phanisra Nuchvanichakul, and Nawamin Intrarat.

The University of California, Santa Cruz (UCSC), where I earned my bachelor's degree in physics (astrophysics): Jonathan Fortney, Jose Carlos Torres Hernandez, Luis Hernandez, Jose Carlos, Eric Tran, Giovanni Maldonado, and Craig Hu. Your belief in me helped me complete my bachelor's degree and supported me in pursuing this PhD, even when I doubted myself.

Looking back, I appreciated Ruangnapha Poorungruang, Krittaporn Puakanokhirun, and Roojira Wongsaeng, my pre-university teachers who inspired me in optics, allowing me to use microscopes after school and taught me basic optics knowledge, respectively. There are other pre-university teachers that I love and thankful for as well, just not in optics, such as the English language teachers, the subject I deeply used to write this thesis, and the music teachers (Kru Panor, Jaree Sookboonsang, Ammara Sookboonsang, Thitima Inthawong, Tanya Merchant, Undang Sumarna, Brian Baumbusch), who taught me to enjoy life.

I deeply owe the highest gratitude to everyone for accepting, pushing, and encouraging me to finish my undergraduate studies and pursue doctoral studies. Honourable mention: Jonathan Fortney, Christophe Buisset, Supang Sirisapjanan, Jose Carlos Torres Hernandez, Luis Hernandez, Jose Carlos, Eric Tran, Giovanni Maldonado, Panupong Yordwong, and Jang Khamchan. Their support elevated me from depression.

Thank you to my random nighttime friends in Durham who helped me develop social skills I once feared to try. Thanks to my favourite pubs, the Victoria Inn, the Hill Island Brewery, and their regulars.

I also thank my body, despite a poor diet, bad posture and a stupid lifestyle, for enduring these years and helping me reach this milestone. I promise to take good care of you after this.

Special thanks to the creators of online content that kept my mind nourished with virtual delights and cute animals I missed while living in the UK.

And, thank goodness, my cats, Kaew, Kla, Kao, and Kwag, couldn't wake me up in the middle of the night during my PhD, as they are nearly a quarter of the Earth's circumference away in Thailand. I still hope they've not forgotten me entirely since I have not visited them (or Thailand, my home country) during my entire study. Cats will be cats.

Well ... as a follow-up ... during the correction in Thailand, my cats didn't recognise me at first, but as soon as I headed toward my old room, they turned super friendly and demanded constant petting for weeks. So they either remembered me, or felt lonely, or were super friendly. Furthermore, every time I opened my laptop for corrections, they helped me out by typing with all of their limbs. Sadly, what they typed was unreadable.

Please pardon my memory and attention while I wrote this acknowledgement. I might have missed some people's names worthy of mention, to whom I owe gratitude. As you can see, there are more than a hundred names in this list. In addition, please forgive me for I have not listed all the deeds that they have done selflessly for me.

All in all, I am so grateful to everyone in my life. I really don't know if I could have made it through without everyone. I have grown from being a super self-centred, ungrateful, paranoid, indefinitely angry, lack of self-care person into a much reduced symptom person – self-proclaimed better. Laugh out loud with a mix of all of the ahh-i-could-have-been-better tears (if there are any left!!!).

Lastly, I thank myself for hanging on through two bouts of depression (as far as I reckons), graduating undergraduate degree (even if it's late), persevering through multiple postgraduate applications, securing new funding when previous fell through, finding relevant work, recovering from heartbreak, finding moments of peace, surviving UK weather and food, and growing into the person I am today.

Contents

Declaration

The work in this thesis is based on research carried out at the Centre for Advanced Instrumentation (CfAI), Department of Physics, University of Durham, England. No part of this thesis has been submitted elsewhere for any other degree or qualification, and it is the sole work of the author unless referenced to the contrary in the text.

Some of the work presented in this thesis has been published in journals and conference proceedings - the relevant publications are listed below.

Generative or large language model artificial intelligence (AI) is used in this thesis to refine previously written texts, analyses, and plots by the author. The author then reviewed the accuracy.

Publications

Proceedings Volume 13097, Adaptive Optics Systems IX; 130975U (2024), `https://doi.org/10.1117/12.3019648`, Event: SPIE Astronomical Telescopes + Instrumentation, 2024, Yokohama, Japan

List of Figures

List of Tables

Nomenclature

AO	Adaptive Optics
CoG	Centre-of-Gravity
CM	Control Matrix
DM	Deformable Mirror
DFT	Discrete Fourier Transform
FoV	Field-of-View
FT-Method	Fourier Transform Method
FT-Tilt	Fourier Transform Tilt
G-Method	Averaged Gradient Method
G-Tilt	Averaged Gradient Tilt
IG-Method	Intensity-Weighted Averaged Gradient Method
IG-Tilt	Intensity-Weighted Averaged Gradient Tilt
IM	Interaction Matrix
LoS	Line-of-Sight
MCAO	Multi-Conjugated Adaptive Optics
NEA	Noise Equivalent Angle
OPD	Optical Path Difference
PSF	Point Spread Function
PSD	Power Spectral Density

RMS	Root-Mean-Square
SCAO	Single-Conjugated Adaptive Optics
SH-WFS	Shack-Hartmann Wavefront Sensor
SNR	Signal-to-Noise Ratio
SVD	Singular Value Decomposition
WFE	Wavefront Error
WFS	Wavefront Sensor

1 Introduction

1.1 Background

The Sun has long been observed by humanity since time immemorial. To tell time, humans observed movements of the Sun and invented the sundial and the calendar, aiding the growth of civilisations (Aveni, 1989). Observation of the Sun itself is natural to humans, even the UK's National Health Service (NHS) has to publicise that looking directly at the Sun may cause irreversible eye damage (NHS, 2022). The existence of sunspots has been recorded since ancient China and Greek civilisation (Temple, 1988; Vaquero, 2007). The first drawings in 1128 and the first observation in 1610 through a telescope of sunspots were made by English people (Stephenson and Willis, 1999; Vokhmyanin et al., 2020). After the invention of the telescope. Galileo Galilei also published his sunspot observations in Galilei (1612).

Interestingly, at the Durham University Observatory, Temple Chevallier led the first group in England to start regularly observing sunspots (Monthly Notices of the Royal Astronomical Society, 1874). He employed Richard Carrington as an observer at the Durham University Observatory. Since the observatory was newly formed, Carrington was displeased at the state of the instruments at the observatory and left Durham (Monthly Notices of the Royal Astronomical Society, 1876).

Carrington continued observing sunspots, until 1st September 1859 when he noticed “two patches of intensely bright and white light broke out" (Carrington, 1859). The same event was also published by Hodgson (1859). This solar flare event led to the great auroral storm of 1859, later called the Carrington event (Green et al., 2006). During the event, northern lights could be seen as low latitude as Panama and were so bright that one could read a newspaper with. Telegraph operators were shocked by the electricity induced by the event and could send telegraph messages without the need of power supplies.

Damages, risk assessments, awareness, and preparations for potential solar storms have been studied more and more at the national level (National Research Council (U.S.), 2008; Lloyd’s of London, 2013; Amos, 2014). As humanity becomes more and more dependent on technology, especially electronics, if an event such as the Carrington event were to happen again, all services depending on electronics will be damaged. Such services include electricity power, water, sewage, hospital, banking, trade, and satellites (BBC, 2024; Ferreira, 2024). Solar flares can be monitored and then forecast when solar particles will reach the Earth, avoiding potential damages. Observation of the Sun is crucial for scientific understanding and later predicting the solar activity (National Solar Observatory, 2025b; Darling, 2016).

The observation and simulation of solar dynamics should resolve the photon mean-free path and the pressure height scale at the photosphere, requiring the telescope resolution of 70 km or 0.1 arcsecond on Earth (National Solar Observatory, 2025b). Even though telescopes can be sent closer to the sun, there are various complications limiting the resolution of space telescopes. As of 2020, based on data on National Solar Observatory (2025a), their ground-based telescope (DKIST) can theoretically resolve 30 km, while their space telescope (Solar Orbiter) can resolve only 201 km of solar features in the photosphere.

However, the ground-based telescope cannot actually reach the designed spatial resolution due to the presence of optical turbulence in the atmosphere, also known as seeing (Babcock, 1953). To remediate the optical aberration, Babcock (1953) proposes a system concept that leads to the development of AO systems. An interesting side note about Babcock is that he also researched the Sun's magnetic field (Babcock, 1961). The AO system operates as shown in Figure 1.1 (Max, 2020). The aberrated wavefront from a telescope is corrected by a DM. The residual wavefront is sent toward a WFS and a science channel. The residual wavefront is measured by the WFS. Based on the measurement, the DM control is updated accordingly to compensate for the observed residual wavefront aberrations. The resulting image in the science channel benefits greatly from the corrected wavefront, enabling high spatial resolution imaging limited at the diffraction limit of the telescope, as opposed to the seeing-limited resolution. For the current generation of 4m-class solar telescopes, this can result in an improvement in spatial resolution of factors of up to approximately 100, depending on the wavelength of observation.

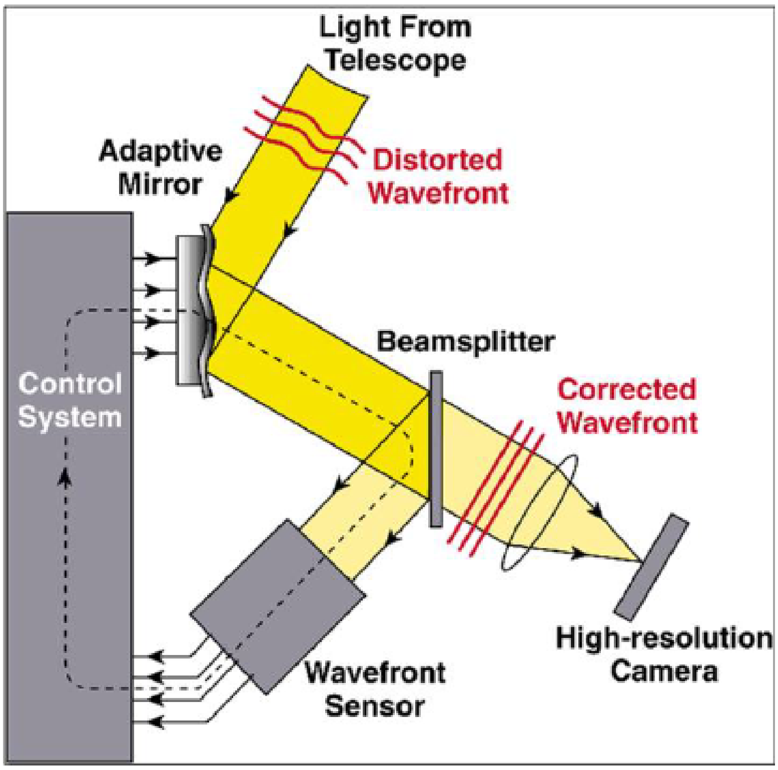

Figure 1.1: *Operation concept of AO. The incoming distorted wavefront from the telescope is corrected by an adaptive mirror. The residual wavefront is split by a beam splitter to a wavefront sensor and a high-resolution camera. The wavefront sensor measures residual wavefront error. The control system calculates and updates the control to the adaptive mirror. Scientific study through the high-resolution camera has improved optical resolution from the corrected wavefront of the control loop (Max, 2020)).*

The AO system configuration shown in Figure 1.1 is typically called classical AO or more commonly for astronomical applications, SCAO. The SCAO has only one DM and one WFS; as a result, it can only provide a high correction along one Line-of-Sight (LoS), the direction along which the WFS samples the turbulence. LoSs off-axis from the WFS LoS at the centre of the field sample, increasingly different turbulence as the angular offset distance increases. As a result, the corrected wavefront quality degrades. The corrected quality of a wide-field image is superb at the centre, but drops rapidly radially away from the highest correction point as shown in Figure 1.2(a). This error is called the anisoplanatic error (Fried, 1981). Since the Sun is an extended source larger than the isoplanatic angle, an alternative AO configuration from SCAO is needed to provide aberration correction over a larger area.

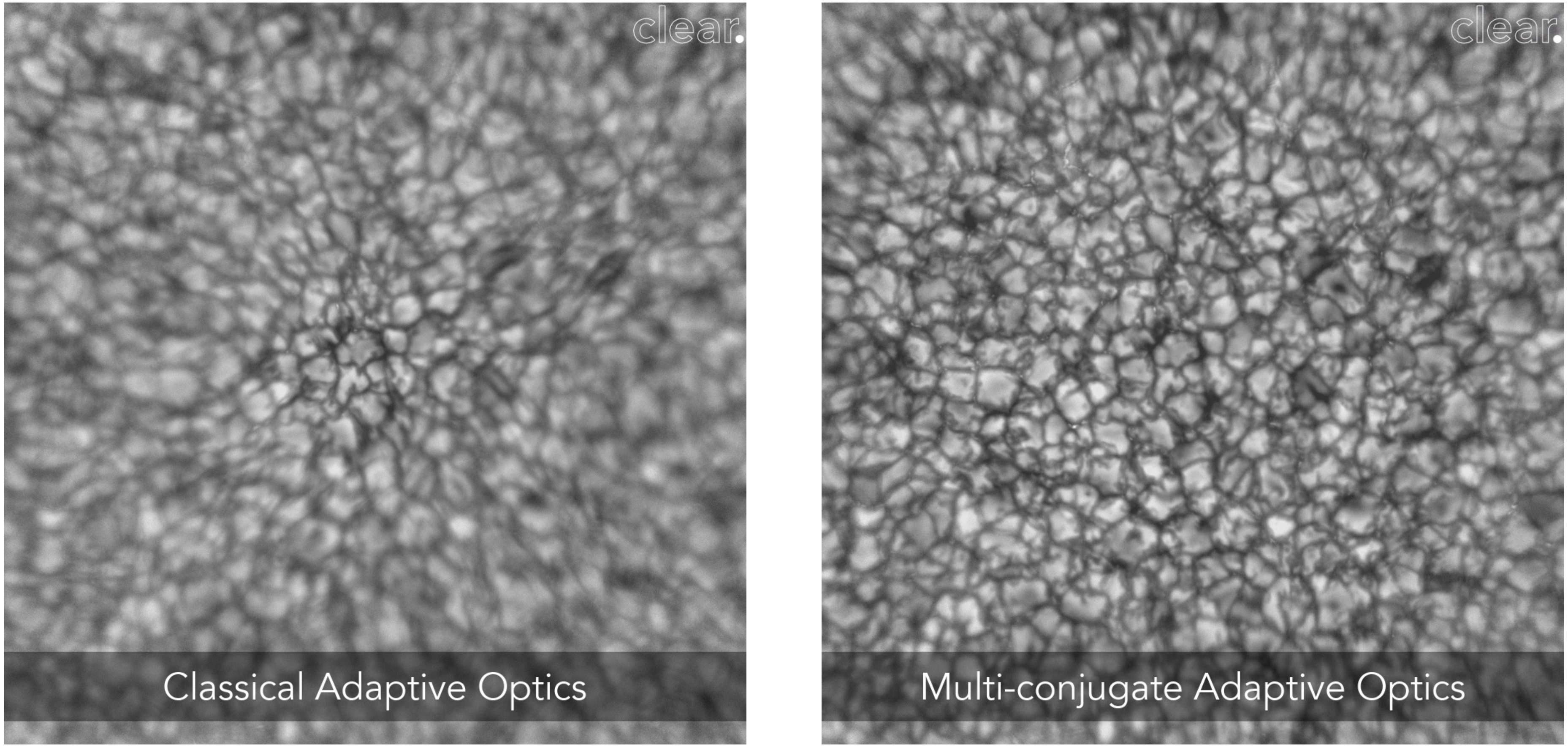

(a) *Single-Conjugated Adaptive Optics (SCAO)*

(b) *Multi-Conjugated Adaptive Optics (MCAO)*

Figure 1.2: *Comparison of adaptive optics corrected images. SCAO (a) has high correction only near the centre, while the MCAO (b) has a larger FoV of the corrected image. Courtesy of Dirk Schmidt from the CLEAR instrument on the New Solar Telescope at the Big Bear Solar Observatory (Schmidt et al., 2017).*

To reduce the anisoplanatic error and increase the corrected FoV of the image, Beckers (1988) proposes a new type of AO called MCAO. The concept of operation of MCAO is shown in Figure 1.3 (Max, 2020) where multiple WFSs and DMs can be used to introduce field-dependent corrections. Field-dependent optical aberrations can be measured by multiple WFSs using the tomographic techniques developed by Tallon and Foy (1990). The optical aberration that can be corrected by the system using multiple DMs as shown in Ragazzoni et al. (2002). An example of an MCAO-corrected image in Figure 1.2(b) with the much larger corrected FoV compared to that of the SCAO in Figure 1.2(a).

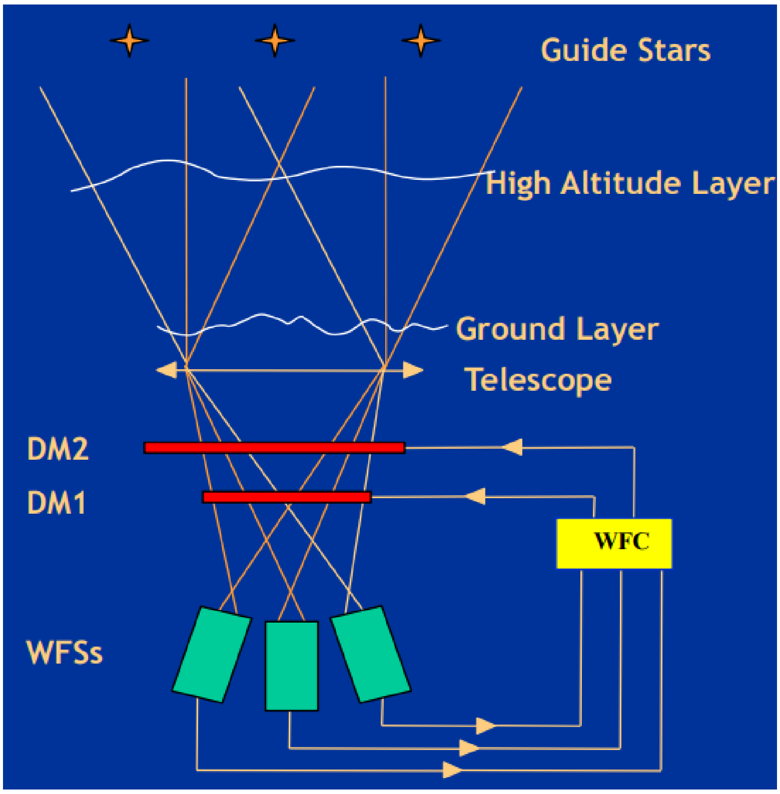

Figure 1.3: *Operational concept of the MCAO (Max, 2020).*

1.2 Challenges

MCAO for solar telescopes is operating under more challenging conditions compared to other applications of AO due to stronger atmospheric turbulence present during the day

(Griffiths et al., 2023; Griffiths, 2024). The Fried parameter (r_0) (Fried, 1966) is used to describe optical turbulence strength with a smaller Fried parameter representing strong turbulence. An example of the evolution of the turbulence strength within a day is shown in Figure 1.4 from Griffiths et al. (2023). It shows a turbulence measurement over 36 hours at the Observatorio del Roque de los Muchachos, La Palma, Spain. The measured Fried parameter of turbulence reduces from 10 cm in the nighttime, then changes to 3 cm in daytime, within 4 hours after sunrise, equivalent to 7.4× increase in the turbulence strength. Another example for comparison is given in Figure 1.5 (taken from Griffiths (2024)) which shows a histogram of day time and night time Fried parameters observed over 70 hours at the Universitat Politecnica de Catalunya in Barcelona, Spain. It shows the median Fried parameter of 4 and 7 cm for daytime and nighttime, respectively. This second dataset was observed over a longer period, the latter study has a smaller difference for median turbulence, with only a 2.5× increase. Both of the samples have a median Fried parameter in the daytime between 3 and 4 cm.

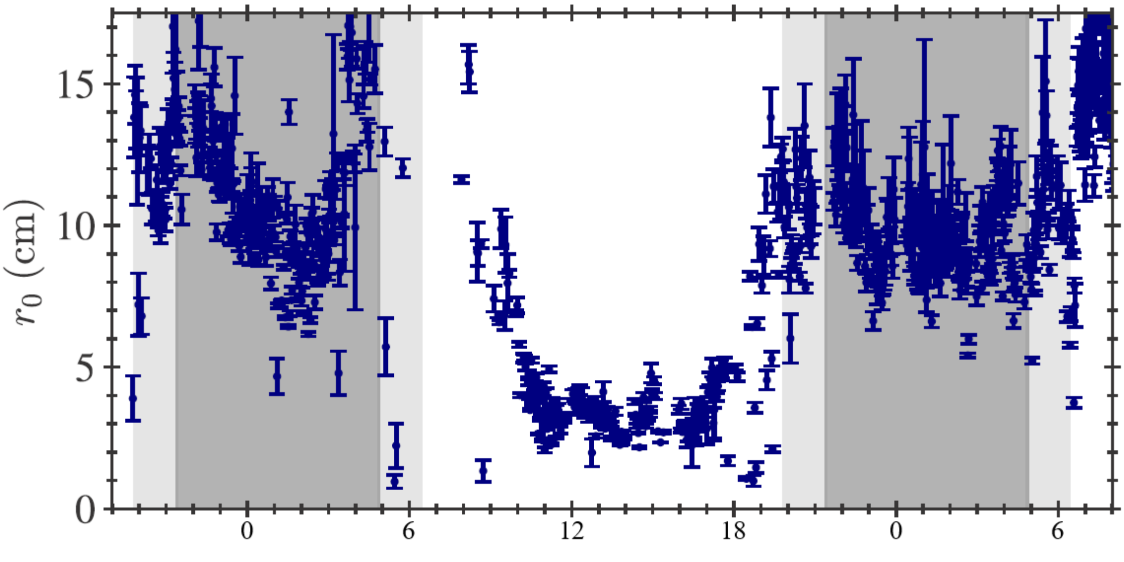

Figure 1.4: *Fried parameter (r_0) versus time in UTC over 36 hours showing evolution of turbulence strength at the Observatorio del Roque de los Muchachos, La Palma, Spain from the 14th to 16th May 2022 using the 24hSHIMM instrument taken from Griffiths et al. (2023). The Fried parameter is projected to the zenith at 500 nm. The dark grey, light grey, and white backgrounds denote the nighttime, twilight, and daytime, respectively.*

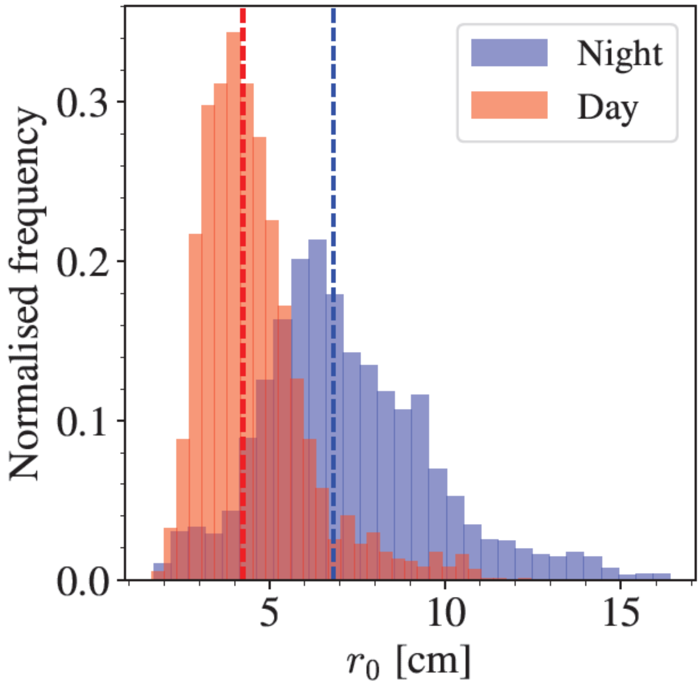

Figure 1.5: *Histogram of turbulence strengths in the nighttime and daytime on top of the CommsensLab building at the Universitat Politecnica de Catalunya (UPC) in Barcelona, Spain, using the TURBO 1 instrument taken from Griffiths (2024). Turbulence strengths at 500 nm, on the x-axis, are stronger with lower values. Blue and red histograms show the nighttime and daytime statistics, respectively.*

Because of the huge increase in turbulence strength and shorter observing wavelengths in solar observations (Rimmele, 2004), optical propagation, diffraction, and scintillation effects become more dominant in MCAO and may reduce MCAO performance (Farley et al., 2017). This thesis focuses on improving the modelling and performance of daytime MCAO. However, this work is not only applicable to the solar MCAO. Other AO applications including optical communications and space surveillance that may need to operate in similar conditions involving daytime turbulence, low elevation angle observations, and scintillation.

1.3 Thesis Outline

In Chapter 2, the theoretical frameworks used within this thesis are introduced, including the Fourier transform, the discrete Fourier transform, the mathematical representation of optical waves, simulation of optical propagation through vacuum and standard optical elements, optical turbulence, and scintillation.

In Chapter 3, the simulation of AO used in this thesis is introduced, implemented using AOtools (Townson et al., 2019) and Soapy (Reeves, 2016). The codes are then comprehensively verified for their accuracy over a wide range of operational conditions. The simulation includes optical turbulence generation, optical propagation from the high-altitude atmosphere throughout the system, wavefront sensing, wavefront corrections, analysis of the residual wavefront, and control of AO. The novel addition that has been made as part of this work is a set of algorithms and metrics that automatically select simulation parameters that ensure that spurious simulation errors are avoided whilst minimising the computational load of the simulation. Lastly, it proposes a method to minimise the required simulation size of high altitude turbulent layers.

In chapter 4, this thesis presents a method to speed up the simulation of SH-WFS in the presence of optical scintillation through a geometrical approximation derived by (Tartarskii, 1971) referred to here as the IG-Method. The speed gain, memory usage and accuracy of this geometric approximation are measured and compared both to the standard Fourier transform-based method of generating SH-WFS images as well as a non-intensity weighted phase gradient. The IG-Method is then extended to include the addition of typical centroiding noise sources including photon noise, read noise and detector thresholding. We confirm over which range of atmospheric/scintillation parameters the SH-WFS slope measurements from the noise-approximated IG-Method match those of the standard FT-Method.

In Chapter 5, this thesis investigates the unavoidable pupil distortion effects present within MCAO systems noted by Hardy (1998) and Van Dam et al. (2020). The pupil distortion effect degrades MCAO control performance. This thesis describes pupil distortion errors in terms of two metrics, namely the DM induced log-amplitude variance and apparent DM's actuator position shift statistics. It proposes analytical equations and measurement methods to describe the pupil distortion in terms of these metrics. Then the effect of pupil distortion on AO control system is simulated, investigating under which conditions the AO control will fail to correct for optical turbulence and which metric best predicts this behaviour.

The research presented in Chapters 4 and 5 both aim to investigate the validity of geometric approximations based on the direct analysis of phase to the physically accurate, but computationally intensive methods that directly calculate optical propagation between relevant conjugate planes within AO simulations in some sort of way. The IG-Method of simulating a wavefront sensor in Chapter 4 and the RMS actuator shift in Chapter 5 both use direct knowledge of the phase that is possible within an AO simulation to avoid complex computations. However, when approximations are used, their validity must be determined. In addition to presenting new metrics, this work presents a novel investigation into the validity of these approximations in the presence of strong atmospheric scintillation conditions. The goal of this thesis is first to determine if approximations can provide data that can a) provide metrics or models that are relevant to AO system performance, b) if they are actually useful in terms of the decrease in simulation complexity, and c) over which range of atmospheric conditions it is valid to use the approximations.

2 Optical Wave Propagation through Atmospheric Turbulence

This thesis requires the simulation of the visible daytime Adaptive Optics (AO). There are several differences and challenges in simulating AO systems in daytime operation, the key aspects of which are:

- Atmospheric turbulence is much stronger during the daytime. Some daytime observing targets, including the Sun and satellites, may require a lower observing elevation angle, amplifying the total turbulence strength along a Line-of-Sight (LoS) even further.
- To enable wide-field correction, multiple atmospheric turbulence layers must be corrected and simulated, placing a large computational burden on the AO simulation.
- Operation at visible wavelength results in stronger diffraction effects, particularly when considering higher altitude turbulence. Diffraction introduces distortion and scintillation or variation in intensity within a pupil.

There are still other key differences such as generating distorted wide-field images, using extended sources as references for the wavefront sensing, and wavefront reconstructions in Multi-Conjugated Adaptive Optics (MCAO), since these concepts are in their own right separate studies. These omitted concepts do not obstruct this thesis study. For example, consider if the wide-field object is to be used as the guide object for the Wavefront Sensor (WFS) in Chapter 4, the Point Spread Function (PSF) information at different field must be simulated first, then convoluted with each field of the object to generate the distorted image. Then the distorted image will be correlated Löfdahl (2010). The peak of the correlation map will determine the slope measurement. Chapter 4 only includes measurement of the PSF and locating the peak. On the other hand, Chapter 5 intentionally avoid the multi-layered wavefront reconstruction to separate only the control error for the study. Because this thesis explored the common features, the wide-field performance can be extrapolated from the point-source study conducted by this thesis.

Scintillation is commonly known as the variation in intensity collected within an aperture, such as the variation in intensity of a star measured by the telescope at a given point in time. This is commonly seen as the twinkle of the stars. However, in this thesis, unless declared otherwise, the scintillation is defined as the spatial variance of the log-amplitude of a point-source over the whole plane of observation. This hypothetical value is difficult to measure when the detector or object size is not infinitesimal, unlike the total intensity over an aperture and the angular size of the object. The hypothetical scintillation can be inferred from the variation of the total intensity based on the derivation by Sasiela (2007).

Scintillation may introduce errors in WFS measurements, including slope measurement being skewed toward high flux regions of the wavefront, even if some regions receiving relatively dim light give good Signal-to-Noise Ratio (SNR). Furthermore, with strong diffraction effects during the visible daytime, the direct addition of phase within the simulation is no longer accurate. Instead, propagation of the wave must be simulated, and the order of operation is important. Next, stronger daytime turbulence requires a larger number of simulation elements for the same telescope size. In addition, with stronger turbulence during the daytime, angular turbulence conditions may change more rapidly, so a larger number of LoS must be simulated, multiplying the simulation size even further. To simulate wide-field visible daytime AO, related mathematical constructs, physics, and simulation methods of optical propagation in turbulence-free medium and atmospheric turbulence, and light propagation in turbulence must be studied. Each topic will be covered in order within this chapter.

2.1 Mathematical Approaches Used within Propagation Simulations

This section revisits the Fourier transform, Discrete Fourier Transform (DFT) and the limitation of DFT. The Fourier transform is a faster method to calculate the propagation equation than integrals. Since in simulation, data are discrete, being represented at several grid points and limited to having a finite number of pixels, DFT and its limitations must be covered.

2.1.1 Fourier Transform

Simulation of wave propagation can be simplified by using the Fourier transform. The Fourier transform decomposes any function into a series of sine and cosine functions of different frequencies with varying amplitudes. The Fourier transform operator, $\mathcal{F}$, on a spatial function, $g\left(x\right)$, can be written as $\mathcal{F}\left\{g\left(x\right)\right\}$. The Fourier transformed function of $g\left(x\right)$, noted by $G\left(f\right)$, is a spatial frequency function of $g\left(x\right)$, where f is the ordinary frequency of x. The unit of f is the inverse unit of x. For example, if the unit of x is m, then the unit of f is m^{-1}. The Fourier transform is defined in its normalised form by

$$G\left(f_x\right) = \mathcal{F}\left\{g\left(x\right)\right\} = \int g\left(x\right) e^{-i2\pi f_x x} dx. \tag{2.1}$$

And the inverse Fourier transform is

$$g\left(x\right) = \mathcal{F}^{-1}\left\{G\left(f_x\right)\right\} = \int G\left(f_x\right)e^{i2\pi f_x x}df_x. \tag{2.2}$$

The Fourier transform is used extensively in optical propagation modelling, forming the Fourier optics field of study (Goodman, 2017).

2.1.2 Discrete Fourier Transform

The Fourier transform describes any function as an integration of an infinite set of modes expanding infinitely, and each mode corresponds to the spatial frequencies present within the function. When using the Fourier transform within a computer model, we are limited in our description of any function to a discrete number of points, and the function cannot extend from negative to positive infinity. Fourier transform with these limiting conditions is adapted by DFT.

An example of discretisation in the simulation of DFT can be explained as follows. If a telescope pupil is to be simulated. The telescope pupil is infinitely sampled. Every point closely connected to another point can be represented in an equation. However, in simulation, we may only have a limited computation resource, say 64x64 pixels, called a simulation screen in this thesis. Now, only the 64x64 locations where each pixel is centred on will have mathematical values represented. With this limited number of pixels within the screen, the data coverage is also limited.

We use the notation described in Equation 2.1 for this. Let $g\left(x\right)$ be a function in x space, and $G\left(f\right)$ be the Fourier transformed of $g\left(x\right)$ sampling in f space which is the frequency of x. Let δ_x be the sampling period of x. In the case of an optical image, this would describe the pixel scale of x. δ_f be pixel scale of f. Let N be the number of points where $g\left(x\right)$ is sampled. Then

$$\delta_{f_x} = \frac{1}{N\delta_x}. \tag{2.3}$$

According to Schmidt (2010) and Cooley et al. (1969), when discrete sampling of the function is considered, the Fourier transform in Equation 2.1 can be written in a numerical form as

$$\begin{aligned} G\left(\frac{m}{N\delta_x}\right) &= \mathcal{F}\left\{g\left(n\delta_x\right)\right\} & (2.4) \\ &= \delta_x \sum_{n=-N/2}^{N/2-1} g\left(n\delta_x\right) e^{-i2\pi mn/N}. & (2.5) \end{aligned}$$

where the indices (m) are

$$\begin{aligned} \text{for even } N\ ;\ m &= -\frac{N}{2}, -\frac{N}{2}+1, \ldots, \frac{N}{2}-1 \text{ and} & (2.6) \\ \text{for odd } N\ ;\ m &= -\frac{N-1}{2}, -\frac{N-1}{2}+1, \ldots, \frac{N-1}{2}. & (2.7) \end{aligned}$$

The inverse Fourier transform in Equation 2.2 can be written as

$$\begin{aligned} g\left(n\delta_x\right) &= \mathcal{F}^{-1}\left\{G\left(m\delta_{f_x}\right)\right\} & (2.8) \\ &= \delta_{f_x} \sum_{m=-N/2}^{N/2-1} G\left(m\delta_{f_x}\right) e^{i2\pi mn/N}. & (2.9) \end{aligned}$$

where the indices (n) are

$$\begin{aligned} \text{for even } N\ ;\ n &= -\frac{N}{2}, -\frac{N}{2}+1, \ldots, \frac{N}{2}-1 \text{ and} & (2.10) \\ \text{for odd } N\ ;\ n &= -\frac{N-1}{2}, -\frac{N-1}{2}+1, \ldots, \frac{N-1}{2}. & (2.11) \end{aligned}$$

For Fourier transform functions presented in common programming libraries, the indices are usually shifted from the indices shown here, and need to be shifted back after the transform to get the proper matching (NumPy Developers, 2024). For example, for an even number of pixels, let's say 4, the ordering shift is

$$\{0, 1, 2, 3\} \rightarrow \{-2, -1, 0, 1\}\,. \tag{2.12}$$

For an odd number of 5, the ordering shift is

$$\{0, 1, 2, 3, 4\} \rightarrow \{-2, -1, 0, 1, 2\}\,. \tag{2.13}$$

When g is transformed into G, based on Equation 2.5, the spatial frequency has its max frequency $f_{Nyquist}$, also known as Nyquist Sampling (Goodman, 2017),

$$|f_{Nyquist}| = \frac{1}{2\delta_x}. \tag{2.14}$$

Limitations of the discrete Fourier transform include aliasing and cyclic boundary. Aliasing happens when any spatial frequency content within the data that is higher than the Nyquist sampling (Equation 2.14) is aliased or misregistered into lower frequencies. For example, if a generated phase screen has turbulence with a significant level of spatial frequencies higher than the Nyquist sampling, all of the higher spatial frequency turbulence will mathematically be aliased into other lower frequencies, which is not correct. This aliasing effect can be prevented by choosing an adequately fine pixel scale (Schmidt, 2010). For the cyclic boundary, due to the computational method, each boundary of the discrete Fourier transform is connected to the other boundary, allowing unphysical phenomena where interactions happen across the boundary Schmidt (2010). Another description for both effects is that they are essentially the same effect, where one shows its effect in the spatial domain and another in the frequency domain.

2.2 General Solutions to Wave Equation

The most basic representation of a wave can be represented with an amplitude (A) and a phase (ϕ), is (Schmidt, 2010)

$$U = Ae^{i\phi}, \tag{2.15}$$

where U is a complex amplitude representation of optical waves.

The intensity of the wave (I) is

$$I = |U|^2 = A^2, \tag{2.16}$$

In most studies of the optical propagation through turbulence, it is common to normalise the intensity over the pupil. After that, it is then presented through the log-amplitude (χ) (Tartarskii, 1971; Andrews and Phillips, 2005; Sasiela, 2007). The log-amplitude is defined as

$$\chi = \ln(A) = \ln\left(\sqrt{I}\right) \tag{2.17}$$

To simplify subsequent mathematical analyses, the complex amplitude can also be presented with

$$U = e^{\chi + i\phi}, \tag{2.18}$$

where the unit of phase (ϕ) is radian, while Log-amplitude (χ) is unitless. The variation in the phase of the wavefront is the wavefront error or the optical path difference. The variation in the log-amplitude of the wavefront is called scintillation Sasiela (2007).

2.3 Propagation through a Uniform Medium

The physics of propagation in turbulence-free conditions covered in this chapter are the paraxial approximation, Fresnel Propagation, Fraunhofer approximation, angular-spectrum propagation, and modification of light by optical components.

According to the Huygens-Fresnel principle, propagation of a wave from one wavefront to another is calculable by treating each point on the previous front as a spherical wave source, and the resulting wavefront is the sum of all diffracting waves of spherical sources on the old wavefront.

2.3.1 One-Step Fresnel Propagation

Let's consider propagation from plane 1 to plane 2 separated by a distance z such that $z_1 = 0$ and $z_2 = z$. Let $U_1 (x_1, y_1, 0)$ be complex amplitude equations at plane 1 and similarly $U_2 (x_2, y_2, z)$ for plane 2. The optical wave at plane 2 relates to that of plane 1 by

$$U_2 (x_2, y_2) = \frac{e^{ikz}}{i\lambda z} e^{\frac{ik}{2z}\left(x_2^2+y_2^2\right)} \mathcal{F} \left\{ U_1 (x_1, y_1) \, e^{\frac{ik}{2z}\left(x_1^2+y_1^2\right)} \right\}, \tag{2.19}$$

where λ is the wavelength of the propagated optical wave. The Fourier transform, based on Equation 2.1, has $x_2/\lambda z$ and $y_2/\lambda z$ as its ordinary frequency. According to Equation 2.3, the output pixel scale of this method will be

$$\delta_2 = \frac{\lambda z}{N \delta_1}, \tag{2.20}$$

where δ_1 and δ_2 denote pixel scale at the source and destination plane, respectively, and N is the total number of elements across the simulated plane wave.

2.3.2 Angular-Spectrum Propagation

Unlike Fresnel propagation using Fourier transform in Equation 2.19 which gives a strict relation between propagation distance, input, and output spatial pixel sampling as shown in Equation 2.3, the angular-spectrum method allows user to use larger variety of input and output pixel scale in any simulation compare to one-step Fresnel propagation which allows a strict relation of pixel scales 2.20.

First, the wave at the source plane is decomposed into different spatial frequencies. This is equivalent to different plane waves tilting at different angles (α_x, α_y) with respect to x and y axis, respectively. The collection of all plane waves to describe a complex amplitude (U) can therefore be expressed as

$$
\begin{aligned}
U\left(x,y\right) &= \iint A\left(\frac{\alpha_x}{\lambda},\frac{\alpha_y}{\lambda}\right) e^{i2\pi\left(\frac{\alpha_x}{\lambda}x+\frac{\alpha_y}{\lambda}y\right)} d\frac{\alpha_x}{\lambda} d\frac{\alpha_y}{\lambda} && (2.21)\\
&= \mathcal{F}^{-1}\left\{A\left(\frac{\alpha_x}{\lambda},\frac{\alpha_y}{\lambda}\right)\right\} && (2.22)\\
A\left(\frac{\alpha_x}{\lambda},\frac{\alpha_y}{\lambda}\right) &= \mathcal{F}\left\{U\left(x,y\right)\right\}, && (2.23)
\end{aligned}
$$

where $(\alpha_x/\lambda, \alpha_y/\lambda)$ is the angular spectrum. The angular spectrum pixel scale is $1/(N\delta)$ (Equation 2.3), and its maximum value is $1/(2\delta)$ (Equation 2.14).

Each plane wave is propagated to the observation plane using a free-space transfer function (Schmidt, 2010). Lastly, undo the transform back to the spatial space. The output wave amplitude U_2 can be calculated from the input U_1 by

$$
U_2\left(x_2,y_2\right) = e^{\frac{ik}{2z}\frac{m-1}{m}\left(x_2^2+y_2^2\right)} \mathcal{F}^{-1}\left\{e^{\frac{-i2\pi^2 z}{km}\left(f_{x,1}^2+f_{y,1}^2\right)} \mathcal{F}\left\{\frac{1}{m} e^{\frac{ik}{2z}(1-m)\left(x_1^2+y_1^2\right)} U_1\left(x_1^2+y_1^2\right)\right\}\right\}, \tag{2.24}
$$

where k is the wavenumber $= 2\pi/\lambda$, and f_{x1}, f_{y1} is spatial frequency coordinate related to x_1, y_1, as shown in Equation 2.5, $m = \delta_2/\delta_1$ is the magnification of pixel scale.

For simplicity, convenience, the pixel size of the source and destination plane is chosen to be the same for the rest of this thesis.

2.4 Propagation through Optical Elements

Transmission of light through an optical element introduces phase differences to an input wavefront. This can be simulated by adding changes in phase to the phase term in U without changes in intensity/amplitude. Common geometrical optics, such as lenses and mirrors, add a static phase term, whilst dynamic optics used within adaptive optics systems, such as a tip-tilt or deformable mirror, introduce time-varying phase terms. Let U_{before} and U_{after} be incoming and outgoing wavefronts right before and after interaction with a geometrical optic. It can be decomposed into amplitude before and after transmission (A_{before} and A_{after}, respectively) and phase before and after (ϕ_{before} and ϕ_{after}, respectively) as shown in Equation 2.15. Let ϕ_{optics} be the phase changes incurred by thin geometrical optics. Then these quantities are related to each other by

$$A_{\text{after}} = A_{\text{before}} \tag{2.25}$$

$$\phi_{\text{after}} = \phi_{\text{before}} + \phi_{\text{optics}} \tag{2.26}$$

$$U_{\text{after}} = U_{\text{before}} e^{i\phi_{\text{optics}}} \tag{2.27}$$

$$U_{\text{after}} = A_{\text{before}} e^{i(\phi_{\text{before}} + \phi_{\text{optics}})}. \tag{2.28}$$

2.4.1 Tip/Tilt Optics

Let x_{in}, y_{in} be coordinates in the incoming wavefront plane and θ be the angle of tip/tilt desired. Then the phase introduced by this tip/tilt optics is

$$\phi_{tip/tilt} = k\theta \left(x_{in} + y_{in} \right). \tag{2.29}$$

2.4.2 Focusing Optics

With a similar notation to the previous subsection, the phase induced by a lens with focal length (f_{focal}), where a positive value represents a converging lens, is

$$\phi_{optics} = -\frac{k}{2f_{focal}}\left(x_{in}^2 + y_{in}^2\right). \tag{2.30}$$

An interesting case is when light is focused by a lens, and the propagation distance is equal to the focal length of the lens. Combining Equation 2.19 with Equation 2.30 will have their quadratic terms cancelling out, resulting in

$$U_{focal\ plane}\left(x_2, y_2\right) = \frac{e^{ikz}}{i\lambda z} e^{\frac{ik}{2z}\left(x_2^2+y_2^2\right)} \mathcal{F}\left\{U_{pupil}\left(x_1, y_1\right)\right\}, \tag{2.31}$$

and

$$I_{focus}\left(x_2, y_2\right) = \left|\mathcal{F}\left\{U_{pupil}\left(x_1, y_1\right)\right\}\right|^2. \tag{2.32}$$

This shows that the intensity at the focal plane can be calculated by simply taking the modulus squared of the Fourier transform of the complex amplitude in the pupil plane. The output scale is determined by Equation 2.20.

2.5 Propagation through Weakly Non-Uniform Medium

The refractive index of the atmospheric air is determined by pressure and temperature. The variation of the refractive index within the atmosphere is minute; for example, the difference between vacuum and room temperature at sea level is only 3×10^{-4} (Sasiela, 2007). The changes in atmospheric temperature and pressure generate turbulence swirling in different sizes. Turbulence in turn generates 'optical turbulence'. This effect can be seen during the sunrise and sunset, where the image of the sun is distorted spatially and temporally. Another popular example is the twinkling of the star. The difference in refractive index of the atmosphere can delay the optical wavefront up to a micrometre.

The analytic solution of the wave equation in a minor change in refractive index can be derived by the perturbation method called Rytov approximation (Sasiela, 2007). The analytic solution can only be derived for cases with a variance of log-amplitude to be small, less than 0.35 rad^2 in general. The variance of log-amplitude has a saturation level at 0.6 rad^2. For this thesis, strong scintillation means log-amplitude variance larger than 0.3 rad^2, and medium scintillation means log-amplitude variance between 0.1 and 0.3 rad^2.

This section covers two possible aberrations in the phasor representation of the optical wave shown in Equation 2.18. The first part will be on the phase variance or the optical path difference induced by the atmosphere. The second part centred on the log-amplitude variance instead, one of its effects is the scintillation. Both of the aberration affects the AO performance.

2.5.1 Wavefront Distortion by Turbulence

Optical turbulence is studied statistically. General approaches include measuring the structure function and power spectrum density. These functions are scaled by turbulence strength (C_n^2). Turbulence strength varies between regions of the atmosphere. Well-known models of optical turbulence are Kolmogorov statistics and von Kármán statistics (Schmidt, 2010). Kolmogorov statistics are proposed in Kolmogorov (1991) and later modified by Fried (1965). The modified von Kármán distribution is the simplest model matching real turbulence behaviour (Andrews and Phillips, 2005). The difference between these two models is the outer scale (L_o) and inner scale (l_o) in the von Kármán model that sets the limit on the turbulence distribution at larger and smaller spatial frequencies. An example of optical turbulence is shown in Figure 2.5. Further explanation can be found in the latter part of this chapter.

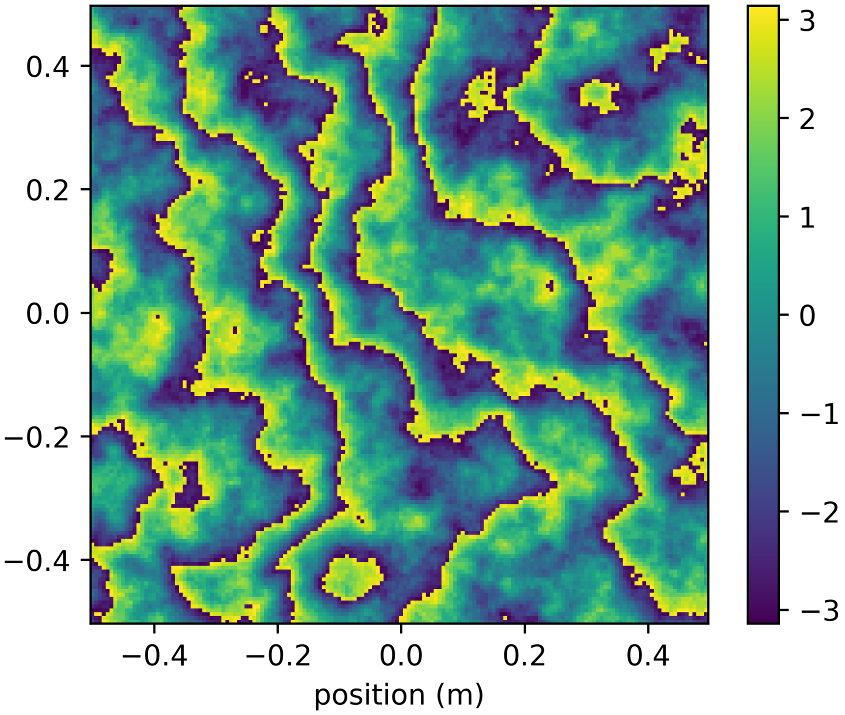

Figure 2.1: *Simulated phase (rad) of optical turbulence of von Kármán statistics at 500 nm with 5 cm* r_0 *and 5 m* L_0*. The phase is wrapped every* 2π *radians.*

2.5.1.1 Turbulence Strength and Coherence Length

Optical turbulence limits astronomical telescope angular resolution. At optical and near-infrared wavelengths, telescope resolution only improves with diameter up to telescope diameters of 30 centimetres, after which the resolution is limited by atmospheric turbulence. This sets an idea of the optical coherence length.

When this turbulence strength (C_n^2) is integrated over the LoS with some scaling, we arrive at the coherence length or Fried parameter (r_0) (Fried, 1965). r_0 is related to C_n^2 by

$$r_0 = \left(0.423k^2 \sec\left(\zeta\right) \int_o^{\infty} C_n^2\left(z\right) dz\right)^{-3/5}, \tag{2.33}$$

where k is wavenumber, z is height of the turbulence from the ground, and $\sec(\zeta)$ is air mass at zenith distance (ζ). Please note that air mass approximation with the secant function is applicable with air mass less than four, as suggested by Young (1994).

Higher r_0 represents a better observing condition, or less turbulence strength. At generally considered good observation sites, such as Mauna Kea and the Canary Islands, during nighttime median r_0 at 500 nm is 10 cm or less, or equivalently 1 arcsecond seeing, as shown in measurements at Mauna Kea by Tokovinin et al. (2005) and at the Canary Islands by Fuensalida et al. (2004). However, in the day situations can be worse as r_0 dropping to approximately 2.5 to 5 cm, as shown in measurements at various sites, such as the Canary island by Marco De La Rosa et al. (2016), Plateau de Calern in France by Aristidi et al. (2020) and Chabé et al. (2020), and Big Bear solar observatory in the United States of America by Kellerer et al. (2012).

Atmospheric turbulence is often distributed vertically with varying speed and direction, as shown in Tokovinin et al. (2005), Fuensalida et al. (2004), Marco De La Rosa et al. (2016), Aristidi et al. (2020), Chabé et al. (2020), and Kellerer et al. (2012). Simulating larger fields of AO correction requires the generation of atmospheric layers at different heights. There are several turbulence profiling methods, such as Scintillation Detection and Ranging (SCIDAR) by Avila et al. (2000), Multiaperture Scintillation Sensor (MASS) by Kornilov et al. (2003), Shadow Band Ranging (SHABAR) by Sliepen et al. (2010), Profiler of Moon Limb (PML) by Chabé et al. (2020), etc.

2.5.1.2 Phase Structure Function

The phase structure function represents the statistical variation of optical phase versus separation. Let the structure function of phase (ϕ) be $D_\phi(r)$. Let r be the separation between any two random points and x be a central point of measurement. The relation can be written mathematically as

$$D_{\phi}\left(r\right) = \langle\left(\phi\left(x\right) - \phi\left(x + r\right)\right)^{2}\rangle. \tag{2.34}$$

The structure function of the phase of Kolmogorov turbulence statistics is realistic for a range between the upper and lower scales (L_o and l_o, respectively). The structure function with Kolmogorov statistics is

$$D_{\phi,K}\left(r\right) = 6.88\left(\frac{r}{r_0}\right)^{5/3}. \tag{2.35}$$

Modified von Kármán structure function of phase can be written as a modification of Kolmogorov statistics. The modification for separation larger than the inner scale (l_o) is

$$D_{\phi,vK}\left(r\right) = D_{\phi,K}\left(r\right) \times 0.895\left(\Gamma\left(\frac{5}{6}\right)\left(\frac{2\pi x}{L_0}\right)^{-5/3} - 1.12\left(\frac{2\pi x}{L_0}\right)^{-5/6} K_{5/6}\left(\left(\frac{2\pi x}{L_0}\right)\right)\right). \tag{2.36}$$

where Γ is the gamma function and $K_{5/6}$ is the Modified Bessel function of the second kind of real order 5/6 (Sasiela, 2007). When the separation is smaller than the inner scale (l_o), the variance would be negligible.

The structure function of Kolmogorov and von Kármán turbulence is plotted in comparison in Figure 2.2. The major difference between the two is the plateau behaviour at large separations introduced by the outer scale (L_o) of von Kármán statistics. The structure function of turbulence of a stronger turbulence strength will shift upward on the y-axis.

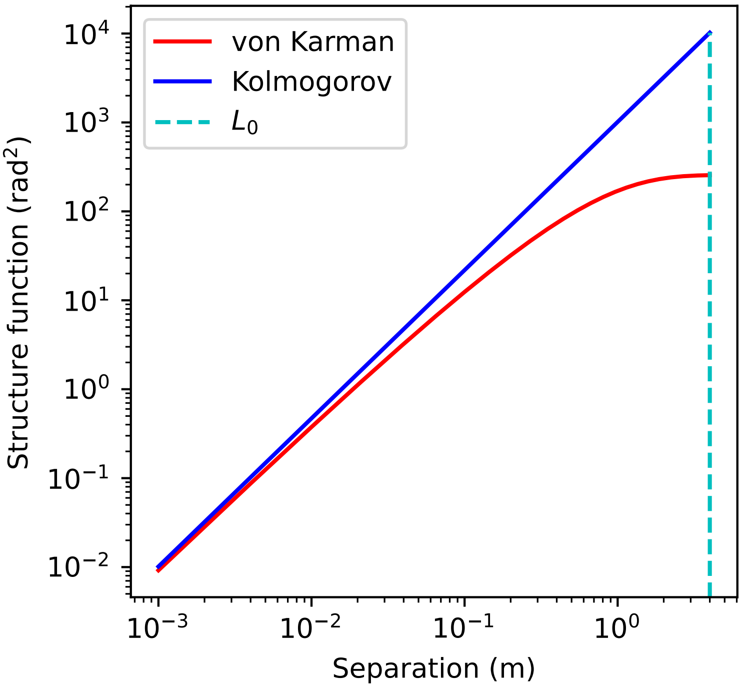

Figure 2.2: *Comparison between structure functions of Kolmogorov (blue) and von Kármán (red) statistics. Turbulence of 5 cm r_0 and 5 m L_0 is shown.*

2.5.1.3 Power Spectral Density of Wavefront Distortion

Power Spectral Density (PSD) describes the statistical power within each spatial frequency in an atmospheric turbulence layer. PSD of values x can be calculated by taking an average of the Fourier transform of the modulus square of the quantity of interest, shown mathematically in Stoica and Moses (2005) by

$$\mathrm{PSD}_x = \langle \mathcal{F}\left\{|x|^2\right\}\rangle. \tag{2.37}$$

The PSD of the phase of Kolmogorov statistics is

$$\Phi_{\phi,K}\left(f\right) = 0.023 r_0^{-5/3} f^{-11/3}, \tag{2.38}$$

where f is spatial frequency, r_0 is Fried parameter. Similarly, the PSD of phase of modified von Kármán statistics is

$$\Phi_{\phi,mvK}\left(f\right) = 0.023r_0^{-5/3}\frac{e^{-f^2/f_m^2}}{\left(f^2+f_o^2\right)^{11/6}}, \tag{2.39}$$

where L_o is the outer scale, which is the largest spatial scale over which turbulence forms, l_o is an inner scale below which turbulence does not occur, $f_m = 0.94/l_0$ and $f_o = 1/L_o$ (Schmidt, 2010). The behaviour of these two statistics is shown in Figure 2.3. Again, Kolmogorov turbulence has no termination of PSD at outer and inner scales. The PSD of modified von Kármán statistics flattens out at lower frequencies, while it drops down rapidly at higher frequencies corresponding to that of outer and inner scales, respectively.

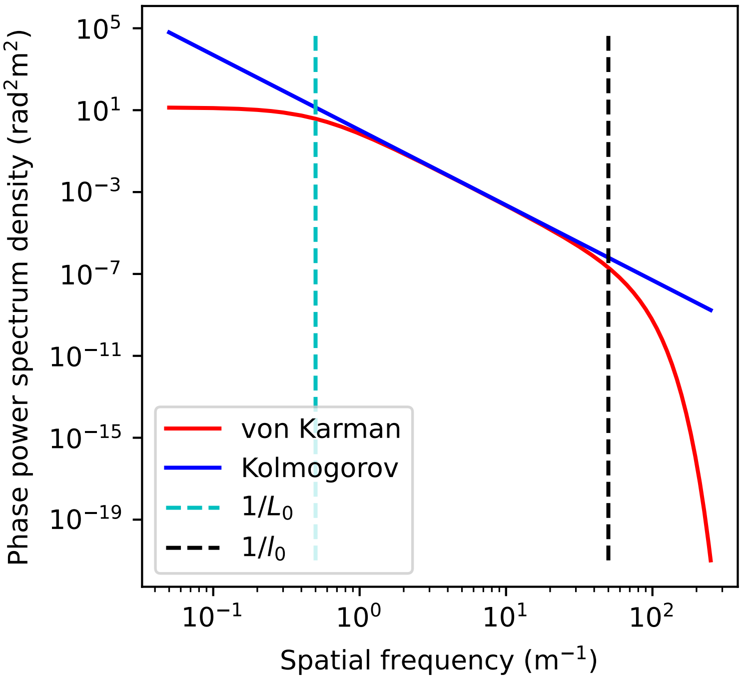

Figure 2.3: *Comparison between phase PSD of Kolmogorov (blue) and von Kármán (red) statistics. Turbulence of 10 cm* r_0*, 20 m* L_0*, and 2 cm* l_0 *is shown.*

2.5.1.4 Zernike Polynomial Decomposition

Optical phase distortions can be analysed by decomposing them into a superposition of orthogonal modes. A common series to use is the Zernike polynomials, which are orthonormalised over a unit-radius circular aperture as a function of radius and angle (Noll, 1976). Each Zernike mode represents different independent optical aberrations such as piston, tip/tilt, defocus, astigmatism, spherical, and coma. Noll (1976) proposed both a numbering scheme and a normalisation scheme that is commonly used. Let Z_n be the nth Zernike mode having the orthonormal property such that

$$Z_i \cdot Z_j = 1; if i = j \tag{2.40}$$

$$Z_i \cdot Z_j = 0; if i \neq j \tag{2.41}$$

where δ_{ij} is Kronecker delta function. The dot product of two different modes equals 0, and the dot product of the same mode equals 1.

Let ϕ be the phase deviation of optical turbulence. By the property of an orthonormal function,

$$\phi = \sum_{i}^{\infty} a_i Z_i \tag{2.42}$$

$$a_i = \phi \cdot Z_i, \tag{2.43}$$

where a_i is power of ith Zernike modes

Noll (1976) presented the mean variance of phase after subtraction of each Zernike mode for a Kolmogorov phase screen. Noll used Kolmogorov's model, according to Equation 2.35; consequently, the results are approximately valid for von Kármán turbulence for spatial scales between the outer and inner scale of turbulence. Variances of each mode $\sigma^2_{a_i}$ are in terms of

$$\sigma^2_{a_i,K} = A \left(\frac{D}{r_0}\right)^{5/3} \text{rad}^2, \tag{2.44}$$

where D is aperture diameter and A is a number derived from Noll (1976). For example, the numbers are 0.4480, 0.0230, and 0.0062 for Zernike modes with radial mode numbers 2, 3, and 4, respectively.

For von Kármán statistics, there is a modification to the Kolmogorov statistics for tip/tilt modes for when aperture D is smaller than outer scale L_o as follows. The difference of higher-order Zernike modes is negligible (Sasiela, 2007).

$$\sigma^2_{\text{tip/tilt,vK}} = \sigma^2_{\phi_{\text{tip/tilt,K}}} \left[1 - 1.42 \left(\frac{D}{L_o}\right)^{1/3} + 3.70 \left(\frac{D}{L_o}\right)^{2} - 4.01 \left(\frac{D}{L_o}\right)^{7/3} + 4.21 \left(\frac{D}{L_o}\right)^{4} - 4.00 \left(\frac{D}{L_o}\right)^{13/3} \right] \text{rad}^2 \tag{2.45}$$

The modal Zernike decomposition of Von Kármán and Kolmogorov atmospheres is shown in Figure 2.4, where the von Kármán statistics have a suppressed tip/tilt power.

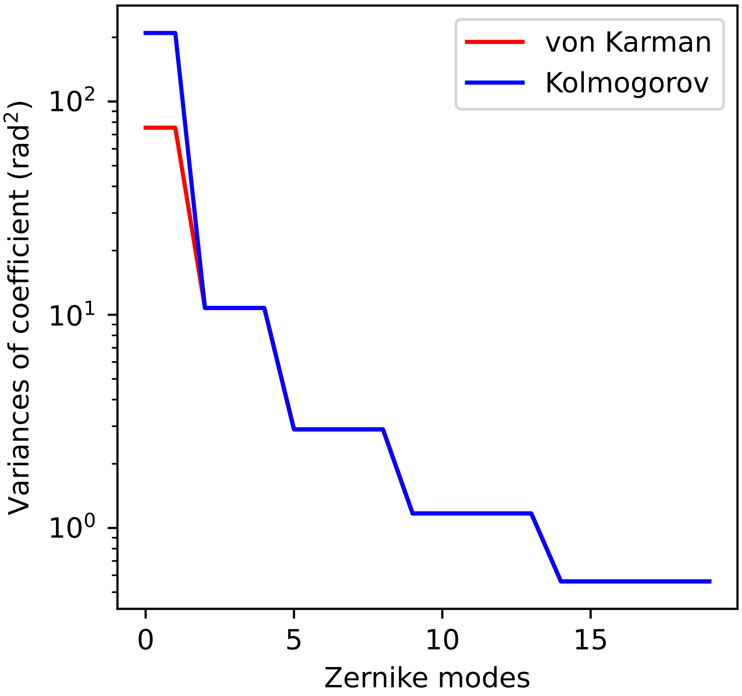

Figure 2.4: *Comparison between Zernike mode decomposition of Kolmogorov (blue) and von Kármán (red) statistics. Turbulence of 5 cm* r_0 *and 20 m* L_0 *with a 2 m aperture size is shown. The majority of the plot overlaps.*

2.5.2 Optical Propagation and Scintillation

Light diffracts as it propagates over a distance. The effect is normally not considered in AO system design for near-infrared astronomy, because its effect is negligible at longer wavelengths and weaker turbulence. In situations where stronger turbulence can be encountered, such as solar astronomy and free-space optical communications, or operation at very short wavelengths, optical propagation through optical turbulence must be included. As the effect of optical propagation through turbulence becomes more pronounced, the variation in intensity increases. This phenomenon is called scintillation. A famous example is the twinkling of the stars. In this thesis, the scintillation is defined by the variance of log-amplitude spatially over the whole plane of observation (Sasiela, 2007), unless declared otherwise.

The log-amplitude variance (σ_χ^2) of a wavefront propagating through turbulence layers can be calculated using Rytov's approximation (σ_R^2), Equation 2.46 (Sasiela, 2007). Even though the approximation of σ_χ^2 is valid from σ_R^2 between 0 and 0.25 (Sasiela, 2007), σ_R^2 can be used as a marker for AO analysis (Roggemann and Koivunen, 2000; Barchers et al., 2003). The Rytov approximation is

$$\sigma_\chi^2 \approx \sigma_R^2 = 0.5631 k^{7/6} \sec^{11/6}(\zeta) \int_0^L z^{5/6} C_n^2(z)\, dz; \text{ for } \sigma_R^2 < 0.35 \tag{2.46}$$

An example of the evolution of both the optical phase and intensity propagating a distance from an optical turbulence is shown in Figure 2.5. The propagation distance has been increased to show different scintillation indices. When $\sigma_R^2 > 0.2$, wavefront sensor measurements may become inaccurate (Barchers et al., 2003). Analytical solutions to propagation through turbulence using smooth perturbation start to fail at $\sigma_R^2 = 0.35$ (Sasiela, 2007). The scintillation becomes saturated at $\sigma_R^2 = 0.6$ (phase tends to be uniformly distributed, resulting in maximum variation in intensity), setting an upper limit where the scintillation effect becomes dominant. In this regime, measurement of the wavefront phase can become inaccurate.

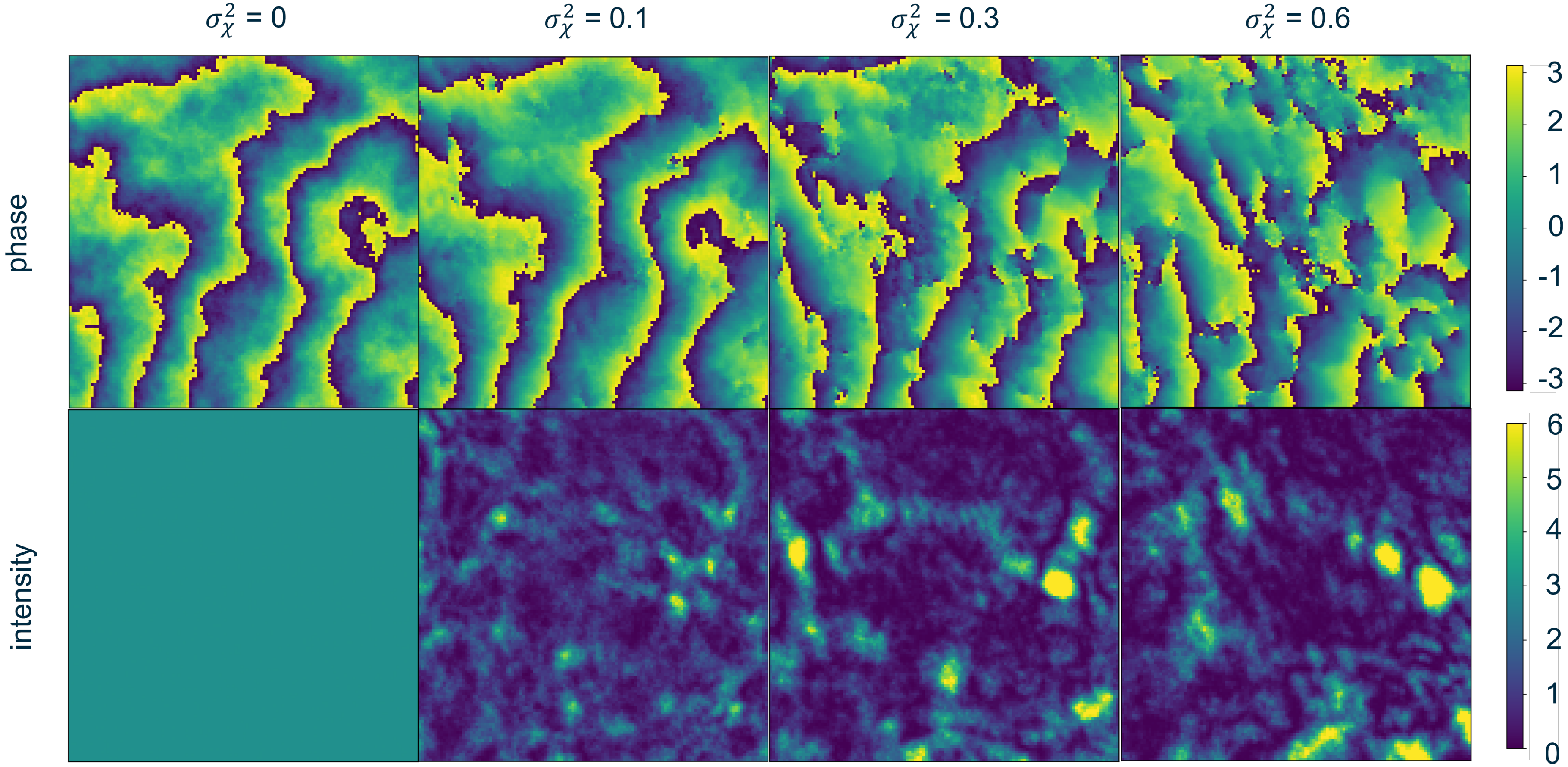

Figure 2.5: *Phase in radians (top) and intensity normalised to the mean (bottom) of a 500 nm, 40 cm aperture, 5 cm* r_0 *turbulence as it propagates down a line of sight at increasing Rytov's approximation* (σ_R^2)*. This is a plane wave propagation from space to ground; hence, there is no pupil and edge effect. Figure from Kongkaew et al. (2024)*

The spatial size of log-amplitude's scintillation pattern can be determined by measuring either the covariance function of log-amplitude (b_χ) (Tartarskii, 1971) or the structure function of log-amplitude (Andrews and Phillips, 2005). The width of the covariance varies with the Fresnel zone size, while the structure function saturates at the Fresnel zone size. The Fresnel zone radius (R) is

$$R = \sqrt{\lambda z}. \tag{2.47}$$

2.6 Conclusion

In this chapter, we have presented the background theory on optical propagation and atmospheric turbulence that is used throughout the rest of the thesis. Subsequent chapters will make extensive use of the angular-spectrum propagation to calculate phase and intensity at principal planes (e.g turbulent atmospheric layers, wavefront sensors and deformable mirrors) within the system.

3 Simulation of Adaptive Optics

This chapter describes the simulations used in this thesis and their validation to ensure that the results coming from the simulations accurately model the system under investigation. The majority of the simulation uses Python Adaptive Optics (AO) related packages, including AOtools (Townson et al., 2019) and Soapy (Reeves, 2016) directly without any adaptation. Optical turbulence generation, Deformable Mirror (DM), Wavefront Sensor (WFS), control laws, and residual wavefront analysis are all unchanged from the base code. Changes made in this work and described in this chapter relate to the implementation of optical propagation and the AO system calibration techniques:

- Though both AOtools and Soapy include optical propagation packages, they do not have an automatic process to determine appropriate propagation parameters suitable for accurate AO simulation. Here I present these tools and describe how they perform.
- Modifications to the simulation calibration scripts which are required to investigate the effects of multiple DMs within a system that can apply control distortions. The analysis of these effects is presented in Chapter 5. Here, we present only the calibration method.

- In some configurations, the mathematically required simulated turbulence at a high altitude layer might be too large compared to what happens physically, using more computational resources than needed. We propose a method to reduce the requirement while maintaining significant accuracy.

In this chapter, I first confirm the validity of the phase screen generation methods used within the simulation by comparing them to theory. Then, investigate and compile a set of requirements to accurately simulate optical propagation. After that, verify the simulated propagation against its theoretical effects, such as the structure function of the scintillation pattern and log-amplitude variances. Later, a method to reduce the size of the mathematically required turbulence screen at high altitude is proposed and verified. Furthermore, I also estimated the reduction in the computational load of this method. I benchmark the simulation process on a point source Shack-Hartmann Wavefront Sensor (SH-WFS), determining its configurations. Finally, I test Soapy's simulation of DMs, wavefront analysis, and AO control and confirm that the simulation of these AO system components recreates expected performance.

The adaptation of Soapy in this thesis can be found in a GitHub code repository (`https://github.com/gqmc62/soapy`) (Kongkaew, 2025b).

3.1 Simulation of Turbulent Optical Phase Layers

Existing processes to generate optical phase turbulence in AOtools and Soapy include the Fourier transform (Schmidt, 2010), the sub-harmonic Fourier transform (Schmidt, 2010), von Kármán infinite phase screen (Assémat et al., 2006), and Kolmogorov infinite phase screen (Fried and Clark, 2008). The Fourier transform and sub-harmonic Fourier transform can only generate one instance of turbulence, limiting the ability to generate time series of turbulence flow, while, as the name suggests, the infinite phase screen methods can. Because the AO simulation needs a time series, the infinite phase screen methods are commonly used, thus we focus solely on these two models.

The von Kármán infinite phase screen was first proposed in Assémat et al. (2006). The method uses an initial screen generated through the Fourier transform methods, then generates the next turbulence flows using the Von Kármán turbulence statistics. As a result, the first generated screen do not have the desired statistics. The screen must be flushed out or regenerated first to allow the next screen to be generated at the correct statistics. As the name suggests, the process should generate von Kármán statistics turbulence. However, Fried and Clark (2008) notices that Assémat et al. (2006)'s method cannot contain statistics larger than the phase screen width, containing only one-third of the width.

Fried and Clark (2008) updates Assémat et al. (2006) to also generate phase screens that follow Kolmogorov statistics. The naming of Fried and Clark (2008)'s method as Kolmogorov-like led AOtools (Townson et al., 2019) to think it is only applicable to the Kolmogorov statistics turbulence, while in fact, it is also applicable to the von Kármán statistics. To investigate the accuracy with which these phase screen generation methods match the theoretical definitions of Kolmogorov and Von Kármán turbulence, we must undertake statistical tests on the generated phase screens. Several tests can be undertaken to demonstrate this, including: phase spatial structure function, phase spatial Power Spectral Density (PSD) analysis, and variance of Zernike mode decomposition on phase.

The generated turbulence using Fried and Clark (2008) or the Kolmogorov infinite phase screen method is tested statistically for PSD in Figure 3.1, structure function in Figure 3.2, and Zernike mode analysis in Figure 3.3. The Kolmogorov infinite phase screen method in AOtools and Soapy is found to match the von Kármán statistics still. This is possible because the AOtools and Soapy use turbulence phase covariance of the von Kármán statistics for the infinite phase screen Kolmogorov statistics (Townson et al., 2019), resulting in having von Kármán turbulence statistics while correcting the unmatches in statistics at longer separation noticed by Fried and Clark (2008).

Figures 3.1, 3.2, and 3.3 analyse 100 infinite phase screens using the Kolmogorov and von Kármán method with 40 cm diameter width, 5-cm Fried parameter, and 4 m outer turbulence scale after generating the next two width sizes, in other words, flushing out two screen widths. Under the same initial parameters, the one-dimensional PSD analysis on the von Kármán method has a larger error, almost comparable in magnitude to the mean value (Figure 3.1). The structure function analysis in Figure 3.2 compares the statistical difference of each point along the row to one of the columns on the edge or vice versa. The von Kármán method has a one-axis structure function noticeably lower than the theoretical values. The drops in one of the axis structure function of the von Kármán method are also noticeable in Zernike mode decomposition in Figure 3.3, where one of the tip/tilt values has less power than the theoretical value. Meanwhile, in all of these analyses, the Kolmogorov method matches the von Kármán turbulence statistics. Consequently, the infinite phase screen Kolmogorov in AOtools and Soapy or Fried and Clark (2008) is used for this thesis.

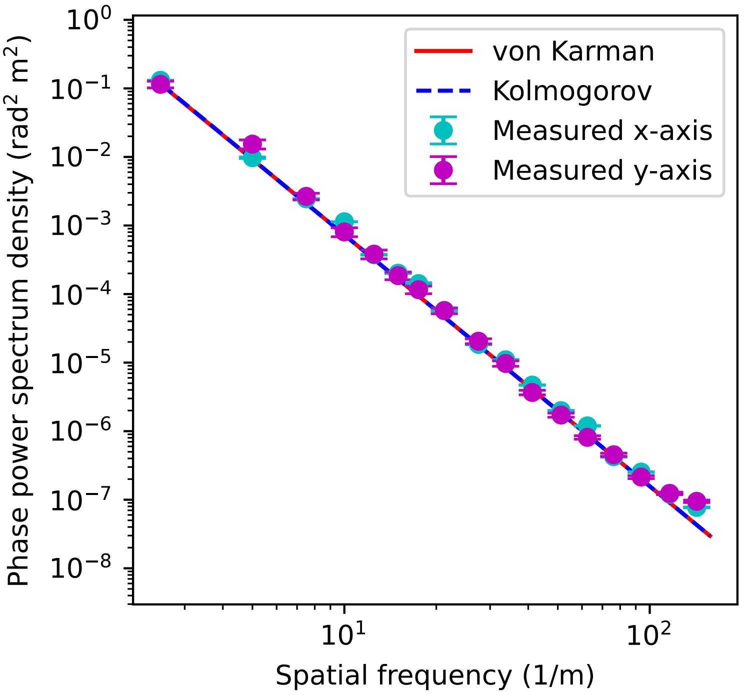

(a) *Kolmogorov infinite phase screen method*

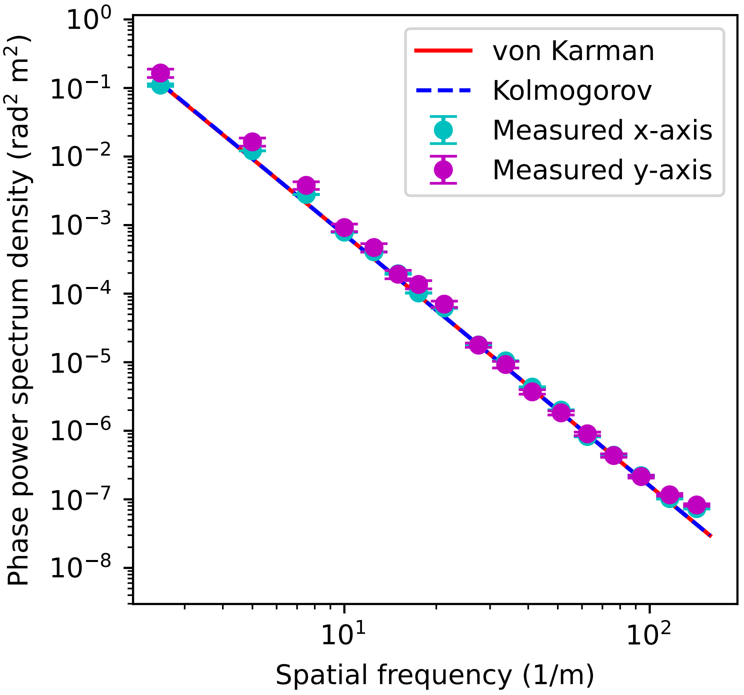

(b) *von Kármán infinite phase screen method*

Figure 3.1: *Mean measured phase PSD of simulated phase screen from the Kolmogorov method (a) and von Kármán method (b) to generate infinite phase screens in Soapy, along the x and y axes. The theoretical PSD for both statistics are shown, and overlaps. The phase screens are generated at x=0, then moved along the x-axis.*

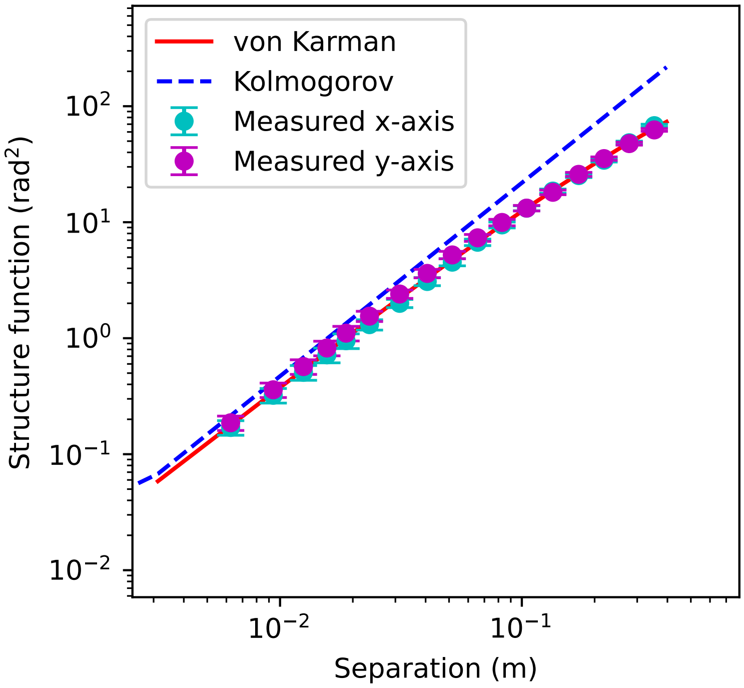

(a) *Kolmogorov infinite phase screen method*

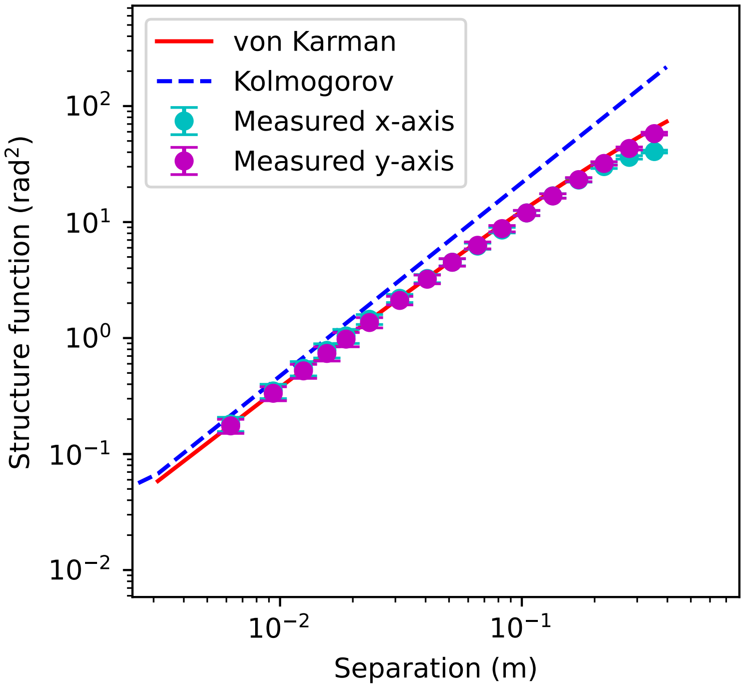

(b) *von Kármán infinite phase screen method*

Figure 3.2: *Mean structure function of simulated phase screen from the Kolmogorov method (a) and von Kármán method (b) to simulate infinite phase screens in Soapy against the separation. The theoretical structure functions are also shown as references. The phase screens are generated at x=0, then moved along the x-axis.*

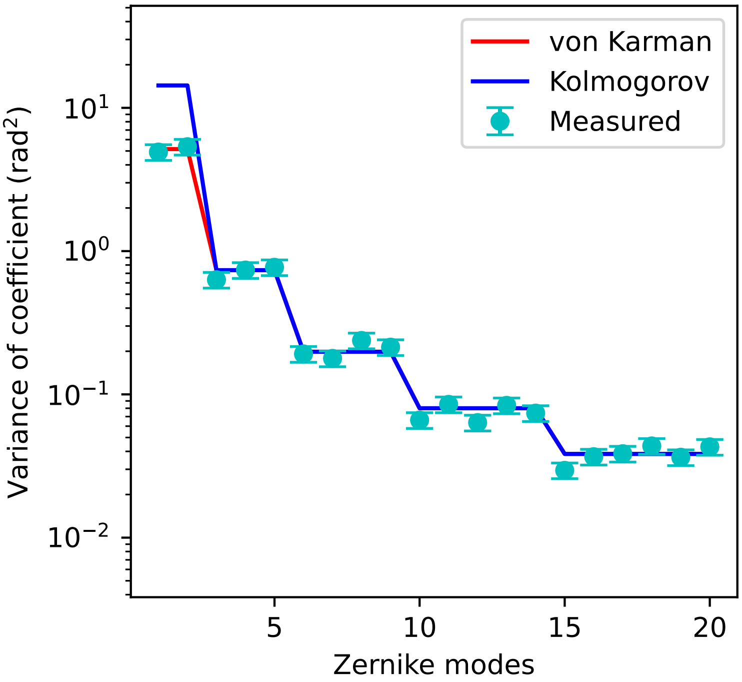

(a) *Kolmogorov infinite phase screen method*

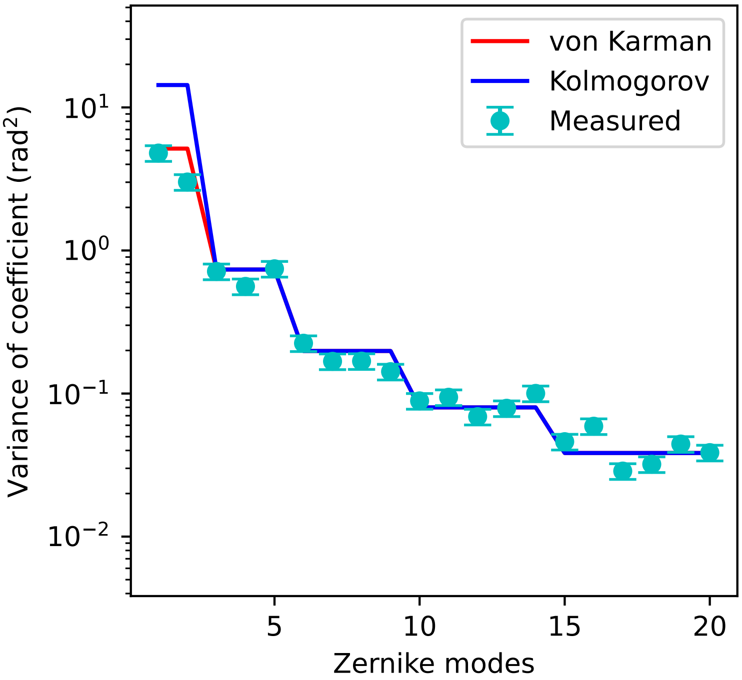

(b) *von Kármán infinite phase screen method*

Figure 3.3: *Mean of Zernike mode power of simulated phase screen from the Kolmogorov method (a) and von Kármán method (b) to simulate infinite phase screens in Soapy. The theoretical values of both statistics are shown as references. The phase screens are generated at x=0, then moved along the x-axis. The second mode corresponds to gradients along the x-axis.*

3.2 Simulation of Optical Wave Propagation

In most astronomical AO simulations, ignoring optical propagation effects between various atmospheric turbulence layers and the principal components in the AO system does not introduce significant errors in the simulation (Van Dam et al., 2020). However, when considering stronger turbulence, such as may be encountered in Solar AO or free-space optical communications (Griffiths et al., 2024), then optical propagation effects can introduce significant degradation of the AO performance (Farley et al., 2017; Biasi et al., 2023).

There are several methods for simulating optical propagation (Schmidt, 2010), including one-step Fresnel, two-step Fresnel or angular spectrum. The angular spectrum propagator is particularly suited to AO simulations because it allows/enables flexible propagation distance and spatial scale of simulation elements at each propagation plane. It can be implemented using Fourier Transforms. However, the simulation parameters must be carefully selected to avoid effects such as wrapping, ripples, and aliasing.

There are conditions to calculate propagation accurately (Schmidt, 2010). The conditions are: there must be no aliasing in any of the exponential terms during forward/backwards Fourier transform, there must be no wrapping effect from the periodic boundary of Discrete Fourier Transform (DFT), and input coverage must cover physical behaviour. Please beware that the propagation simulation only represents one Line-of-Sight (LoS). So for wide-field simulation, multiple LoSs must be simulated. Lastly, unless there are any ‘stops’ that need to be simulated, all propagation distance (z) is measured from the pupil, because any ripple effects start at either the pupil or stops where diffraction occurs.

In this section, we explore methods to mitigate aliasing and wrapping effects and ensure complete optical aberration and angular spectrum frequency coverage of turbulence at high altitudes. After that, we verified the optical propagation result against theory on log-amplitude variance and size of scintillation patterns. I then introduce, verify, and estimate the benefit of reducing the mathematically required to the physically required simulation of high-altitude turbulence size. Lastly, I compile the list of criteria to consider to accurately simulate the optical propagation in the conditions used in this thesis. Then I automate the selection of the required propagation parameters, in order to eliminate worries and hassles in the tedious process.

3.2.1 Aliasing

Due to the cyclical nature of complex numbers, neighbouring pixels with phase (ϕ) difference larger than π will mathematically have a different phase angular distance in the complex plane, as shown in Figure 3.4.

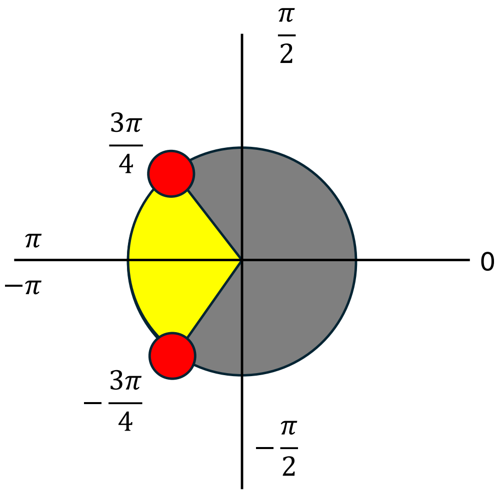

Figure 3.4: *The Phase difference between two points in a complex plane is not always the same as their arithmetic subtraction. For example, phases differ between* $3\pi/4$ *and* $-3\pi/4$*, have their arithmetic subtraction equal to* $6\pi/4$ *(grey-shaded area), even though they are only* $2\pi/4$ *apart (yellow-shaded area).*

When using an optical propagator, we should try to avoid aliasing effects, which can be achieved initially by careful selection of the simulation parameters. These must be assessed for every complex term, and also during mathematical operations that may occur during subsequent simulation steps, such as the addition and multiplication of complex numbers.

Anti-aliasing can be implemented by limiting the maximum local spatial frequency (f_{loc}) to be less than the Nyquist sampling frequency ($f_{Nyquist}$, Equation 2.14). The local spatial frequency is defined as (Schmidt, 2010)

$$f_{Nyquist} \geq f_{loc} = \frac{1}{2\pi}\nabla\phi, \tag{3.1}$$

where $\nabla\phi$ is the phase gradient of each complex term in the simulation process. To ensure that aliasing is not present in the conversion of an optical phase screen into its complex form, the phase difference between adjacent elements must be less than π radians.

Further analysis of anti-aliasing in optical propagation must also consider the curvature (R) of a wavefront. A flat wavefront will have an infinite curvature, whereas a wavefront focusing at a distance f_{fl} will have a curvature of $-f_{fl}$. The complex amplitude of the wavefront with curvature (R) can be written in the following form (Schmidt, 2010),

$$U(x_1, y_1) = A(x_1, y_1)e^{\frac{ik}{2R}(x_1^2+y_1^2)}, \tag{3.2}$$

where U is the complex amplitude representation of the optical wave, A is the real amplitude, k is the wavenumber, and x_1 & y_1 represent spatial coordinates of the plane perpendicular to the propagation axis.

3.2.1.1 Anti-aliasing criterion between pupil and focal planes

Focusing optics from the pupil plane to the focal plane is simply simulated using a one-step Fresnel propagation method (Equation 2.19). To avoid aliasing effects, the following criteria must be met (Schmidt, 2010).

$$\left|\frac{1}{z}+\frac{1}{R}\right|\frac{D_1}{\lambda}\leq\frac{1}{\delta_1}, \tag{3.3}$$

where z is the propagation distance, D_1 is the beam diameter at the pupil plane, and δ_1 is the phase element resolution at the source plane.

A one-step Fresnel simulation will propagate a wavefront through a lens with a defined aperture function, defining the aperture shape and intensity, then focusing at the lens focal point. If the input wavefront is collimated, the simulation will have no aliasing, because it has equally opposite z and R (Equation 2.30 and Equation 3.2).

3.2.1.2 Anti-aliasing criterion between two planes

Propagation from high-altitude turbulence is best modelled using the angular spectrum propagation (Schmidt, 2010). There are two criteria to consider for angular spectrum propagation (Equation 2.24). The first criterion to consider applies to the complex term in the forward Fourier transform, and the other, outside of the inverse Fourier transform (Schmidt, 2010).

$$\left|\frac{1}{z}\left(1-\frac{\delta_2}{\delta_1}\right)+\frac{1}{R}\right|\frac{D_1}{\lambda}\leq\frac{1}{\delta_1} \tag{3.4}$$

Angular propagation of a collimated wavefront ($R=\infty$) between the source and destination plane with the same element resolution at original and target plane(δ_1 and δ_2 respectively) always passes this criterion.

Similarly, the anti-aliasing criterion for the complex term inside the inverse Fourier transform is (Schmidt, 2010),

$$N\geq\frac{\lambda z}{\delta_1\delta_2}, \tag{3.5}$$

where N is the number of elements across a simulated propagation plane.

3.2.2 Wrapping

The output of the DFT wraps values at its boundary (Schmidt, 2010). This can introduce spurious artefacts in the optical propagation, and subsequent propagation can preserve the effect. Simulation parameters must therefore be selected to avoid any wrapping effects between propagation layers. In this section, according to Equation 2.14 and 2.23, the maximum angular spectrum frequency (α_{max}) that can be sustained by a Fourier transform is

$$\frac{\alpha_{max}}{\lambda} = \frac{1}{2\delta_1}. \tag{3.6}$$

If this plane wave propagates for a distance of z, then it would have travelled in a plane orthogonal to the optical axis by

$$\alpha_{max} z = \frac{\lambda z}{2\delta_1}. \tag{3.7}$$

Figure 3.5, shows how the criterion to avoid wrapping effects is determined for an angular spectrum propagator.

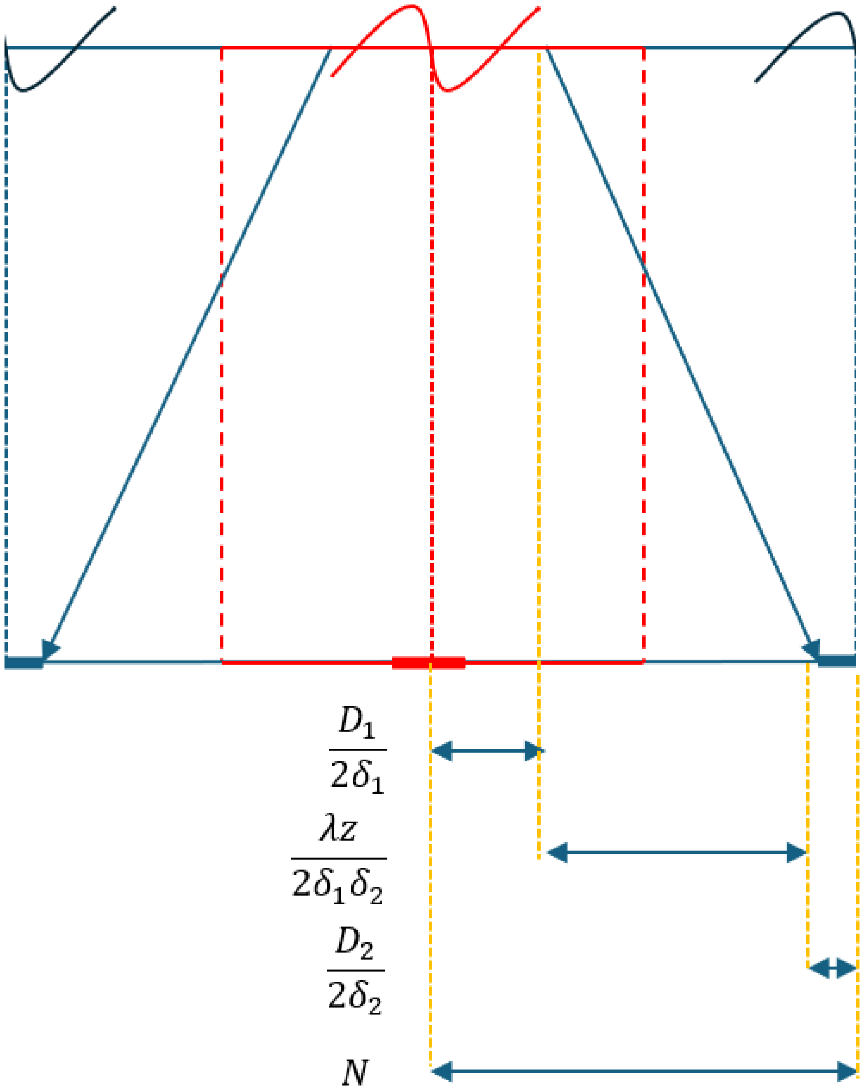

Figure 3.5: *Diagram showing propagation of light between two planes. To avoid wrapping effects, the simulation must zero-pad the complex amplitude at the upper layer up to area within the red dashed line. Due to the cyclical nature of the discrete Fourier transform, the larger region defined by the dashed blue lines must also be considered to avoid wrapping effects in the propagated complex amplitude at the lower plane.*

Let D_1 and D_2 be the desired accurate simulation size at the source and destination plane, respectively. The total simulation screen size must be larger than

$$N \geq \frac{D_1}{2\delta_1} + \frac{D_2}{2\delta_2} + \frac{\lambda z}{2\delta_1\delta_2}. \tag{3.8}$$

For one-step Fresnel propagation where $\delta_2 = \lambda z / N\delta_1$, this inequality can further be simplified to

$$N \geq \frac{D_1}{\delta_1} + \frac{D_2}{\delta_2} \tag{3.9}$$

3.2.3 Complete Coverage of Input

In this section, two cases are considered to ensure that optical aberration from a high altitude turbulent layer, which reaches the target region of interest, has the desired aberration and maintains its angular spectrum. The first case is essentially the same as the previous section on wrapping. Nonetheless, the concept of the complete input still holds and should not be taken lightly, because the second case results in a different conclusion.

The first case is when the wavefront at the source plane has stops, and is considered a desirable part of the simulation. The second case is when there are no stops at the source plane, such as the sunlight from the high atmosphere. In the latter case, the simulated turbulence at the high altitude must cover the region where it would reach the target region of interest (Schmidt, 2010).

3.2.3.1 Without Pupil

For the second case, consider the propagation of a beam in free space, such as the propagation of light between turbulent layers in the atmosphere (top) to the telescope pupil (bottom) in Figure 3.6. The solid blue arrows from top to bottom mark the highest mathematical reach, while the dashed blue arrows mark a highest reach of some high percentage, say 97% of light. The relative size between the mathematical and physical reach presented here is exaggerated. If the difference between the mathematical and physical is indeed this huge, the question is: why should we simulate the excess part? The answer is: if we do not fill in with optical turbulence, filling the excess region with zeros instead, we will essentially simulate an optical stop, which does not exist on the sky. The second question is: why can't we count the blue region of the simulated turbulence as the buffer? The answer is: because we only simulated the red region, so the boundary between the red and blue is not continuous. The uncontinuity will introduce a high spatial frequency not contained within the angular spatial frequency of the system. Without any mitigation, the turbulence must be generated fully. Fortunately, I will introduce the mitigation of this in the future section.

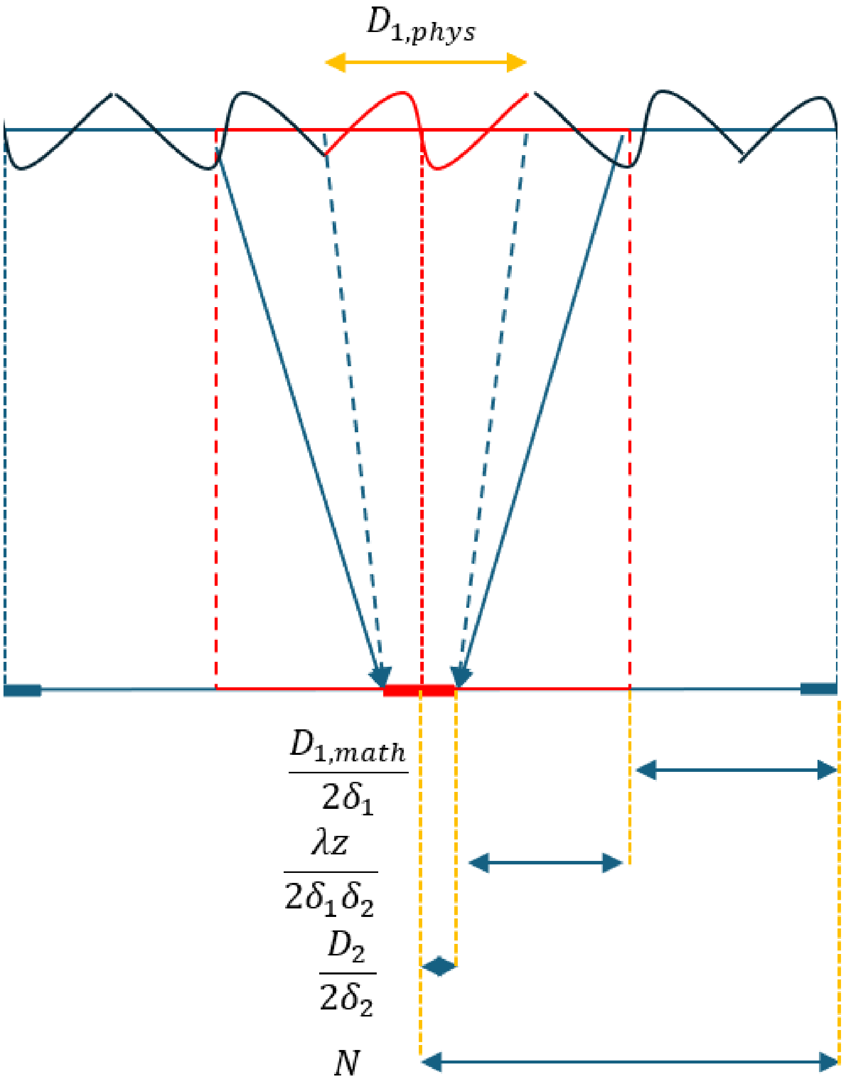

Figure 3.6: *Diagram showing propagation of light between two planes. Light propagating to the region of interest (denoted by the thick red line in the lower plane) can come from outside the region in the upper layer defined by physical properties alone due to the cyclical nature of the Fourier Transform. The larger region described by the dashed red lines must be included within the simulation to avoid rippling effects at the edge of the region of interest.*

Meanwhile, the criterion for propagation from space is

$$\frac{D_{z,math}}{2\delta_z} \geq \frac{D_{pupil}}{2\delta_{pupil}} + 2\frac{\lambda z}{2\delta_{pupil}\delta_z}, \tag{3.10}$$

where $D_{z,math}$ is the unwrapped non-zero-padded diameter at propagation distance z, δ_z is the resulting/required pixel scale at distance z from the pupil, D_{pupil} and δ_{pupil} is the telescope pupil diameter and phase resolution element size at the pupil plane, respectively.

In some configurations, the required simulated input turbulence might be too large for accessible computational power. The next few sections propose a method to reduce the requirement while maintaining significant accuracy.

3.2.4 Expansion of Projected Pupil Size

The projected pupil size expands with increasing distance from the telescope as defined by the and due to atmospheric refraction. Due to atmospheric refraction, akin to seeing, the meta-pupil at a distance z from the pupil will be expanded by a factor relating to the atmospheric seeing as defined by r_0 (Schmidt, 2010). These effects will be present within the simulation and must therefore be accounted for when selecting the key simulation parameters. To simulate a turbulent layer at a distance (z) from a telescope of pupil diameter (D_0) at wavelength (λ), we must include the atmospheric diffraction at the telescope pupil with total turbulence strength (r_0), then the projected diffracted telescope pupil size (D_{pz}) at altitude (z) within one LoS across a field of view FoV, is

$$D_{pz} = D_0 + c_e\frac{\lambda z}{r_0} + FoV z, \tag{3.11}$$

where we define c_e as a coefficient describing the *light-coverage* factor. With $c_e = 2$, about 97% of light is covered, while with $c_e = 4$, about 99% of light is covered (Schmidt, 2010). For this thesis light-coverage factor of 2 is used. The coverage at each altitude can be tailored down layer by layer with the equivalent r_0 of each layer before that layer, including ground; however, for simplicity, this simulation used the accumulated r_0 for all layers from having the maximum dispersion.

This physical effect of pupil expansion in Equation 3.11 is usually much smaller than that of the mathematical expansion described in Equation 3.10. Generating a much larger amount than physically needed is daunting, so this thesis proposes and validates a mitigation method in the next few sections.

3.2.5 Complete Coverage of Angular Spectrum

If the simulation is using angular spectrum propagation, the maximum angular spectrum should be larger than most light travelling angles, including Field-of-View (FoV) in a LoS and atmospheric diffraction angle introduced in the last section.

$$\begin{aligned} \frac{\lambda}{2\delta} &= \alpha_{max} \qquad (3.12) \\ &\geq \frac{FoV}{2} + c_e \frac{\lambda}{2r_0} \qquad (3.13) \end{aligned}$$

3.2.6 Verification against Known Effects

Lastly, the propagation using the proposed method is analysed for log-amplitude variance (σ_χ^2) and size of intensity variation pattern as seen in Figure 2.5. The size of the intensity variation pattern is the separation where the intensity structure function plateau, adapted from Tartarskii (1971). The results are shown in Figure 3.7 and 3.8, respectively, matching the expected theoretical behaviour.

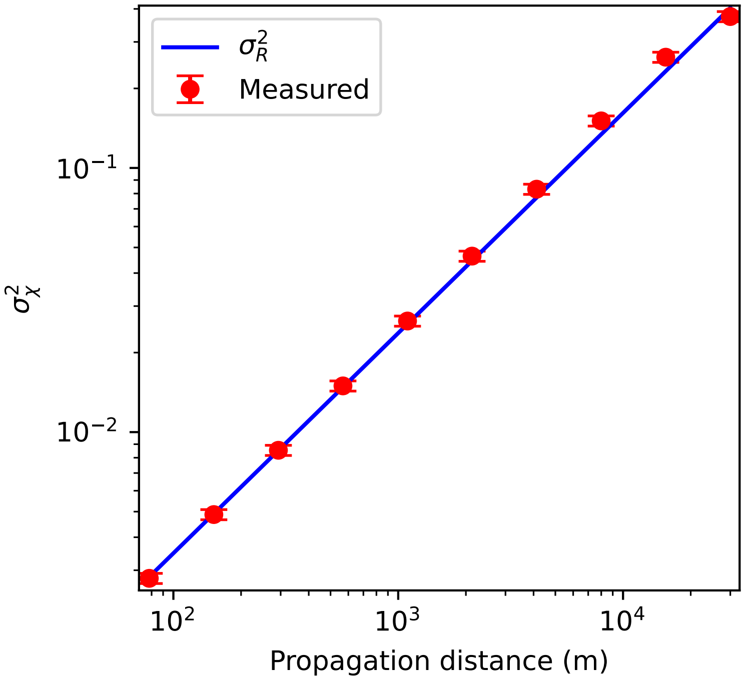

Figure 3.7: *The simulated (red dots) and Rytov approximation (blue line) of the log-amplitude variances (y-axis) are shown against propagation distance (x-axis).*

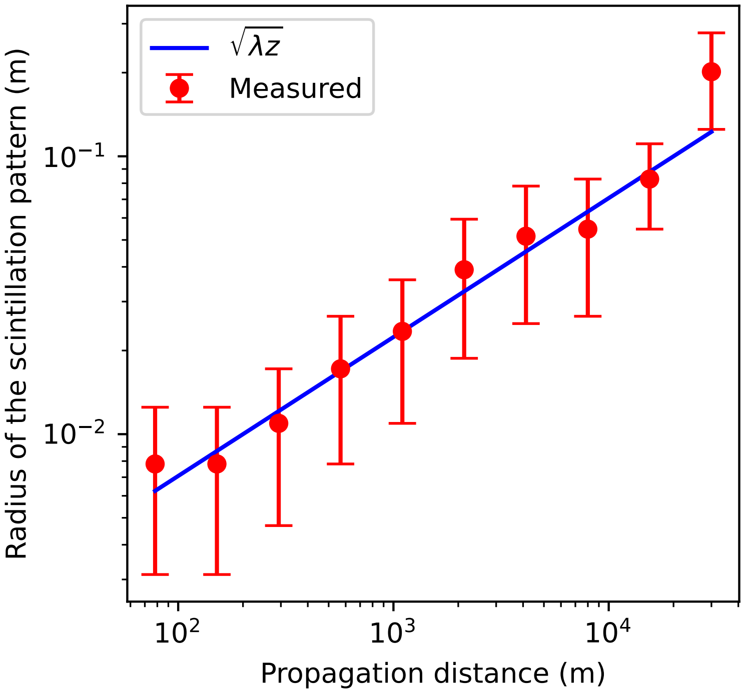

Figure 3.8: *The simulated (red dots) and the Fresnel zone radius (blue line) of the spatial scintillation size (the separation where the structure function of the intensity starts to saturate) (y-axis) are shown against propagation distance (x-axis).*

3.2.7 Method to Reduce the Required Size of Simulated Phase Screens

Due to the required input, the number of simulation elements (i.e. phase screen size) that is required to avoid mathematical effects such as wrapping and aliasing described in Equation 3.10 is much larger than the size of the screen required to avoid diffraction/refraction effects defined in Equation 3.11. This thesis proposes a mitigation method to simulate only the physically required region, in exchange for some inaccuracies, reducing unnecessary use of computational memory and time resources.

This computational waste in generating a phase screen can be reduced. According to angular spectrum decomposition and propagation in Equation 2.23 and Equation 2.24, respectively, the propagation is calculated based on the input angular spectrum frequency. Consider phase screen $\mathcal{A}$, $\mathcal{B}$, and $\mathcal{C}$. $\mathcal{A}$ has the size of $D_{z,phys}$ according to Equation 3.11. $\mathcal{B}$ has size $D_{z,math}$ according to Equation 3.10. The centre of $\mathcal{B}$ within the size of $D_{z,phys}$ is the same as $\mathcal{A}$, while the outer is the symmetric padding of $\mathcal{A}$. The symmetric padding is shown in Figure 3.9, to reduce discontinuities within the mathematically desired region. Any discontinuity, if it exists, will generate an extremely high spatial frequency that doesn't exist in the original phase screen $\mathcal{A}$ - aliasing into other spatial frequencies. Lastly, $\mathcal{C}$ is generated with size $D_{z,math}$ with the centre $D_{z,phys}$ equal to $\mathcal{A}$. $\mathcal{A}$ will share the same angular spectrum frequency as $\mathcal{B}$. The error in this method comes from the fact that $\mathcal{B}$ is not the same as $\mathcal{C}$ that was generated fully at $D_{z,math}$. However, the different input is not expected to reach the desired output region. The effect of this shortcut must be tested.

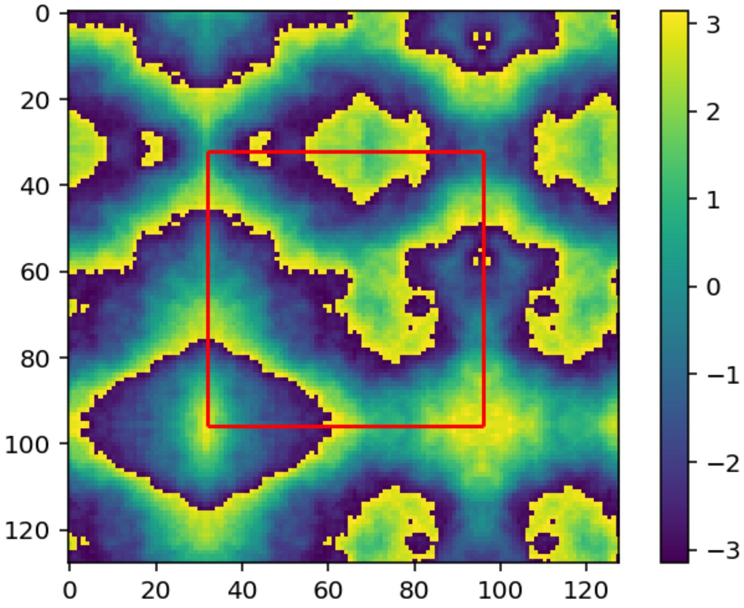

Figure 3.9: *An example of the symmetric pad. The simulated phase screen in the red region is symmetric padded to a larger size. Doing so extends the phase screen to a larger size while maintaining the spatial frequency.*

To test whether or not the hypothesised reduction in the size of the simulated turbulence region can achieve the same quality, characteristics, etc. as operating at the full screen required to satify all sampling/propagation criteria. For this we should determine what will be the wavefront difference between them. However, branch points can occur within propagated screens where the wavefront gradient can be high but contributes no intensity, skewing the analysis. We will instead measure its root intensity-weighted mean squared Wavefront Error (WFE) ($IWFE$) between two complex amplitudes U_a and U_b, here defined as

$$IWFE = \sqrt{\frac{\Sigma\left(I_{a,b}\Delta\phi_{a,b}^2\right)}{\Sigma\left(I_{a,b}\right)}}, \tag{3.14}$$

where between $I_{a,b}$ is the mean intensity between a and b, $\Delta\phi_{a,b}$ is the phase difference between a and b. The $\Delta\phi_{a,b}$ must be calculated by $\arg\{U_a/U_b\}$, where the phasor term can be subtracted safely without worry of aliasing.

We developed a simulation that propagated optical turbulence from a high-altitude layer to the telescope pupil using the parameter values defined by Equation 3.10. This simulation was then repeated using the proposed simulation size reduction method and the wavefronts compared.

In Figure 3.10, we show an example propagation result using the reduction method. It shows the resulting intensity, phase and the intensity-weighted error in each simulation element before taking the mean. The resulting intensity and phase at a glance give a visual impression as same as those in Figure 2.5. There is a ripple-like structure in the residual intensity-weighted wavefront error. The structure raises some concerns over the accuracy of the method. However, because the error is less than 10 nm at 500 nm wavelength, equivalent to a 2% drop in Strehl ratio, it is negligible.

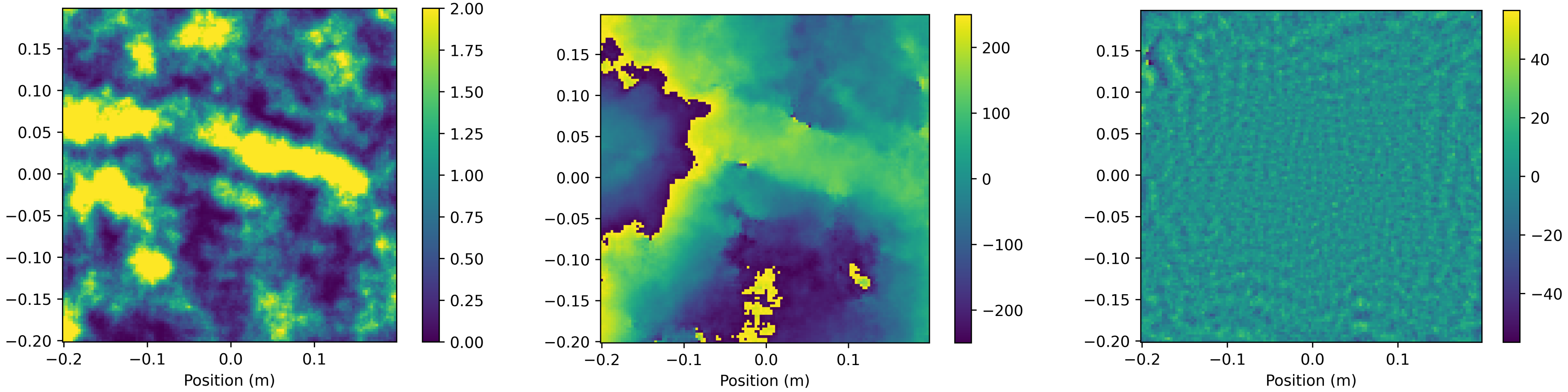

(a) *Intensity (normalised)* **(b)** *Phase (nm)* **(c)** *Intensity* × *WFE (nm)*

Figure 3.10: *Sample of propagated turbulence using the proposed method to reduce the generated phase screen size at 500 nm. The pre-propagated turbulence has 10 cm* r_0*. Propagation distance is 10 km. The intensity (normalised) and phase (nm) are shown in (a) and (b). The intensity* × *WFE from adopting the method is shown in (c). Square aperture is used.*

The intensity-weighted mean difference for a propagated phase screen using the reduction method is measured in various turbulence conditions and propagation distances that are used in this thesis. The result is shown in Figure 3.11. The intensity-weighted wavefront error is less than 10 nm compared to the 500 nm simulated wavelength.

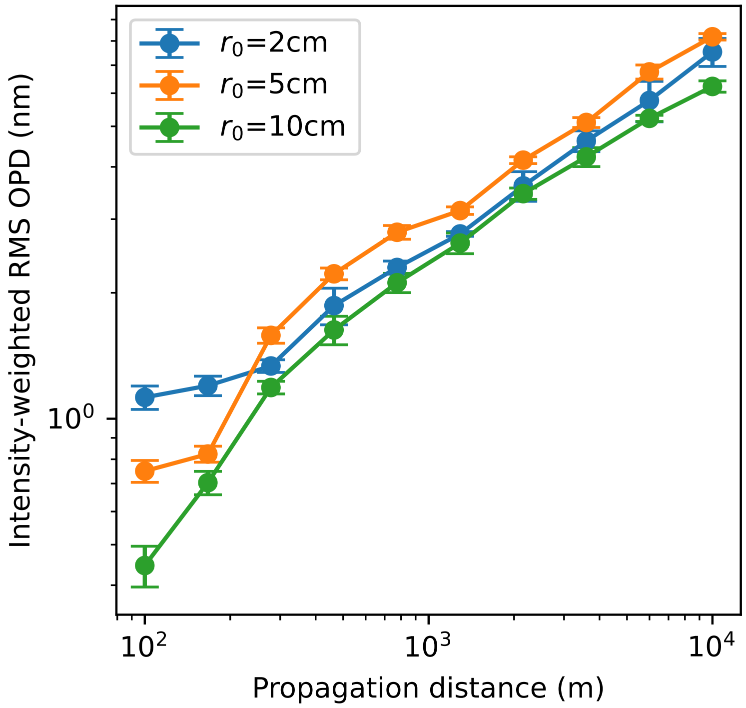

Figure 3.11: *Intensity-weighted WFE between the propagation using the generated phase screen at a full size and the proposed method to reduce the generated phase screen size for the propagation (y-axis) against the propagation distance (x-axis) of varying corresponding Fried parameter in a layer.*

Since the proposed reduction method has less than 10 nm intensity-weighted mean wavefront difference, this thesis will use this method throughout.

3.2.7.1 Potential Applications

This method for reducing the number of simulation elements for the turbulence phase screen has a limited impact on the computational resources on Multi-Conjugated Adaptive Optics (MCAO) systems with a large FoV. However, it will have a huge impact on optical communication.

Consider simulating the European Solar Telescope (EST) (Femenía-Castella et al., 2022) at its median turbulence condition (7 cm r_0 at 500 nm). The EST has 4.2 m telescope pupil, operating WFSs at 500 nm, 60" MCAO FoV, 10" WFS FoV, and the highest DM's distance from the pupil is 20 km. Let's follow the presented conditions. If only one LoS is considered

- Complete angular spectrum requires the simulation element to have at least 8.0 mm. - Equation 3.13.
- The physical projected pupil at altitude in a LoS is 5.5 m., equivalently 685 simulation elements. - Equation 3.11.
- The mathematical projected pupil at altitude in a LoS is 6.7 m., equivalently 843 simulation elements. - Equation 3.10.
- The number of simulation elements for the turbulence in a LoS, the reduction in simulation elements across the simulation is (843-685)/843 = 19%.
- Compared to the benchmark turbulence generation time, the reduction time to generate a new phase screen is 35%. - Figure 3.12.
- When adding the extra simulation elements required in a LoS to the whole FoV of the telescope,the reduction in simulation elements across the simulation is 11%. Equivalent to 20% reduction in phase screen generation time.
- Follow the previous process, for the EST at 2 cm r_0, the reduction in time to generate turbulence is 27%.

On the other hand, the reduction of simulation time for downlink optical communications is different. For example, ALASCA with 1 m pupil, operating at 1500 nm, operating at 2 cm r_0, considering turbulence 20 km away, with 1.2" FoV (Biasi et al., 2023). A similar calculation to the above can be done. The final result is that the reduction will be 55%.

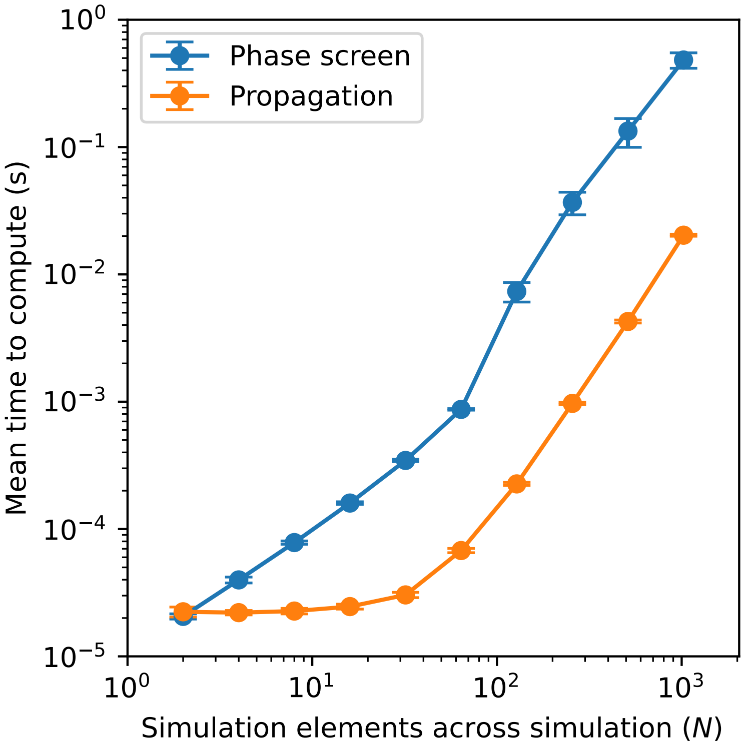

Figure 3.12: *Calculation time and its distribution required to simulate a new infinite phase screen from an existing screen and angular propagation against the number of simulation elements across the simulation screen (N). The mean and the standard deviation are calculated from 10,000 independent slope measurements. Please note that the simulation element across the simulation for the propagation includes all of the buffering of data required.*

So, the reduction in generated turbulence phase screen time is 27% for the EST, a solar MCAO system, and 55% on an optical communication system. The main reason why it has a limited impact on the MCAO is because of their large FoV and large pupil.

3.2.8 Summary

In this section, we have derived a set of criteria that, when satisfied, will allow an angular spectrum propagation of light between two planes that avoids phase wrapping and aliasing effects. These criteria also consider the field of view of an instrument and the effects of atmospheric turbulence.

All of the listed and discussed constraints in optical propagation simulation in the previous sections are now listed for applications used in this thesis, including focusing a spot from the pupil plane and propagation between atmospheric layers. The one-step Fresnel propagation is chosen for the focus, requiring the input wave, before passing through a focus lens, to have zero curvature. The conditions in Table 3.1 are used.

Constraint	Equation
Anti-aliasing in input	$\Delta\phi \leq \pi$
Anti-aliasing in simulation	Satisfied by focusing.
Wrapping	$N \geq D_{pupil}/\delta_{pupil} + D_{focal}/\delta_{focal}$
Complete input	Same with wrapping.
Output scale	$\delta_{focal} = \lambda f / N \delta_{pupil}$

Table 3.1: *All simulation constraints for focusing a near collimating beam to focus using one-step Fresnel propagation.* $\Delta\phi$ *notes the phase difference between any neighbouring phase elements.* N *is the total number of phase elements used in the simulation.* D_{pupil} *and* D_{focal} *are diameters of the desired accurate region at the pupil and focal plane; similarly,* δ_{pupil} *and* δ_{focal} *are for the size of the phase element.* f *is the focal length.* λ *is the wavelength of light being simulated.*

Table 3.2 describes the simulation parameter constraints when propagating between two atmospheric planes using the angular spectrum method. These constraints assume that the simulated phase elements at both propagation planes are required to have the same size.

Constraint	**Equation**
Anti-aliasing in input	$\Delta\phi \leq \pi$
Anti-aliasing in the forward FT	satisfied by maintaining the phase pixel scale.
Anti-aliasing in backward FT	$N \geq \lambda z_{max}/\delta^2$
Wrapping	$N \geq D_{pupil}/2\delta + D_{z,max}/2\delta + \lambda z_{max}/2\delta^2$
Adjusted complete input	$D_z \geq D_{pupil} + c_e \lambda z / r_0 + FoV z$
Reducing phase screen size	Symmetric pad D_z to $N\delta$
Complete angular spectrum	$\lambda/2\delta \geq FoV/2 + c_e \lambda/2r_0$

Table 3.2: *Simulation constraints for propagating wavefront through the atmosphere and within the AO system using angular spectrum propagation method with equal pixel scale at every plane from high-altitude atmosphere through the telescope pupil and beyond.* $\Delta\phi$ *notes the phase difference between any neighbouring phase elements.* N *is the total number of phase elements used in the simulation.* D_{pupil} *and* D_z *are diameters of the desired accurate region at the pupil plane and a plane at a distance* z *away in front of the pupil.* z_{max} *is the highest altitude being simulated.* δ *is the size of the phase element at every plane.* λ *is the wavelength of light being simulated.* r_0 *is the cumulative Fried parameter of the turbulence.* FoV *is the field-of-view of the instrument.* c_e *is the pupil expansion factor covering 97 and 99% when equal to 2 and 4, respectively.*

Propagation in Soapy is simulated separately for each WFS and science cameras (Reeves, 2016). Each object will therefore have a required number of phase elements determined using the constraints defined in the tables above. Optical turbulence layers and DMs are generated with some other phase element size. Soapy will interpolate both turbulence layers and DMs into the same phase element size as that required by each WFSs and science cameras. After that, the proposed propagation method can be used to obtain images of each WFS and science cameras.

3.3 Simulation of Deformable Mirror

The fast piezo method from Soapy (Reeves, 2016) is used to simulate DMs in this thesis. The simulated DM under AO control behaves according to the theoretical fitting error as shown in Figure 3.13. The theoretical fitting error is

$$\sigma^2_{fitting} = K_{fitting} \left(\frac{ap}{r_0} \right)^{5/3}, \tag{3.15}$$

where $\sigma^2_{fitting}$ is residual wavefront error in rad^2, $K_{fitting}$ is DM's fitting characteristic varying DM to DM, ap is DM's projected actuator pitch (Hardy, 1998).

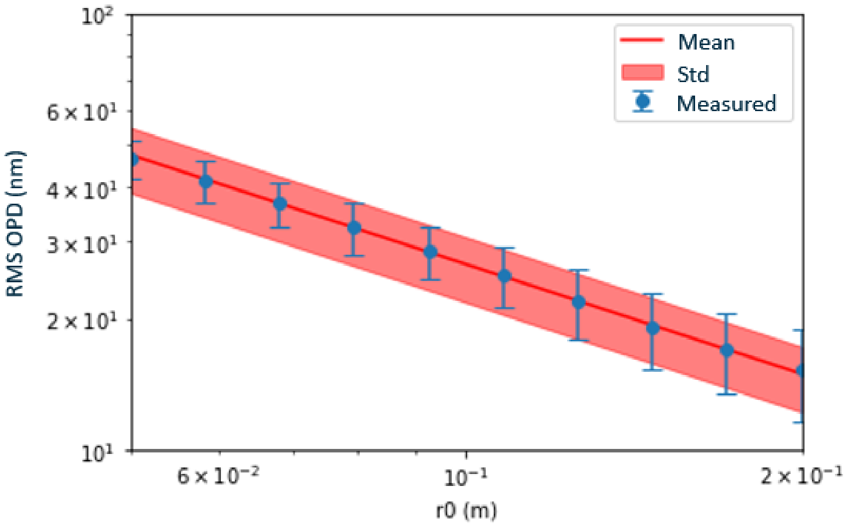

Figure 3.13: *Residual WFE (y-axis) of turbulence with varying Fried parameter (r_0) (x-axis). The measurement (blue marks) is shown against the fitted equation (red).*

3.4 Shack-Hartmann Wavefront Sensor Simulations

There are two different simulations of SH-WFS in this thesis. Simulations presented in Chapter 4 use a custom simulation using one-step Fresnel propagation (referred to hereafter as the Fresnel WFS model), while simulations in Chapter 5 use the Soapy SH-WFS model. (Reeves, 2016). Since we configured the Soapy's WFS corresponding to the Fresnel propagation, there is only one model to test.

In this section, we investigate the performance and accuracy of different Centre-of-Gravity (CoG) used in the SH-WFS slope measurement, highlighting how the threshold level in the CoG process reduces bias and Root-Mean-Square (RMS) error in the SH-WFS.

The Fresnel WFS model is configured to ensure the simulated detector pixel scale samples the diffraction limit with a scale equal to $\lambda f/2D_{pupil}$. This constraint is in line with the 'Output scale' and 'Wrapping' requirements in Table 3.1, where $D_{pupil}/\delta_{pupil} = N/2$ and $D_{focal}/\delta_{focal} = N/2$ respectively. Converting variables into parameters relevant to the design of a SH-WFS, the angular pixel scale at the detector is $\alpha = \lambda/2d_{sub}$, $N/2 = d_{sub}/\delta = FoV/\alpha = n$, where α is the detector angular pixel scale, λ is the operating wavelength, d_{sub} is the subaperture diameter, N is the total amount of simulation element, and FoV is the FoV of the detector.

To maximise the speed of the fast Fourier transform, the number of simulation elements should be even (Cooley and Tukey, 1965), however, using an even number of simulation elements introduces an effect that can limit WFS model accuracy. Consider focusing a plane wave through a lens onto a point. The point would be positioned at the centre of the lens by symmetry. Due to the mathematical properties of the Fourier transform, one simulated pixel represents zero 'frequency' (Equation 2.19) component in the input complex amplitude. This means that the resulting image will be centred on a single pixel.

Not recentering the spot centre to be at the middle of the detector will introduce a potential measurement bias, where the wing of the Point Spread Function (PSF) on one side is higher than the other. Without a suitable threshold level to remove the uneven values.

To recenter, an image offset of a half pixel can be added by introducing a small tip/tilt phase across the pupil (or each subaperture). We calculate the tip/tilt phase from Equation 2.29. The shifting direction needed is on the negative side. The tip/tilt phase to be added (TT) is

$$TT = -\frac{\pi}{N}\left(x_{1,px} + y_{1,px}\right), \tag{3.16}$$

where $x_{1,px}$ and $y_{1,px}$ are physical positions relative to the centre of the aperture in units of pixels, D_1 is the lenslet diameter, and N is the number of elements across the simulation of a lenslet (including zero-pad).

Starting from the complex amplitude of the wave at the pupil plane (U_p), using one-step Fresnel propagation (Equation 2.32) while considering limitations and constraints of the simulation (Section 3.2), the intensity profile (I_f) of a spot at the focal plane can be calculated.

$$I_f \propto \left| \text{crop}\left\{\mathcal{F}\left\{\text{pad}\left\{U_p \times TT\right\}\right\}\right\}\right|^2 . \tag{3.17}$$

3.4.1 Shack-Hartmann slope calculation

The SH-WFS slope is calculated through centring of lenslet spots using the CoG method. The wavefront slope measurement can be represented by Optical Path Difference (OPD) over a lenslet, which is commonly used in SH-WFS analysis (Thomas et al., 2006). The OPD is the absolute wavefront difference between the wavefront phase at the extremes of the edges of the lenslet. It is also mathematically equivalent to the wavefront difference projected from the wavefront averaged gradient in the scintillation-free regime (Tartarskii, 1971). The OPD can be presented by either the spatial distance in nanometres, the phase difference in radians, or the number of waves. This thesis chooses to present the OPD in nanometres because it provides a wavelength-independent metric (Hardy, 1998). The relation between the OPD and the centre of the SH-WFS spot is shown in Figure 3.14.

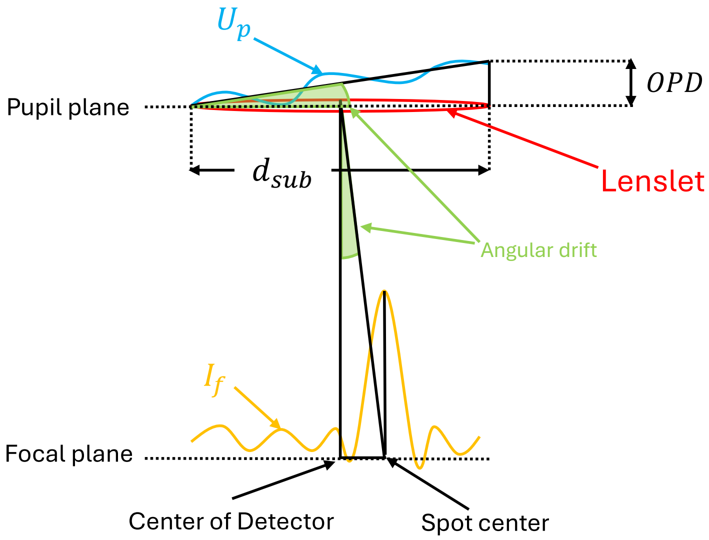

Figure 3.14: *The geometrical relation between wavefront at a lenslet of a SH-WFS, OPD due to an incoming wavefront tilt of θ, and the resulting displacement of spot on the focal plane are shown. The OPD is the averaged tip/tilt projection over a lenslet of the wavefront at the pupil plane of a SH-WFS (U_p). The angular displacement of the spot centre on the SH-WFS focal plane is equal to the tip/tilt on the pupil plane.*

Once the intensity profile of the lenslet spot (I_f) is calculated (Equation 3.17), the slope of the wavefront can be derived from the position of the spot through the CoG method. The calculation of the spot motion along the x and y axes is identical; therefore, only the x position is considered here. The CoG of the spot is given by:

$$\Sigma_x(I_f W_x)/\Sigma(I_f). \tag{3.18}$$

where (W_x) is a weighting function equal in length to the size in pixels of the image along the x-axis. After that, a conversion of the spot offset in pixels from the centre to OPD per lenslet in metres can be applied. Offset in pixel is first multiplied by the angular pixel scale (α). Then multiplied by the subaperture size (D_1) to get OPD per lenslet in meters.

The OPD can be calculated from the focal plane intensity profile by

$$OPD_m = \alpha D_1 \frac{\Sigma \left(I_f x_{pixel} \right)}{\Sigma I_f}. \tag{3.19}$$

The simulated SH-WFS should show a linear response to the wavefront slope of the input; however, factors such as the method and intensity threshold levels may affect this. The linearity can be measured by comparing a flat wavefront with a known tip/tilt gradient to the measurement of the spot offset within the SH-WFS. In this thesis, applying a threshold level on the SH-WFS measurement means excluding detector pixels with intensity lower than the threshold level multiplied by the maximum intensity in a detector pixel from the CoG calculation.

Figure 3.15 shows the linearity of centroid response of a SH-WFS to an increasing wavefront gradient (wavefront tilt) using a 64x64 detector pixel subaperture image with a pixel scale equal to $\lambda/2d_{sub}$ (where d_{sub} is the SH-WFS subaperture diameter). We then measure the centroid for varying threshold levels at a 500 nm wavelength. At first glance, the measurement matches the given tip/tilt for all of the threshold levels. However, on closer inspection of the measurement error, the error increases gradually with the input tip/tilt, then rapidly increases near the edge of the SH-WFS detector - a measurement bias. There are measurement bias when using 0 and 0.0001 threshold level, as high as 7.5 nm over 1000 nm. While the 0.01 threshold level shows negligible bias. However, since the Figure 3.15 did not show the distribution of the measurement error for readability. It is misleading to believe that 0.01 threshold level is suitable. However, the most suitable condition is 0.0001.

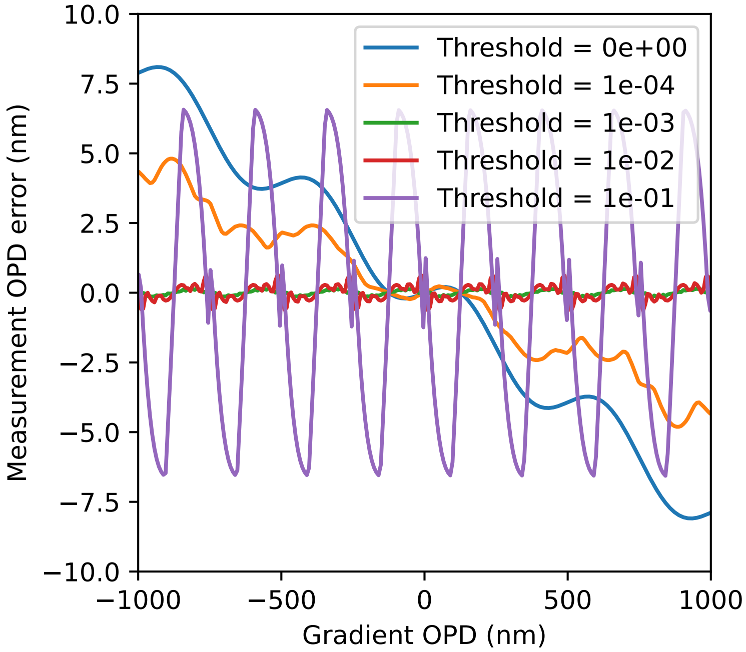

Figure 3.15: *Measurement error between expected and measured OPD using the "full" detector for the measurement. The simulation has 64x64 pixels detector with* $\lambda/2d_{sub}$ *angular pixel scale operating at 500 nm. The whole 64x64 pixels were used within the CoG calculation. Line colours represent the mean bias of different threshold levels. The threshold level of 0 and* $1{\times}10^{-4}$ *has a growing bias as the OPD increases. The RMS OPD distribution are not shown here for readability.*

Figure 3.16 shows the measured centroid if we crop the 64x64 image down to a 17x17 pixel sub-region centred around the spot maximum, then use the 17x17 for the CoG calculation. The OPD bias can be reduced to less than 6 nm for all threshold levels. Reducing the number of pixels to be used in the CoG will, however, reduce its overall accuracy (Thomas et al., 2006). Again, since the Figure 3.16 did not show the distribution of the bias, the threshold level of 0.01 seems to be the most suitable.

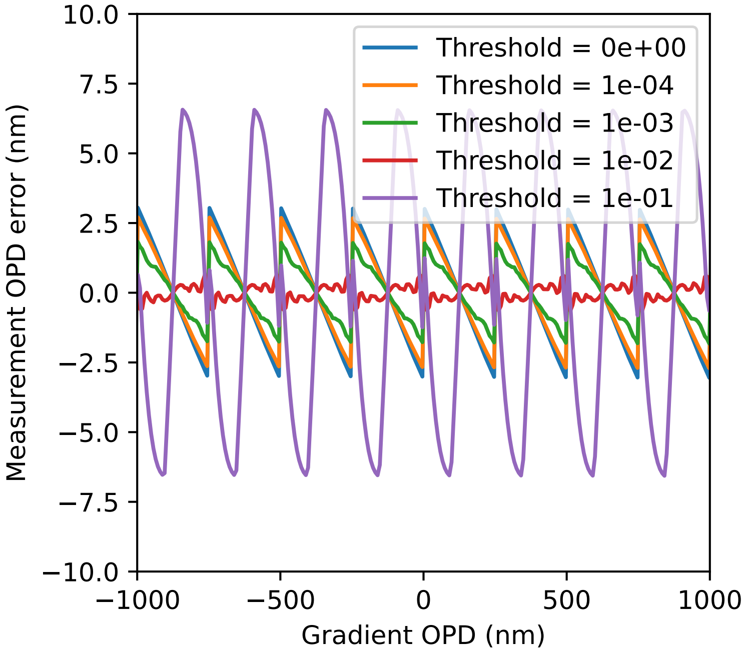

Figure 3.16: *Error between expected and measured OPD using a sub-region of the detector for the measurement. The simulation has 64x64 pixels detector with* $\lambda/2d_{sub}$ *angular pixel scale operating at 500 nm. Only 17x17 out of 64x64 pixels centred on the pixel with the highest intensity were used within the CoG calculation. Line colours represent the mean bias of different threshold levels. None of the threshold levels has a growing bias as the OPD increases. The RMS OPD distribution are not shown here for readability.*

The error in the bias was initially measured by evenly sampled all of the entire range. However, the atmospheric optical gradient distribution will have more OPD around 0 than at larger OPD. Therefore, the distribution of the bias on the SH-WFS is now measured with the atmospheric turbulence distribution instead. After OPD of turbulence with varying subaperture size to the turbulence Fried parameter ratio (d/r_0) is measured using the Fourier transform and subsequent image centroiding algorithm, and they are compared against the OPD from turbulence mean gradient, through RMS difference.

Figure 3.16 shows the RMS difference between SH-WFS with varying normalised threshold level and CoGs. It shows that using the entire 64x64 pixels for the CoG ("full") has lower RMS error than using only 17x17 out of 64x64 pixels for the CoG ("partial"). The choise of threshold level is now clear, that the 0.0001 is best for the "full" CoG, and threshold $\leq$ 0.001 is suitable for the "partial" CoG.

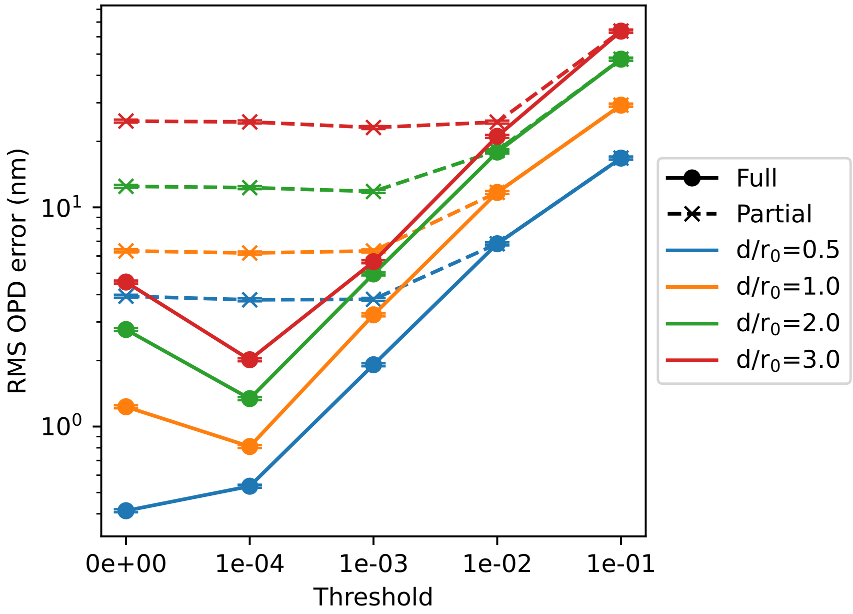

Figure 3.17: *RMS wavefront OPD measurement error of the SH-WFS (y-axis) using the whole of 64x64 ("full", solid) and only 17x17 centred on the highest intensity pixel ("partial", dashed) with varying threshold level applied (x-axis). Different turbulence statistics against the SH-WFS pitches (d/r_0) are shown in colours.*

3.5 Analysis of Residual Wavefront

Standard analysis of residual wavefront provided by Reeves (2016) includes Strehl ratio and RMS WFE.

3.5.1 Strehl Ratio

The Strehl ratio is defined as the ratio of maximum intensity in PSF profile between image with (I) and without aberrations (I_0), as in Hardy (1998),

$$S/ = \frac{I}{I_0}. \tag{3.20}$$

3.5.2 Wavefront Error

For analysis in negligible scintillation, the RMS WFE can be calculated directly from the phase (or residual phase after correction by the deformable mirror),

$$\sigma_w = \sqrt{\frac{\Sigma\phi^2}{N_\phi}}, \tag{3.21}$$

where ϕ is the residual phase of wavefront (with its mean subtracted), and N_ϕ is the number of phase elements being calculated (Hardy, 1998).

If scintillation is dominant, phase elements with lower intensity will have a smaller impact on the RMS WFE, so the RMS WFE should be intensity-weighted. The intensity-weighted RMS WFE (σ_i) as in (Goodno et al., 2010) is

$$\sigma_i = \sqrt{\frac{\Sigma I\phi^2}{\Sigma I}}. \tag{3.22}$$

3.5.3 Log-amplitude Variance

The log-amplitude variance (σ_χ^2) can be measured from

$$\sigma_\chi^2 = var\left(\ln|U|\right), \tag{3.23}$$

where U is the residual complex amplitude of the wavefront, with its amplitude normalised to its mean amplitude (Sasiela, 2007).

3.6 Adaptive Optics Control

To control adaptive optics systems, the interaction between DM and WFS must be measured. In most AO systems it is trivial to measure changes in WFS slopes corresponding to the influence of each DM actuator, however it is the inverse of this calibration that the AO system requires during operation; given observed changes in WFS slopes, what is the DM shape that this corresponds to.

The Interaction Matrix (IM)s between a WFS and DM is generated by measuring the difference in WFS slopes before and after poking of each actuator sequentially. A matrix describing the measurement of the WFS slope differences for each actuator is called the IM. The linear relation between DM strokes (a), WFS residual slope measurement (s) and IM ($\mathbf{M}_i$) can be written as (Van Dam et al., 2020)

$$s = \mathbf{M}_i a. \tag{3.24}$$

Because $\mathbf{M}_i$ is rarely a square matrix, the solution for DM actuator strokes for given WFS slopes can be solved using the pseudo-inverse (noted by $^+$ operator) matrix of IM. The pseudo-inverse is called Control Matrix (CM) ($\mathbf{M}_c$) (Van Dam et al., 2020).

$$\mathbf{M}_c = \mathbf{M}_i^+ \tag{3.25}$$

$$a = \mathbf{M}_c s \tag{3.26}$$

The pseudo-inverse can be calculated by Singular Value Decomposition (SVD) (Gavel, 2003), requiring a normalised conditioning parameter (Strang, 2009). The conditioning parameter for the pseudo-inverse is normally selected to optimise observed or simulated AO performance. The conditioning value yielding the highest Strehl ratio is chosen. The measured AO performances with varying singular value thresholds are shown in

Figure 3.18. It shows that SVDs between 0.037 and 0.121 yield a high Strehl ratio. SVD value of 0.05 is chosen as it is roughly in the middle of the range.

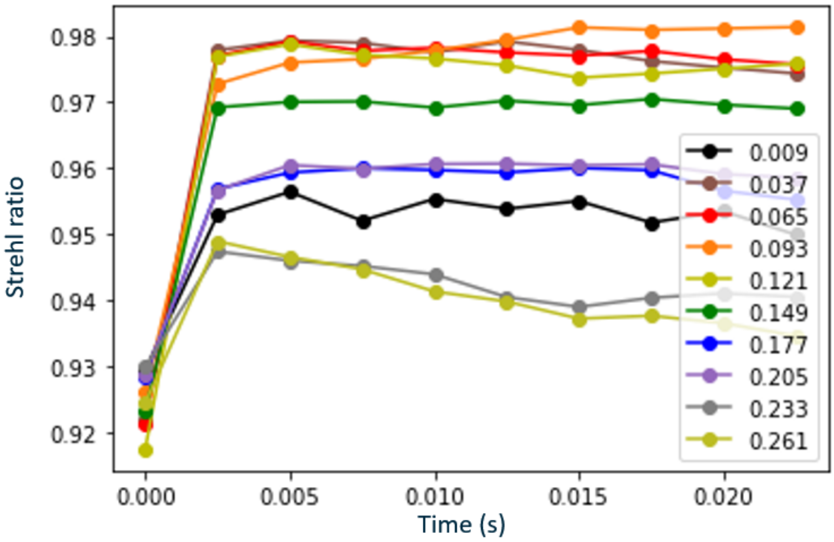

Figure 3.18: *Optimising the normalised conditioning values of in pseudo-inversion of the interaction matrix using the singular-value-decomposition method for an AO system with 0.4-m pupil and 5-cm SH-WFS subaperture diameter. The resulting Strehl ratio (y-axis) through using different conditioning values is shown against the number of control iterations (x-axis). The conditioning values between 0.037 and 0.121 show similar optimised performance.*

For closed-loop control of adaptive optics, we implement a simple integrator control law. At time $t+1$, DM actuator commands (a_{t+1}) depend on WFS measures wavefront residuals (s_t) and DM commands (a_t) at time t:

$$a_{t+1} = a_t - g\mathbf{M}_c s_t, \tag{3.27}$$

where g is the control loop gain.

The higher control loop gain applies correction faster. Choices of gain may affect the system stability (Hardy, 1998).

With suitable control, AO will reduce RMS WFE from the typical atmospheric turbulence aberration level. Figure 3.19 shows AO correcting a static turbulent phase screen.

For this simulation, the WFS was noiseless; therefore, the expected residual should converge to the DM fitting error.

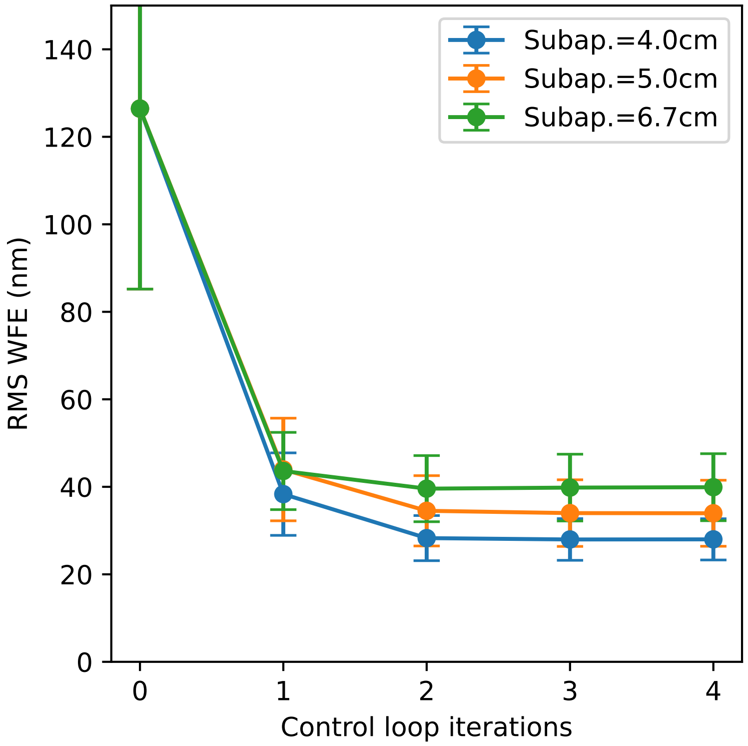

Figure 3.19: *Residual WFE and its distribution (y-axis) is reduced as AO with 0.4-m pupil diameter with different SH-WFS subaperture size (colour) applying close loop corrections on a static turbulence with 10 cm* r_0*. Different systems may have different residue wavefront errors.*

The residual wavefront after corrections are applied will have its power of lower-order Zernike modes considerably reduced, as shown in Figure 3.20.

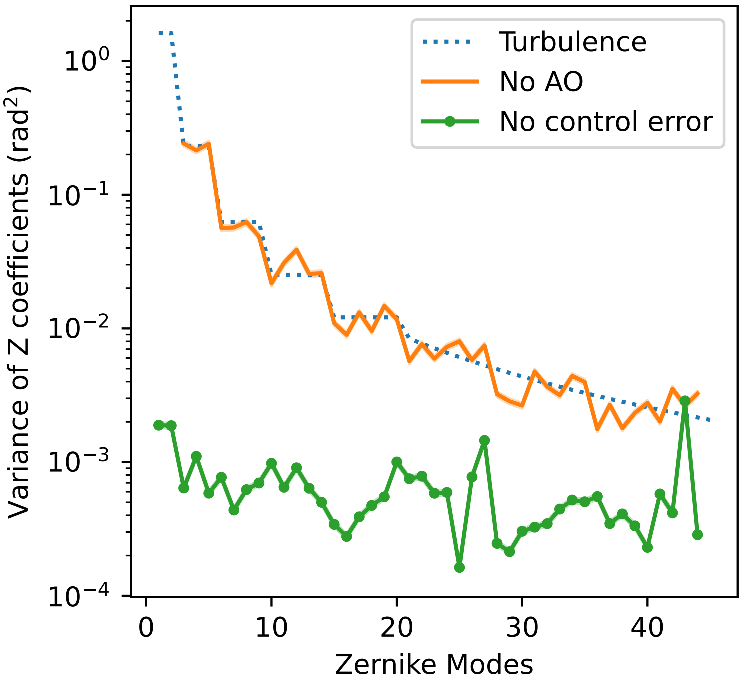

Figure 3.20: *Variance of each Zernike mode and its error of 10 cm r_0 turbulence and residues after AO corrections. The AO has 0.4-m pupil and SH-WFS of 4 cm subaperture diameter. The theoretical values of the turbulence are shown as a reference.*

Similarly, power in lower spatial frequency PSDs is also reduced as shown in Figure 3.21 up to the AO's sampling or Nyquist frequency.

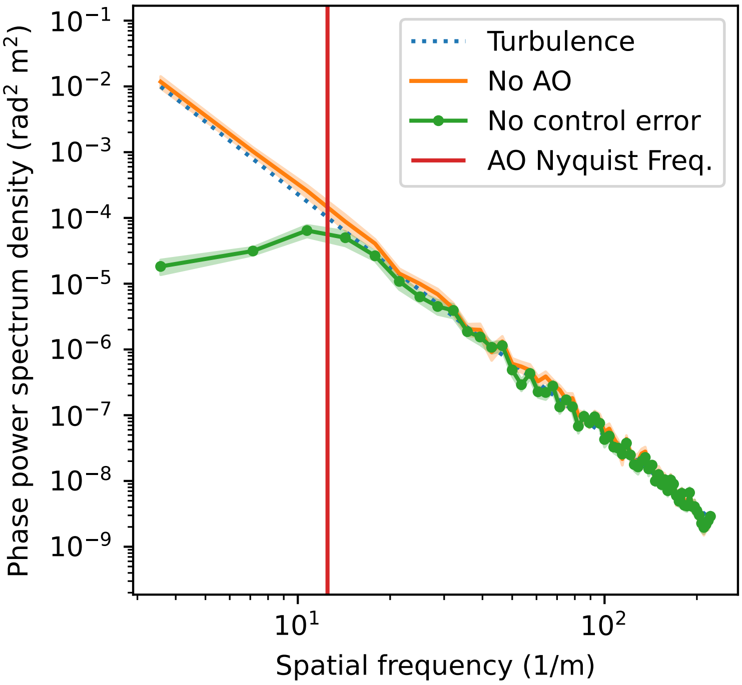

Figure 3.21: *Spatial PSD and its error of the mean of each spatial frequency of 10 cm r_0 turbulence and residues after AO corrections. The AO has 0.4-m pupil and SH-WFS of 4 cm subaperture diameter. The theoretical values of the turbulence and the system's Nyquist frequency are shown as a reference.*

3.7 Conclusion

This thesis implements automatic propagation parameter calculation for optical propagation in Soapy. All of the simulations of AO used in this thesis are now introduced and tested. Now this thesis will explore various effects of optical propagation in AO. Firstly, this thesis investigates speeding up of SH-WFS measurement through the intensity-weighted wavefront gradient, an approximation from Tartarskii (1971), in Chapter 4. Secondly, this thesis investigates the distortion of MCAO control of other DMs in the system, applying some corrections to the atmosphere in Chapter 5.

Not only did this chapter verify the existing simulation packages, but it also clarified existing routines to simulate an infinite turbulence phase screen in Soapy, where two of them have a misleading name. The Soapy's von Kármán infinite phase screen based on Assémat et al. (2006) does not have tip/tilt variance along its extruding axis as the von Kármán statistics expected, as observed through the structure function, PSD, and variance of Zernike mode analysis on the phase. Since Fried and Clark (2008) had already noticed this fact and suggested a different routine, this chapter only clarified the confusion. On the other hand, Soapy's Kolmogorov infinite phase screen based on Fried and Clark (2008) does not have the Kolmogorov statistics, but matches the von Kármán statistics exactly, as seen through the same set of analysis. This mismatching of names comes from the misleading in Fried and Clark (2008)'s article title, and Soapy happens to use the von Kármán statistics inside its Kolmogorov method.

Next, this chapter compiled and wrote a script to automate the selection of parameters to simulate the optical propagation accurately, relieving users from tedious calculations and reconfigurations every time there are new changes to the system design.

Lastly, noticing the unnecessary generation of high altitude turbulence with a spatial size to what is mathematically required, a larger area than where most of the lights will physically pass through. The turbulence can be generated to only physically required, and then symmetrically padded to the mathematically required size. Doing so reduces the spatial size to generate the turbulence while maintaining the angular spectrum. Consequently, the intensity-weighted mean wavefront difference is only 10 nm. The reduction in time to simulate a layer of high-altitude turbulence is 27% at max for the new generation solar telescope MCAO systems, which might not be a significant change. However, for downlink simulation of optical communication, the reduction can be as much as 55%.

Key Contributions

1. Clarified the generated turbulence statistics of Soapy's methods to simulate the infinite phase screen.
2. Implemented an automated simulation parameter allowing accurate optical propagation.
3. Introduced a method to reduce the mathematically required generated high altitude turbulence size, reducing the required computational resources. The reduction in computational time is limited for new generation solar MCAOs, only 27% at max. However, it will reduce up to 55% for optical communication systems.

4

Intensity-Weighted Mean Gradient Wavefront Sensor

This chapter proposes the use of an Intensity-weighted mean gradient wavefront sensor as an approximation of a Shack-Hartmann Wavefront Sensor (SH-WFS) simulation. It is expected that adopting this newly proposed method will reduce the required computational memory and time, without significant loss of accuracy.

Simulations of Adaptive Optics (AO) in conditions with non-negligible scintillation need a full wave propagation modelling as discussed previously in Chapter 2. All common propagation methods use discrete Fourier transforms, which require extra data or zero padding to prevent wrapping and aliasing effects as discussed in Chapter 3. This can greatly increase the computational complexity and, therefore, the time taken to run a simulation.

Wide-field solar Multi-Conjugated Adaptive Optics (MCAO) simulations require more slope calculations than other AO systems for the following reasons. Firstly, Solar MCAO operates during the daytime, where optical turbulence is stronger, thus a higher number of subapertures per SH-WFS are required to achieve a scientifically useful level of AO correction. Turbulence coherence length encountered during daytime can be as much as half that of that encountered at nighttime (Griffiths et al., 2023). Secondly, like all MCAO systems, Solar MCAO needs more than one Wavefront Sensor (WFS). Lastly, each SH-WFS typically has a Field-of-View (FoV) larger than the anisoplanatic angle of turbulence to enable tracking of solar granulation patterns (Schmidt et al., 2022; Griffiths et al., 2023). As a result, multiple observations should be made within each SH-WFS subaperture to account for anisoplanatism. Multiple lines-of-sight may be needed to accurately model the wide-field Solar MCAO SH-WFS. For example, the Daniel K. Inouye Solar Telescope (DKIST) has 9 SH-WFSs, each with 43 subapertures across the pupil (about 1400 subapertures in total) and a 10" FoV operating at 550 nm (Schmidt et al., 2022). Assume (prehaps pessimistically) that one slope calculation is required for each anisoplanatic angle. For typical daytime turbulence conditions, the anisoplanatic angle at this wavelength is 1" (Schmidt et al., 2022; Griffiths et al., 2023). To model the full-field anisoplanatism present within a single DKIST SH-WFS image, about 1,000,000 (100x100 anisoplanatism patches per subaperture x 9 SH-WFS x 1400 subapertures per SH-WFS) slope calculations would be needed per AO loop iteration. On the other hand, if a simulation of the MCAO of the DKIST telescope for a star observation during the nighttime, only 10,000 slope calculations are needed (100 times less).

The simulation process of the SH-WFS slope measurement can be sped up if it can be approximated at the pupil plane without calculating the SH-WFS focal plane directly, avoiding the calculation of the focal plane intensity that uses two-dimensional Fourier transforms completely. From now on, the simulation of the SH-WFS measurement that uses the Fourier transforms and subsequent centroiding on the resulting images is called the Fourier Transform Method (FT-Method). Tartarskii (1971) derived that the movement of the spot on the focal plane (equivalent to the slope measurement of SH-WFS) is proportional to the intensity-weighted mean gradient at the pupil plane. From now on, this method will be called the Intensity-Weighted Averaged Gradient Method (IG-Method). The approximation can be further simplified to just the mean gradient, called the Averaged Gradient Method (G-Method). Ignoring intensity variation, the G-Method might be less accurate, but finds itself suitable for the scintillation-free regime. The approximation is used in Barchers et al. (2003). However, validation of its accuracy has never been published. Assuming that the approximation is accurate, how much faster will the determination of the slope measurement be? For the specific case of strong turbulence, are the analytical noise models of SH-WFS for the weak turbulence regime with negligible turbulence, (Thomas et al., 2006) still applicable?

Key Objectives

1. Present the methods to simulate the SH-WFS measurement.
2. Compare the computational memory and time usage of the different methods.
3. Compared to processes to simulate optical turbulence layers and optical propagation between the turbulence layers and the Deformable Mirror (DM)s, what is the potential percentage time reduction?
4. Determine the accuracy that each of the models can recreate SH-WFS performance in turbulent conditions with scintillation in the high signal case.
5. Is there any method to include detector noise for the IG-Method?
6. Does the measurement noise of the SH-WFS models change with scintillation?

4.1 Algorithm comparison

This section introduces the FT-Method, IG-Method and the G-Method, then compare their requirements on memory space and time. All of the algorithms used in this Chapter are listed in a GitHub repository (`https://github.com/gqmc62/PhD-Codes`) (Kongkaew, 2025a). Our results show that the IG-Method and G-Method use only approximately 0.38 and 0.24 memory space of that required by the FT-Method, respectively, and only approximately 0.2 and 0.6 times of that required by the FT-Method, respectively. Depending on the accuracy of the approximations to the FT-Method to be tested in the next section, there will be regions where using the IG-Method or G-Method is advantageous.

In order to standardise the calculation method, both methods must follow these requirements. Firstly, their input data will be the complex amplitude of the light wave at the pupil plane (U_p). Secondly, the slope reading must be Optical Path Difference (OPD) over a lenslet in nm as shown in Figure 3.14, which is commonly used in SH-WFS analysis (Thomas et al., 2006). However, this thesis chooses the OPD in nm because it is nearly independent of the wavelength and can be projected in AO budget more easily (Hardy, 1998).

The memory usage reflects the amount of numbers used during the calculation stored in RAM, while the computational speed represents how fast the CPU/GPU can compute those numbers. Since the memory and speed are limited by different parts of the computer, they must be evaluated separately. Depending on the specs of the machine, some might be limited by the memory usage or the computational speed, either by funding or technological capability.

4.1.1 Fourier Transform Method

The simulation of the SH-WFS using the FT-Method has been described in Chapter 3. Reciting the process, the slope measurement on the x-axis using the FT-Method ($s_{FT,x}$), without considering photon and detector noise or applying any threshold, can be calculated from the complex amplitude of the optical wave at the pupil plane (U_p) through

$$I_f = |crop\left(\mathcal{F}\{pad\left(U_p\right)\}\right)|^2 \tag{4.1}$$

$$s_{FT,x} = \frac{\Sigma I_f x}{\Sigma I_f}, \tag{4.2}$$

where *pad* pads the simulation data with zeros on the edges by $n/2$ on each side, *crop* crops the outer edges of the simulation data by $n/2$ on each side, x is the detector pixel location on the x-axis, equal to zero where the centre of the diffraction-limited spot with no tip/tilt would be. The calculation for the y-axis can be done similarly. The pyFFTW package (Gomersall, 2025) is used to calculate the Fourier transform.

4.1.2 Intensity-Weighted Mean Gradient Method

Tartarskii (1971) analysed a statistical wandering of the telescope image of a point source induced by optical turbulence. This is the same as a statistical displacement of a spot on the focal plane of the SH-WFS lenslet because both processes focus an aberrated wavefront into a spot. During the process, Tartarskii derived that the displacement of the spot is the intensity-weighted mean gradient at the pupil plane. This means that the slope measurement of the SH-WFS can be calculated solely from the wave complex amplitude at the pupil plane (U_p) without needing to calculate the intensity profile at the focal plane (I_f). This shows a promising speed-up of the calculation, and this chapter will compare the calculation time used between the proposed intensity-weighted mean gradient at the pupil and the popularly used Fourier transformed method that calculates the focal plane intensity, then calculates the centre-of-gravity of the wavefront sensor spot.

The calculation of the intensity-weighted mean gradient requires evaluating the intensity and phase calculation at the pupil plane of each simulation element, then the phase difference and intensity between each simulation element at the pupil plane, and lastly the intensity-weighted mean gradient.

The intensity (I_p) and phase (ϕ_p) in the pupil plane must be calculated. The intensity (I_p) is

$$I_p = |U_p|^2 \,. \tag{4.3}$$

The calculation of the phase in the pupil plane (ϕ_p) from the complex amplitude in the pupil plane (U_p) will be the argument of the complex number at each simulation element, which is cyclical in nature.

$$\phi_p = \arg\left(U_p\right) \tag{4.4}$$

Note that this phase in the pupil plane (ϕ_p) will be between $-\pi$ and π, and that $-\pi$ and π are actually the same point. Even though this is a physically and mathematically correct representation of the wave, this does not show a continuous wavefront. Imagine two wavefronts which are exactly the same, but one of them has a global shift in phase. These two waves should behave similarly. In other words, the zero point on the phase value is just a reference point. As such, the mathematical difference of phase on the pupil plane between neighbouring simulation elements may not be the actual difference, due to the aliasing of phase. Assuming that the complex amplitude at the pupil plane is well-sampled, all points should differ from their neighbouring points by less than π, which is half of the full circle. Consequently, any phase difference larger than π is actually a full circle or 2π less. Similarly, for the opposite.

The phase difference ($\Delta\phi_p\left[x_{i+0.5}\right]$) between point x_i and x_{i+1} can be calculated from the phases at those two points ($\phi_p\left[x_i\right]$,$\phi_p\left[x_{i+1}\right]$) as follows.

$$\begin{aligned}
\Delta\phi_{p,x}\left[x_{i+0.5}\right] &= \phi_p\left[x_{i+1}\right] - \phi_p\left[x_i\right] + 2\pi && \text{if } \phi_p\left[x_{i+1}\right] - \phi_p\left[x_i\right] < -\pi, && (4.5)\\
&= \phi_p\left[x_{i+1}\right] - \phi_p\left[x_i\right] - 2\pi && \text{if } \phi_p\left[x_{i+1}\right] - \phi_p\left[x_i\right] > \pi, && (4.6)\\
&= \phi_p\left[x_{i+1}\right] - \phi_p\left[x_i\right] && \text{otherwise.} && (4.7)
\end{aligned}$$

Because the calculated phase difference ($\Delta\phi_p$) has its position and number of points different from the intensity (I_p). To match the number and position, the easiest way is to average either the phase or the intensity. Because averaging over the phase is complicated with the aliasing of the phase, averaging the intensity is chosen.

$$I\left[x_{i+0.5}\right]=\frac{I_p\left[x_{i+1}\right]+I_p\left[x_i\right]}{2} \tag{4.8}$$

Because the mean of all phase differences over a simulation element within a lenslet is the mean of the phase difference across the lenslet, there is no need for conversion. Lastly, the intensity-weighted mean gradient $(s_{IG,x})$ can be calculated by

$$s_{IG,x}=\frac{\Sigma\left(I\left[x_{i+0.5}\right]\Delta\phi_{p,x}\left[x_{i+0.5}\right]\right)}{\Sigma I\left[x_{i+0.5}\right]}. \tag{4.9}$$

4.1.3 Mean Gradient Method

The G-Method is similar to the IG-Method except that it is not weighted by the intensity. The slope measurement of the G-Method $(s_{IG,x})$ is

$$s_{G,x}=\overline{\Delta\phi_{p,x}}. \tag{4.10}$$

4.1.4 Computational Memory Comparison

Each method uses different memory spaces during the computation. Arrays of data, which must be calculated or pre-calculated for each method, are listed separately. Assuming that the wavefront complex amplitude has n by n simulation elements or n number of simulation elements across the subaperture of the SH-WFS. Simulation elements are numpy.float64 or numpy.complex128, occupying 64 and 128 bits per simulation element, respectively. The complex numbers contain two numpy.float64 for real and complex parts, maintaining the precision.

Based on my code, the variables that are declared and preallocated are included in Table 4.1, and plotted in Figure 4.1. The IG-Method and G-Method use only approximately 0.38 and 0.24 memory space of that required by the FT-Method, respectively.

FT-Method	**Array Size**	**Data Type**	**Memory Usage (bit)**
U_p	n^2	complex	$128n^2$
$\mathcal{F}_{in}$	$4n^2$	complex	$512n^2$
$\mathcal{F}_{out}$	$4n^2$	complex	$512n^2$
I_f	n^2	real	$64n^2$
x	n^2	real	$64n^2$
y	n^2	real	$64n^2$
Total			$1344n^2$

IG-Method	**Array Size**	**Data Type**	**Memory Usage (bit)**
U_p	n^2	complex	$128n^2$
ϕ	n^2	real	$64n^2$
I_p	n^2	real	$64n^2$
$I_{p,x}$	$n^2 - n$	real	$64n^2 - 64n$
$I_{p,y}$	$n^2 - n$	real	$64n^2 - 64n$
$\Delta\phi_{p,x}$	$n^2 - n$	real	$64n^2 - 64n$
$\Delta\phi_{p,y}$	$n^2 - n$	real	$64n^2 - 64n$
Total			$512n^2 - 256n$

G-Method	**Array Size**	**Data Type**	**Memory Usage (bit)**
U_p	n^2	complex	$128n^2$
ϕ	n^2	real	$64n^2$
$\Delta\phi_{p,x}$	$n^2 - n$	real	$64n^2 - 64n$
$\Delta\phi_{p,y}$	$n^2 - n$	real	$64n^2 - 64n$
Total			$320n^2 - 128n$

Table 4.1: *Memory cost comparison between the FT-Method, the IG-Method and the G-Method.*

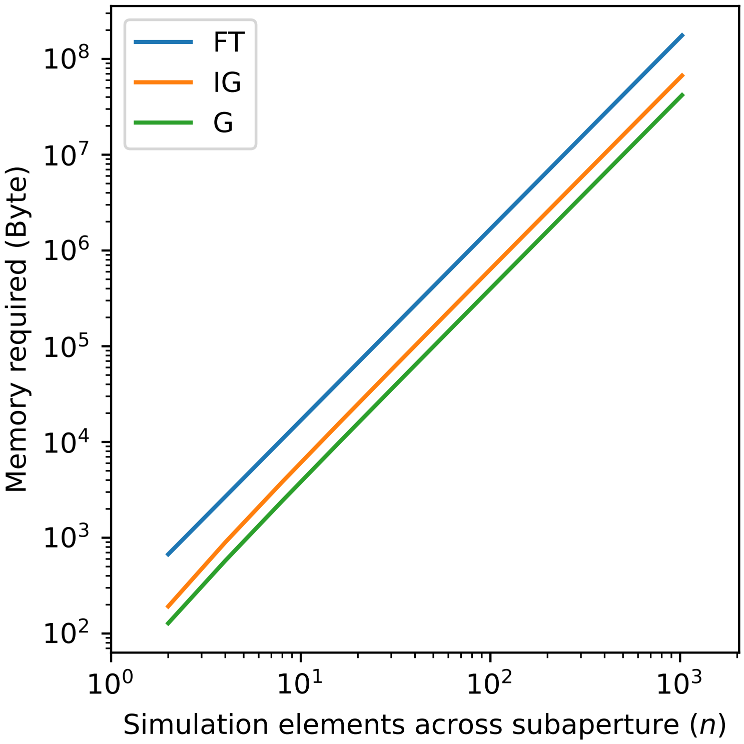

Figure 4.1: *Memory space required by different simulations of SH-WFS (1 Byte = 8 bit) against the number of simulation elements in a subaperture of the SH-WFS (n). The required memory space is calculated based on Table 4.1.*

The FT-Method requires almost triple the amount of memory compared to the IG-Method. This will be critical in memory-limited simulations.

4.1.5 Calculation Speed Comparison

The memory usage analysis is estimated in the last subsection. This subsection will compare the computational step reflected in the speed. Computational complexity is how the computational steps/times scale with simulation elements. At lower simulation elements, the computational time may not scale with this analysis because of other limitations, such as addition, multiplication, data retrieval, communication within the computer, etc.

The FT-Method has a Fourier transform. The complexity of a one-dimensional Fourier transform of an N-length array is $\mathcal{O} N \log N$ (Cooley and Tukey, 1965), where N is the number of simulation elements across the simulation. Since the two-dimensional Fourier transform is equivalent to performing the one-dimensional Fourier transform once for each dimension, the two-dimensional Fourier transform of an N by N array is $\mathcal{O}2N(N\log N) \rightarrow \mathcal{O}N^2\log N$ (Mahmood et al., 2018).

Now, let's analyse our application. The FT-Method contains $2n$ simulation elements across the simulation, where n is the number of simulation elements per subaperture of the SH-WFS. The complexity does not change, because $\mathcal{O}(2n)((2n)\log(2n)) \rightarrow \mathcal{O}n^2(\log(n)+\log 2) \rightarrow \mathcal{O}n^2\log(n)$. The complexity of the Centre-of-Gravity (CoG) in the FT-Method is not included in the calculation because it is smaller (having $\mathcal{O}n^2$ complexity). Meanwhile, because the CoG, IG-Method, and G-Method do not have any transform, they only have $\mathcal{O}n^2$ complexity.

The derived computational complexity only shows the calculation trend at a larger number of simulation elements. It does not exactly show how the algorithm behaves at a specific size. To grasp the situation more precisely, the time taken to complete each algorithm can be measured using time.perf_counter package in Python. The speeds of each method are measured for an increasing number of simulation elements across the SH-WFS lenslet pupil (n) using code from Kongkaew (2025a). Because there is no confirmation on how to incorporate it into the other approximation methods yet, the threshold process on any process is not included in this section. So that the process time can be compared more directly. This thesis will not consider conventional speed-up procedures such as parallelisation, using GPUs, because both methods will definitely benefit. This thesis uses a Linux server (version: Red Hat 11.5.0-5) of the Centre for Advanced Instrumentation to measure time performances. The server has 96 AMD EPYC 74F3 24-Core Processors.

For reference, other processes required to simulate the wavefront sensing processes using a point source as a reference are also included, so readers may grasp an idea of how much adopting the IG-Method can speed up the overall simulation. The other processes include simulating optical turbulence layers and optical propagations between turbulence layers and optical components. Unfortunately, processes related to SH-WFS on extended objects such as solar AO are excluded. This is because I do not have enough expertise in the wide-field extended image generation.

The calculation time in decreasing order is FT-Method, IG-Method, and G-Method. The order is maintained for all numbers of simulation elements across the complex amplitude (Figure 4.2). For a simulation smaller than 32 simulation elements across the subaperture, the speed of FT-Method, IG-Method, and G-Method is limited to 49 μs, 30 μs, and 26 μs, respectively. The limitation is potentially the upload time of the server, such as the time for the CPU to retrieve data from RAM.

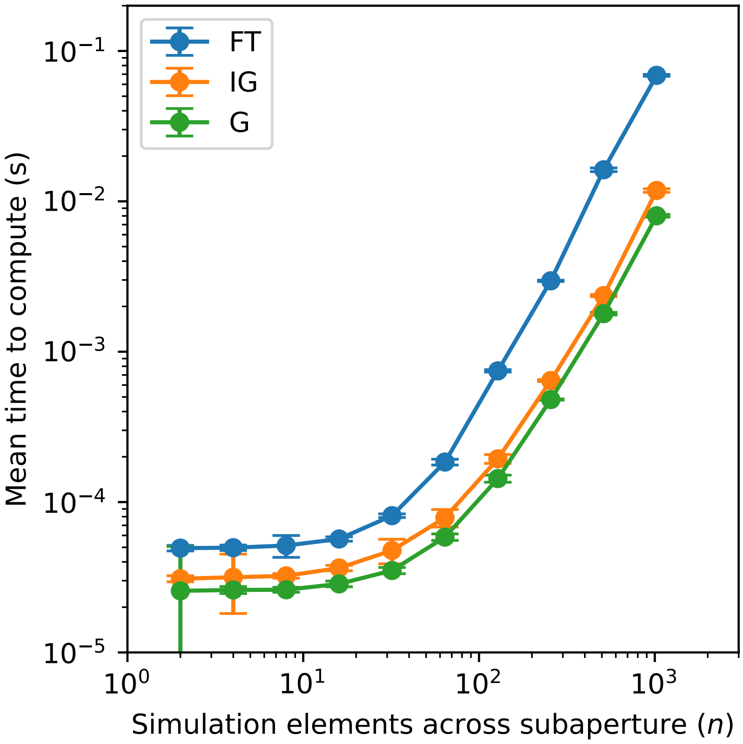

Figure 4.2: *Calculation time and its distribution required to calculate slope measurement over a lenslet of SH-WFS for FT-Method and IG-Method against the number of simulation elements across the lenslet (n). The mean and the standard deviation are calculated from 10,000 independent slope measurements.*

Figure 4.3 plots the ratio of the time taken to calculate wavefront sensor slopes using the IG-Method compared to the FT-Method. The IG-Method uses 64%, 43%, and 17% of the time taken for the FT-Method to complete one slope calculation at $n = 16$, $n = 64$, and $n = 1024$, respectively. On the other hand, the G-Method uses 50%, 32%, and 12% of the time for $n = 16$, $n = 64$, and $n = 1024$. The G-Method is at least twice as fast as the FT-Method for all numbers of simulation elements across the subaperture, while the IG-Method is twice as fast as the FT-Method when the number of simulation elements is 64 or higher.

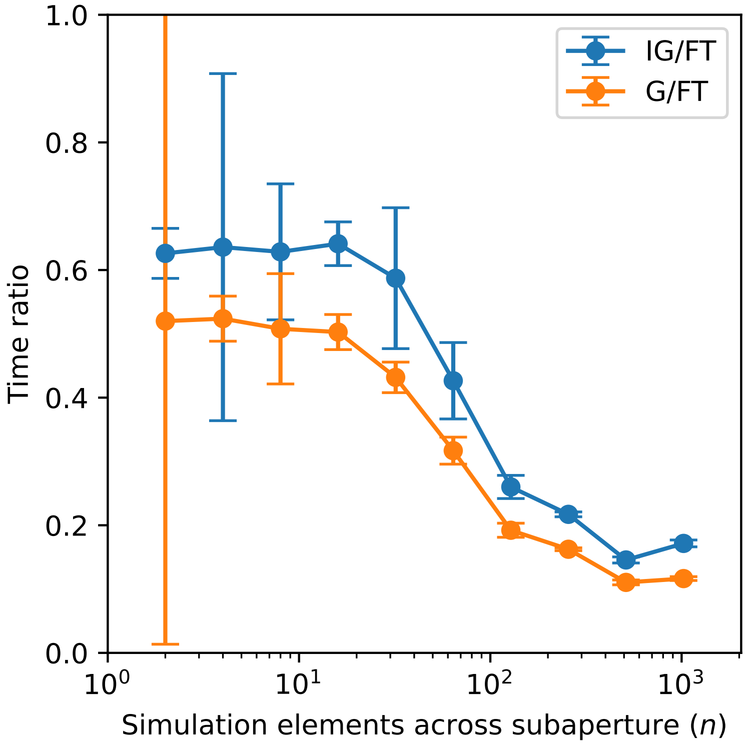

Figure 4.3: *Time spent and its distribution on IG-Method compared to FT-Method to calculate a slope measurement over a lenslet of SH-WFS against the number of simulation elements across the lenslet. The mean and the standard deviation are calculated from 10,000 independent slope measurements.*

Whilst further optimisations are possible, this test successfully shows that IG-Method and G-Method are faster than the FT-Method. Further optimisation can potentially be done on the IG-Method. The author is not an expert in software engineering after all. The written IG-Method and G-Method use the Numpy package in the Python computing language without any parallelisation. In contrast, the FT-Method uses the pyFFTW, a self-proclaimed 'the fastest Fourier transform in the west', to increase the speed of the Fourier transform. Because there exist gaps in coding efficiency between the expertly written pyFFTW and my simple IG-Tilt algorithm, it is most likely possible that the IG-Tilt can be much further optimised.

To show some relevance, the time performances of other processes crucial to AO simulation are also measured. The optical turbulence generation and the optical propagation simulation from Townson et al. (2019) are chosen. Figure 4.4 shows the time used by each process against the number of simulation elements across the simulation (N).

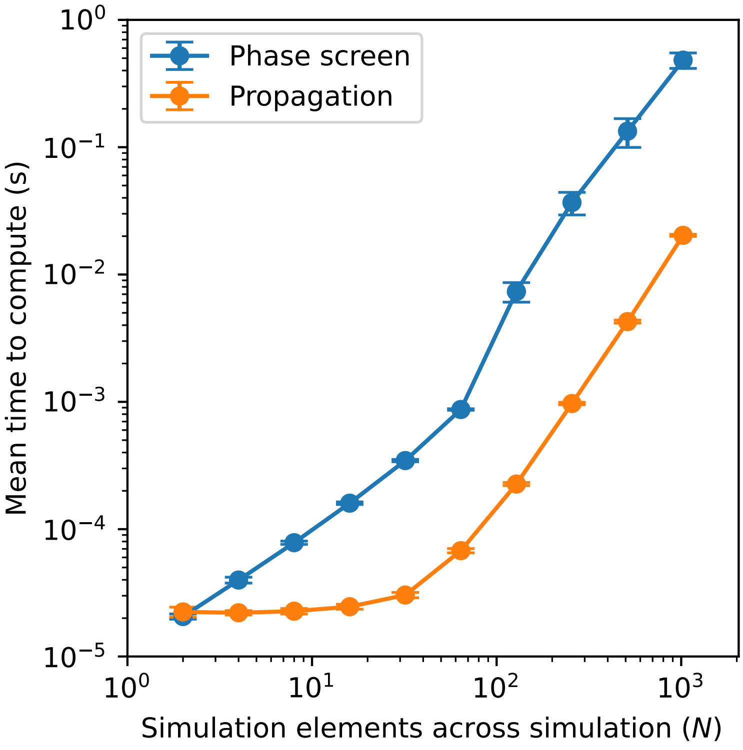

Figure 4.4: *Calculation time and its distribution required to simulate a new infinite phase screen from an existing screen and angular propagation against the number of simulation elements across the simulation screen (N). The mean and the standard deviation are calculated from 10,000 independent slope measurements. Please note that the simulation element across the simulation for the propagation includes all of the buffering of data required, as explained in Chapter 3.*

Based on existing MCAO system designs, including DKIST (Schmidt et al., 2022), EST (Femenía-Castella et al., 2022), MAD (Marchetti et al., 2003), and MORFEO (Busoni et al., 2022), total time estimates needed for different processes for each system are calculated as shown in Table 4.2. Data in Table 4.2 are estimated for one temporal measurement of SH-WFSs in MCAO using a point source. Parallelisation is not used. For nighttime applications, only 16 simulation elements across the subaperture are needed since they mostly operate in a negligible scintillation regime. In comparison, both 16 and 64 simulation elements are estimated for the solar MCAOs. Since I do not have enough expertise in the wide-field extended image generation, estimation time on wavefront sensing using extended objects has to be excluded from this chapter.

	DKIST-16	DKIST-64	EST-16	EST-64	MAD	MORFEO
Single turbulence layer generation time (s)	1.53×10^{0}	2.00×10^{1}	3.84×10^{0}	5.02×10^{1}	5.25×10^{-2}	2.08×10^{0}
Single propagation time (s)	5.73×10^{-1}	2.52×10^{1}	1.16×10^{0}	7.06×10^{1}	9.59×10^{-3}	1.24×10^{0}
Single FT-Method Line-of-Sight (LoS) measurement (s)	5.68×10^{-5}	1.84×10^{-4}	5.68×10^{-5}	1.84×10^{-4}	5.68×10^{-5}	5.68×10^{-5}
Single IG-Method LoS measurement (s)	3.64×10^{-5}	7.87×10^{-5}	3.64×10^{-5}	7.87×10^{-5}	3.64×10^{-5}	3.64×10^{-5}
Single G-Method LoS measurement (s)	2.85×10^{-5}	5.84×10^{-5}	2.85×10^{-5}	5.84×10^{-5}	2.85×10^{-5}	2.85×10^{-5}
Total turbulence layer generation time (s)	4.59	60.00	19.20	251.00	0.11	6.24
Total propagation time (s)	25.79	1134.00	198.36	12072.60	0.32	55.80
Total FT-Method LoS measurement (s)	0.74	2.40	2.33	7.56	0.03	1.97
Total IG-Method LoS measurement (s)	0.48	1.03	1.50	3.24	0.02	1.26
Total G-Method LoS measurement (s)	0.37	0.76	1.17	2.40	0.02	0.99
Adopting IG-Method time gain (s)	0.27	1.38	0.84	4.33	0.01	0.71
Adopting G-Method time gain (s)	0.37	1.64	1.16	5.16	0.02	0.98
Total simulation time - FT-Method-based (s)	31.12	1196.40	219.89	12331.16	0.45	64.01
Percentage time gain from adopting IG-Method (%)	0.86	0.12	0.38	0.04	2.49	1.10
Percentage time gain from adopting G-Method (%)	1.19	0.14	0.53	0.04	3.45	1.53

Table 4.2: *Reduction in simulation time per one temporal measurement of the SH-WFS* ***operating with a point source****. Gains are estimated for various existing multi-conjugate adaptive optics systems when adopting the IG-Method over the Fourier transform method. DKIST-16 and DKIST-64 are DKIST simulations with 16 and 64 simulation elements per subaperture, respectively. Similarly, EST-16, EST-64. Parameters used in this table for DKIST, EST, MAD, and MORFEO are generated based on Schmidt et al. (2022), Femenía-Castella et al. (2022), Marchetti et al. (2003), and Busoni et al. (2022), respectively. Simulation of distorted extended images in each SH-WFS subapertures are NOT included.*

Table 4.2 only shows the expectation time to compute wavefront sensing with a point source. If it were to be extrapolated for an extended source, the expected time for the correlation process for the DKIST-16, DKIST-64, EST-16, and EST-64 were 1.18, 4.97, 3.70, and 15.62 s, respectively. These additional times are approximately four times larger than the gain from adopting the IG-Method, reducing the usefulness. Moreover, if the Point Spread Function (PSF) of each section of the extended source were to be measured at every isoplanatic patch, the new propagation times are as much as $9 \times 10^{1}0$s on a single core, a ridiculously high number. This is an overestimate, where each isoplanatic patch must be simulated entirely independently.

Simulation of the SH-WFS measurement is commonly done by using the FT-Method can be sped up using the IG-Method and G-Method. The reduction in calculation time depends on the number of simulation elements across the subaperture of the SH-WFS (n). To complete one slope measurement with n equal to 16, 64, and 1024, the IG-Method only uses 64%, 43%, and 17% of the time taken for the FT-Method, respectively. On the other hand, the G-Method uses 50%, 32%, and 12%, respectively. Even though time reduction is preferable for the common simulation size, it is negligible compared to the time required for the propagation process. For example, MAD simulation is estimated to have 71% and 24% of the simulation time used by propagation and turbulence generation, respectively. As such, the time reduction percentage from adopting the IG-Method or G-Method instead of FT-Method when including propagation steps between all turbulence layers and DMs is less than 3%, considering existing MCAO systems. For example, MAD has the highest percentage of time reduction. This estimate is for SH-WFS in MCAO operating on a point source. Depending on the method of wide-field image generation, the time reduction achieved by adopting the approximation will vary. At this point, no specific projection can be made.

Further studies can be conducted in the future, once more information becomes available. Firstly, how to simulate a wide-field distorted image on the SH-WFS. Secondly, how many propagation steps are required for the wavefront sensing process? Can the propagation steps be used together with other processes in the MCAO simulation? Lastly, further studies are needed to determine whether applying a threshold to the IG-Method and FT-Method affects their measurement accuracy in the scintillation regime. This thesis does not include the study of the threshold effect.

The next section will show whether or not the IG-Method and G-Method can maintain the FT-Method accuracy, and for which turbulence conditions.

4.2 Algorithm Accuracy

To replace the FT-Method of simulation of the SH-WFS with the IG-Method and G-Method for AO in non-negligible scintillation, the verification must be made whether or not the IG-Method reproduces the SH-WFS slope measurement generated using the Fourier Transform Tilt (FT-Tilt) method in contrast to the G-Method. This section first selects turbulence conditions to study and then simulates them. Then determine the Root-Mean-Square (RMS) gradient difference in the high-signal case. After that, the effect of threshold on the CoG of the SH-WFS is studied. Lastly, measure the RMS slope difference for various observing conditions that may affect centroiding accuracy.

Note that the goal here is to replace the FT model with a faster approach that emulates the SH-WFS response. The goal is not to find a model that most accurately determines wavefront phase gradients across a subaperture.

4.2.1 Selection of Turbulence Conditions

The strength of the scintillation depends on the wavelength being measured by the SH-WFS. This study is primarily aimed at Solar MCAO application; 500 nm is selected in line with the WFS design described in (Schmidt et al., 2022).

Integrated turbulence strengths are chosen to have 2, 5, 8, and 11 cm coherence length (r_0) at 500 nm. These values cover a wide range of daytime turbulence strength conditions (Griffiths et al., 2023). The outer scale is chosen to be 60 times larger than the SH-WFS subaperture size, behaving in Kolmogorov-like statistics. The corresponding layer heights are tuned to provide Rytov parameters (σ_R^2) values of 0.00, 0.01, 0.03, 0.10, and 0.30. This range covers negligible to moderate scintillation conditions. To generate the scintillation strength, a two-layer turbulence model is used with one layer at the ground level and another placed at high altitude. For simplicity, the zenith angle of the observation is chosen to be zero ($\zeta = 0$). Since the distribution of scintillation pattern evolves over the propagation distance as discussed in Equation 2.47, the height of the high-altitude turbulent layer (H) will also be varied from 5, 10, 15, and 20 km. Lastly, since the subaperture size of the SH-WFS affects the spot image quality, the ratio between the SH-WFS subaperture size to turbulence coherent length (d/r_0) must also be specified. The chosen values are 0.5, 1, 2, and 3 to match existing SH-WFS analysis literature (Thomas et al., 2006), which presents the SH-WFS measurement noise analysis in the negligible scintillation regime that should be validated in the scintillation regime. All of the discussed parameters are listed in Table 4.3.

Parameter	**Value(s)**
Turbulence layers	2 layers
Coherence length at 500 nm (r_0)	2, 5, 8, 11 cm
Turbulence outer scale (L_0)	60 d_{sub}
Rytov parameter (σ_R^2)	0.00, 0.01, 0.03, 0.10, 0.30
Subaperture size to coherence length ratio (d_{sub}/r_0)	0.5, 1, 2, 3
High altitude turbulence height (H)	5, 10, 15, 20 km
Wavelength (λ)	500 nm
Elements per lenslet at pupil plane	64 simulation elements
simulation elements per lenslet at focal plane	64 simulation elements
Angular simulation element resolution at focal plane	$\lambda/2d_{sub}$

Table 4.3: *Key simulation parameters to compare measurement differences between the IG-Method and G-Method against the FT-Method in scintillation*

Using these constraints, it is possible to calculate the turbulence strength of each turbulence layer.

- Given the coherence length (r_0), the total turbulence strength ($C_{n,T}^2$) can be calculated from Equation 2.33.
- Next, with only a single turbulent layer at altitude, the turbulence strength of the high altitude turbulence can be calculated from Equation 2.46 to give the required Rytov parameter and high altitude layer height.
- If the turbulence strength of the high altitude ($C_{n,H}^2$) is larger than the total turbulence strength, then the given turbulence condition is not physically possible, and should be ignored.
- Finally, the turbulence strength of the ground layer turbulence ($C_{n,0}^2$) can be calculated.

The distribution of turbulence strength with respect to the desired turbulence conditions is listed in Table 4.4.

r_0	σ_R^2	H	$C_{n,0}^2$	$C_{n,H}^2$	r_0	σ_R^2	H	$C_{n,0}^2$	$C_{n,H}^2$
11	0.01	5	87.07	12.93	11	0.01	10	92.74	7.26
11	0.01	15	94.82	5.18	11	0.01	20	95.93	4.07
11	0.03	5	61.21	38.79	11	0.03	10	78.23	21.77
11	0.03	15	84.47	15.53	11	0.03	20	87.78	12.22
11	0.10	5	N/A	N/A	11	0.10	10	27.43	72.57
11	0.10	15	48.24	51.76	11	0.10	20	59.27	40.73
11	0.30	5	N/A	N/A	11	0.30	10	N/A	N/A
11	0.30	15	N/A	N/A	11	0.30	20	N/A	N/A
8	0.01	5	92.39	7.61	8	0.01	10	95.73	4.27
8	0.01	15	96.96	3.04	8	0.01	20	97.60	2.40
8	0.03	5	77.18	22.82	8	0.03	10	87.20	12.80
8	0.03	15	90.87	9.13	8	0.03	20	92.81	7.19
8	0.10	5	23.95	76.05	8	0.10	10	57.32	42.68
8	0.10	15	69.56	30.44	8	0.10	20	76.05	23.95
8	0.30	5	N/A	N/A	8	0.30	10	N/A	N/A
8	0.30	15	8.67	91.33	8	0.30	20	28.14	71.86
5	0.01	5	96.53	3.47	5	0.01	10	98.05	1.95
5	0.01	15	98.61	1.39	5	0.01	20	98.91	1.09
5	0.03	5	89.58	10.42	5	0.03	10	94.15	5.85
5	0.03	15	95.83	4.17	5	0.03	20	96.72	3.28
5	0.10	5	65.25	34.75	5	0.10	10	80.50	19.50
5	0.10	15	86.09	13.91	5	0.10	20	89.06	10.94
5	0.30	5	N/A	N/A	5	0.30	10	41.50	58.50
5	0.30	15	58.27	41.73	5	0.30	20	67.17	32.83
2	0.01	5	99.25	0.75	2	0.01	10	99.58	0.42
2	0.01	15	99.70	0.30	2	0.01	20	99.76	0.24
2	0.03	5	97.74	2.26	2	0.03	10	98.73	1.27
2	0.03	15	99.09	0.91	2	0.03	20	99.29	0.71
2	0.10	5	92.45	7.55	2	0.10	10	95.77	4.23
2	0.10	15	96.98	3.02	2	0.10	20	97.62	2.38
2	0.30	5	77.36	22.64	2	0.30	10	87.30	12.70
2	0.30	15	90.94	9.06	2	0.30	20	92.87	7.13

Table 4.4: *Distribution of turbulence strength (%) at ground ($C_{n,0}^2$) and altitude ($C_{n,H}^2$) for different Fried parameters (r_0) cm, Rytov parameters (σ_R^2), and turbulence distance (H) km. Unphysical conditions are marked with N/A.*

4.2.2 Methodology

With all simulation parameters selected, the validation of the IG-Method measurement against the FT-Method for noiseless SH-WFS can start.

To validate if the IG-Method can replace the FT-Method for noiseless SH-WFS, slope measurement (OPD) in nm from both methods will be compared against each other. For comparison, measurement from the G-Method will also be included.

Ground and high-layer turbulent phase screens are generated using the infinite phase screen method (Assémat et al., 2006; Fried and Clark, 2008; Reeves, 2016) as discussed in Chapter 3. A uniform intensity wavefront passes through the high altitude turbulence layer, and is then propagated to the ground layer using the angular-spectrum method (Schmidt, 2010) described in Chapter 2 and 3. The technique to reduce phase screen size in Chapter 3 is not used to avoid its error. Also, the technique had not been studied when this chapter was studied. The ground layer phase is then added and used as sampled turbulated wavefronts. The method described in Section 3.2 is used to define the overall simulation resolution while avoiding effects such as aliasing and wrapping.

Each wavefront distortion is measured using three different methods to determine the SH-WFS subaperture slope measurements, including the G-Method, the IG-Method, and the FT-Method. The slope measurements of each method are called Averaged Gradient Tilt (G-Tilt), Intensity-Weighted Averaged Gradient Tilt (IG-Tilt), and FT-Tilt, respectively. If the G-Method is as accurate as the IG-Method, then using G-Method will be much simpler. If the IG-Method is not accurate enough to approximate the FT-Method, then the IG-Method should not be used as the approximation.

The slope measurements are presented through OPD in nm. The relation between the OPD and slope measurement are explained in Chapter 3. The difference between the IG-Method and G-Method against the FT-Method is called OPD error. The RMS of the difference of the OPD is called RMS OPD error.

During the simulation process, some of the turbulence screens cannot be generated using available computation resources, either demanding too much memory space or requiring much longer computation time. The turbulence conditions that are simulated in the study are listed in Table 4.5.

r_0	d/r_0	σ_R^2	H	r_0	d/r_0	σ_R^2	H	r_0	d/r_0	σ_R^2	H
11	0.5	0.01	5	11	0.5	0.01	10	11	0.5	0.03	5
11	0.5	0.03	10	11	0.5	0.10	10	11	1.0	0.01	5
11	1.0	0.01	10	11	1.0	0.01	15	11	1.0	0.01	20
11	1.0	0.03	5	11	1.0	0.03	10	11	1.0	0.03	15
11	1.0	0.03	20	11	1.0	0.10	10	11	1.0	0.10	15
11	1.0	0.10	20	11	2.0	0.01	5	11	2.0	0.01	10
11	2.0	0.01	15	11	2.0	0.01	20	11	2.0	0.03	5
11	2.0	0.03	10	11	2.0	0.03	15	11	2.0	0.03	20
11	2.0	0.10	10	11	2.0	0.10	15	11	2.0	0.10	20
11	3.0	0.01	5	11	3.0	0.01	10	11	3.0	0.01	15
11	3.0	0.01	20	11	3.0	0.03	5	11	3.0	0.03	10
11	3.0	0.03	15	11	3.0	0.03	20	11	3.0	0.10	10
11	3.0	0.10	15	11	3.0	0.10	20	8	0.5	0.01	5
8	0.5	0.03	5	8	0.5	0.10	5	8	1.0	0.01	5
8	1.0	0.01	10	8	1.0	0.01	15	8	1.0	0.01	20
8	1.0	0.03	5	8	1.0	0.03	10	8	1.0	0.03	15
8	1.0	0.03	20	8	1.0	0.10	5	8	1.0	0.10	10
8	1.0	0.10	15	8	1.0	0.10	20	8	1.0	0.30	15
8	1.0	0.30	20	8	2.0	0.01	5	8	2.0	0.01	10
8	2.0	0.01	15	8	2.0	0.01	20	8	2.0	0.03	5
8	2.0	0.03	10	8	2.0	0.03	15	8	2.0	0.03	20
8	2.0	0.10	5	8	2.0	0.10	10	8	2.0	0.10	15
8	2.0	0.10	20	8	2.0	0.30	15	8	2.0	0.30	20
8	3.0	0.01	5	8	3.0	0.01	10	8	3.0	0.01	15
8	3.0	0.01	20	8	3.0	0.03	5	8	3.0	0.03	10
8	3.0	0.03	15	8	3.0	0.03	20	8	3.0	0.10	5
8	3.0	0.10	10	8	3.0	0.10	15	8	3.0	0.10	20
8	3.0	0.30	15	8	3.0	0.30	20	5	1.0	0.01	5
5	1.0	0.03	5	5	1.0	0.10	5	5	2.0	0.01	5
5	2.0	0.01	10	5	2.0	0.01	15	5	2.0	0.01	20
5	2.0	0.03	5	5	2.0	0.03	10	5	2.0	0.03	15
5	2.0	0.03	20	5	2.0	0.10	5	5	2.0	0.10	10
5	2.0	0.10	15	5	2.0	0.10	20	5	2.0	0.30	10
5	2.0	0.30	15	5	2.0	0.30	20	5	3.0	0.01	5
5	3.0	0.01	10	5	3.0	0.01	15	5	3.0	0.01	20
5	3.0	0.03	5	5	3.0	0.03	10	5	3.0	0.03	15
5	3.0	0.03	20	5	3.0	0.10	5	5	3.0	0.10	10
5	3.0	0.10	15	5	3.0	0.10	20	5	3.0	0.30	10
5	3.0	0.30	15	5	3.0	0.30	20	2	2.0	0.01	5
2	2.0	0.03	5	2	2.0	0.10	5	2	2.0	0.30	5
2	3.0	0.01	5	2	3.0	0.01	10	2	3.0	0.03	5
2	3.0	0.03	10	2	3.0	0.10	5	2	3.0	0.10	10
2	3.0	0.30	5	2	3.0	0.30	10				

Table 4.5: *Simulated turbulence condition. The conditions show* r_0 *(cm),* d/r_0*,* σ_R^2*, and* H *(km).*

4.2.3 Excluded Turbulence Conditions

This study has so many missing conditions as shown in Figure 4.5, making the results not represent those omitted conditions. The omitted data in summary are: $d/r_0 = 0.5$, $r_0 = 2$ cm (limited resources), and 0.3 Rytov parameter at large r_0 (unphysical). Excluding the unphysical conditions will not affect the analysis. Even though excluding 0.5 d/r_0 may overestimate the error when analysing with respect to other parameters, since it samples the turbulence at a high rate, the error is small. On the other hand, excluding most of 2 cm r_0 will underestimate the error.

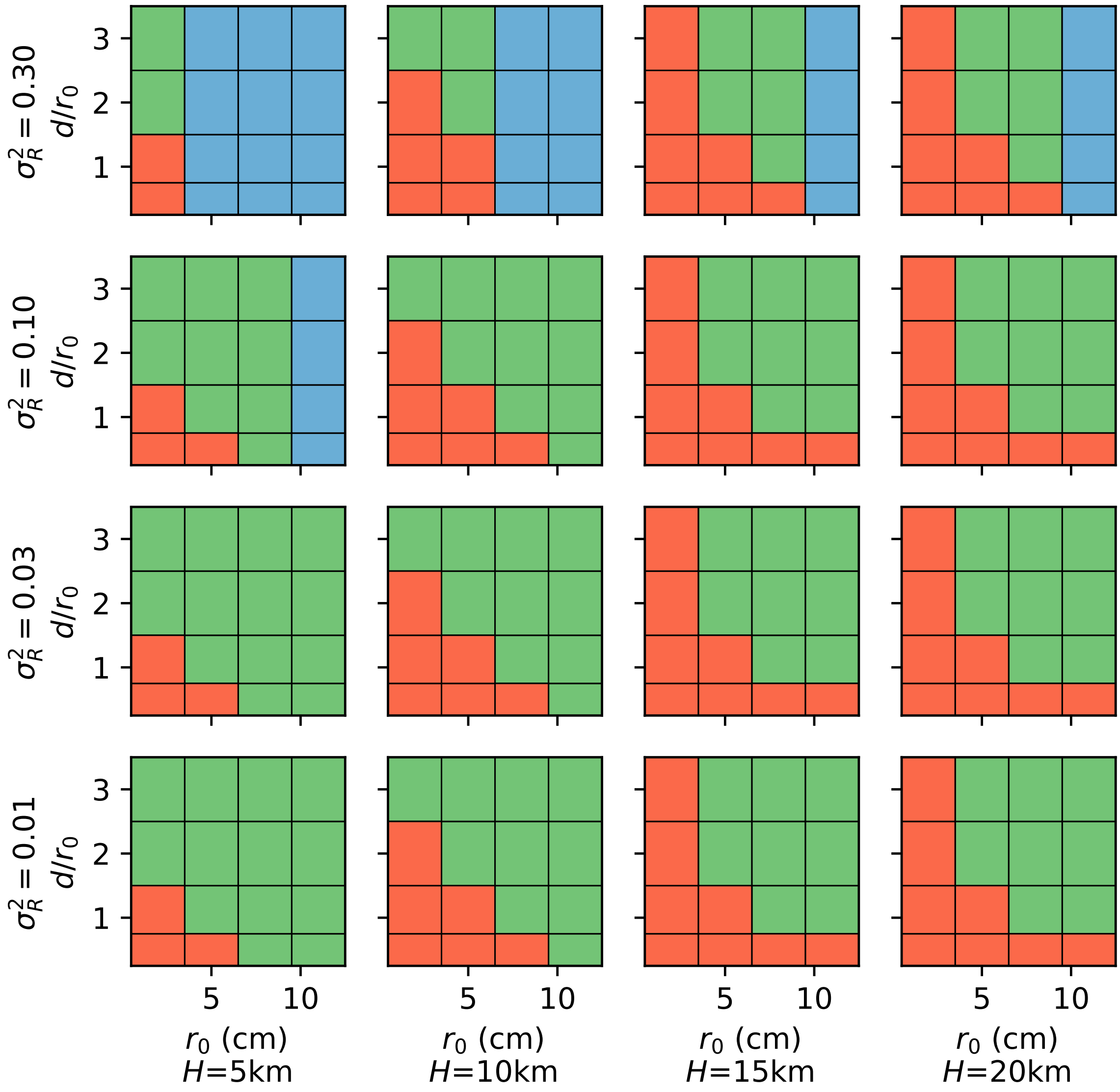

Figure 4.5: *List of turbulence conditions in this study that are simulated (green), unphysical (blue), and computationally limited (red). The outer x-axis and y-axis mark the distance of the high altitude layer (H) and the Rytov parameter (σ_R^2), respectively. While the inner x-axis and y-axis mark r_0 and d/r_0, respectively.*

In summary, analysis at 2 cm r_0 will underestimate the error. This means that the following analysis on 2 cm $_0$ will only represent the sampled conditions, but not the whole possible condition.

4.2.4 Slope Measurement Results

I would like to verify if all of the methods have the same range of slope measurement throughout all of the simulated turbulence conditions. Assuming that the FT-Method configuration in no scintillation can also be used exactly for turbulence with scintillation. Indeed, all of the methods still have the same range reflecting through the RMS OPD depending on d/r_0 as shown in Figure 4.6. The RMS OPD of 0.5 d/r_0 under the simulated scintillation is 10 nm higher than in no scintillation (10% larger). Because all of the measurement methods have the same behaviour, the bias must be from the sampled turbulence conditions; most of 0.5 d/r_0 is excluded from the study as discussed in the last section.

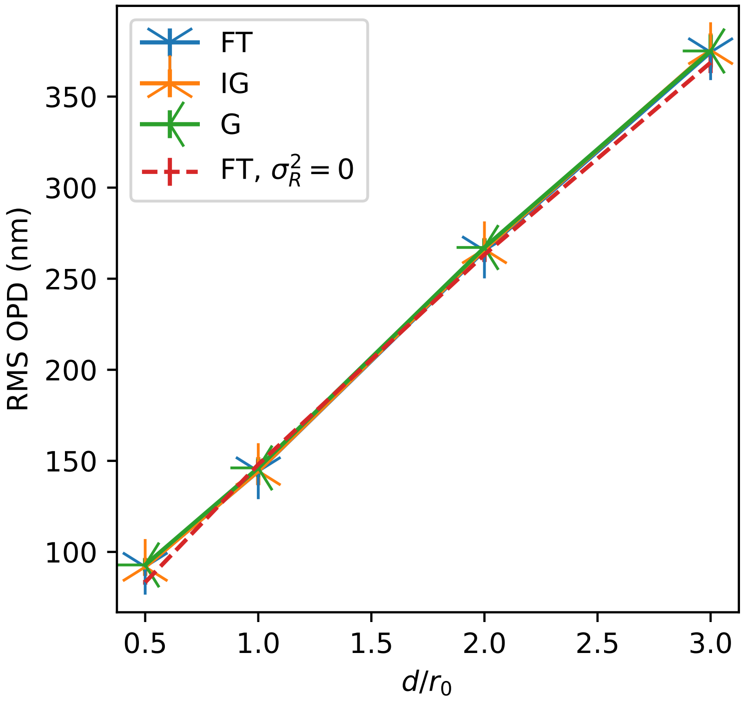

Figure 4.6: *RMS of the measured OPD using the FT-Method against various d/r_0 with and without scintillation.*

4.2.5 Thresholding Effect on the Measurement

This section aims to use the FT-Method of the SH-WFS as a standard to compare against the other methods. The last section shows that extending the same configuration of the FT-Method in the no scintillation case to the scintillation case can still measure the same RMS OPD. This section will analyse deeper on how the RMS OPD error with respect to the FT-Method changes with threshold level in the CoG process of the FT-Method, similar to a benchmark study in Figure 3.17.

Assuming that if either the approximation methods can represent the FT-Method, when the FT-Method varies its threshold level, the RMS error should also behave approximately the same with the FT-Method in no scintillation in Figure 3.17 for both the ‘full’ and ‘partial’ CoG. The Figure 3.17 is also based on a 64x64 detector pixel in a lenslet, same as this Chapter. The benchmark is: the threshold level of 1×10^{-4} yields the least RMS error of the FT-Method using ‘full’ CoG against mean gradient, having 0.5 nm RMS error at $d/r_0 = 0.5$.

RMS measurement error of the G-Method and the IG-Method vs the FT-Method of all the simulated turbulence with Rytov parameter at least 0.01 is measured. Then they are averaged and plotted against varying threshold levels and d/r_0.

Figure 4.7 and Figure 4.8 present the RMS error of different approximation methods against the FT-Method using the ‘full’ and ‘partial’ CoG, respectively. Both figure shows that the G-Method always has larger errors than the IG-Method. Using the 1×10^{-4} threshold level still gives the smallest error compared to the other threshold levels.

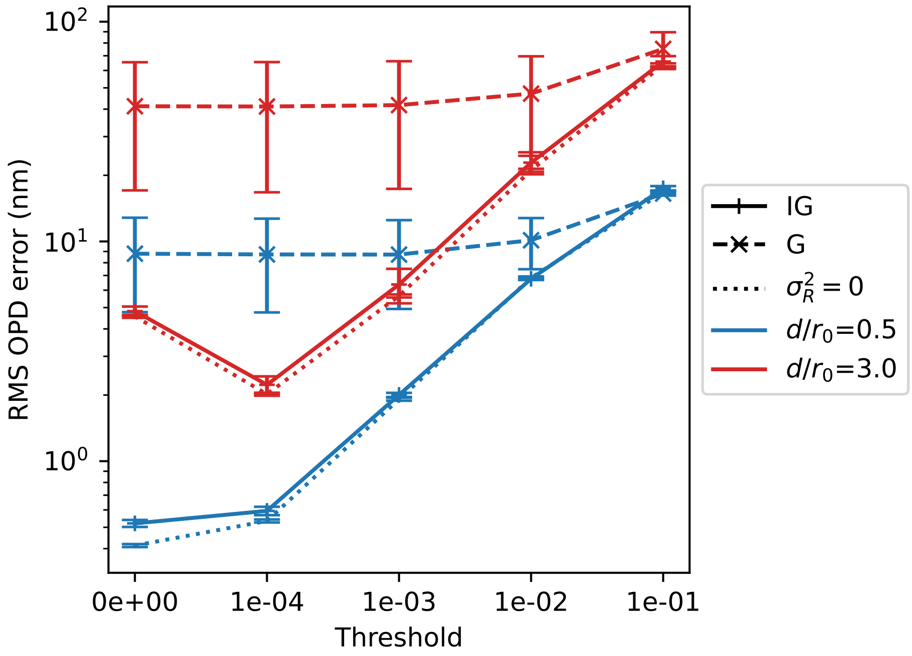

Figure 4.7: *Threshold on 'Full' CoG in scintillation: RMS OPD error and its distribution against the FT-Method (y-axis) versus the threshold level on the FT-Method (x-axis) for varying d/r_0 (colours).*

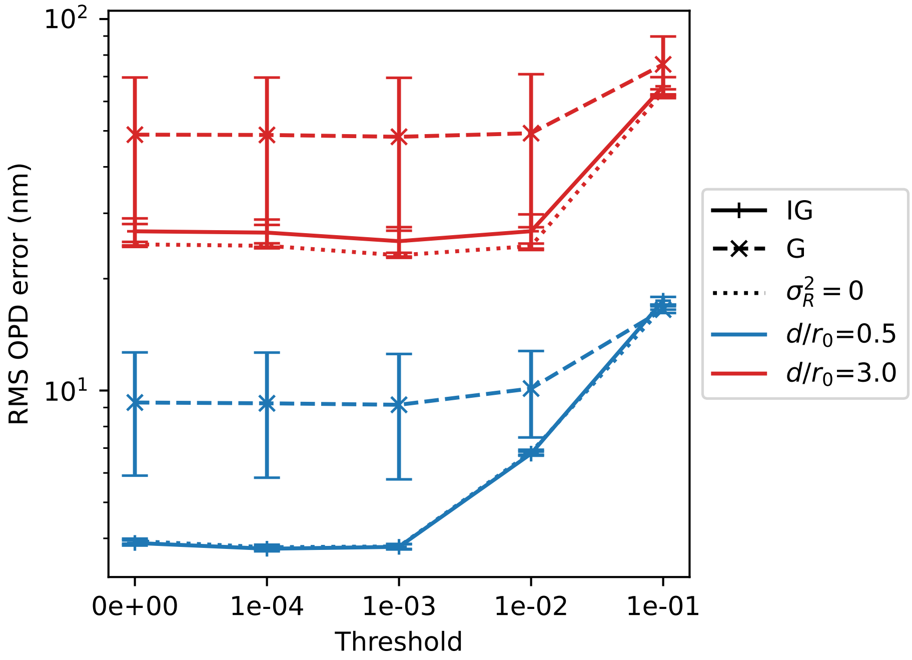

Figure 4.8: *Threshold on 'Partial' CoG in scintillation: RMS OPD error and its distribution against the FT-Method (y-axis) versus the threshold level on the FT-Method (x-axis) for varying d/r_0 (colours).*

With the FT-Method using the 'full' CoG with 1×10^{-4} threshold level as standard in Figure 4.7. The RMS error for the G-Method in scintillation is higher than that in Figure 3.17, also plotted in Figure 4.7 as no scintillation case. The IG-Method has 9 nm RMS error at $d/r_0 = 0.5$, while the IG-Method has only 5 nm, matching the benchmark. This raises a notice that the G-Method cannot approximate the FT-Method when the Rytov parameter is at least 0.01. Furthermore, it highlights that the IG-Method can approximate the FT-Method in scintillation up to a 0.3 Rytov parameter.

In conclusion, the FT-Method in scintillation RMS measurement error to the G-Method does not have a similar threshold effect when the Rytov parameter is larger than or equal to 0.01 is considered, while the IG-Method does. This potentially means that the IG-Method is a proper representation of the G-Method when scintillation is considered. Since the FT-Method using the 'full' CoG with 1×10^{-4} threshold level still have the lowest RMS error to the IG-Method in scintillation, it will be used as the standard reference in the latter sections.

4.2.6 Measurement Bias

This section would like to inspect if there is bias between the measurement methods. Whether or not the error increases as the measured OPD using the FT-Method increases in size. For a strong turbulence condition at $d_{sub}/r0 = 3$, $r_0 = 2$ cm, $\sigma_R^2 = 0.3$, and $H = 10$ km, the error of the G-Method and IG-Method are plotted against the FT-Method measurement in Figure 4.9. The measurement error of the G-Method is much larger than that of the IG-Method, obscuring any bias. On the other hand, Figure 4.10 zooms in on the errors of the IG-Method. It shows approximately only 5 nm bias over a 500 nm range, which is relatively small. The bias level is the same as the benchmark in Figure 3.15. The error in Figure 3.15 and Figure 4.10 is equally opposite in sign due to the subtractions. The prior has FT-Method - IG-Method, while the latter has IG-Method - FT-Method. Furthermore, the measurement error of the IG-Method in no scintillation is also included in Figure 4.10, having a similar but smaller error distribution at a glance.

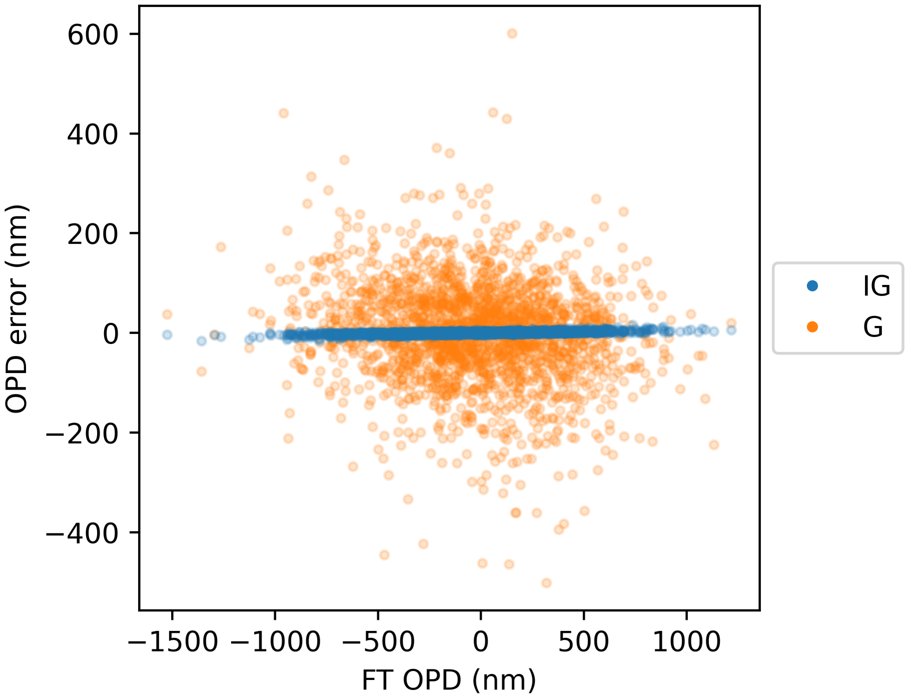

Figure 4.9: *Measurement errors of both the G-Tilt (orange) and the IG-Tilt (blue) compared to the FT-Tilt at* $d_{sub}/r0 = 3$, $r_0 = 2$ *cm*, $\sigma_R^2 = 0.3$, *and* $H = 10$ *km*

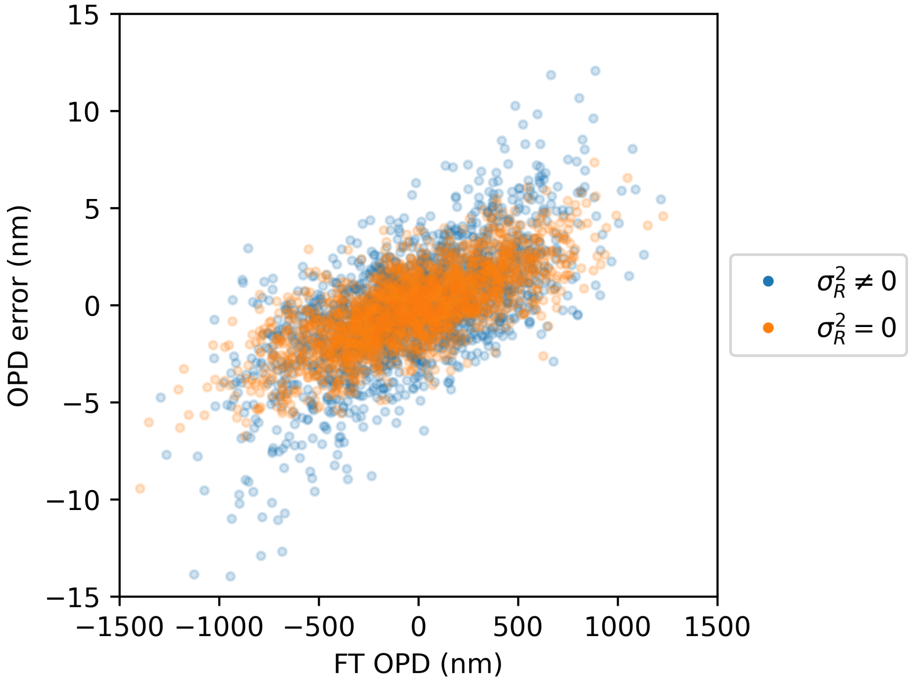

Figure 4.10: *Measurement errors of the IG-Tilt (blue) compared to the FT-Tilt at* $d_{sub}/r0 = 3$, $r_0 = 2$ *cm,* $\sigma_R^2 = 0.3$, *and* $H = 10$ *km. The IG-Tilt measurement error in no scintillation (orange) is also included for reference.*

4.2.7 Analysis of Scintillation Effect on RMS Measurement Error

The analysis will be focused first on the G-Method compared to the IG-Method. After that, the analysis of the IG-Method will be inspected closely in comparison to the no-scintillation cases. In all cases, the IG-Method has a small difference to the no scintillation cases, while the G-Method has a noticeably larger error.

The parameter that has the highest impact on the slope measurement of both the G-Method and the IG-Method for both with and without scintillation case is the ratio of subaperture size to the Fried parameter (d_{sub}/r_0) as shown in Figure 4.11. Again, the G-Method has a much larger RMS error than the IG-Method. The G-Method has the RMS error varies between 10 and 40 nm, while the IG-Method has 0.6 to 2 nm. Since the d/r_0 parameter has the highest impact on the RMS error measurement, the other analysis will be done separately for each d/r_0 parameter.

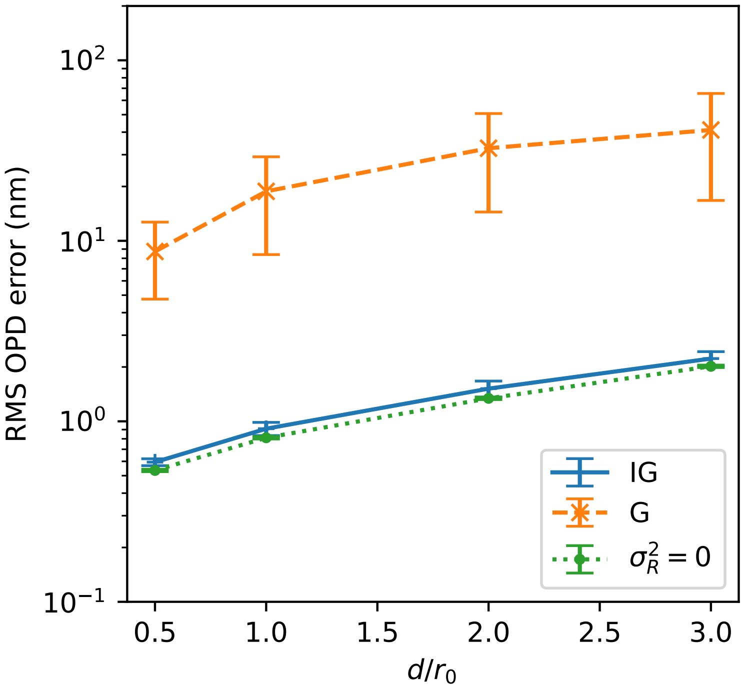

Figure 4.11: *RMS OPD error and its distribution from using the IG-Method and G-Method compared to the FT-Method against* d/r_0*.*

In contrast to the measurement RMS error with respect to varying d/r_0, the error with respect to r_0 appears to have a small effect on the IG-Method varying within 1 nm RMS but a significant effect on the G-Method varying up to 40 nm RMS at d/r_0 equals 3, when the simulated data is averaged over the other parameters as shown in Figure 4.12.

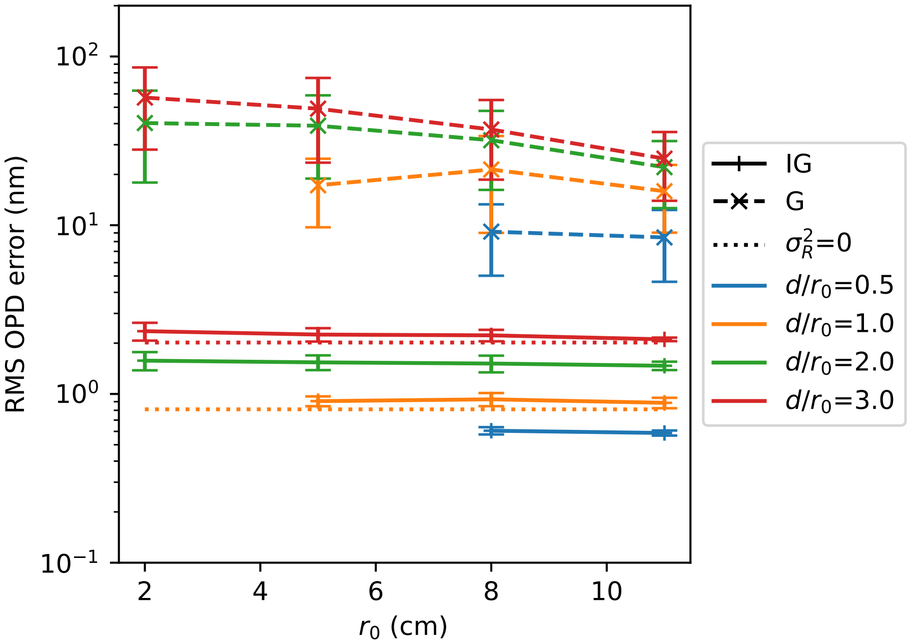

Figure 4.12: *RMS OPD error and its distribution from using the IG-Method and G-Method compared to the FT-Method against Fried parameter.*

So far, the RMS error of the approximation methods is compared against turbulence parameters that are applicable to both with and without scintillation cases. Now, they will be compared against parameters existing only in cases with scintillation. The first parameter to be inspected is the Rytov parameter. Figure 4.13 shows the evolution of the RMS error against the Rytov parameter. Please note that the x-axis is normally in a standard log scale, except for the 0 Rytov parameter, which is cosmetically placed, since it does not exist in a log scale. Consequently, the plot appears to have a sharp change in behaviour at the 0 Rytov parameter. The IG-Method has a minimal increase in the RMS error, having less than 1 nm RMS. On the other hand, the G-Method has a huge increase between 0 and 0.01 Rytov parameter up to 20 nm RMS, after that it jumps another 80 nm RMS at d/r_0 equals 3. This shows that the G-Method is not suitable for Rytov parameters larger than or equal to 0.01. With respect to Table 4.4, this means that at 11 cm r_0, a layer with 5% strength at 20 km, will have 40 nm RMS error at d/r_0 equals 0.5. In comparison, Femenía-Castella et al. (2022) uses only 1% turbulence strength at 20 km, so this effect might not even be of concern to solar telescopes at the current usage, unless its turbulence conditions were to be extended.

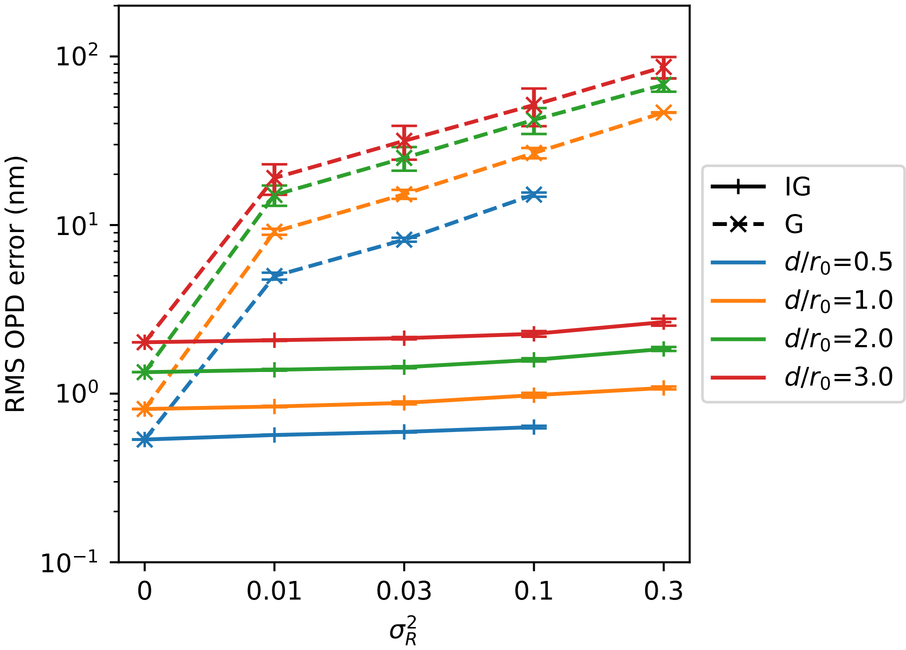

Figure 4.13: *RMS OPD error and its distribution from using the IG-Method and G-Method compared to the FT-Method in various expected Rytov parameter.*

The last parameter's impact on the RMS error to be studied is the high altitude turbulence distance to the ground (H) as shown in Figure 4.14. The RMS error of the G-Method increases only 10 nm, and that of the IG-Method only 1 nm for d/r_0 equals 3. The increase is much smaller compared to the r_0 influence. This is potentially caused by bias as higher turbulence distances miss lower r_0 values, as shown in Figure 4.5 due to computational power. Though the 2 cm r_0 at 20 km distance at 0.01 Rytov parameter will have the high altitude strength at less than 0.71% and even has the turbulence distribution included in Femenía-Castella et al. (2022), it only occurs 10% of the time in the LoS up to 40 degrees elevation. So, the bias on the high altitude turbulence distance should not be of concern.

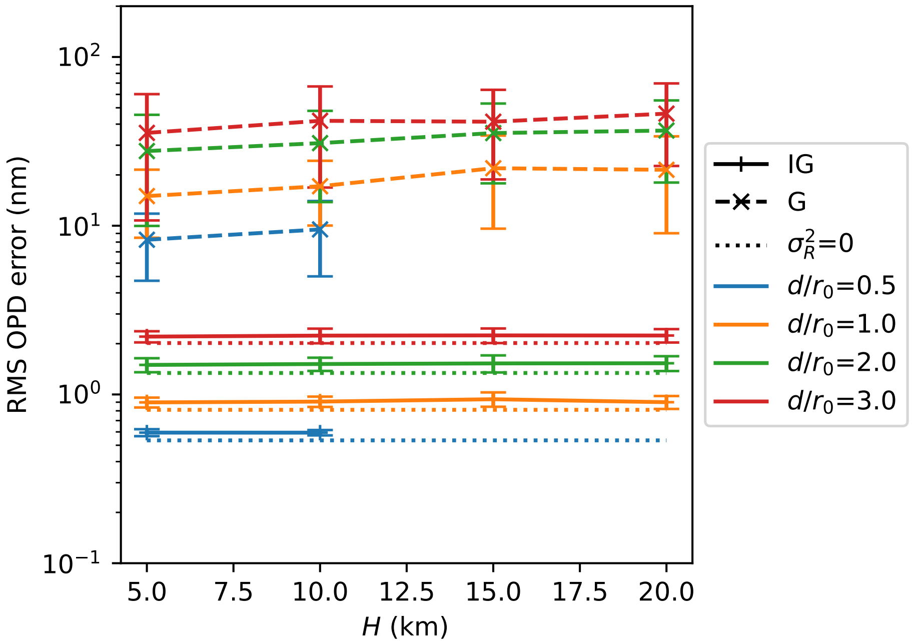

Figure 4.14: *RMS OPD error and its distribution from using the IG-Method and G-Method compared to the FT-Method against distance of the high altitude turbulence.*

Currently, all of the RMS error comparisons between the IG-Method and G-Method are covered. The close-up analysis on the G-Method is presented in Figure 4.15. Among all of the parameters explored, the parameters with the highest to lowest impact within the sampled turbulence conditions are d/r_0, Rytov parameter, r_0, and H, having approximately 2, 0.75, 0.5, and 0 nm RMS increases. The H parameter has the highest overall difference to the no scintillation case, but it is only 0.25 nm RMS, raising no concerns (reducing Strehl ratio by 0.0001 at 500 nm wavelength). In addition, the influence of r_0 is not expected since it does not have any in no scintillation cases, but again has only 0.5 nm RMS increases, raising no concerns.

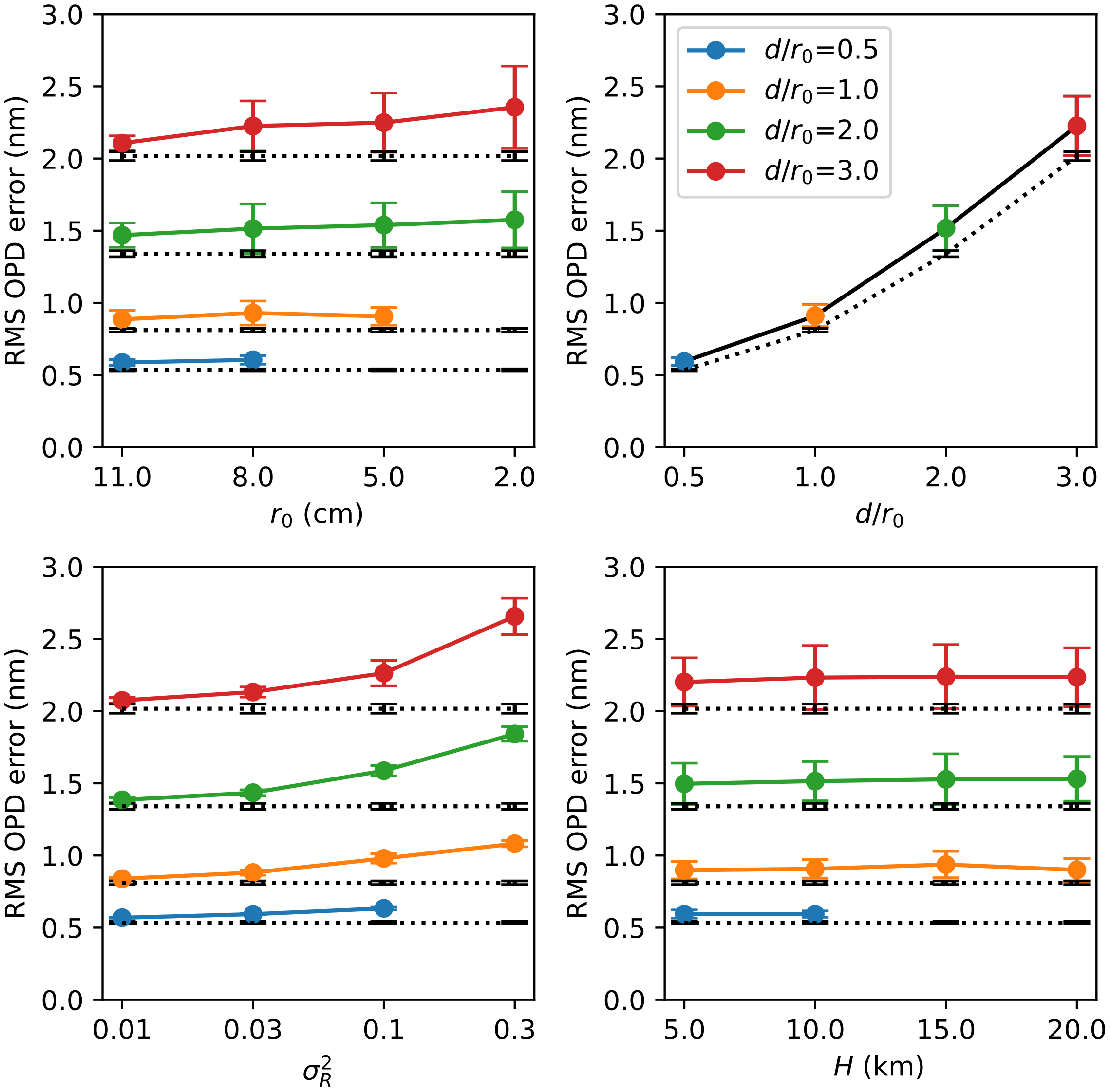

Figure 4.15: *RMS OPD error and its distribution from using the IG-Method compared to the FT-Method against r_0, d/r_0, σ_R^2 and H (upper left, upper right, lower left, and lower right, respectively). Values with the same conditions except for the parameter being investigated are linked by lines. d/r_0 of 0.5, 1, 2, and 3 are marked with blue, orange, green, and red, respectively. The RMS error in no scintillation is shown with black lines.*

In conclusion, in low SH-WFS noise conditions, the FT-Method using all of the 64x64 detector pixels for the CoG computation with 1×10^{-4} threshold level has the least RMS error to both the IG-Method and the G-Method. The IG-Method has almost 20 times smaller RMS error than the G-Method, 3 nm RMS at max compared to 60 nm. There is bias in the IG-Method compared to the FT-Method, having 5 nm bias at 500 nm. Turbulence parameters from the highest to lowest contributions to RMS error of the IG-Method are d/r_0, Rytov parameter, r_0, and H, having 2, 0.75, 0.5, and 0 nm RMS increase, respectively. The increase in RMS error for the IG-Method is negligible, because it only contributes to the Strehl ratio up to 0.1%. Consequently, the IG-Method is more preferable to approximate the FT-Method at Rytov parameter larger than or equal to 0.01. At a lower Rytov parameter, the advantage has not yet been studied.

Now the IG-Method is proven to have negligible RMS error to the FT-Method in high signal or low noise conditions of the SH-WFS. The next question is, how should the noise be approximated?

4.3 Noise Approximation

This section investigates the addition of typical SH-WFS and detector noise terms to the IG-Method. The key noise terms affecting SH-WFS measurement include photon ($\sigma^2_{\phi,N_{ph}}$) and readout noise (σ^2_{ϕ,N_r}).

This section aims to apply the existing noise model on scintillation-free SH-WFS to the IG-Method in the scintillation case. Because measurements of the IG-Method are close to the FT-Method, having only 3 nm RMS difference. Consequently, the Noise Equivalent Angle (NEA) generated from a Gaussian distribution can be added to the measurement. However, it is questionable if the existing noise models are applicable in scintillation. This section needs to evaluate noise on the FT-Method, and then compare the noise in the case with and without scintillation.

Thomas et al. (2006) and Rousset (1999) present an analysis of SH-WFS measurement error in the presence of photon and readout noise. The measurement noise due to photon noise in rad^2 ($\sigma^2_{\phi,N_{ph}}$) is estimated by

$$\sigma^2_{\phi,N_{ph}} \approx 2\frac{W}{N_{ph}}, \tag{4.11}$$

where W is the FoV of the focal plane in terms of λ/d_{sub} and N_{ph} is the number of detected photo-electrons in a lenslet.

The measurement noise due to the detector readout noise in rad^2 is estimated by

$$\sigma^2_{\phi,N_r} = \frac{\pi^2}{3}\frac{N_r^2}{N_{ph}^2}\frac{N_s^4}{N_{samp}^2}, \tag{4.12}$$

where N_r is the RMS of readout electrons per pixel, N_s is the number of detector pixels used in the centroiding calculation, and N_{samp} is defined as $(\lambda/d_{sub})/p$, where p is the angular pixel scale.

4.3.1 Methodology

To measure noise distribution, 256 of 64x64-pixel images within a lenslet of the FT-Method with varying scintillation conditions are drawn from the previous section. After that, for each image, measure 256 slope measurements with varying noise and threshold conditions. After that, to match existing instruments more closely, only the 17x17-pixel centred on the pixel with the maximum intensity is used for the CoG calculation (‘partial’ method described in Chapter 3). Consequently, in this simulation, $W = 64/2 = 32$, $N_s = 17$, and $N_{samp} = 2$.

In detail, the noise is added, and a threshold is applied as follows.

- Grab the intensity profile from the last section, and scale its total number of photo-electrons to the desired level.
- Add photon noise through a Poisson distribution, then a readout noise through a Gaussian distribution with a matching noise level.

- Subtract the threshold level from the intensity.
- Any pixels with intensity less than zero are set to zero. Applying the threshold level with this method ensures that the intensity profile is continuous.
- Resume to CoG measurement as usual.

Noise levels are calculated from $RMS\{s_{n,t} - s_0\}$, which is RMS difference between noisy slope or with irregular threshold ($s_{n,t}$) and slope with high signal analysed in the last section (s_0).

Simulated noise conditions range between a hundred and a million photo-electrons (N_{ph}) and 0.1 to 10 RMS readout electrons per pixel (N_r). The threshold varies between 0 and 0.1 of the maximum intensity registered by the detector.

Parameter	**Value(s)**
Number of optical turbulence phase screens	256
Number of measurements for each phase screen	256
Number of photoelectrons (N_{ph})	10^2, 10^3, 10^4, 10^5, 10^6
RON (e^-/pixel)(N_r)	0, 0.1, 0.3, 1, 3, 10
Normalized threshold level	0, 10^{-4}, 10^{-3}, 10^{-2}, 10^{-1}
Number of phase pixels in CoG calculation	17x17 pixels

Table 4.6: *Key simulation parameters to study the effect of scintillation on noise of SH-WFS using the FT-Method*

4.3.2 Photon Noise

The photon noise is calculated from the RMS of the difference between slope measurement with photon noise included ($s_{P,0}$) and without applying photon noise ($s_{0,0}$), $RMS\{s_{P,0} - s_{0,0}\}$.

Figure 4.16 shows the contribution of photon noise to the measurement error against the model on the photon noise previously introduced. The photon noise level varies among different d/r_0 levels more than from having scintillation or not. Please note that the photon noise level in this section is the total number of photons in a lenslet - not the flux, which is the number of photons per unit area. At 100 photoelectrons with 3 d/r_0, the noise with and without scintillation is unnoticeable in the figure, overlaying perfectly. Meanwhile, at 100 photoelectrons, 3 d/r_0 has 60 nm noise RMS, while 0.5 d/r_0 has 35 nm noise RMS (25 nm difference).

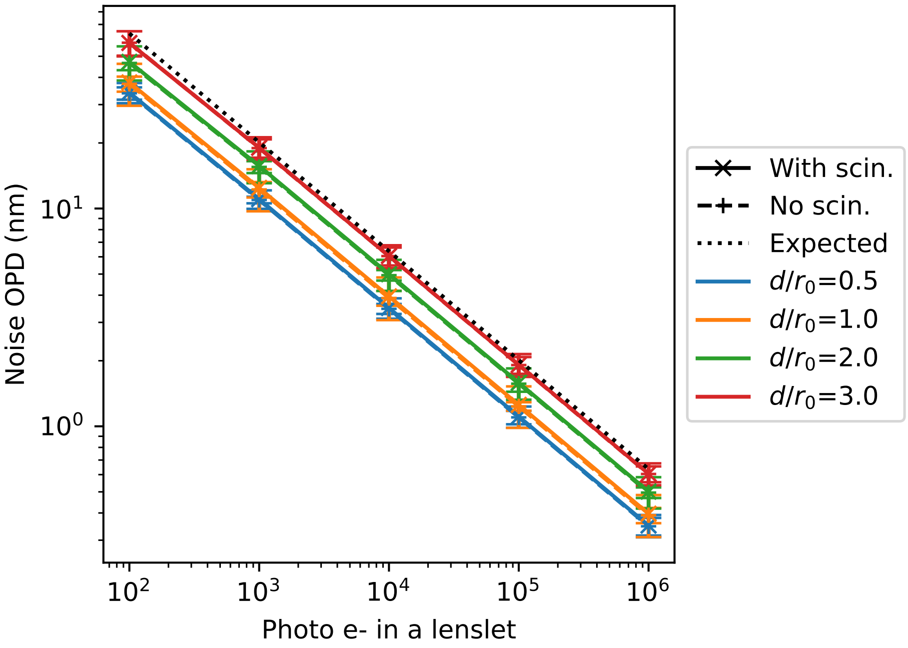

Figure 4.16: *Photon noise: RMS OPD measurement and its distribution due to photon noise of different d/r_0 parameters over all simulated scintillation conditions.*

Next, inspect closely the measured noise compared to the noise model presented earlier. The linearly subtracted measured noise RMS from the model. In other words, the distance from the solid and dashed lines to the dotted line in Figure 4.16, is shown in Figure 4.17. It shows how much the model overestimates the measured photon noise. The difference of noise RMS between scintillation and scintillation-free is negligible for all photoelectron numbers and d/r_0.

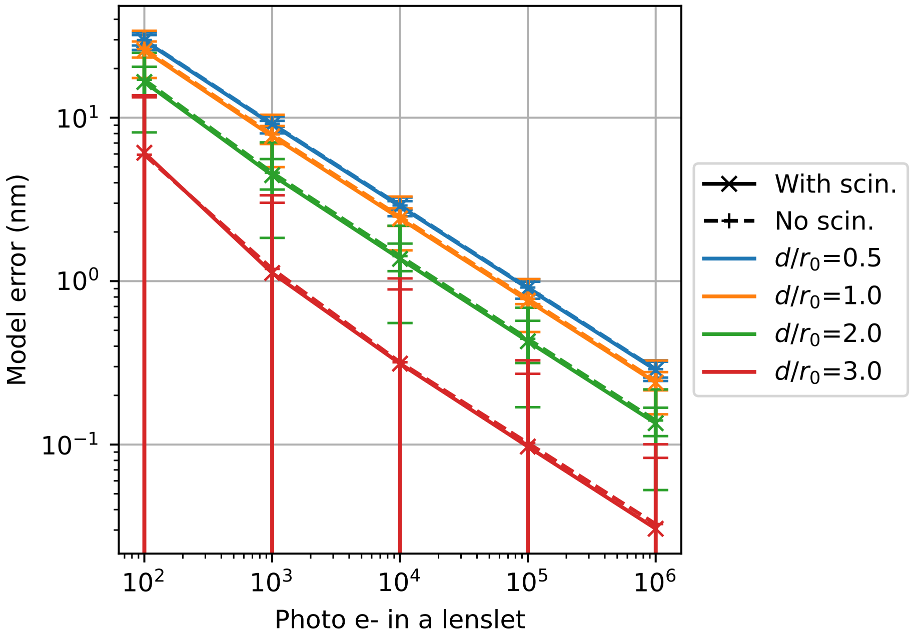

Figure 4.17: *Photon noise difference to the model. Shows how much the model overestimates the measured noise in scintillation and scintillation-free, with only photon noise applied.*

4.3.3 Readout Noise

The noise from RMS readout electrons per pixel (R) at conditions with number of total photons in a lenslet (P) is calculated from $\sqrt{RMS_{P,R}^2 - RMS_{P,0}^2}$, where $RMS_{P,R}$ is the RMS measurement error with both photon and readout noise applied ($RMS\{s_{P,R} - s_{0,0}\}$) and $RMS_{P,0}$ has only the photon noise applied ($RMS\{s_{P,0} - s_{P,0}\}$).

Figure 4.18 shows the measured readout noise contribution compared to the readout noise model previously introduced at 2 d/r_0. The readout noise error is larger than what the model predicts in 10^6 photoelectrons and 0.3 - 1 RMS readout electrons per pixel, because the readout electrons are much smaller than the threshold level of $1 \times 10^{-4} \times 10^6 = 100$. At 100 - 1000 photoelectrons per lenslet (64x64 pixels), due to the low number of photon electrons distributed per pixel, the model largely overestimates the noise measurement.

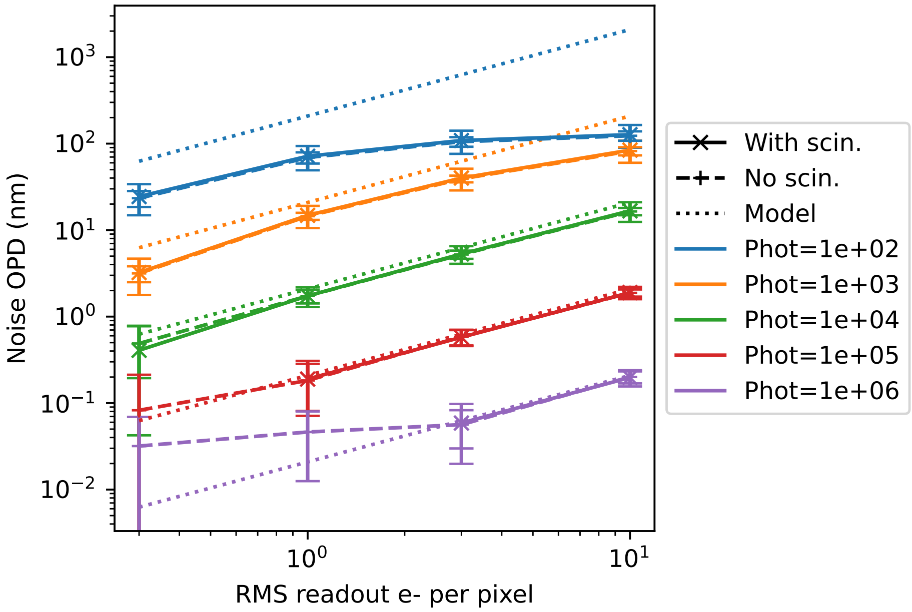

Figure 4.18: *Readout noise: RMS OPD and its distribution due to readout noise over all simulated scintillation conditions at* $d/r_0 = 2$.

From Figure 4.18, the linear difference between the measured noise RMS and the model noise RMS is calculated. In other words, the distance from the solid and dashed lines to the dotted lines. The difference is plotted in Figure 4.19. Errors of the readout models are larger at a low number of photoelectrons. The model error of the scintillation case and the scintillation-free case is negligible.

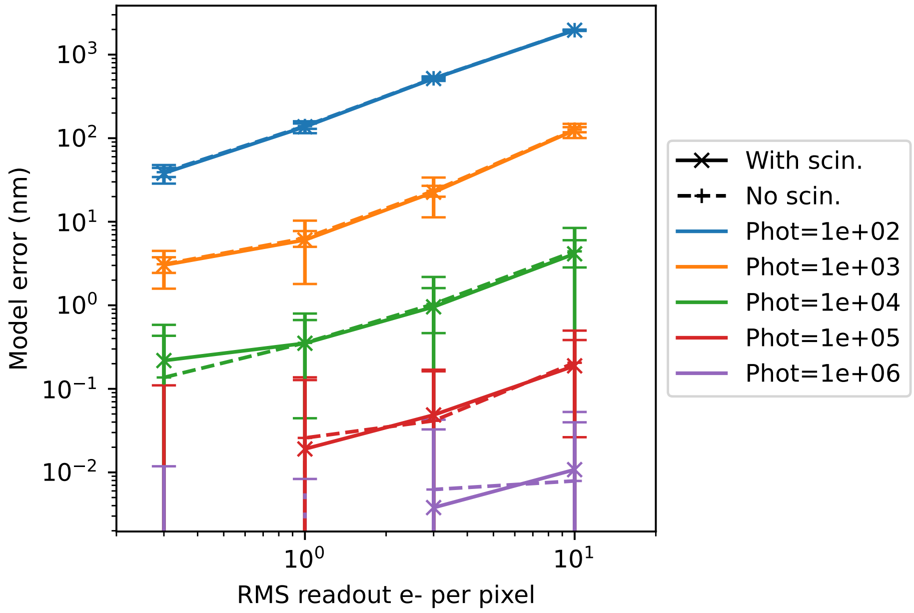

Figure 4.19: *Readout noise: Shows how much the model overestimates the measured noise in scintillation and scintillation-free, at* $d/r_0 = 2$.

4.3.4 Difference of Measured Noise RMS between Scintillation and Scintillation-Free

The previous sections investigated the existing noise model on the SH-WFS with and without scintillation, showing that the linear difference between the model and measured noise with scintillation is relatively the same as that without scintillation. The model can estimate measurement noise in scintillation as well as scintillation-free conditions. The next question is how much the difference is between the measured RMS noise with scintillation and without scintillation, or what is the error of the measured NEA between scintillated and scintillation-free SH-WFS. In other words, the RMS of the linear distance between the solid and dashed lines in Figure 4.17 and 4.19. Consequently, the linear percentage difference is measured and plotted against the noise in scintillation-free in Figure 4.20. The figure includes the error of the NEA for just photon noise, photon and readout noise, and when a non-standard threshold is applied. The difference is shown to be less than 4%, 7.5%, and 10% of the scintillation-free case for when only photon noise, photon and readout noise, and non-standard threshold, respectively.

Consider a SH-WFS in some photoelectrons and a readout electron. If that system has 10 nm RMS measurement noise in scintillation-free conditions, not necessarily the same as from the model. The SH-WFS measurement in scintillation with the same photoelectron and RMS readout electron as the mentioned case will be 10 ± 1 nm.

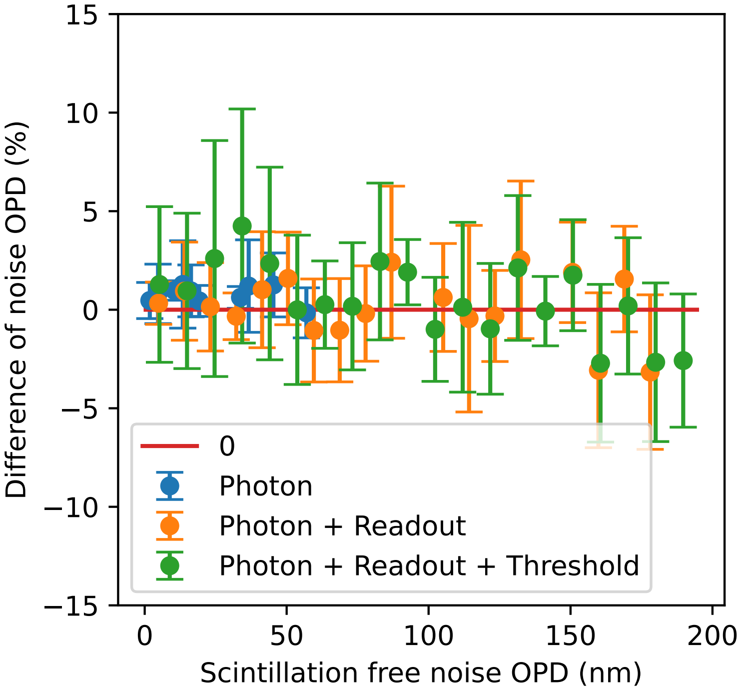

Figure 4.20: *Error of the NEA between the SH-WFS measurement using the FT-Method with and without scintillation (y-axis) against the measured noise in no scintillation (x-axis). Positive values representing the noise in the scintillation case are higher than those without scintillation.*

In summary, since the IG-Method measurement only has less than 3 nm RMS to the FT-Method of the SH-WFS, noise estimations of the FT-Method in scintillation can be used to generate NEA as noise directly on the IG-Method. However, there only exist noise models for the FT-Method in scintillation-free cases (Thomas et al., 2006) and (Rousset, 1999). The question is whether or not the existing noise models in the scintillation-free cases can also be used for the scintillation cases. The noise models are then compared against the measured noise of the FT-Method in scintillation and scintillation-free conditions. It is found that the noise model can estimate the measured noise in scintillation, as well as it can estimate the scintillation-free cases. The difference in measured noise between the scintillation and scintillation-free is within 10% of the measured noise in scintillation-free.

4.4 Conclusion

The IG-Method is proposed as a faster alternative to the FT-Method of simulating a SH-WFS while maintaining simulation accuracy even in the presence of scintillation. Adopting the IG-Method significantly reduces simulation time, requiring only 0.6 to 0.2 of the time needed for the FT-Method. In addition, the IG-Method uses only 30-40% of the computational memory required by the FT-Method. However, the time required to simulate a full solar MCAO simulation is dominated by the propagation process. Without minimising the propagation process time, adopting the IG-Method is not useful.

The IG-Method provides a better approximation of FT-Method compared to G-Method, with an OPD difference of less than 3 nm RMS across Rytov parameter range of 0.01 (negligible scintillation) to 0.3 (medium/strong scintillation), regardless of the turbulence strength (r_0) and turbulence layer distance from ground.

The IG-Method can utilise a NEA approximation to include the effects of both photon and detector read noise on WFS performance. The measured NEA has ± 10% error between scintillation-free and scintillation SH-WFS by 4%, 7.5%, and 10% in photon noise dominated, readout noise dominated, and using a non-standard threshold, respectively. Thus, the accuracy of the noise model is limited by the model's capability to estimate the scintillation-free SH-WFS.

Since the IG-Method is a geometrical approximation of a propagation effect in the FT-Method is found to have only 3 nm RMS in Rytov parameter, less than 0.3, a negligible error. Is it possible to also apply a similar approximation to the propagation process, which is the most time-demanding process to simulate the solar MCAO?

Currently, for MCAO operating on a point source, the propagation process occupies 85% of the computational time. If it can be approximated similarly to the IG-Method, the total computational time of the solar MCAO can be reduced by 35 - 60%. The applicability of using the IG-Method for propagation can be studied in the future.

More studies on the applicability of the IG-Method on simulation of actual solar MCAO systems are left to be done, because this chapter did not include the wavefront sensing with extended objects, such as the correlation SH-WFS (Löfdahl, 2010). To generate the distorted wide-field image used in the process, aberrations within the image anisoplanatism must be measured first. Simulations of this effect require an increasing number of LoS to be measured, and it is possible that the geometrical approximation of the IG-Method could be used to either generate distorted extended images required in the correlation SH-WFS, or potentially to emulate the response of the wide-field correlation-based SH-WFS directly. These extended studies was not undertaken as part of this thesis however but are a logical next step to demonstrate the usefulness of the IG-Method to Solar AO simulations.

The next chapter investigates the effects of optical propagation on the performance of the MCAO control system. Since the geometrical approximation in this chapter is found to be accurate, it gives an inspiration on how to characterise the reduction of the control performance due to the optical propagation.

Key Findings

1. The IG-Method to simulate the SH-WFS uses only 30-40% memory and 35-60% of the time used in the FT-Method, depending on the spatial resolution of the simulation.
2. However, this speed improvement is negligible because the time taken for propagation between atmospheric layers and deformable mirrors dominates the simulation time. In the example presented, adopting the IG-Method only has a 3% reduction, while the propagation process and turbulence simulation use 71% and 24%, respectively.
3. The IG-Method has RMS OPD error compared to the FT-Method less than 3 nm at 3 $d/r0$ and Rytov parameter less than 0.3. The IG-Method therefore provides an accurate representation of the response SH-WFS, even in moderate stregnth scintillation.
4. The G-Method has higher error than the IG-Method in the presence of scintillation. It has up to 30 nm RMS OPD error for $d/r0 = 3$. We would not however recommend use of the G-Method for quickly simulating SH-WFS in the presence of even minimal scintillation.
5. Noise of the IG-Method can be generated by using NEA with estimated noise values from analytical models of SH-WFS noise.
6. The use of the NEA to emulate realistic noise sources present within a SH-WFS in scintillation conditions is measured to be ± 10% of the actual noise observed.

5 Distortion of Multi-Conjugate Adaptive Optics Control

This chapter explores the degradation of Multi-Conjugated Adaptive Optics (MCAO) control due to pupil distortion. MCAO enhances the resolution of wide-field observations through optical turbulence layers by utilising multiple Deformable Mirror (DM)s and Wavefront Sensor (WFS)s. Each WFS observes multiple DMs on top of each other in a Line-of-Sight (LoS). Control errors can arise from either misalignment between the DM and WFS (Heritier et al., 2021), or, as is the focus of this chapter, from the perturbation of other DMs when MCAO is active. For example, consider an MCAO system where light after the telescope pupil travels through **DM1** first, then **DM2**, and lastly WFS. When the **DM2** applies a phase correction, it can distort the image and calibration of **DM1**s if the applied phase is sufficiently strong (e.g., during solar observation in the optical range). Consequently, commands sent to these more distant DMs become incorrect (Kongkaew et al., 2024).

Performance of daytime MCAO is degraded by pupil distortion (Von Der Luhe, 2004; Schmidt et al., 2012; Van Dam et al., 2020). Conditions like daytime, low-elevation angles, shorter wavelengths, or urban environments lead to stronger atmospheric turbulence. This, in turn, results in more pronounced scintillation and distortion. These situations are primarily applicable to solar astronomy, free-space optical communications, directed energy, and ultraviolet observation.

Pupil distortion involves shifting in the location of objects on the pupil plane, including the location of the DMs' actuators compared to the WFS and blurring of influences of DMs' actuators. Examples of pupil distortion on an existing MCAO are obtained from the GREGOR solar telescope as shown in Figure 5.1 (Schmidt et al., 2014). Their key notable differences are as follows. Figure 5.1 (a)'s distortion is minimal. Figure 5.1 (b)'s left spider leg is split into two lines, half a subaperture apart, instead of one. Figure 5.1 (c)'s outer edge of the annular oblates horizontally. Its central obscuration and vertical spider legs are slightly shifted to the left by 50% of the subaperture, compared to (a). Figure 5.1 (d)'s lower spider leg is out of focus and distorted. The vertical spider's leg in Figure 5.1 (b) and (c) is shifted by 50% of the subaperture, compared to (a).

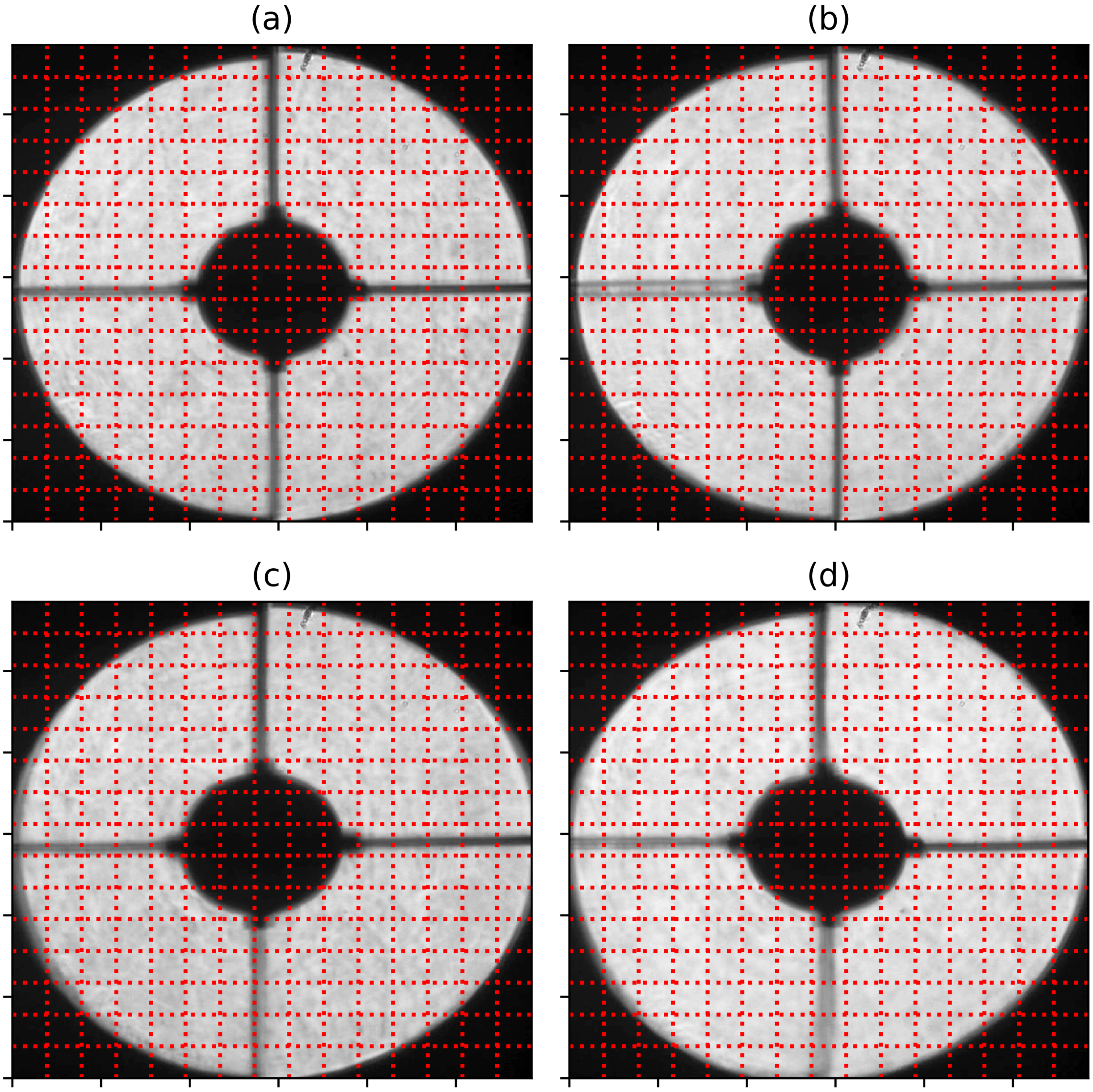

Figure 5.1: *Selected images near pupil plane after DMs corrections in GREGOR solar telescope with MCAO on an instrument run during an afternoon of 29 May 2014 (Courtesy of Dirk Schmidt). These images illustrate various instances of pupil distortion. Red lines denote the WFS subaperture boundaries, separated by 10 cm on the telescope pupil (Schmidt et al., 2014).*

Control errors due to perturbation of DMs can be implied from Flicker (2001), Farley et al. (2017), and Van Dam et al. (2021), where they discuss DMs arrangement and ordering. Should MCAO correct turbulence in optical order from the ground up to the high altitude, the opposite, or any order at all? Farley et al. (2017) suggests correcting from the ground up to the high altitude, so that each DM can correct most of the turbulence. While Van Dam et al. (2021) suggests that there are no significant errors contributed from the ordering, while using regularisation to avoid misregistration (and extensively control error). Van Dam et al. (2020) simulated an MCAO system with propagation effect using Farley et al. (2017)'s DM ordering with regularisation. This simulation has a correct order of turbulence correction according to Farley et al. (2017), but it still shows poor Adaptive Optics (AO) correction performance at an r_0 of 8 cm and lower. Van Dam et al. (2020) expected MCAO corrected 0.28 Strehl ratio (calculated from the paper) at 500 nm when observing through 8 cm r_0 looking at 45^o elevation angle, but only get 0.06 Strehl ratio. According to Van Dam et al. (2020), this was due to the high level of regularisation used in his simulation, trading the attainable correction level for the stability, agreeing with Gavel (2003). This poor performance is concerning because it is much weaker than a common turbulence condition at an excellent observing site during the daytime, which could have 2–4.0 cm r_0 (Kellerer et al., 2012; Song et al., 2020; Griffiths et al., 2024). Is it possible to recover the performance drop?

With a large enough regularisation parameter, the pupil distortion will be ignored as noise (Gavel, 2003). Rather than generalising the control randomness, since the pupil distortion is created by active DMs and DMs' control is known, the pupil distortion should be predictable. If the control can be updated in real time, similar to misalignment correction studies including Heritier et al. (2021), Lai et al. (2021), and Taylor et al. (2024), the control error can potentially be minimised.

To assess the effect of Interaction Matrix (IM) distortion on AO performance, we developed an AO simulation that incorporates optical propagation between DMs and the WFS. The study to reduce MCAO control error is divided into several steps. Firstly, compare MCAO performances between with and without updating control for static turbulence; the objective of this chapter. Then, in future research, compare with frozen flow turbulence, and determine how to update the control based on MCAO commands.

The first section hypothesises the main drives of control error behaviours, defined here as the dynamic misalignment indices. The dynamic misalignment indices include Rytov parameter induced by DMs ($\sigma^2_{R,DM}$) and Root-Mean-Square (RMS) apparent DM's actuator shifts compared to its pitch (RMS_{AS}), the latter of which was proposed and studied briefly by Schmidt et al. (2012). After that, the thesis section derives analytical equations, predicting the parameters. The second section designs a simulation to single out the control error effect for further analysis. The third section designs measurement methods for the dynamic misalignment indices and compares the behaviour against the derived analytic equation. The fourth section measures and compares the distorted calibration of an MCAO system. It also shows degradation of the control against the dynamic misalignment indices. The fifth section analyses the degradation of the AO performance from using the distorted control. In addition, the dynamic misalignment indices' impacts on the control performance are defined. Lastly, the sixth section projects dynamic misalignment indices and expected AO performance drops to existing MCAO systems.

This chapter finds the following. There are negligible effects on the existing nighttime MCAO systems, unless they observe within 30 degrees from the horizon. Solar MCAO performance will drop during bad afternoon or evening conditions. This chapter finds that the control of DMs cannot correct optical turbulence when the induced Rytov parameter is larger than 0.1 or the induced actuator shift RMS is larger than 10% of the actuator pitch.

Key Objectives

1. Hypothesise key parameters explaining the control error: expected log-amplitude variance induced by ($\sigma^2_{R,DM}$) and statistical apparent shift in actuator positions of DMs as detected by WFSs (RMS_{AS}).
2. Derive and compare analytic equations and measurement methods to quantify the dynamic misalignment indices.
3. Measure and compare the undistorted and distorted calibration of an MCAO system.
4. Design a simulation to measure the effects of the control error using optical propagation.
5. Compare performances between the MCAO without and with control error.
6. Identify relations between the control error and the dynamic misalignment indices.
7. Predict if any existing MCAO systems suffer the control errors under what observing conditions.

5.1 Distortion of Control

In MCAO, a DM may distort another DM's control. This distortion is quantified by the dynamic misalignment, namely, the induced log-amplitude variance and the RMS actuator shift. This section hypothesises their behaviour.

AO systems correct optical turbulence effects by reconstructing DM actuator commands based on WFS slope measurements. As explained in Chapter 3, Slope measurements and actuator commands are mapped linearly through a matrix representation with IM mapping DM commands to WFS slopes, and Control Matrix (CM) mapping the opposite. The IM and the CM will be each other's pseudo-inverse matrices. The IM of a system is generated by measuring the difference in slope measurements before and after an actuator is poked. After that, the CM is computed from the pseudo-inverse of the IM. Doing so satisfies the least-square residue (Gavel, 2003).

Before proceeding with further discussion, it is important to establish some definitions in this chapter. Consider the simplest MCAO configuration involving two DMs. Let **DM1** and **DM2** denote the first and second DMs in the optical path, respectively, as illustrated in Figure 5.2.

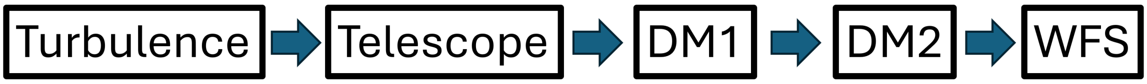

Figure 5.2: *Diagram illustrating the light path through each principal component in an MCAO system, used extensively as an example in this chapter, unless mentioned otherwise.* ***DM1*** *is the first DM in the light path, and* ***DM2*** *is the second. The specific conjugation of* ***DM1*** *and* ***DM2*** *can vary depending on the system design. Figure adapted from Kongkaew et al. (2024).*

Depending on the MCAO design, the conjugation order of DMs can be different. *In this thesis, the order is chosen to be the ground first, then the high altitude,* based on Flicker (2001); Farley et al. (2017), to allow the best DM correction power.

When the ground-conjugated deformable mirror/**DM1** is being calibrated, most MCAO systems will flatten their altitude-conjugated deformable mirror/**DM2**, resulting in a non-distorted control matrix. If this non-distorted control matrix is used to correct only the ground turbulence layer, with **DM2** flat, it would result in a performance without any DM-induced control error. However, common MCAO will use this non-distorted control to correct both the ground turbulence layer and the high-altitude turbulence layer simultaneously. Doing so, the control of **DM1** is now distorted by **DM2**, resulting in control errors.

Distortions of MCAO control behaviours are categorised into two effects, independent of each other or not. Firstly, RMS of apparent shifting in **DM1** actuator location as detected by WFS caused by **DM2**. In this work, this effect will be called the actuator shift RMS. Secondly, the variation of intensity at the WFS pupil during the calibration induced by **DM2**. This effect is observable when taking the MCAO out of the sky while maintaining **DM2** commands. When shining light of uniform intensity through the pupil, there will be an intensity variation caused by **DM2**. In detail, the difference in the DM-induced log-amplitude variance during the calibration process between with/without distortion applied. It is debatable whether or not the effect of the changes in the **DM1**'s influence function is comparable to the residual turbulence at a higher spatial scale than the **DM1**'s actuator pitch, because both are errors in corrections at a perhaps similar frequency. Consequently, the DM-induced log-amplitude variance may have a smaller effect on MCAO control performance than the other contributors. Nonetheless, the distortion of the influence function is still included in this study as a separate effect, because there are also possibilities that, in certain conditions, this effect might be larger than the regular residual turbulence. Since both effects on the control of **DM1** are created by **DM2**, correcting turbulence at the different altitudes. The DM-induced log-amplitude variance is used as the other source of control distortion. These two dynamic misalignment indices evolve together, as they both depend on turbulence strength and propagation distance between deformable mirrors.

During AO operation, the **DM2** surface shape will apply turbulence correction, introducing phase distortion to the image of **DM1**; thus, the image of **DM1** is now distorted (Schmidt et al., 2012; Kongkaew et al., 2024). As a result, the image of **DM1** and its effective actuator positions at the lenslet plane of the Shack-Hartmann Wavefront Sensor (SH-WFS) will be shifted, as shown in Figure 5.3. In addition, the shape will also be distorted by propagation between DMs and SH-WFS (Figure 5.4). IM of the ground-conjugated deformable mirror (**DM1**) distorted by active altitude-conjugated deformable mirror (**DM2**) are shown in Figure 5.5 with increasing dynamic misalignment indices; induced log-amplitude variance and actuator shift RMS.

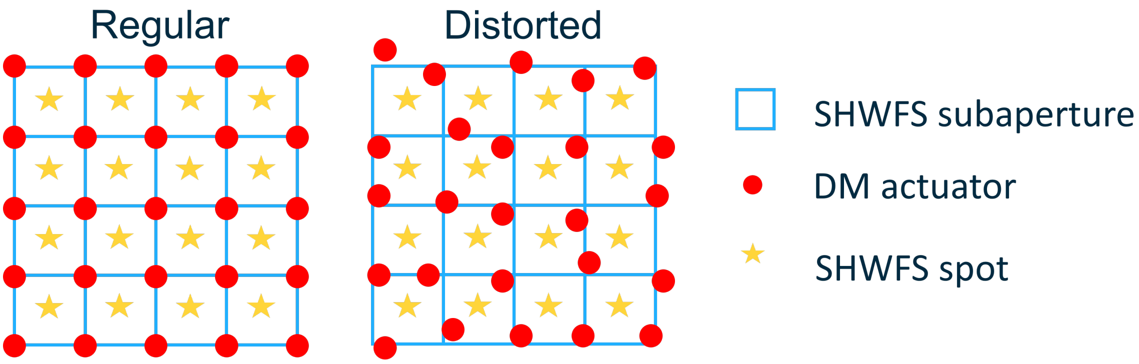

Figure 5.3: *Sketch illustrating the effect of pupil distortions on Fried geometry between* ***DM1*** *and SH-WFS with* ***DM2*** *under two conditions. On the left, during calibration with* ***DM2*** *held flat, the actuators are positioned, maintaining Fried geometry. On the right, during operation,* ***DM2*** *is not held flat, which introduces pupil distortion, causing the apparent actuator positions to shift randomly away from the subaperture corners, disrupting the original geometry. The figure is derived from Kongkaew et al. (2024).*

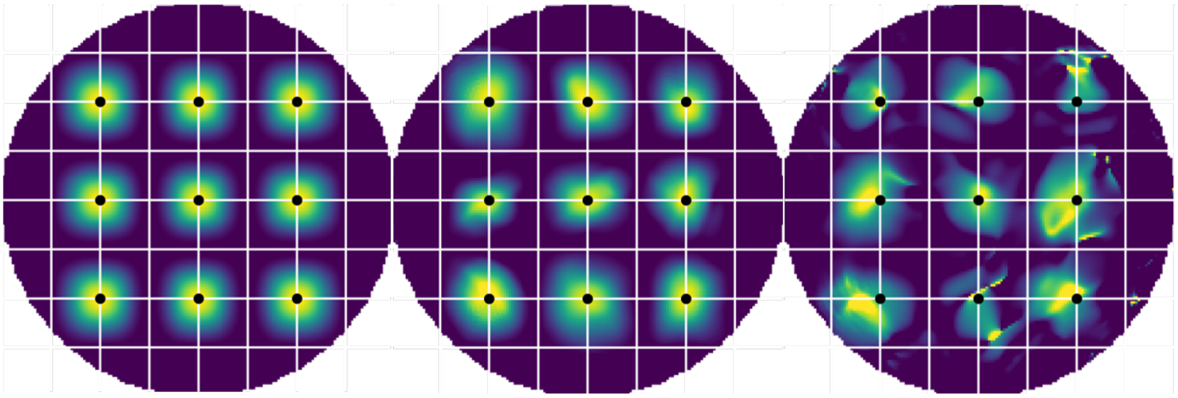

Figure 5.4: *The distorted influence function of* ***DM1*** *actuator pushed forward for 500 nm at the SH-WFS with 5.0 cm subapertures, through active* ***DM2****, which is correcting 5.0 cm* r_0 *turbulence.* ***DM2*** *propagation distances to the WFS are 0, 2.3, and 5.7 km, respectively, from left to right. The influence functions are normalised to the pushed distance. Their colour scale is reported on the side. Figure from Kongkaew et al. (2024).*

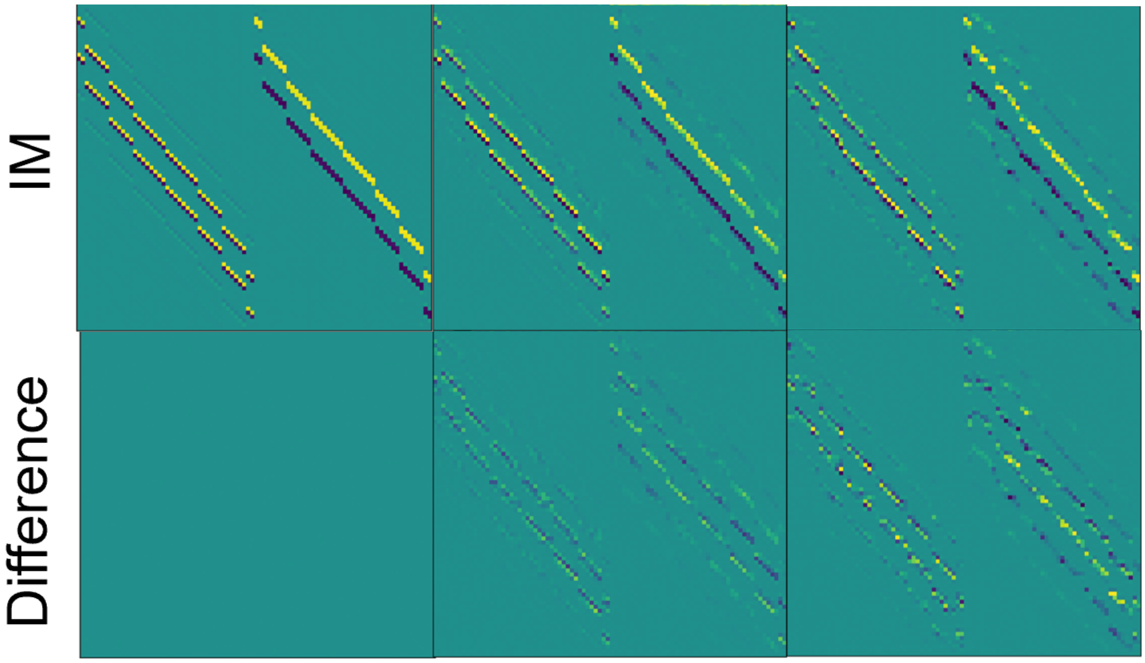

Figure 5.5: *Figure showing the impact of **DM2**-induced distortions on an IM of **DM1** measured using a SH-WFS, where **DM1** and **DM2** are conjugated to the ground and altitude turbulence, respectively. Each row of the IM describes the SH-WFS slope response of each subaperture to the influence of a deformable mirror actuator in each column. The measured slope response is normalised to the max and min of the non-distorted IM (left). The top row of IMs shows the measured IM, with the bottom row showing the difference between the non-distorted (left) and distorted (the others). AO geometry distortion increases from left to right. The propagation distances between **DM2** and the SH-WFS are 0, 2.3, and 5.7 km, respectively. These simulations were conducted for a 9x9 actuator DM with a SH-WFS using 5.0 cm subapertures at a wavelength of 500 nm. The figure is derived from Kongkaew et al. (2024).*

The amount of observed induced log-amplitude variance and actuator shift RMS is dependent upon the MCAO system configuration and turbulence profile being corrected. Here, the thesis presents more details and the equations explaining their behaviours.

5.1.1 Log-amplitude Variance Induced by Deformable Mirrors

The log-amplitude variance induced by DMs is inspired by the log-amplitude variance caused by the atmosphere, as seen through scintillation. The scintillation is generated by the presence of optical turbulence at high altitudes. The log-amplitude variance can be estimated by the Rytov parameter.

AO suffers from log-amplitude variance when the Rytov parameter of the atmosphere (σ_R^2) exceeds 0.2. At this strength, the wavefront sensor measurements can become inaccurate (Barchers et al., 2003). Analytical solutions for turbulence propagation using smooth perturbation start to fail at $\sigma_R^2 = 0.35$ (Sasiela, 2007). The scintillation effect becomes saturated at $\sigma_R^2 = 0.6$, where the phase distribution becomes uniform, causing maximum scintillation and setting an upper limit beyond which scintillation dominates, potentially leading to no AO correction.

As described in Chapter 2, scintillation in astronomy is caused by the propagation of light after aberration by optical turbulence. However, the distortion of MCAO control is not an atmospheric effect, but is caused by an active DM correcting the optical turbulence, as shown in Figure 5.6. If the intensity distribution at the pupil of the telescope is uniform, the pupil image at the WFS should also be uniform. This is the case when the MCAO system is inactive. However, it is no longer true once the system is active. This gives an impression of experiencing the log-amplitude variance in astronomy, but driven by the DM instead. Thus, this chapter coins a new word, the DM-induced log-amplitude variance. Although they are not the same, they have a direct relationship.

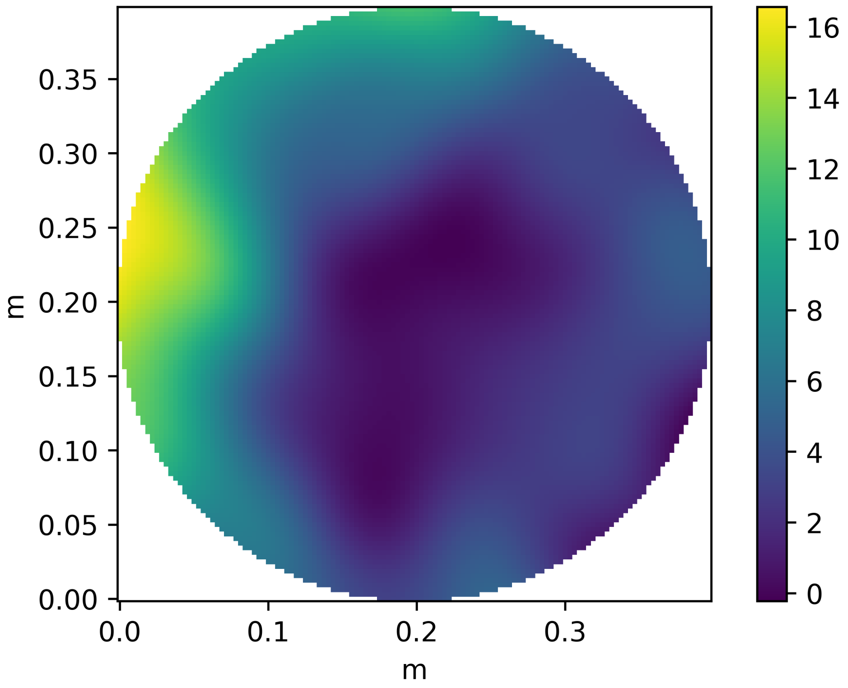

(a) *Applied optical phase (rad) by/at* ***DM2***

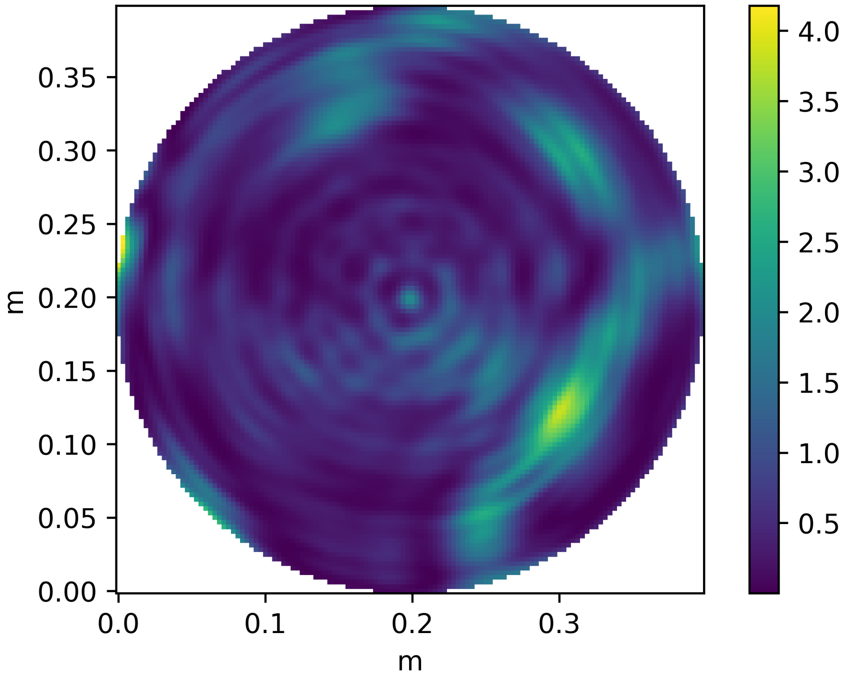

(b) *Intensity variation induced by* ***DM2*** *at the WFS (arbitrary unit).*

Figure 5.6: *As* ***DM2*** *is applying a correction of 5.0 cm* r_0 *equivalent turbulence at 10 km distance with 5.0 cm DM's pitch (a), if a uniform light shines through the pupil to take the pupil image, the pupil image intensity is no longer uniform, being modified by the* ***DM2****. The pupil image as seen by the WFS is shown in (b). This effect is defined as induced log-amplitude variance.*

For simplicity, the log-amplitude variance driven by DM ($\sigma^2_{\chi,DM}$) will be estimated using the Rytov estimation of atmospheric log-amplitude variance. It is most likely that the equation cannot properly explain the behaviour, but it is convenient and provides a link to an already well-known parameter. The modified equation for the induced Rytov parameter ($\sigma^2_{R,DM}$) is shown by

$$\sigma^2_{\chi,DM} \approx \sigma^2_{R,DM} = 0.5631 k_0^{7/6} \sec^{11/6}\zeta \int_{DM} C_n^2(h) h^{5/6} dh, \tag{5.1}$$

where the vertical turbulence profile is denoted by $C_n^2(h)$ is integrated ($\int_{DM} \cdot dh$) over the effective DM correction vertical heights (h), with k_0 denoting the wavenumber of the wavelength that the WFSs are detecting and ζ being the zenith distance of the guiding object. Turbulence profile in a LoS can be estimated from the vertical turbulence profile. The corrected turbulence thickness and turbulence strength being corrected by a DM are estimated accordingly using the method in Ragazzoni et al. (2002).

This thesis assumes that the induced Rytov parameter of a DM can be calculated by adding all log-amplitude variances induced by other DM between the DM in question and the WFS.

5.1.2 Apparent Deformable Mirror Actuator Position Shift RMS

The effect of misregistration or actuator shift on AO calibration in the scintillation-free case has been widely studied for many AO systems (see, for example, Engstrom and Schmidt (2009); Schmidt et al. (2012); Heritier et al. (2018)). These studies typically consider uniform shifts or rotations between the WFS and DM. It is a commonly used rule-of-thumb in atmospheric adaptive optics that misregistration or rotation, which results in a wavefront sensor shift greater than 10-30% of the subaperture diameter, will begin to negatively impact AO performance (Hardy, 1998; Heritier et al., 2021).

In this study, the source of misregistration is not due to hardware misalignment. For example, when a secondary mirror DM is blown off alignment during strong winds.

Schmidt et al. (2012) had previously identified and studied this effect. The mathematical model of the distorted control was analysed. It was discovered that the slope solutions can no longer be solved linearly from the actuator commands. The misregistration was considered in the MCAO study through simulation and laboratory experiment. However, no further analysis on this effect was done.

The active apparent shift in actuator position of DM further away from DMs closer to the WFSs is described in Figure 5.7. There are three DMs in the figure. The optical path order from the telescope pupil to the SH-WFS is **DM1**, **DM2**, and **DM3**, respectively. This is different to the rest of the chapter where there are only **DM1** and **DM2**. The reason is to show the importance of the absolute distance travelled by the ray. The absolute distance between two components is named as z, where its subscript marks the optical element. For example, the total propagation distance between **DM1** and **DM2** is $z_{1,2} = |z_1 - z_2|$. The angle at which **DM2** and **DM3** deflect a collimated ray of light from **DM1**'s actuator toward the WFS by an angle of θ_2 and θ_3, respectively. The total distance that the actuator ray is displaced is now called the apparent actuator shift in the position of **DM1** (AS_1).

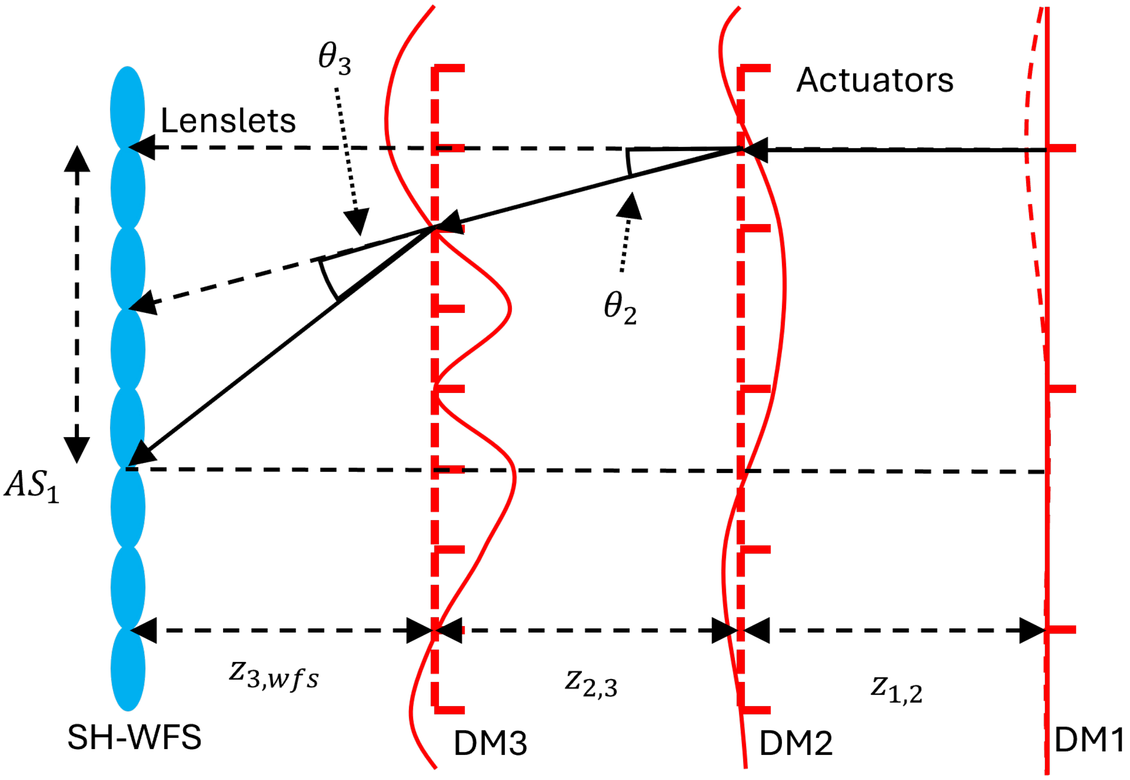

Figure 5.7: *Shift in apparent* ***DM1*** *actuator position (AS_1) induced by* ***DM2*** *and* ***DM3*** *along the path. Solid horizontal red lines show the actuators of each DM. Lenslets of SH-WFS are shown by blue ellipses. Red solid curvy lines show instantaneous phase corrections of each deformable. The deviated angles applied by* ***DM2*** *and* ***DM3*** *are shown with θ_2 and θ_3, respectively. The total absolute distance travelled between each component is shown by z. Ray tracings of* ***DM1*** *poked actuator positions are shown in black solid arrows.*

The apparent actuator shift in position of **DM1** (AS_1) of the example equals

$$AS_1 = \theta_2(z_{2,3} + z_{3,wfs}) + \theta_3 z_{3,wfs}. \tag{5.2}$$

As the MCAO are active, there will be some variance of the apparent **DM1** actuator position shift (σ^2_{AS1}), which equals

$$\sigma^2_{AS1} = \alpha^2_2(z_{2,3} + z_{3,wfs})^2 + \alpha^2_3 z^2_{3,wfs}, \tag{5.3}$$

where α^2_2 and α^2_3 are the variance of the deviation angle initiated by **DM2** and **DM3**, respectively.

Kongkaew et al. (2024) assumed that the deviation angle variance of the DMs can be derived from angle-of-arrival statistics of atmospheric turbulence that the DMs are correcting over a subaperture without tip/tilt removed over the aperture. This is not practical because most MCAO systems already have a dedicated tip/tilt mirror. Consequently, the tip/tilt over the DM aperture is removed in this chapter, leaving only a smaller amount of tip/tilt variance. Here we derive the variance with a global tip/tilt remove that will better reflect the values observed in a real system. The angle-of-arrival variance without tip/tilt removed (α'^2) between DM actuators' pitch can be obtained from the angle-of-arrival variance over a square aperture (Saint-Jacques, 1998).

$$\alpha'^2 = 0.162\lambda^2 r_0^{-5/3} d^{-1/3}, \tag{5.4}$$

where d is the spacing between actuators, r_0 is the Fried parameter of the turbulence layer the DM is correcting, and λ is the operating wavelength of WFS.

Similarly angle-of-arrival variance (α'^2_{DM}) over the whole DM with active aperture D is

$$\alpha'^2_{DM} = 0.162\lambda^2 r_0^{-5/3} D^{-1/3}. \tag{5.5}$$

So the local angle-of-arrival after global tip/tilt removed (α^2) in WFS subaperture or DM actuator spacing is

$$\begin{align}
\alpha^2 &= \alpha'^2 - \alpha^2_{DM} \tag{5.6}\\
&= 0.162\lambda^2 r_0^{-5/3} d^{-1/3} - 0.162\lambda^2 r_0^{-5/3} D^{-1/3} \tag{5.7}\\
&= 0.162\lambda^2 r_0^{-5/3} \left(d^{-1/3} - D^{-1/3}\right) \tag{5.8}\\
&= 0.162\lambda^2 r_0^{-5/3} d^{-1/3} \left(1 - \left(\frac{D}{d}\right)^{-1/3}\right). \tag{5.9}
\end{align}$$

Now the variance of the apparent DM's actuator location shift can be calculated with all of the given equations. In this thesis, the RMS apparent shift ratio percentage to the actuator pitch is used extensively instead of the variance itself, so that it will have a comparable unit to the misregistration parameter used commonly elsewhere, such as those in Heritier et al. (2021); Lai et al. (2021); Taylor et al. (2024). The RMS actuator shift percentage ratio (RMS_{AS}) is then

$$RMS_{AS} = \frac{\sqrt{\sigma_{AS}^2}}{d}, \tag{5.10}$$

where d is the actuator pitch of the DM whose actuator shift RMS is being calculated. This value is often presented by percentage.

5.2 Simulation

We developed an AO simulation that incorporates optical propagation within the systems to accommodate the scintillation effect commonly observed in the solar MCAO, as explained in Chapter 3. The DM's conjugation distances and turbulence strengths are selected to cover a range that could be encountered at typical observing sites. **DM1** is conjugated to the ground turbulence layer, and **DM2** is conjugated to the turbulence at altitude. WFS runs at 500 nm. WFS and all DMs have the same actuator pitch in the Fried geometry. Selected numbers of subapertures across the telescope pupil are 10, 8, and 6 to explore their dependencies on the actuator shift RMS. Due to computational limitations, a telescope pupil diameter of 0.4 m was selected, resulting in actuator pitches of 4.0, 5.0, and 6.7 cm, respectively.

The operating wavelength of the SH-WFS are chosen to be 500 nm, typical of solar observations. The Field-of-View (FoV) of the SH-WFS lenslets were set to approximately only 4 times of the worst seeing, to preserve the linearity of the SH-WFS (Thomas et al., 2006). The detector pixel scale of SH-WFS was set to at max half of a diffraction-limited spot. Some directly calculated values can be in accessible, so the nearest values satisfying all of the above criteria are chosen. For example, the desired FoV and the angular pixel scale will result in a fraction of pixels.

Based on this information, the number of simulation elements across the pupil and its physical size can be estimated. The smallest simulation element scale is chosen to simulate turbulence. The outer scale of all optical turbulence layers is set to 4 m due to computational limitations. This value is 10 times larger than the telescope pupil, potentially indicating Kolmogorov-like turbulence. Residual wavefronts are also calculated using the same simulation elements scale. The choice of the Singular Value Decomposition (SVD) conditioning parameter and control gain will be explained in further sections. The other simulation parameters are automatically chosen by the simulation presented in Chapter 3. The key simulation parameters are listed in Table 5.1.

Parameter	**Value**
Telescope diameter	0.4 m
SH-WFS wavelength	500 nm
Science Camera wavelength	500 nm
Turbulence outer scale	4 m
ground turbulence layer r_0	10 cm
SH-WFS subaperture size, **DM1** pitch	[4.0, 5.0, 6.7] cm
DM2 spatial frequency	less than [2.0, 2.5, 3.3] cm
Number of subapertures across the aperture	[10, 8, 6]
SH-WFS FoV	[21, 17, 17] arcseconds
Number of SH-WFS detector pixels	[18, 18, 22]
Science camera FoV	9 arcseconds
Number of science camera pixels	180 pixels
Simulated simulation elements across the pupil	180 pixels
Control gain	0.8
SVD conditioning parameter	0.05
Number of AO control iterations	5 iterations
Number of random samples	50 realizations
DM2's $r_{0,DM}$	2 to 50 cm
DM2's conjugation height	1 to 10 km

Table 5.1: *Key simulation parameters to study dynamic misregistration effect in AO control*

DM2 is chosen to correct a turbulence layer at given distances and strengths. It also corrects the same spatial frequency as **DM1**. Due to computational limitations, the maximum height for **DM2** is chosen to be 10 km. The strongest turbulence strength for **DM2** is chosen to be 2 cm r_0. At a stronger strength, the simulated turbulence can no longer sample the turbulence well enough at 500 nm wavelength, because there is a high chance that the phase difference between the neighbouring simulation elements is larger than half of the wavelength (the Nyquist frequency of the optical wave).

Varying combinations of the **DM2**'s height and correcting turbulence strength are chosen to give the desired levels of dynamic misalignments. The lowest distortion level tested is 0.01 induced Rytov parameter and 2% RMS actuator shift, well below the expected conditions where these effects will cause any control distortions (Barchers et al., 2003; Heritier et al., 2021). The maximum distortion level tested is 0.6 induced Rytov parameter and 75% RMS actuator shift, where the distortion level should seriously affect the AO control performance.

5.3 Characterisation of the dynamic misalignment indices

The first section proposed the concept and derived the analytic equations of the dynamic misalignment indices, namely, the induced log-amplitude variance and the actuator shift RMS. The second section designs a simulation to measure the distortions on the control of the system. This section will validate the analytic equations that explain the behaviour of the induced log-amplitude variances and the apparent actuator shift RMSs. To achieve this, it will propose measurement methods for both simulation and practice. After that, it will compare the measured values against the previously derived analytical equations.

The relationships between the measured and expected values of the dynamic misalignment indices, including the DM-induced log-amplitude variance and apparent actuator shift RMS, allow comparisons between the observation condition directly to other analyses in this thesis that mainly use the analytic equation as the metric.

Commonly, calibration of **DM1** is measured when **DM2** is held flat, resulting in no calibration error, or dynamic misalignment indices are zero. The distortion of **DM1** calibration by **DM2**, or the dynamic misalignment indices, can be measured by applying **DM2** correction during the usual calibration. To simulate the impact of **DM2**-induced pupil distortions on **DM1**, we low-pass filter a phase screen corresponding to the strength of turbulence present at high altitude. The low-pass filter removes optical turbulence with higher spatial frequency, leaving the **DM2** with only the lower spatial frequencies. Lastly, the distorted **DM1** IM is measured. The dynamic misalignments are measured during the calibration process or measurement of the IM. The details are as follows.

5.3.1 Induced Log-amplitude Variance

The DM-induced log-amplitude variance is measured by taking the log-amplitude variance of the pupil image during the calibration, with **DM2** applying some turbulence correction. Unlike the simulation, measuring this effect requires isolating the AO system from the telescope light and using a separate light source to illuminate just the AO system.

The relationship between the estimated and the measured DM-induced log-amplitude variance is shown to be linear on a log-scale, as shown in Figure 5.8. Since the expected analytic equation is derived from the Rytov approximation of the atmospheric log-amplitude variance, the expected value is called the induced Rytov parameter ($\sigma^2_{R,DM}$).

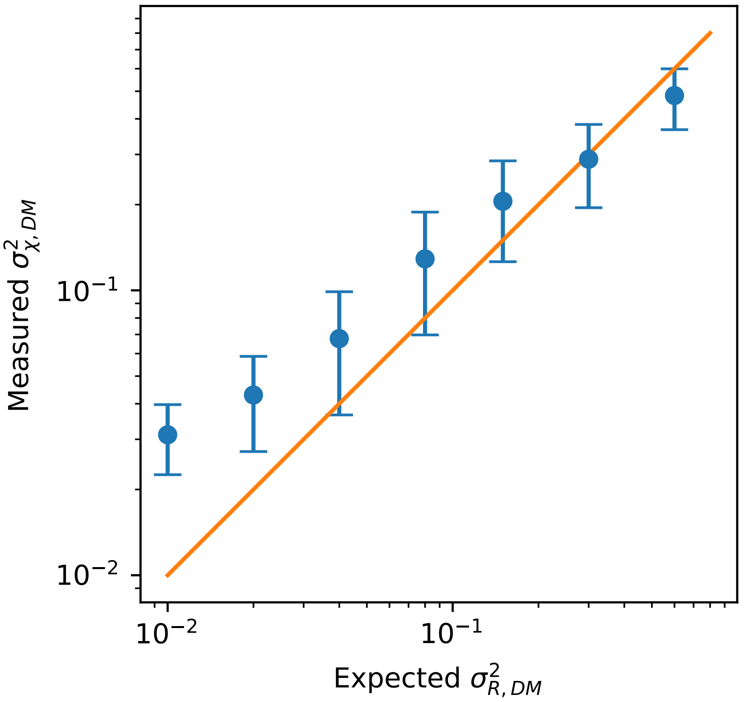

Figure 5.8: *Comparison between the measured induced log-amplitude variance ($\sigma^2_{\chi,DM}$) and the estimated induced log-amplitude variance represented by the induced Rytov parameter ($\sigma^2_{R,DM}$). The induced log-amplitude variances are induced by **DM2** distorting the control of **DM1**. The orange line designates the region where the estimated and measured values are equal.*

The measured induced log-amplitude variance is higher than the expected at low values. At log-amplitudes of 0.3 and higher, the measured values are slightly lower than the expected values. The discrepancy is hypothesised to be caused by two reasons. Firstly, because the DM does not have all spatial frequencies of the atmospheric turbulence, using the Rytov approximation of the atmospheric-induced log-amplitude variance is not entirely correct. Lastly, there are diffractions caused by the telescope pupil that are distorted by **DM2** and cannot be recombined into a smooth edge, interfering with the measurement.

If there is log-amplitude variance induced by the atmosphere during the observation already, using the observing target light to measure the **DM** induced log-amplitude variance will result in incorrect measurement. Consequently, this requires a separate light source to measure. Depending on the system, measurement of the induced log-amplitude variance during observation may be less convenient than calculating the expected induced Rytov parameter directly from the WFS measurement and DM commands statistics.

5.3.2 Actuator Shift RMS

This chapter proposes that actuator shift RMS can be estimated using two methods: the influence function method and the slope method. The influence method requires correlation of the undistorted and distorted influence functions of **DM1**. On the other hand, the slope method uses the slope response of **DM1** detected by the SH-WFS. Though both the influence and slope methods use the same data with a high number of phase elements, the slope method has a lower accuracy because it reduces the number of phase elements to just a few slope measurements. In practice, the slope method might be more convenient. It can use slope measurements from the wavefront sensor, while the influence method needs to measure the phase influence function first. Despite its accuracy, if the influence method cannot be done, the slope method can still be used to measure the expected actuator shift RMS through a relation presented in this section.

5.3.2.1 Influence Measurement Method

The influence function method measures the statistical distribution of the position of the highest correlation function between the distorted and undistorted influence functions. This uses the same approach as how a solar SH-WFS measures wavefront slopes using an image of solar granulation. (Löfdahl, 2010). An example of an instant actuator shift using the influence function method is shown in Figure 5.9.

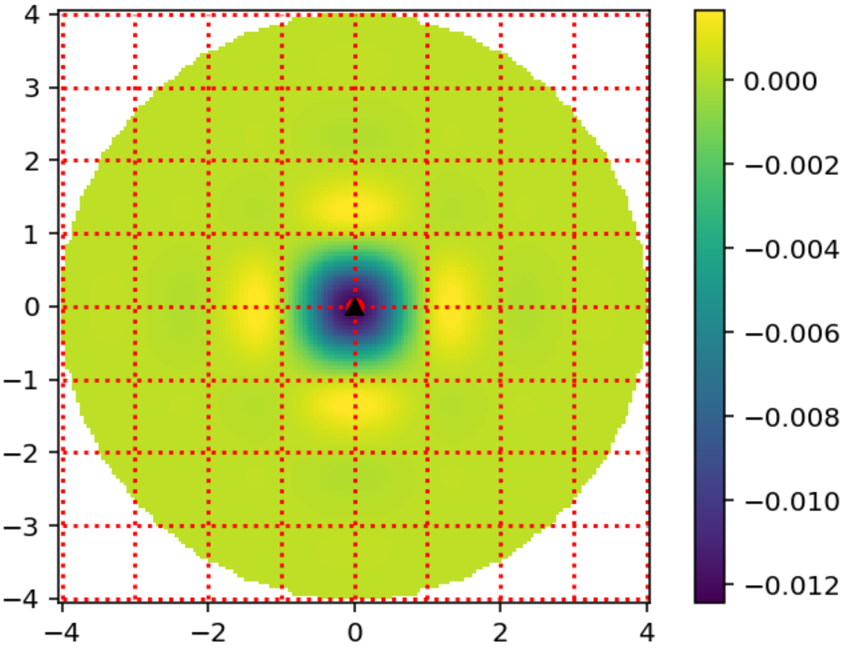

(a) *No aberration*

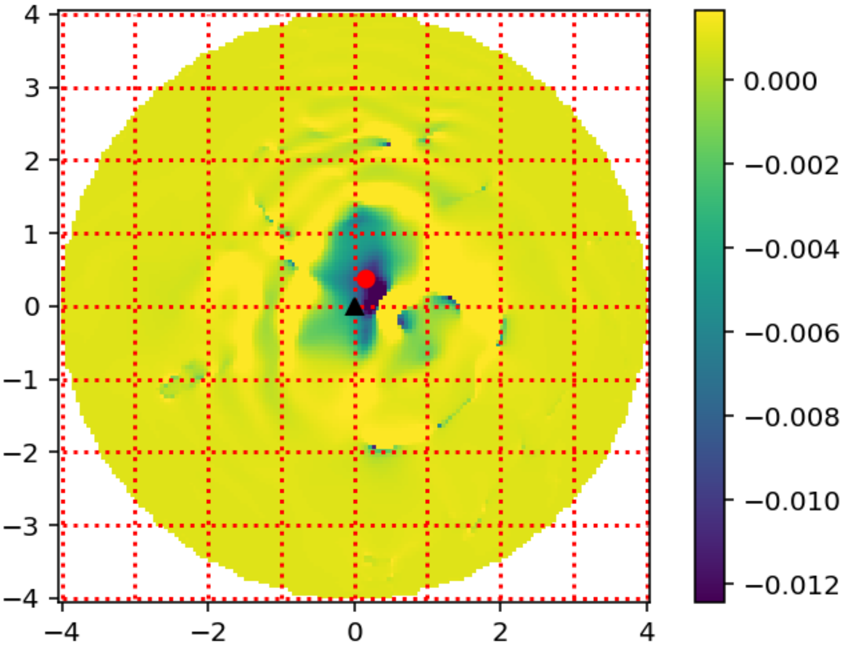

(b) *With aberration*

Figure 5.9: *Phase maps (radians) representing the influence function of* ***DM1*** *actuator at the pupil plane without (a) and with (b) aberration from (****DM2****) at 0.6 induced Rytov parameter and 38% actuator shift RMS compared to* ***DM1****'s actuator pitch. The inferred actuator position (red circle) with original position (black triangle) is overlaid on the boundary of the SH-WFS lenslet (red dotted lines).*

The actuator shift RMS measurements through the influence function method generally slightly under-estimates the expected values, as shown in Figure 5.10. As a result, the analytic equation explaining the apparent actuator shift RMS in the previous section is confirmed by the measurement. The actuator shift RMS can be measured by the influence method for all the simulation conditions and parameters.

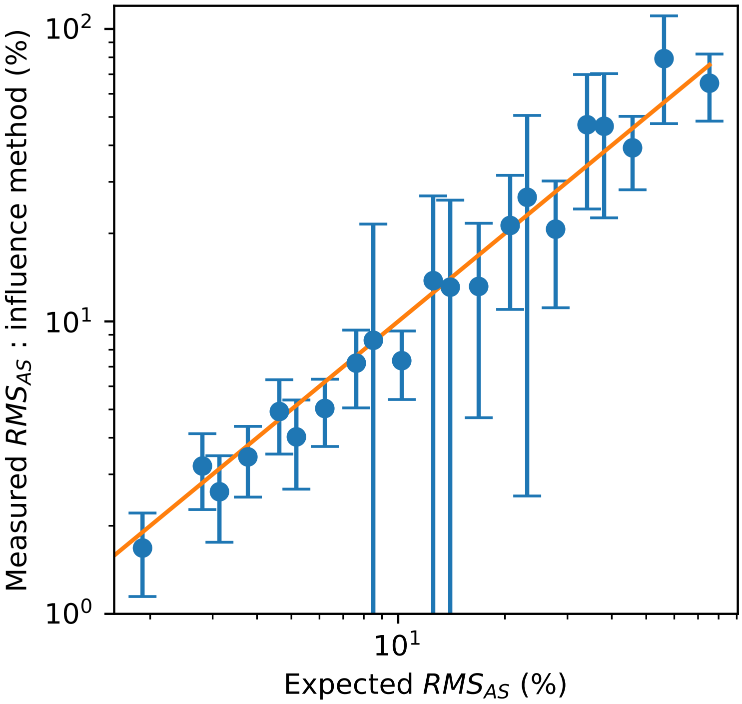

Figure 5.10: *Comparison between measured apparent actuator shift RMS (RMS_{AS}) percentage compared to the DM's actuator pitch using the influence method and the expected values. The straight line denotes regions where both values are equal.*

5.3.2.2 Slope Measurement Method

The slope method measures the observed location of DM actuators by analysis of the distorted IM directly. From each combination of slope measurement pairs, their intersections infer apparent actuator centre candidates. The candidates weighted centre using the Centre-of-Gravity (CoG) inspired method is assumed to be the apparent actuator shift. An example of a measured apparent actuator shift using the slope method is shown in Figure 5.11.

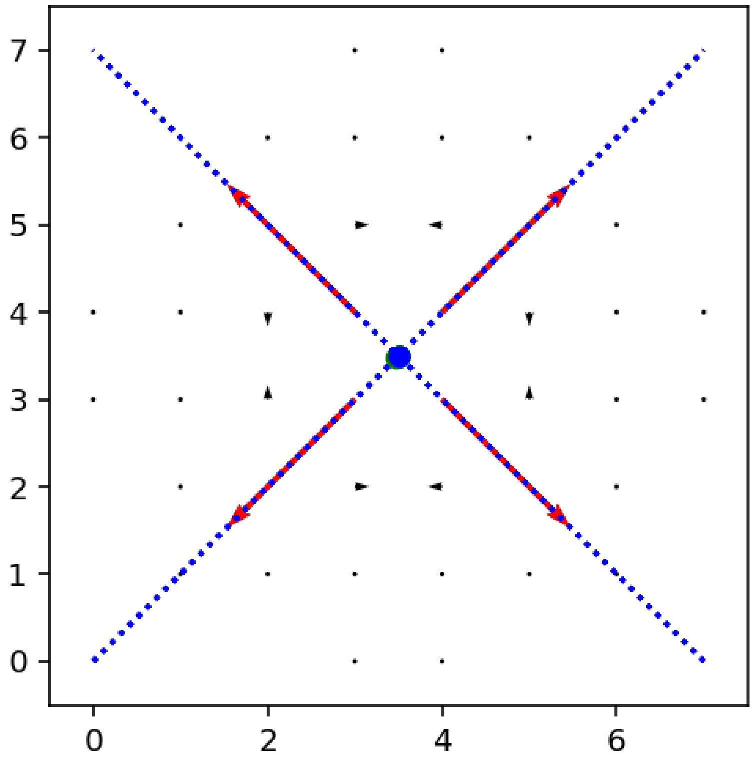

(a) *No aberration*

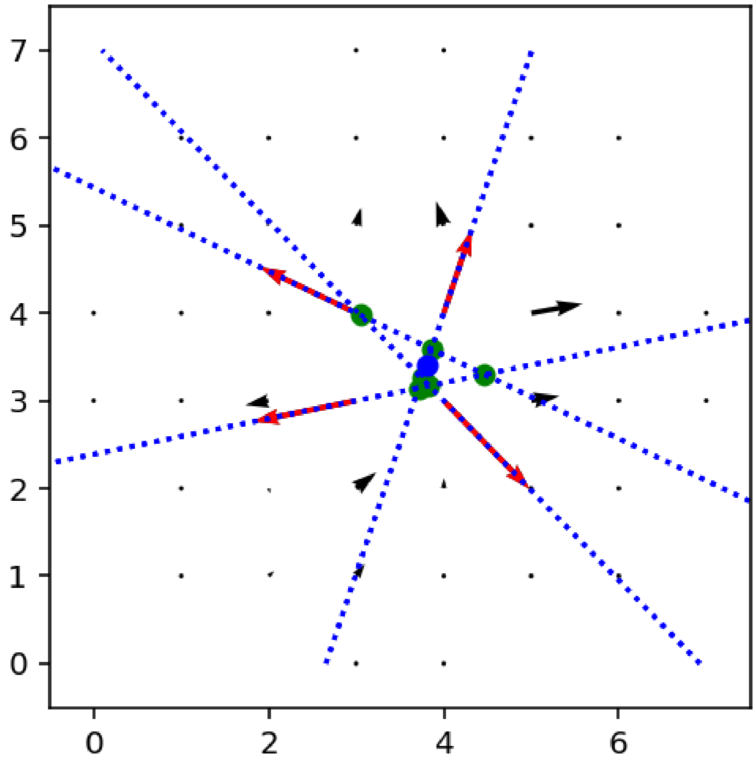

(b) *With aberration*

Figure 5.11: *Inferred actuator position (blue circle) from the intersections (green circles) of the significant SH-WFS slopes (red arrows) without (a) and with (b) an aberration of 0.6 induced Rytov parameter and 38% actuator shift RMS. The other slopes are shown in black.*

When an actuator is poked (the centre-most in the example), the slope measurement of the SH-WFS influenced by the poke is shown with black and red arrows. We define a slope threshold that selects only the largest slope measurements of an actuator poke (red arrows). The threshold used in this work was defined as a quarter of the largest measured WFS slope amplitude for each actuator, and only the four highest slopes were used for the calculation. The threshold level on the slope amplitude and the maximum number of slopes are imposed mainly to reduce the calculation data points. They can be adjusted, but this was not investigated further.

Each pair of slopes from a subaperture defines a vector that points either towards or away from the location of the actuator in WFS space. In this example, the slopes point away from the actuator centre. The valid candidates will be the interceptions of the two slopes where they both point away from, shown with green circles.

To determine the estimated location of the actuator, each vector is weighted by its amplitude, and a mean is taken. Weighting with amplitude is applied to reflect the subapertures with higher actuator influences. The weighted-amplitude mean position (blue circle) is calculated by

$$|s_i||s_j| = \sqrt{\left(s_{x,i}^2 + s_{y,i}^2\right)\left(s_{x,j}^2 + s_{y,j}^2\right)} \tag{5.11}$$

$$\overline{x} = \frac{\Sigma_{i\neq j} x_{i,j} |s_i||s_j|}{\Sigma_{i\neq j} |s_i||s_j|}, \tag{5.12}$$

where s_i and s_j is the ith and jth slope measurement with x and y representing the x and y component of the slope, respectively. The $x_{i,j}$ is the x position of the valid intersection between the ith and jth slope. The $\overline{x}$ is the weighted-amplitude mean position. The y component can be done using the same method. The weighted-amplitude mean position is the apparent actuator shift for one actuator. The RMS actuator shift can be calculated from every actuator shift of the DM.

Comparison between the RMS apparent actuator shift measured using the slope method and the expected values is shown in Figure 5.12. The measurement values increase as the expected values increase. However, the slope method always overestimates the expected values throughout the sampled range. At low expected actuator RMS, the measurements extremely deviate from the expected values. This is possibly an indication of the measurement uncertainties. Currently, there is a constant measurement error of approximately 5% of the actuator pitch.

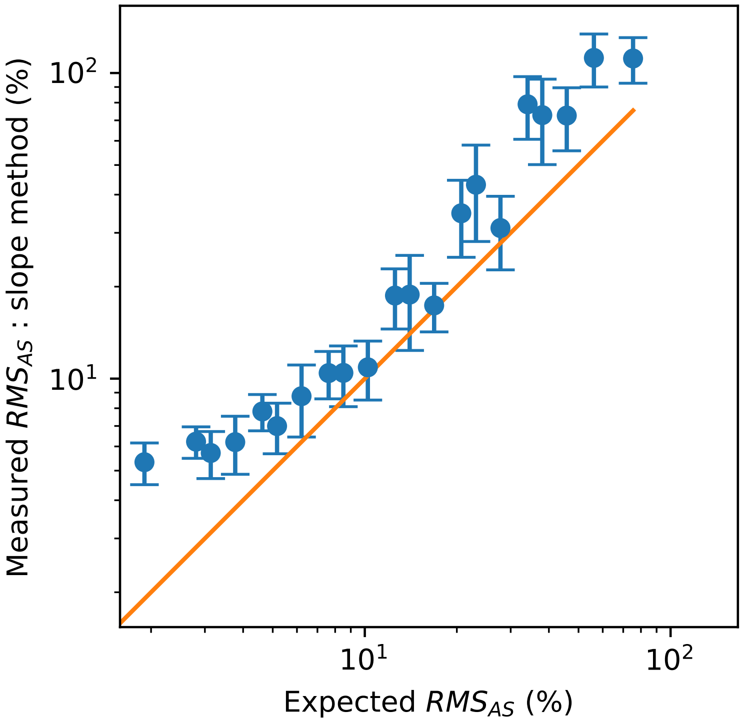

Figure 5.12: *Comparison of the measured RMS apparent actuator shifts (RMS_{AS}) using the slope method in percentages of the actuator pitch against its analytic expected values. The straight line denotes regions where both values are equal.*

5.3.2.3 Comparison between Measurement Methods

Instantaneous measurements of instant actuator shifts using the slope and influence methods do not correlate with each other, as shown in Figure 5.13. Both methods show the same mean value around zero, but different distributions. The slope method predicts a higher instant actuator shift compared to the influence method.

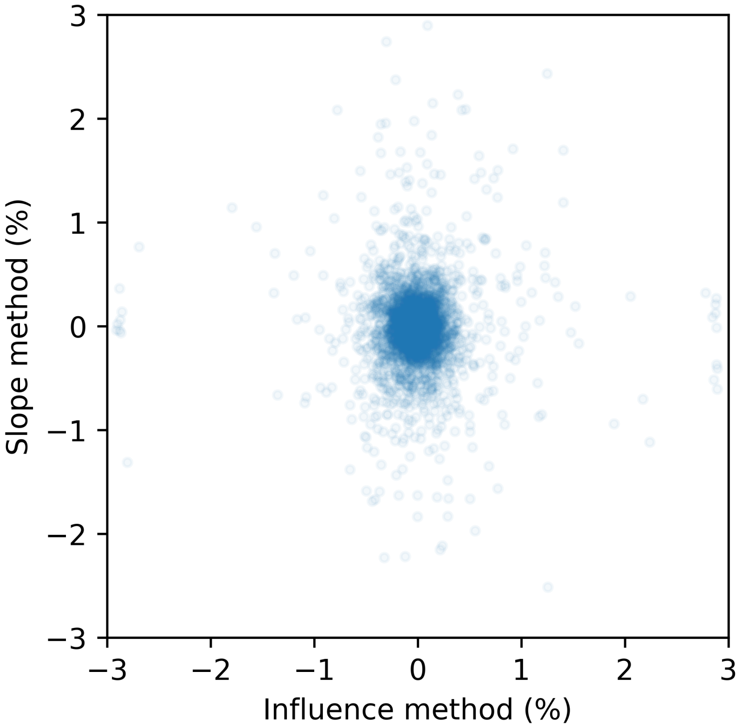

Figure 5.13: *Comparison of instantaneous actuator shift measurements using the slope method (y-axis) versus the influence method (x-axis).*

There are examples depicting why both methods do not always agree. In Figure 5.14, two phase-maps of distorted influence functions with the slope and influence methods plotted are presented. Both methods don't always have the same estimation. In some instances, both method estimates the same actuator shift (top), but some estimate a much different shift (bottom). There are two reasons why the slope method cannot properly estimate the actuator shift. Firstly, because the slope method uses slope measurement of the SH-WFS that are already averaged the slope into a smaller number of data points, losing information. Secondly, at strong distortions, there tend to be more conditions that cannot be solved by the slope method (bottom). The influence method might be more difficult to measure in reality, while the slope method can be used directly with data from wavefront sensor measurements.

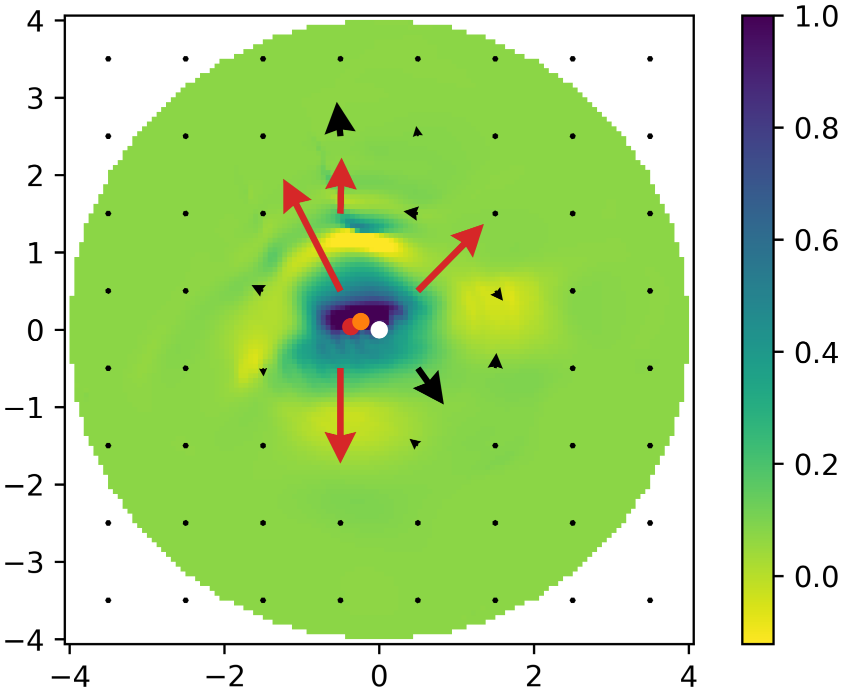

(a) *Measurements agree*

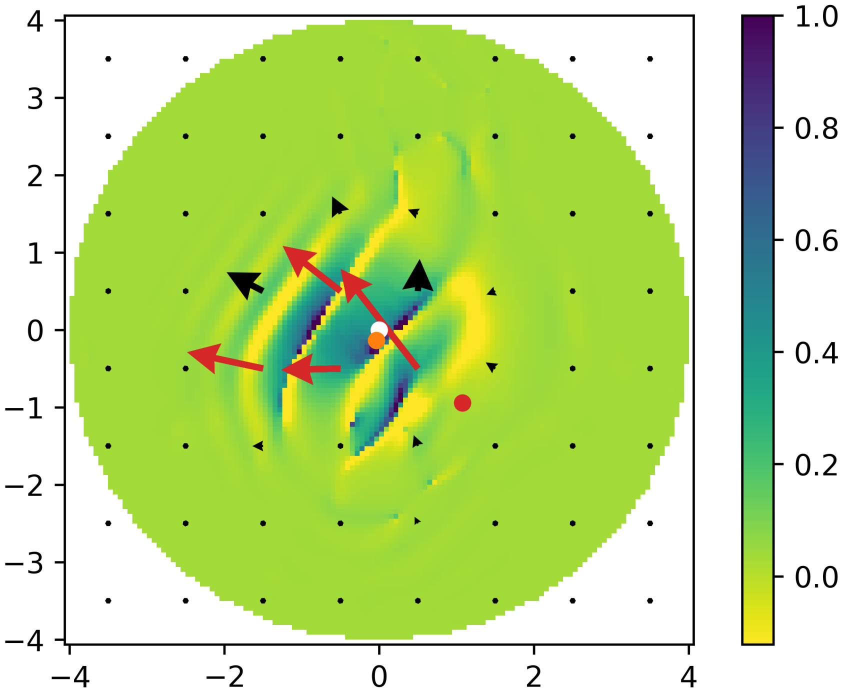

(b) *Measurements disagree*

Figure 5.14: *Two phase-maps showing two distorted influence functions (colour), normalised to the non-distorted phase map, where the slope and influence methods agree (a) and do not agree (b) on the apparent actuator position (red and orange circle, respectively) against the subaperture/lenslet pitch and the actual position (white circle). WFS slope measurements are separated into insignificant (black arrows) and significant (red arrows).*

Although there is no correlation between instant actuator shift measurements using the influence and slope method (Figure 5.13), there is a correlation between their RMS measurements (RMS_{AS}), as shown in Figure 5.15. Except for RMS actuator shift less than 5% of actuator shifts, both methods follow the same trend, with the slope method generally predicting values about 1.5 times greater than those of the influence method. Additionally, the slope method exhibits higher measurement error at lower values, approximately 5 per cent of the DM pitch.

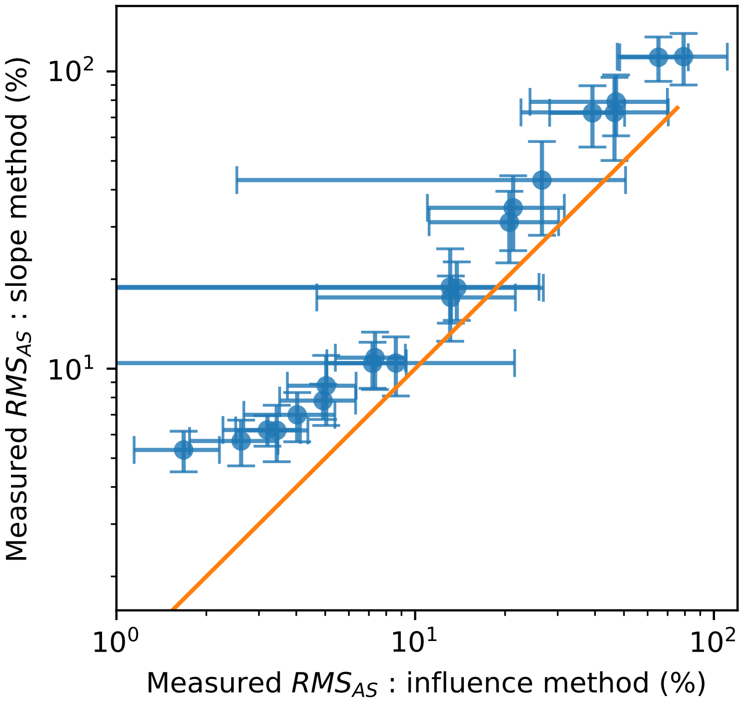

Figure 5.15: *The actuator shift RMS (RMS_{AS}) is measured using the influence method (x-axis) and the slope method (y-axis). The orange line draws the 1:1 relation region.*

The influence method is the most accurate measurement of the RMS actuator shift, predicting values correctly. On the other hand, the slope method cannot properly estimate the RMS actuator shift at low expected values, predicting 5% actuator pitch at a minimum. Otherwise, the slope method also overestimates the actuator shift RMS by 1.5 times the expected value. If estimation of the phase map of the actuator influence functions is possible, it is best to use the influence method. If the influence function cannot be obtained, the slope method can be provisionally used.

We have now confirmed the behaviour of the hypothesised dynamic misalignment indices, namely induced log-amplitude variance and actuator shift RMS, through simulations. The measured induced log-amplitude variance is higher than the expected values when the induced Rytov parameter is less than 0.1. While at higher induced Rytov parameters, the approximation is more accurate. The RMS actuator shift can be measured through either the influence or slope methods. The measured RMS actuator shift through the influence method always agrees with the expected behaviour. On the other hand, the slope method always measured higher values, especially when the expected RMS actuator shift is less than 10%, always reports 5% at the minimum. Though there is no correlation between instant actuator shift measurement methods, the RMS actuator shift is. The slope method overestimates the RMS by 1.5 times when the influence method RMS is 5% or higher. Next, this thesis will quantify the degradation of the system calibrations as the dynamic misalignment indices increase.

5.4 Degradation of the Calibration

The wavefront reconstructions of the MCAO require a calibration of the system through the IM. After that, depending on the technique, the CM can be calculated and further used for the control of the MCAO. This thesis adopted the least-square reconstruction with the truncated SVD method, as explained in Chapter 3. As explained earlier in the introduction of this chapter, when **DM2** is applying some wavefront corrections during the MCAO control, it also distorts the IM. Consequently, the SVD of the IM is also distorted. Lastly, the CM is also distorted. This section measures degradations in the IM, SVD, and CM of the MCAO systems as the dynamic misalignment indices increase, including the induced log-amplitude variance and RMS actuator shift previously presented.

Despite the degradation of the simulated IMs and CMs that are measured, they are not quite meaningful, yet. Their effect on control performance must be measured first. The relation will be presented in the next sections. Meanwhile, the SVD analysis on the IMs can tell how many modes of control are included or excluded from the system (Gavel, 2003). Consequently, only the degradation of the SVD will be reported here.

5.4.1 Singular Value Decomposition of Distorted Interaction Matrices

This thesis uses the truncated SVD method to generate the CM from the IM. This process is explained by (Horn and Johnson, 1985; Gavel, 2003). The SVD analysis shows the power of each vector mode of the matrix. In other words, the number of correction modes the AO can correct. Performance of the CM generated by this method depends on the conditioning parameter, the minimum level of the SVD included in the pseudo-invert process, because it is the noise rejection level.

This chapter will not attempt the optimisation of the SVD conditioning level for distorted IMs, because optimising the conditioning value is not guaranteed to suppress the waffle modes (Gavel, 2003). Instead, only the non-distorted IM having a 0.4-m telescope pupil with 8 subapertures across the pupil is optimised. The selected normalised conditioning SVDs is 0.05 as shown in Chapter 3. It is used for all of the other simulations with a different number of subapertures across the pupil and control distortions.

All of the previously measured distorted IMs are calculated for the SVDs. Figure 5.16 shows the degradations of the SVDs at a high distortion condition, to stress the severity. The distortion is generated by another DM at 8.5 km away, correcting 4.2cm-r_0 equivalent turbulence. This distortion has a 0.6 induced Rytov parameter and 75, 56, and 38% RMS actuator shift for the system with 4.0, 5.0 and 6.7 cm subaperture diameter, respectively. Those with a smaller subaperture size have a larger impact. In the figure, at the worst samples, the 4.0, 5.0 and 6.7 cm subaperture diameter systems can only control approximately 53 of 87, 39 of 59, and 26 of 35 modes, or 60, 66, and 74% of the original modes, respectively.

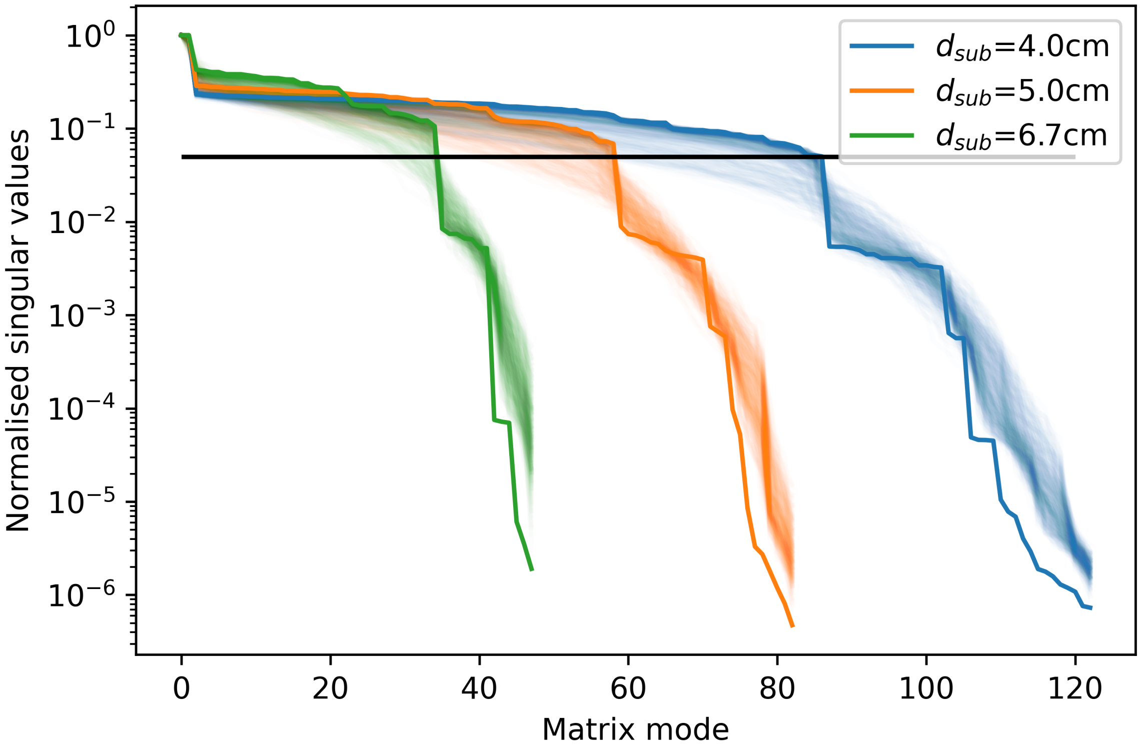

Figure 5.16: *Normalised singular values (y-axis) against different modes (x-axis) of various distorted IMs (faint colours) versus the non-distorted (solid colours). The horizontal black line shows the condition value optimised through simulation in the non-distorted case. The distorted IMs are generated with an active deformable mirror at 8.5 km correcting a 4.2cm-r_0 turbulence. The subaperture diameters of 4.0, 5.0, and 6.7 cm are shown in blue, green, and orange, respectively.*

Possibly, there are other methods to handle this problem, for example, choosing different truncating SVD values to reflect 'energy' of the control, or constricting the number of modes to correct. If a constricting number of modes is selected, the control might be more susceptible to now noisy modes. As such, the system will potentially be more accurate in trading for its stability. Consequently, selecting a constant SVD conditioning parameter, as in this chapter, will underestimate the control noise. If a condition is mentioned as concerning, it really is concerning.

5.5 Degradation of Control Performance

Since the calibration of **DM1** is measured with **DM2** flattened, which is not true during the operation, the control of **DM1** is no longer correct. The difference in MCAO performance will be called the control error. To reduce the control error, MCAOs should use the instantaneously calibrated control as **DM2** is applying different corrections. The calibration of this instantaneous control is measured and analysed in the previous sections.

To properly simulate MCAO correction for this system with multiple turbulent layers, DMs, and WFSs, we must also consider the tomographic wavefront reconstruction technique, fitting errors from multiple DM corrections and all noise sources within the system. This introduces a huge number of parameters to optimise and control, adding complexity and uncertainty to the results. Therefore, we should adopt a simpler approach to investigate control errors due to DM-induced distortions reduced using only a single WFS and LoS.

Because the control error ultimately arises from applying a calibration for unmatched conditions, rather than applying different controls on a full MCAO system, applying the different controls on a Single-Conjugated Adaptive Optics (SCAO) system will also single out the control error. Doing so reduces the number of DM and turbulence layers to be simulated and controlled.

Each different generated CMs from IMs using 0.05 SVD conditioning values, as explained in the last section, is used to correct the 10 cm r_0 ground turbulence layer while keeping **DM2** flat in a closed-loop control system. Throughout this study, a closed-loop control gain (g) of 0.8 is applied. At this gain value, the undistorted control converges by the fifth iteration of AO correction.

After 5 iterations of AO corrections, residual wavefronts are measured, as the residual Wavefront Error (WFE) for the non-distorted control would normally converge. Due to the simulation configuration, there is no log-amplitude variance in the residual wavefront, thus avoiding possible optical branch points and branch cuts, where the phase is undefined. The residual wavefront is then measured for RMS WFE in nm, power spectrum density, and decomposed into Zernike mode coefficients.

5.5.1 Residual Phase Wavefront Error

The close loop truncated SVD AO control can normally correct the ground turbulence layer within the first few loop iterations, namely 5 in this chapter, as shown in Chapter 3. The non-distorted control performance is shown in Table 5.2. However, with control distortion, it cannot, and even amplifies the optical WFE in a various runaway fashion, depending on the distortion condition, as shown in Figure 5.17. Because the runaway control loop sometimes never converges to any values, the control error could not be quoted statistically by RMS WFE in nm, unlike other AO errors such as fitting and delay errors. Nonetheless, this thesis will try to quantify this for comparisons between different distortion cases.

Subaperture size (cm)	4.0	5.0	6.7
Residual RMS WFE (nm) No control error	28±5	34±8	40±8

Table 5.2: *Residual RMS WFE of the simulated AO systems with no control error.*

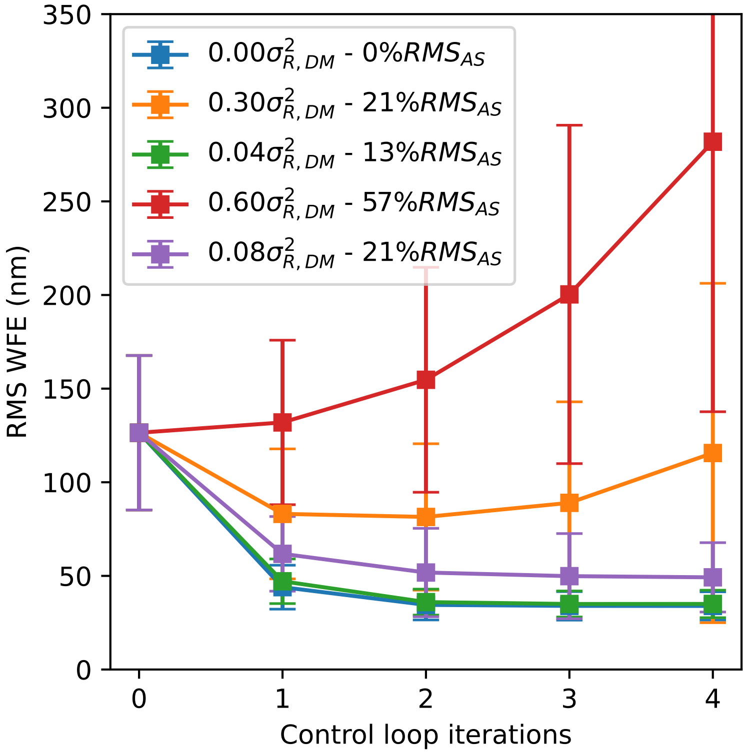

Figure 5.17: *Evolution of WFE in systems operating with extremely distorted control. The control is distorted by **DM2** with 5.0 cm actuator spacing, correcting 4.2cm-r_0 turbulence at 8.5 km distance.*

The samples with large residual WFE are inspected. The common features are the waffle modes as shown in Figure 5.18. The runaway DM actuator commands exhibit an alternating pattern of push/pull values, displaying a waffle-like or chequered pattern. The most pronounced spatial frequency in the pattern is half the actuator spatial frequency, or the Nyquist frequency of the AO system. As discussed in the previous sections, optimising the SVD conditioning values cannot guarantee the removal of the waffle modes (Gavel, 2003).

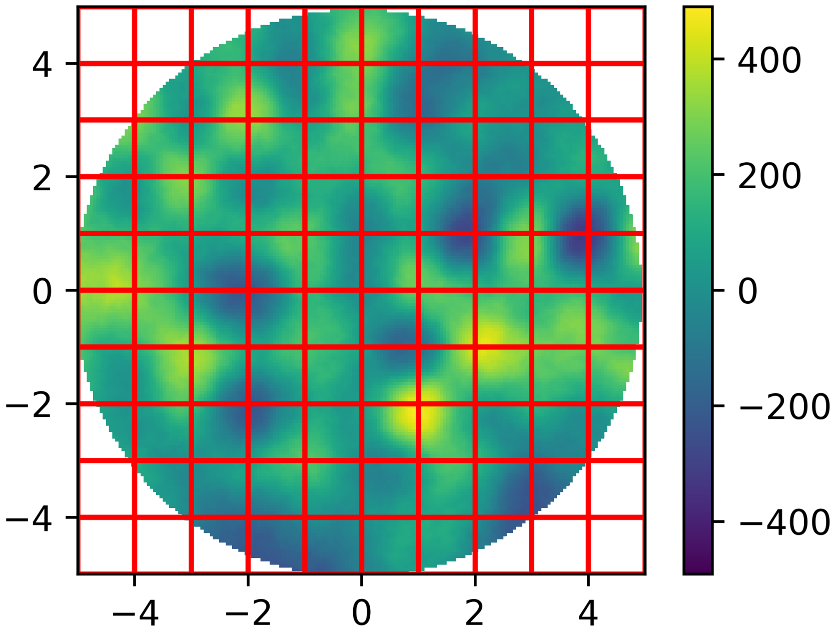

Figure 5.18: *Residual WFE (nm) of an AO system with 4.0 cm subaperture diameter using undistorted (left) and distorted (right) control. The dynamic misalignment is 0.6 induced log-amplitude variance and 75 RMS actuator shift. The boundaries of each SH-WFS lenslet are overlaid with red lines. Centres of DM actuators are at the intersections of the red lines.*

With the control performance tested, the relationship between the distortion of the IM main actuators and the system performance error can now be studied. Figure 5.19 shows a relationship between the distortion level of the IM or the RMS percentage error against the error arising from using unmatched IM (excluding the error that existed in the non-distorted control). The 4.0 cm subaperture system shows a drastically different performance compared to the other systems. This is possibly because of the SVD conditioning parameters selected in the previous section. The conditioning parameter is optimised for the 5.0 cm subaperture diameter, not for the 4.0 cm. In Figure 5.16, the selected conditioning parameter is on the edge of the second drop in the SVD of the 4.0 cm. This may reduce the performance of the 4.0 cm control considerably. Future study is required. Besides the 4.0 cm system, the other systems show a closely knit performance, where the RMS percentage larger than 50% results in a control error larger than 50 nm. As mentioned earlier, the control error might depend on the selection of the SVD conditioning parameter. Unless further studies are done, it is too early to specify when the percentage error of IMs guarantees high control error.

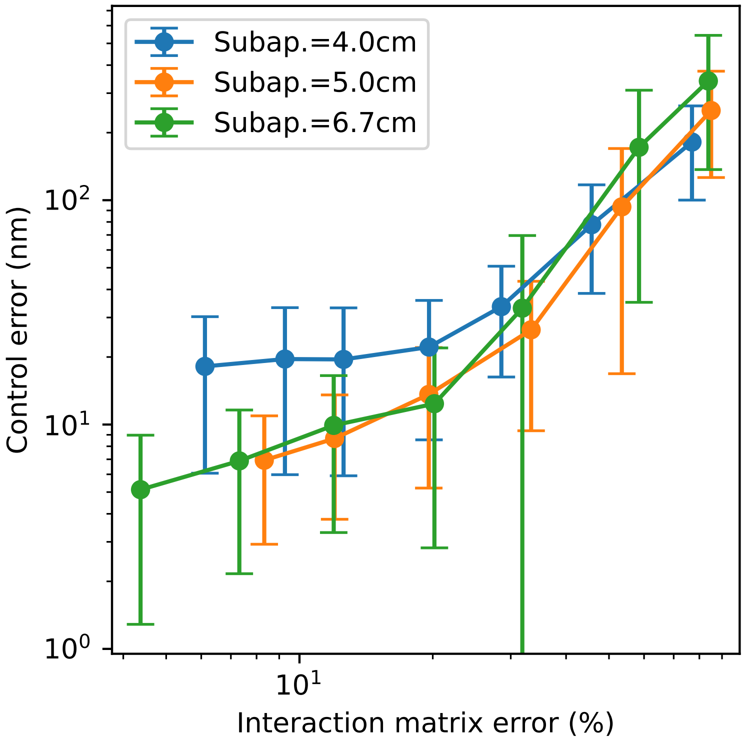

Figure 5.19: *5-iteration control error of AO systems from using an unmatched control versus the percentage error of the main elements of the IMs.*

The RMS WFE after the fifth AO loop corrections of the distorted AO subtracted by the undistorted performance are shown compared to the turbulence strength and distances of **DM2** in Figures 5.20. The expected dynamic misalignment indices are shown with contour lines. For the 5.0 cm subaperture systems, only **DM2** correcting approximately 8 cm r_0 or stronger turbulence layer at 3 km or further (upper right corner) suffer at least 50 nm control error. This finding signifies that only limited conditions will need to address the control errors.

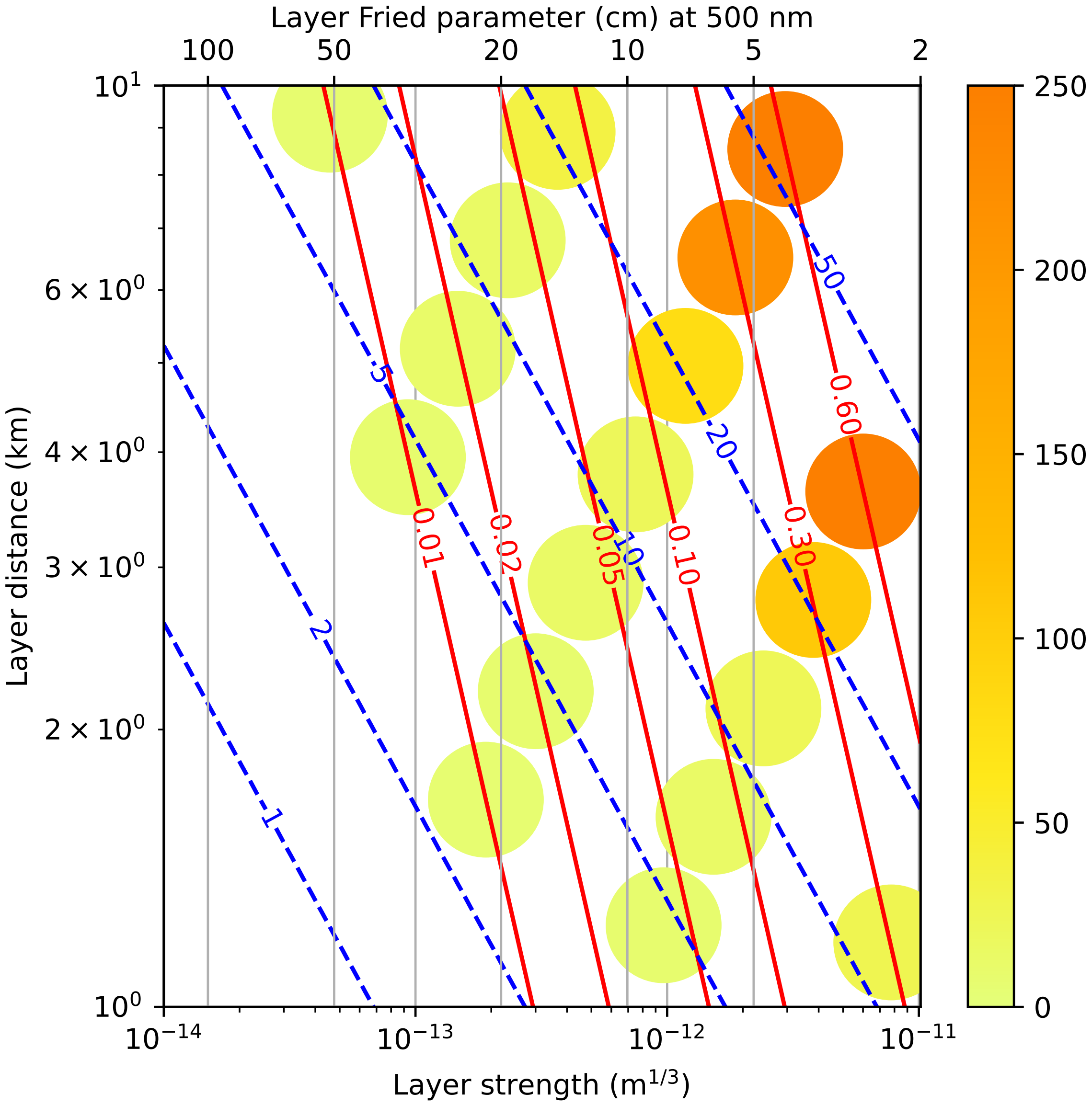

Figure 5.20: *5-iteration RMS control error (nm) of an AO system with 5.0 cm subaperture diameter using distorted control in various situations. Control error (colour) is shown against turbulence strength corrected by* ***DM2*** *(lower x-axis), Fried parameter (upper x-axis), and* ***DM2****'s distance (y-axis). Contours of the induced Rytov parameter of the distortion are shown with red solid lines. Contours of the actuator shift RMS of the distortion in percentage of actuator pitch are shown with blue dashed lines.*

The terminal RMS WFE shown in Figure 5.20 is replotted compared to the dynamic misalignment indices in Figure 5.21. The general trends now appear, where the terminal RMS WFE increases compared to the dynamic misalignment indices. The control error appears to increase more with the RMS actuator shift than the induced Rytov parameter. Region with 50 nm control error is between 0.1 and 0.3 induced Rytov parameter and 15 to 20% RMS actuator shift.

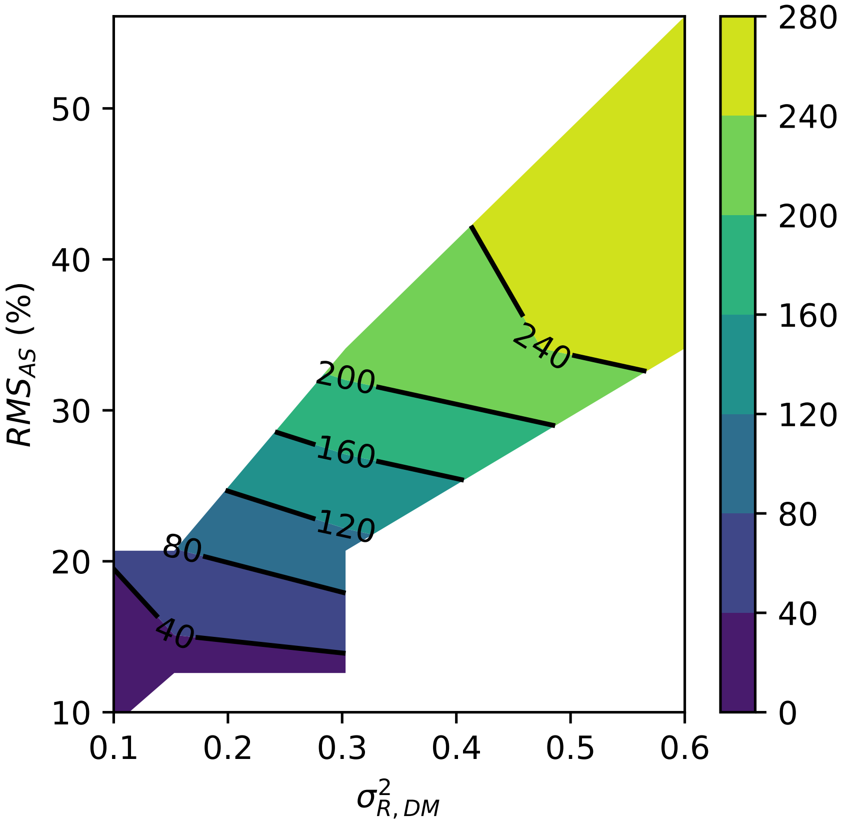

Figure 5.21: *5-iteration control error in nm (colour) against induced Rytov parameters (x-axis) and actuator shift RMSs (y-axis) of an AO system with 5.0 cm subaperture diameter. Regions not simulated are shown in white.*

To further separate the effect of each dynamic misalignment indices on the terminal RMS WFE, Figure 5.21 are replotted compared to the induced Rytov parameter in Figure 5.22 on the x-axis with the expected actuator shift RMS encoded in the colour. Figure 5.23 does similarly but for the RMS actuator shift. The terminal RMS WFE increases rapidly when the induced Rytov parameter is larger than 0.3 and the expected actuator shift RMS statistic is larger than 15% of the subaperture, between 50 and 100 nm.

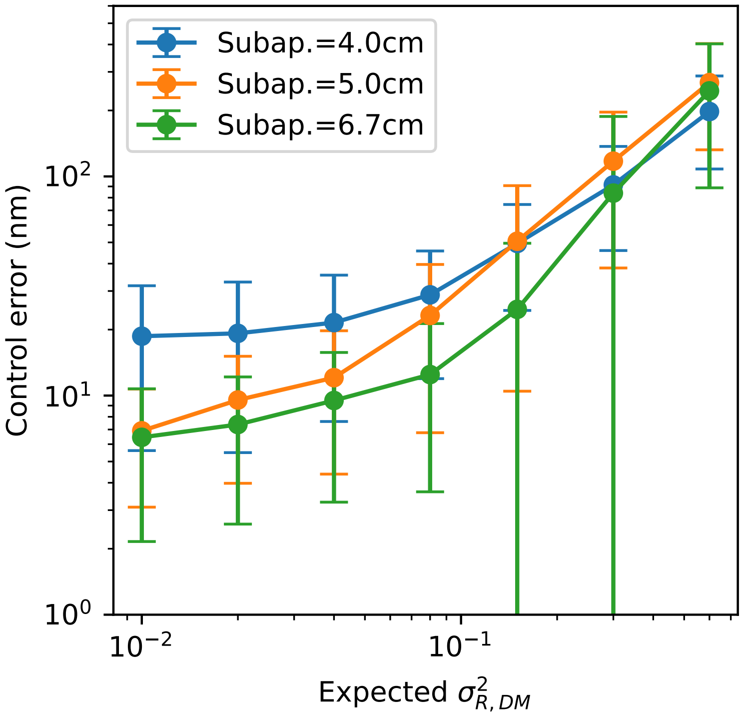

Figure 5.22: *5-iteration control errors in nm (y-axis) against induced Rytov parameter (x-axis) for various subaperture diameters (colour).*

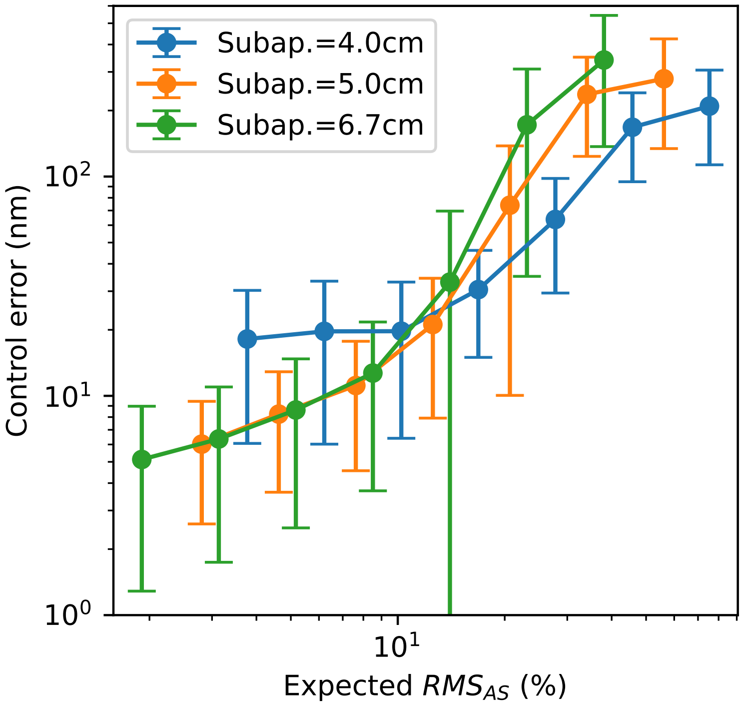

Figure 5.23: *5-iteration control errors in nm (y-axis) against actuator shift RMS for various subaperture diameters (colour).*

Regarding the previously concerns on the system with 4.0 cm subaperture diameter, its control errors are higher than the other systems at similar dynamic distortion indices, as seen in Figure 5.19, 5.22, and 5.23. The question is, if the SVD conditioning parameter changes to a lower value, will its control error drop and match the other system? The simulation is run again with 0.01 SVD conditioning value. The results are presented in Table 5.3. Only the weakest dynamic distortion cases are tested for the 4.0 cm system. The new results show promising matches in performance with the other systems. Further study is still required.

Figure	x-axis	x-values	WFE (nm)	Uncertainty (nm)
5.19	IM percentage error (%)	11%	5.9	4.4
5.22	Induced Rytov parameter	0.01	7.3	4.3
5.23	RMS actuator shift (%)	3.8%	6.7	4.0

Table 5.3: *Residual RMS WFE of the 4.0 cm subaperture system with 0.01 SVD conditioning values instead of the previously used 0.05.*

With the current simulated results, given a desired level of RMS WFE, certain limit on the control parameters can be set and calculated for the similar MCAO configuration to determine if such system would need to manage the control from the distortion of the AO calibrations.

5.5.2 Residual Phase Wavefront Power Spectrum Density

All of the residual wavefront errors after the fifth AO loop correction are analysed for the Power Spectral Density (PSD) against the spatial frequency. In Figure 5.24, the wavefront error of the undistorted CM are presented as a benchmark. The wavefront errors of the distorted CMs, mainly with the largest dynamic misalignment indices, are shown. Conditions with low distortion have a similar analysis to the no-distortion case. The undistorted CMs reduce PSD at lower frequencies than the Nyquist frequency of the SH-WFS and **DM1** to be lower than the uncorrected turbulence. There is a limited number of data points with a lower frequency than the Nyquist frequency because only the phase within the square inscribed inside the pupil is used; avoid using the pupil function in the Fourier transform. Meanwhile, the distorted CMs not only cannot correct, but also amplify the PSD at the Nyquist frequency. This represents the waffle mode error, as shown in Figure 5.18, which cannot be mitigated through the truncated SVD method used to generate the CM from the IM (Gavel, 2003). In brief, with control distortions, AO system cannot correct turbulence, and may even amplify the aberration.

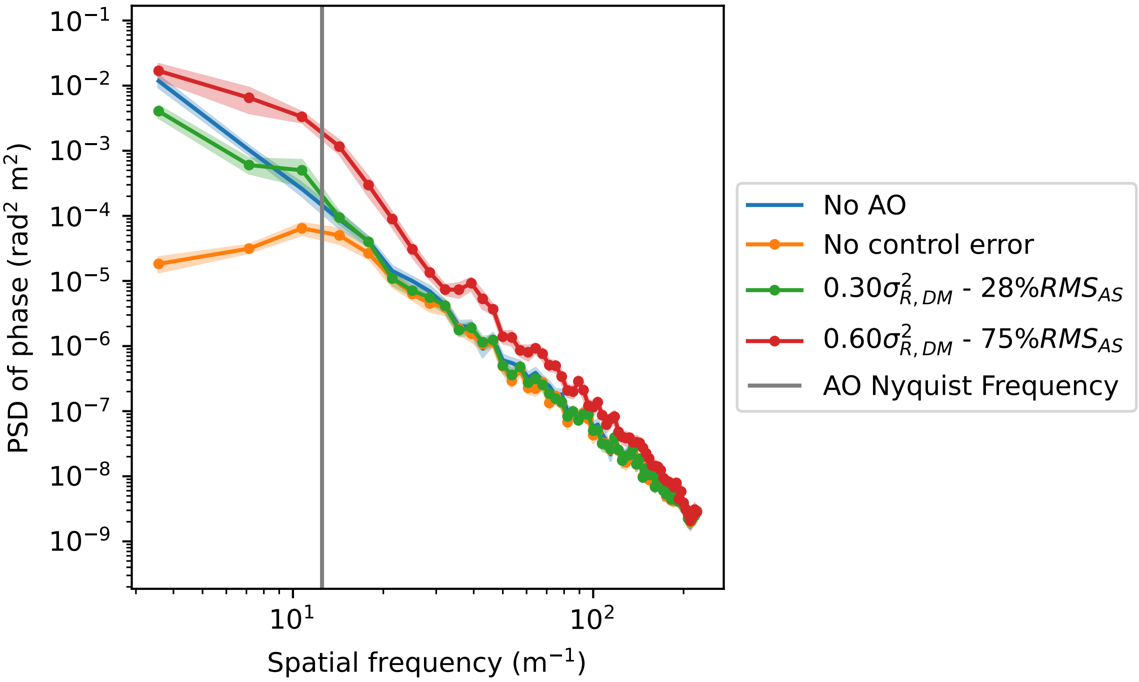

Figure 5.24: *Mean PSD of phase (y-axis) of residual WFE and its error of the mean is plotted against spatial frequency (x-axis) for a system with 4.0 cm subaperture diameter. Various dynamic misalignments are shown (colours). The system's Nyquist frequency is marked.*

5.5.3 Residual Phase Wavefront Zernike Mode Decomposition

The residual wavefront errors are also decomposed into different Zernike modes for analysis, as shown in Figure 5.25. The undistorted CMs reduces all Zernike mode coefficients of the turbulence layer. The distorted CMs can reduce lower Zernike mode powers, but at a reduced performance. At higher Zernike mode orders, the distorted CMs increases the Zernike mode powers to some power level. This behaviour reminds the behaviour of noises, potentially due to waffle modes again, since higher Zernike modes contain higher spatial frequency patterns. The noise level increases as the dynamic misalignment indices increase. At low enough dynamic misalignment indices, the noise level might still be lower than the turbulence statistics, but higher than the AO corrected level.

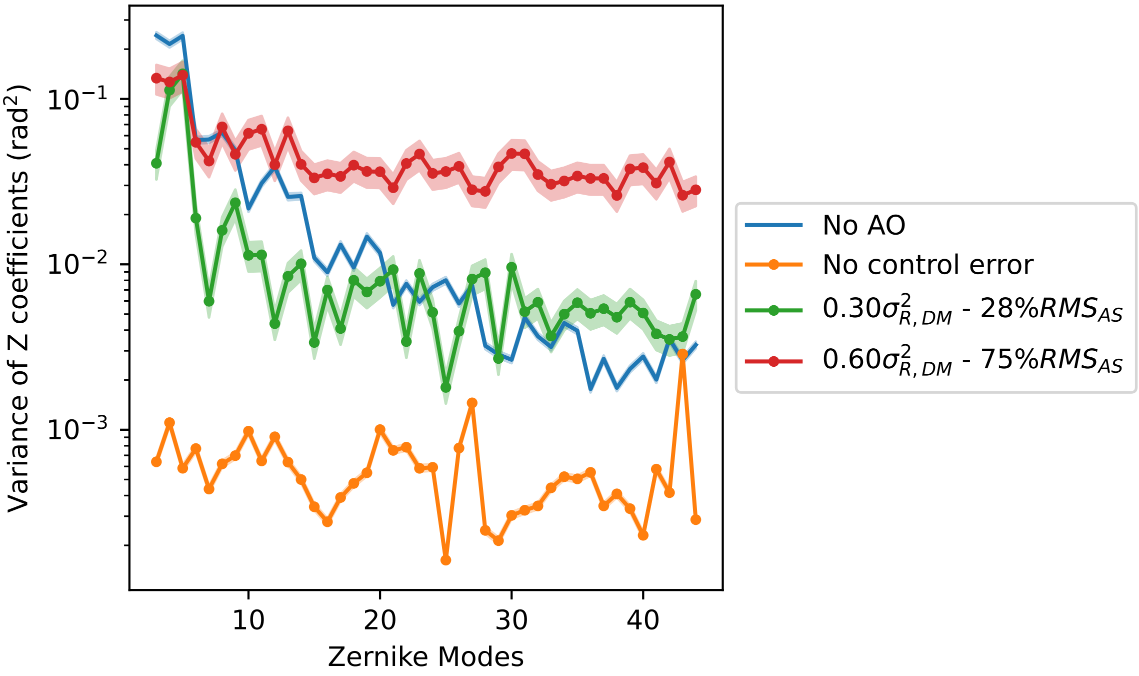

Figure 5.25: *Mean of Zernike modes power of residual wavefront error (y-axis) against different modes (x-axis) for a system with 4.0 cm subaperture diameter. Various dynamic misalignments are shown (colours).*

5.6 Effect on Existing Multi-conjugate Adaptive Optics

Although this chapter did not simulate different MCAO configurations such as **DM1** conjugated to altitude and **DM2** conjugated to the ground configuration or a higher number of DMs, it proposes equations to predict the control parameters, which behave accordingly within the simulation of this chapter. Assuming that the equation holds for other systems, some predictions of the concern level can be made. The expected dynamic misalignment indices of selected existing MCAO systems, including both daytime and nighttime, are calculated. The selected systems include DKIST (Schmidt et al., 2022), EST (Femenía-Castella et al., 2022), GeMS (Rigaut et al., 2014), MAD (Marchetti et al., 2003), MAVIS (Greggio et al., 2022), MORFEO (Busoni et al., 2022), NFIRAOS (Crane et al., 2018), and GREGOR (Schmidt et al., 2010). Turbulence profiles used in the calculation are separated into two types: continental (Paranal (Osborn et al., 2015)) or island (La Palma Hoegemann et al. (2004)). The median profile is a combination of the median turbulence at each height. Turbulence distributions along a slant path, non-zero zenith angle, are estimated from the vertical profiles assuming the infinite atmosphere.

Parameter	**DKIST**	**EST**	**GeMS**	**MAD**
Tel. Pupil Diam. (m)	4	4.2	8	8
MCAO FoV (arcsec)	60	60	120	120
Number of DMs	3	5	3	2
DM Conj. Height (km)*	[0, 4, 11.2]	[5, 9, 12, 20, 0]	[0, 4.5, 9]	[0, 8.5]
DM Pitch (cm)*	[9.3, 12, 27]	[23.2, 33.3, 25.9, 33.4, 8.4]	[50, 50, 100]	[88.9, 88.9]
WFS Wavelength (nm)	550	500	589	550
WFS Pitch (cm)	9.3	8	50	100
Turbulence Profile	Island	Island	Continental	Continental
Median r_0 (cm)	9	7	14	14

Parameter	**MAVIS**	**MORFEO**	**NFIRAOS**	**GREGOR**
Tel. Pupil Diam. (m)	8.2	38.5	30	1.5
MCAO FoV (arcsec)	120	160	120	68
Number of DMs	3	3	2	3
DM Conj. Height (km)*	[6, 13.5, 0]	[7, 17.5, 0.6]	[0, 11.8]	[0, 25, 8]
DM Pitch (cm)*	[25.3, 31.5, 22]	[85, 125, 50]	[40, 48.4]	[18.8, 121.8, 51.7]
WFS Wavelength (nm)	589	589	589	550
WFS Pitch (cm)	21.6	55	50	[10, 50, 50]
Turbulence Profile	Continental	Continental	Island	Island
Median r_0 (cm)	14	14	19	7

Table 5.4: *Existing MCAO system configurations. (*) The order of these values is according to the light path from the telescope pupil (leftmost values) to the WFS (rightmost values). Data gathered from Schmidt et al. (2022), Femenía-Castella et al. (2022), Rigaut et al. (2014), Marchetti et al. (2003), Greggio et al. (2022), Busoni et al. (2022), Crane et al. (2018), and Schmidt et al. (2010).*

The concern RMS WFE level in this chapter is set at 50 nm. The reasoning is as follows. Currently, the EST has a 40% Strehl requirement (Montoya Martínez et al., 2018), equivalent to 76 nm at 500 nm. The number of the previously determined observation conditions that passed the requirement will be reduced. Under the presence of the control error of 25, 50, and 75 nm control error, the previously determined Strehl ratios of 45, 60, and 100% will be reduced to 40%, respectively. Based on this analysis, a 50 nm control error is most likely the concerning level. Based on the simulation result, the observing condition with the induced Rytov parameter higher than 0.1 - 0.2 or RMS actuator shift higher than 10 - 20% is concerning.

For all of the selected MCAO systems at their median turbulence conditions, only the EST 0km-DM, the furthest away from the WFS, pointing at an 80-degree zenith angle, will have a concerning 10.7% actuator shift RMS and 0.088 induced Rytov parameter. In a similar note, the GREGOR without separating the on-axis and multi-directional WFS, the ground-DM at 80-degree zenith would have the highest misregistration of 7.6% actuator shift RMS and 0.46 induced Rytov parameter. This configuration showcased the dynamic misregistration, so the control was later separated (Schmidt et al., 2010). However, with its already adjusted control separation, the 25km-DM pointing at 80-degree zenith will have 0.2% actuator RMS and 0.048 induced Rytov parameter. Meanwhile, the DKIST's DM with the largest expected dynamic misregistration, the 11km-DM pointing at 80-degree zenith angle, only has 0.8% actuator shift RMS and 0.015 induced Rytov parameter. The airmass effect on the turbulence is included. So, generally, none of the existing MCAO systems will need to correct for the distortion of their control, unless they want to extend their observing conditions to smaller r_0 or lower elevation angles.

If those systems were to extend their observation conditions beyond their median conditions, many of them would now need to handle the dynamic misalignment effect. The systems under conditions that have a higher predicted induced Rytov parameter larger than 0.1 and actuator shift RMS larger than 10% of the actuator pitch, which may have RMS WFE larger than 50 nm, are listed in Table 5.5 and 5.6. Lots of the listed entries are mainly at Fried parameter smaller than 5.0 cm, which is rare for the nighttime systems (Farley et al., 2018). However, the 2 to 5.0 cm Fried parameter turbulence might exist for the solar telescope systems Griffiths et al. (2023). Some of the turbulence strength and pointing angle listed for the solar telescope might not be observed, due to the sun's pointing angle and the turbulence strength tend to correlate, as turbulence becomes stronger as the sun rises in pointing altitude.

System	r_0 (cm)	ζ (°)	DM Height (km)	RMS RMS_{AS} (%)	σ_R^2
DKIST	2	80	11.2	2.8	0.180
EST	2	80	0.0	30.5	0.712
EST	2	80	9.0	2.1	0.199
EST	2	80	12.0	4.6	0.363
EST	2	80	20.0	5.0	0.504
EST	2	70	0.0	20.8	0.330
EST	2	70	12.0	3.2	0.170
EST	2	70	20.0	3.4	0.231
EST	2	60	0.0	19.0	0.256
EST	2	60	12.0	2.5	0.105
EST	2	60	20.0	2.7	0.149
EST	2	45	0.0	20.3	0.268
EST	2	45	20.0	2.4	0.107
EST	2	30	0.0	14.6	0.153
EST	2	30	20.0	2.4	0.104
EST	2	0	0.0	12.8	0.144
EST	2	0	20.0	2.8	0.135
EST	3	80	0.0	21.8	0.362
EST	3	80	9.0	1.5	0.101
EST	3	80	12.0	3.3	0.185
EST	3	80	20.0	3.6	0.256
EST	3	70	0.0	14.8	0.168
EST	3	70	20.0	2.4	0.117
EST	3	60	0.0	13.6	0.130
EST	3	45	0.0	14.5	0.136
EST	3	30	0.0	10.4	0.078
EST	5	80	0.0	14.2	0.155
EST	5	80	20.0	2.3	0.109

Table 5.5: *Existing MCAO systems under observing conditions where their control has the expected either actuator shift RMS larger than 10% or induced Rytov parameter larger than 0.1. (Excluding nighttime systems at low observing elevation angle)*

System	r_0 **(cm)**	ζ **(°)**	**DM Height (km)**	**RMS** RMS_{AS} **(%)**	σ_R^2
GREGOR-all	2	80	0.0	21.6	3.724
GREGOR-all	2	80	25.0	0.6	0.385
GREGOR-all	2	70	0.0	17.9	2.571
GREGOR-all	2	70	25.0	0.6	0.231
GREGOR-all	2	60	0.0	14.5	1.676
GREGOR-all	2	60	25.0	0.4	0.136
GREGOR-all	2	45	0.0	11.4	1.038
GREGOR-all	2	30	0.0	10.0	0.737
GREGOR-all	2	0	0.0	9.1	0.669
GREGOR-all	3	80	0.0	15.4	1.895
GREGOR-all	3	80	25.0	0.5	0.196
GREGOR-all	3	70	0.0	12.8	1.309
GREGOR-all	3	70	25.0	0.4	0.117
GREGOR-all	3	60	0.0	10.3	0.852
GREGOR-all	3	45	0.0	8.1	0.528
GREGOR-all	3	30	0.0	7.1	0.406
GREGOR-all	3	0	0.0	6.5	0.340
GREGOR-all	5	80	0.0	10.1	0.809
GREGOR-all	5	70	0.0	8.4	0.558
GREGOR-all	5	60	0.0	6.7	0.364
GREGOR-all	5	45	0.0	5.3	0.225
GREGOR-all	5	30	0.0	4.7	0.173
GREGOR-all	5	0	0.0	4.3	0.145
GREGOR-all	8	80	0.0	6.8	0.369
GREGOR-all	8	70	0.0	5.6	0.252
GREGOR-all	8	60	0.0	4.5	0.166
GREGOR-all	8	45	0.0	3.6	0.103
GREGOR-all	11	80	0.0	5.2	0.217
GREGOR-all	11	70	0.0	4.3	0.150
GREGOR-all	14	80	0.0	4.3	0.148
GREGOR-MD	2	80	25.0	0.6	0.385
GREGOR-MD	2	70	25.0	0.5	0.231
GREGOR-MD	2	60	25.0	0.4	0.136
GREGOR-MD	3	80	25.0	0.5	0.196
GREGOR-MD	3	70	25.0	0.4	0.117

Table 5.6: *(Continue) Existing MCAO systems under observing conditions where their control has the expected either actuator shift RMS larger than 10% or induced Rytov parameter larger than 0.1. (Excluding nighttime systems at low observing elevation angle). 'GREGOR-all' notes the previous GREGOR system where all the ground DM is not controlled separately, while the 'GREGOR-MD' notes the GREGOR system with the ground and high-altitude DM have separate controls.*

Table 5.5 and 5.6 show a limited occasion where the DKIST and the GREGOR with control separation may suffer from control distortion, while the EST and GREGOR without control separation will suffer at a higher rate. This is due to the higher number of DMs and the high conjugated elevation of the DMs. The GREGOR system chose to separate its control to mitigate the dynamic misregistration (Schmidt et al., 2010).

The future MCAO designs that may experience the concerning level of expected dynamic misalignment indices would be those with large numbers of DMs, as the errors are accumulated through different layers. If AO systems are to operate in the photometric U band centring at 365 nm (Johnson and Morgan, 1953), a band supported by the DKIST telescope (National Solar Observatory, 2025b), the actuator shift RMS will reduce to 73% while the induced Rytov parameter will increase to 144%. The dynamic misalignment indices vary in the opposite direction under the wavelength change. There is a problem as a consequence of adopting a shorter wavelength. The atmosphere is more opaque (Döhring, 2017).

5.7 Conclusion

This chapter investigates pupil distortion effects and their impact on MCAO system performance. The major direct effects from the pupil distortion are the shifting of the DM actuator position (different to uniform misregistration commonly studied), and another being the DM-induced log-amplitude variance or optical propagation effect induced by other DMs in the system. These sources of error are now called the dynamic misalignment indices. This chapter hypothesises that both of these effects will introduce dynamic misalignment of the DMs that are behind other DMs in the WFS's point of view. This misalignment cannot be corrected by existing calibration methods.

Equations and methods to calculate the expected dynamic misalignment indices are proposed. Methods to measure these values both in simulation and during observations are also proposed. The induced log-amplitude variance can be measured through pupil imaging of the system. The RMS actuator shift can be measured by the influence method, using either the apparent phase map of the actuators' influence, or by the slope method, analysing the apparent slope influence of the actuators. The influence method gives the best estimate. Though the slope method has limitations, since it uses slope which can be acquired from the WFS, it is more accessible. This chapter recommends using the influence method to estimate the RMS actuator shift.

Simulation of MCAO system with two DMs is simulated and tested in one LoS for control error for only one DM order, namely ground-**DM1** and altitude-**DM2**. Doing so isolates error from scintillation during the AO corrections and in turbulence layer tomography. This order has the highest theoretical turbulence correction ability. Though the test in only one LoS cannot represent the actual MCAO systems, it is a check-point before starting the full analysis on the MCAO. If the one LoS simulation shows any sign of error, the full MCAO will definitely do.

The simulation includes optical propagation effects between the key conjugate planes in the system. It confirms that the proposed expected dynamic misalignment indices equations are true and match the proposed measure methods.

The residual WFE of an AO system running with distorted CMs generated by the truncated SVD method are shown to have degradation, increasing as dynamic misalignment indices increase, mainly due to the actuator shift RMS rather than the induced log-amplitude variance. The simulation found that the distorted CMs introduce waffle modes as seen in the PSD analysis, amplifying the turbulence at the AO spatial Nyquist frequency. There are some reductions of turbulence aberration in the lower-order Zernike modes, while higher modes are dominated by noise from the waffle modes effect. The RMS WFE after 5 iterations of AO loop correction with 0.8 gain, where undistorted control would have already reached the theoretical correction values, would have a 50 nm increase in the RMS WFE at the induced Rytov parameter of 0.1 and the actuator shift RMS of 10% of the actuator pitch, potentially turn previously 60% Strehl ratio at 500 nm down to 40%.

With the proposed expected dynamic misalignment indices, equations, and some insights into the MCAO control performance, predictions can be made about existing MCAO performance. Most of the existing MCAO systems will not suffer from the distortion of the control at their median observing conditions. However, if they would like to expand their observing conditions, mainly for the daytime turbulence, some systems may need to consider correcting for the control distortion effect. Lastly, because the dynamic misalignment indices are expected to add linearly through several DMs, systems with a higher number of DMs will potentially need to correct for the control distortion effect.

There are several possible follow-up studies for this Chapter. This chapter uses the same spacing for the WFS and DMs, which is not always true in different MCAO designs. Simulations of systems with more than 2 DMs or various DM's orders are required. Effects of choices of the SVDs conditioning parameter for the truncated SVD methods to generate the CM should be studied, as well as testing other generation methods.

Key Findings

1. While running MCAO, active DMs near the WFS distort further DMs control. This can be seen as pupil distortion.
2. The distortion of MCAO control comes from two sources: DM-induced log-amplitude variance and apparent shift in position of the DM actuator.
3. Both sources of dynamic misalignment can be predicted and measured. The relation between them are presented in the chapter.
4. The induced log-amplitude variance can be measured through intensity variation of pupil image of the system during the operation. The proposed expectation equation does not match the actual behaviour at the expected Rytov parameter less than 0.1.
5. The RMS actuator shift can be measured by either the influence or the slope method. The influence method under-estimated the expectation, while the slope method over-estimate hugely and only applicable at 10% or larger actuator shift.
6. Within this chapter simulation, the concerning level of control error is 50 nm RMS WFE at 500 nm. This level of error or larger exists when the induced Rytov parameter is larger than 0.1 or the actuator shift RMS is larger than 10%.
7. Depending on observing and turbulence conditions, existing MCAO systems for solar telescopes are potentially suffering from control error if they were to extend their observing conditions, assuming that the proposed parameter prediction in this chapter is correct.

6 Conclusion

As global infrastructure increasingly relies on technology, susceptibility to threats from solar activity escalates. High-resolution solar observations using ground-based solar telescopes are essential for understanding these threats; however, they suffer from atmospheric turbulence–induced optical distortions. Multi-Conjugated Adaptive Optics (MCAO) mitigates these effects, enabling high-resolution imaging across a wide field of view. Implementing solar MCAO is particularly complex due to pronounced daytime turbulence and shorter wavelength observations, which increase scintillation and complicate system control.

The simulation of Adaptive Optics (AO) in consideration of optical propagation is implemented based on AOtools and Soapy by Townson et al. (2019) and Reeves (2016). To provide confidence in the results of subsequent chapters and provide a comprehensive description of the base simulation used throughout this thesis, the performance of the simulation is verified against expected or theoretical values in Chapter 3. I implemented an automated script to generate simulation parameters satisfying any requirements and limitations listed. In addition, I also verified that the high altitude turbulence layers required for the propagation can be generated at a smaller size with only 10 nm intensity-weighted mean wavefront error. This reduces simulation time to generate new turbulence aberrations in a layer by up to 15% for typical solar MCAO applications, but 43% for optical communication applications.

The simulation is then used to investigate two methods of enhancing solar MCAO simulations. The first method presented in Chapter 4 accelerates the Shack-Hartmann Wavefront Sensor (SH-WFS) model through the introduction of the Intensity-Weighted Averaged Gradient Method (IG-Method). The IG-Method offers a more efficient alternative to full modelling the SH-WFS using the conventional Fourier Transform Method (FT-Method). The IG-Method uses only 35–60% of simulation time and 30-40% memory usage of the FT-Method, while preserving accuracy within 3 nm Root-Mean-Square (RMS). This result is relevant across a Rytov parameter range of 0.01 – 0.3, regardless of turbulence strength (2 cm $< r_0 <$ 11 cm) or layer distance (5 km $<$ $H <$ 20 km). Compared to the Averaged Gradient Method (G-Method) of determining an SH-WFS measurement directly from the wavefront phase, the IG-Method performs significantly better in scintillation, where G-Method errors reach up to 30 nm RMS Optical Path Difference (OPD). Although adopting the IG-Method provides substantial local speed improvements, its overall benefit is limited since the propagation processes dominates simulation time, occupying 85% of total computation for a typical solar MCAO simulation. If a geometrical approximation similar to the IG-Method could be applied to the propagation process, total MCAO simulation time could be reduced further.

The IG-Method can utilise a Noise Equivalent Angle (NEA) with noise model of the FT-Method in scintillation-free conditions to include the effects of both photon and detector read noise on the SH-WFS performance. This is possible because the FT-Method with and without scintillation is found to have similar behaviour in this study. SH-WFS used in the study has 64x64 detector pixels at $\lambda/2d$ angular scale but only uses 17x17 pixels for the Centre-of-Gravity (CoG) process. Detected photon counts between hundred to million per lenslet and 0.1 - 10 electron RMS readout noise per pixel are included in the study with varying normalised intensity threshold levels between 0.0001 and 0.1 in the CoG process. Differences between scintillation-free and scintillation conditions of the FT-Method are limited to 4%, 7.5%, and 10% in photon-noise-dominated, readout-noise-dominated, and non-standard threshold cases, respectively. Based on results from the baseline FT-Method SH-WFS. The error of the NEA of the scintillated to scintillation-free FT-Method is ± 10%.

The IG-Method thus provides a reliable geometrical approximation of FT-Method propagation effects, introducing negligible error (3 nm RMS at Rytov < 0.3). Future studies should explore whether similar approximations can be extended to the propagation process itself, which represents the most time-demanding part of MCAO simulation. Further work is also needed to assess IG-Method performance for extended-object wavefront sensing, such as correlation SH-WFS, where anisoplanatism and wide-field aberrations must be incorporated.

Beyond SH-WFS simulation, this thesis also investigates pupil distortion and its effects on MCAO performance. Two major contributors are identified: DM-induced log-amplitude variance and RMS shifts of Deformable Mirror (DM) actuator positions, distinct from uniform DM to WFS misregistration that is typically studied. Together, these effects constitute dynamic misalignment indices, which introduce misalignment in downstream DMs from the Wavefront Sensor (WFS) perspective and cannot be corrected by existing calibration methods. Equations and methods are proposed to predict and measure these indices. This thesis verified their accuracy within 0.01-0.6 induced Rytov parameter and 2-50% of DM's pitch RMS actuator shift. The induced log-amplitude variance can be quantified via pupil imaging, while RMS actuator shifts can be assessed using either the influence method (most accurate) or the slope method (less reliable, tending to overestimate at small shifts but accessible via WFS data).

Simulations of MCAO systems with two DMs validate these methods and confirm that distorted Control Matrix (CM)s generated by truncated Singular Value Decomposition (SVD) degrade AO performance. The distortions amplify turbulence at the AO Nyquist frequency through waffle modes while reducing lower-order aberrations. Residual Wavefront Error (WFE) increases by 50 nm RMS at induced Rytov = 0.1 and RMS actuator shift = 10% of DM's pitch, potentially reducing Strehl ratio from 60% to 40% at 500 nm. These results establish thresholds beyond which DM-induced Rytov parameter (> 0.1) or RMS actuator shifts (>10% of DM's pitch) cause significant degradation in MCAO correction. Although most current MCAO systems are unlikely to suffer major distortion under median observing conditions, extending their range to harsher daytime turbulence may require active correction for dynamic misalignment. Because misalignment effects increase with the number of DMs, systems with larger DM counts are more susceptible.

Since the RMS actuator shift can be successfully approximated using a geometrical approximation of the wavefront, it is possible that a geometrical approximation can be used to update the AO control.

In summary, this work introduces the IG-Method as a fast and memory-efficient alternative to the FT-Method for SH-WFS simulation, achieving substantial gains without compromising accuracy in the presence of scintillation. While the propagation process remains the computational bottleneck, the demonstrated success of geometrical approximations suggests future opportunities for accelerating this component as well. Furthermore, the identification and characterisation of pupil distortion effects (particularly DM-induced scintillation and RMS actuator misalignments) provides critical insights for predicting and mitigating control errors in solar MCAO. Together, these contributions advance the modelling and optimisation of solar MCAO systems and highlight directions for further research into approximate optical propagation to generate distorted extended objects used in wavefront sensing and dynamic misalignment correction through geometrical approximations.

Bibliography

J. Amos. UK Met Office opens ’solar storm’ centre. *BBC*, Oct. 2014. URL https://www.bbc.co.uk/news/science-environment-29525154.

L. C. Andrews and R. L. Phillips. *Laser beam propagation through random media.* SPIE Press, Bellingham, Wash, 2nd ed edition, 2005. ISBN 978-0-8194-5948-0. URL https://doi.org/10.1117/3.626196.

E. Aristidi, A. Ziad, Y. Fantéï-Caujolle, J. Chabé, C. Giordano, C. Renaud, and H. Lantéri. Monitoring daytime and nighttime optical turbulence profiles with the PML instrument, Feb. 2020. URL http://arxiv.org/abs/2002.04947.

F. Assémat, R. Wilson, and E. Gendron. Method for simulating infinitely long and non stationary phase screens with optimized memory storage. *Optics Express*, 14(3):988, 2006. ISSN 1094-4087. doi: 10.1364/OE.14.000988. URL https://opg.optica.org/oe/abstract.cfm?uri=oe-14-3-988.

A. F. Aveni. *Empires of time: calendars, clocks, and cultures.* Basic Books, New York, 1989. ISBN 978-0-465-01950-2.

R. Avila, J. Vernin, M. R. Chun, and L. J. Sanchez. Turbulence and wind profiling with generalized scidar at Cerro Pachon. In P. L. Wizinowich, editor, *Proc. SPIE 4007, Adaptive Optical Systems Technology*, pages 721–732, Munich, Germany, July 2000. doi:

10.1117/12.390317. URL http://proceedings.spiedigitallibrary.org/proceeding.aspx?articleid=898738.

H. W. Babcock. The Possibility of Compensating Astronomical Seeing. *Publications of the Astronomical Society of the Pacific*, 65:229, Oct. 1953. ISSN 0004-6280, 1538-3873. doi: 10.1086/126606. URL http://iopscience.iop.org/article/10.1086/126606.

H. W. Babcock. The Topology of the Sun's Magnetic Field and the 22-YEAR Cycle. *The Astrophysical Journal*, 133:572, Mar. 1961. ISSN 0004-637X, 1538-4357. doi: 10.1086/147060. URL http://adsabs.harvard.edu/doi/10.1086/147060.

J. D. Barchers, D. L. Fried, D. J. Link, G. A. Tyler, W. Moretti, T. J. Brennan, and R. Q. Fugate. Performance of wavefront sensors in strong scintillation. In P. L. Wizinowich and D. Bonaccini, editors, *Adaptive Optical System Technologies II*, page 217, Waikoloa, Hawai'i, United States, Feb. 2003. doi: 10.1117/12.457126. URL http://proceedings.spiedigitallibrary.org/proceeding.aspx?doi=10.1117/12.457126.

BBC. The threat of solar storms explained, Oct. 2024. URL https://www.bbc.co.uk/reel/video/p0jd9cnj/the-threat-of-solar-storms-explained.

J. Beckers. Increasing the Size of the Isoplanatic Patch with Multiconjugate Adaptive Optics. In *Very Large Telescopes and their Instrumentation, ESO*, page 693, Garching, Oct. 1988. European Southern Observatory (ESO). URL https://ui.adsabs.harvard.edu/abs/1988ESOC...30..693B/abstract.

R. Biasi, D. Bonaccini Calia, M. Centrone, M. Enderlein, M. Faccini, O. Farley, D. Gallieni, D. Gooding, P. Haguenauer, P. Janout, D. Jenkins, F. Lison, J. Luis, N. Martinez Rey, J. Osborn, C. Patauner, D. Pescoller, M. Reyes, L. Sabatini, L. Salvi, Z. Sodnik, D. Alaluf, M. Tintori, M. Tordi, M. Townson, H. Virdee, D. P. Wei, and W. L. Clements. ALASCA: the ESA Laser Guide Star Adaptive Optics Optical Feeder Link demonstrator facility. In K. Minoglou, N. Karafolas, and B. Cugny, editors, *International Conference on Space Optics — ICSO 2022*, page 186, Dubrovnik, Croatia, July 2023. SPIE. ISBN 978-1-5106-6803-4 978-1-5106-6804-1. doi: 10.1117/12.2690989. URL https://www.spiedigitallibrary.org/conference-proceedings-of-spie/12777/

2690989/ALASCA--the-ESA-Laser-Guide-Star-Adaptive-Optics-Optical/10.1117/12.2690989.full.

L. Busoni, G. Agapito, C. Plantet, G. Carlà, S. Oberti, M. Bonaglia, T. Lapucci, M. Xompero, C. Arcidiacono, Z. Hubert, P. Rabou, B. Salasnich, A. Baruffolo, I. Foppiani, G. M. Pariani, M. Munari, D. Magrin, M. Riva, and P. Ciliegi. MAORY/MORFEO @ ELT: preliminary design of the adaptive optics subsystem. In D. Schmidt, L. Schreiber, and E. Vernet, editors, *Adaptive Optics Systems VIII*, page 178, Montréal, Canada, Aug. 2022. SPIE. ISBN 978-1-5106-5351-1 978-1-5106-5352-8. doi: 10.1117/12.2629606. URL https://www.spiedigitallibrary.org/conference-proceedings-of-spie/12185/2629606/MAORY-MORFEO--ELT--preliminary-design-of-the-adaptive/10.1117/12.2629606.full.

R. C. Carrington. Description of a Singular Appearance seen in the Sun on September 1, 1859. *Monthly Notices of the Royal Astronomical Society*, 20(1):13–15, Nov. 1859. ISSN 0035-8711, 1365-2966. doi: 10.1093/mnras/20.1.13. URL https://academic.oup.com/mnras/article-lookup/doi/10.1093/mnras/20.1.13.

J. Chabé, E. Aristidi, A. Ziad, H. Lantéri, Y. Fanteï-Caujolle, C. Giordano, J. Borgnino, M. Marjani, and C. Renaud. PML: a generalized monitor of atmospheric turbulence profile with high vertical resolution. *Applied Optics*, 59(25):7574, Sept. 2020. ISSN 1559-128X, 2155-3165. doi: 10.1364/AO.384504. URL https://opg.optica.org/abstract.cfm?URI=ao-59-25-7574.

J. Cooley and J. Tukey. An Algorithm for the Machine Calculation of Complex Fourier Series. *Mathematics of Computation*, 19(90):297–301, 1965. doi: 10.2307/2003354. URL https://www.jstor.org/stable/2003354.

J. Cooley, P. Lewis, and P. Welch. The finite Fourier transform. *IEEE Transactions on Audio and Electroacoustics*, 17(2):77–85, June 1969. ISSN 0018-9278. doi: 10.1109/TAU.1969.1162036. URL http://ieeexplore.ieee.org/document/1162036/.

J. Crane, D. R. Andersen, J. Atwood, P. Byrnes, J. Fitzsimmons, O. Lardière, A. Densmore, T. Hardy, G. Herriot, B. Hoff, D. Kerley, M. Smith, J. Stocks, J.-P. Véran, J. S. Dunn, C. Boyer, L. Wang, G. Trancho, M. Trubey, and K. Jackson. NFIRAOS adaptive optics for the Thirty Meter Telescope. In D. Schmidt, L. Schreiber, and L. M. Close, editors, *Adaptive Optics Systems VI*, page 144, Austin, United States, July 2018. SPIE. ISBN 978-1-5106-1959-3 978-1-5106-1960-9. doi: 10.1117/12.2314341. URL `https://www.spiedigitallibrary.org/conference-proceedings-of-spie/10703/2314341/NFIRAOS-adaptive-optics-for-the-Thirty-Meter-Telescope/10.1117/12.2314341.full`.

S. Darling. NASA: Understanding the Magnetic Sun, Jan. 2016. URL `https://www.nasa.gov/science-research/heliophysics/nasa-understanding-the-magnetic-sun/`.

T. Döhring. Critical discussion on the UV absorption properties of Earth's atmosphere. In M. F. P. Martins Costa, editor, *Third International Conference on Applications of Optics and Photonics*, page 28, Faro, Portugal, Aug. 2017. SPIE. ISBN 978-1-5106-1383-6 978-1-5106-1384-3. doi: 10.1117/12.2271645. URL `https://www.spiedigitallibrary.org/conference-proceedings-of-spie/10453/2271645/Critical-discussion-on-the-UV-absorption-properties-of-Earths-atmosphere/10.1117/12.2271645.full`.

N. D. Engstrom and J. D. Schmidt. Misregistration in adaptive optics systems. In R. A. Carreras, T. A. Rhoadarmer, and D. C. Dayton, editors, *Advanced Wavefront Control: Methods, Devices, and Applications VII*, page 74660A, San Diego, CA, Aug. 2009. doi: 10.1117/12.825356. URL `http://proceedings.spiedigitallibrary.org/proceeding.aspx?doi=10.1117/12.825356`.

O. Farley, J. Osborn, T. Morris, A. Reeves, and R. Wilson. Deformable Mirror configuration in MCAO: is propagation a fundamental limit on visible wavelength correction? In *Proceedings of the Adaptive Optics for Extremely Large Telescopes 5*. Instituto de Astrofísica de Canarias (IAC), 2017. doi: 10.26698/AO4ELT5.0091. URL `http://research.iac.es/congreso/AO4ELT5/pages/proceeding0091.html`.

O. J. D. Farley, J. Osborn, T. Morris, M. Sarazin, T. Butterley, M. J. Townson, P. Jia, and R. W. Wilson. Representative optical turbulence profiles for ESO Paranal by hierarchical clustering. *Monthly Notices of the Royal Astronomical Society*, Sept. 2018. ISSN 0035-

8711, 1365-2966. doi: 10.1093/mnras/sty2536. URL http://arxiv.org/abs/1809.07551. arXiv:1809.07551 [astro-ph].

B. Femenía-Castella, M. A. Núñez Cagigal, M. Barreto, M. Belío-Asin, J. Bienes, S. Bonaque-González, M. Collados, J. Cózar-Castellano, H. M. Chulani, N. Feijóo, J. M. González-Cava, Y. Martín Hernando, A. Mato, I. Montilla, L. Montoya, C. Padilla-Hernández, J. Quintero Nehrkorn, C. Quintero Noda, H. Rodriguez Delgado, J. Sánchez-Capuchino, M. Soler, J. J. Vaz-Cedillo, and N. Vega. Adaptive Optics at the European Solar Telescope: status and future developments. In D. Schmidt, L. Schreiber, and E. Vernet, editors, *Adaptive Optics Systems VIII*, page 71, Montréal, Canada, Aug. 2022. SPIE. ISBN 978-1-5106-5351-1 978-1-5106-5352-8. doi: 10.1117/12.2629516. URL https://www.spiedigitallibrary.org/conference-proceedings-of-spie/12185/2629516/Adaptive-Optics-at-the-European-Solar-Telescope--status-and/10.1117/12.2629516.full.

A. Ferreira. How a solar superstorm could send Earth back to the Stone Age. *financialmail*, Oct. 2024. URL https://www.businesslive.co.za/fm/life/2024-10-24-how-a-solar-superstorm-could-send-earth-back-to-the-stone-age/.

R. C. Flicker. Sequence of phase correction in multiconjugate adaptive optics. *Optics Letters*, 26(22):1743, Nov. 2001. ISSN 0146-9592, 1539-4794. doi: 10.1364/ol.26.001743. URL https://opg.optica.org/abstract.cfm?URI=ol-26-22-1743. Publisher: Optica Publishing Group.

D. L. Fried. Statistics of a Geometric Representation of Wavefront Distortion. *Journal of the Optical Society of America*, 55(11):1427, Nov. 1965. ISSN 0030-3941. doi: 10.1364/JOSA.55.001427. URL https://opg.optica.org/abstract.cfm?URI=josa-55-11-1427.

D. L. Fried. Optical Resolution Through a Randomly Inhomogeneous Medium for Very Long and Very Short Exposures. *Journal of the Optical Society of America*, 56(10):1372, Oct. 1966. ISSN 0030-3941. doi: 10.1364/JOSA.56.001372. URL https://opg.optica.org/abstract.cfm?URI=josa-56-10-1372.

D. L. Fried. Anisoplanatism in adaptive optics. *Journal of the Optical Society of America*, 72 (1):52, July 1981. doi: 10.1364/JOSA.72.000052. URL https://opg.optica.org/josa/fulltext.cfm?uri=josa-72-1-52&id=58288.

D. L. Fried and T. Clark. Extruding Kolmogorov-type phase screen ribbons. *Journal of the Optical Society of America A*, 25(2):463, Feb. 2008. ISSN 1084-7529, 1520-8532. doi: 10.1364/JOSAA.25.000463. URL https://opg.optica.org/abstract.cfm?URI=josaa-25-2-463.

J. J. Fuensalida, S. Chueca, J. M. Delgado, B. M. Garcia-Lorenzo, J. M. Gonzalez-Rodriguez, C. K. Hoegemann, E. G. Mendizabal, M. Reyes, M. Verde, and J. Vernin. Turbulence profiles in the observatories of the Canary Islands: preliminary statistics for adaptive optics. In A. L. Ardeberg and T. Andersen, editors, *Proc. SPIE 5382, Second Backaskog Workshop on Extremely Large Telescopes*, page 619, Backaskog, Sweden, July 2004. doi: 10.1117/12.566324. URL http://proceedings.spiedigitallibrary.org/proceeding.aspx?doi=10.1117/12.566324.

G. Galilei. *Istoria e dimostazioni intorno alle macchie solari e loro accidenti.* Appresso Giacomo Mascardi, Rome, 1612. URL https://archive.org/details/istoriaedimostra00gali/page/n63/mode/2up.

D. T. Gavel. Suppressing anomalous localized waffle behavior in least-squares wavefront reconstructors. In P. L. Wizinowich and D. Bonaccini, editors, *Adaptive Optical System Technologies II*, page 972, Waikoloa, Hawai'i, United States, Feb. 2003. doi: 10.1117/12.459686. URL http://proceedings.spiedigitallibrary.org/proceeding.aspx?doi=10.1117/12.459686.

H. Gomersall. pyFFTW, 2025. URL https://pypi.org/project/pyFFTW/.

J. W. Goodman. *Introduction to Fourier Optics.* W.H. Freeman and Company, 4th edition, 2017. ISBN 978-1-319-11916-4.

G. D. Goodno, C.-C. Shih, and J. E. Rothenberg. Perturbative analysis of coherent combining efficiency with mismatched lasers. *Optics Express*, 18(24):25403, Nov. 2010. ISSN 1094-

4087. doi: 10.1364/OE.18.025403. URL https://opg.optica.org/oe/abstract.cfm?uri=oe-18-24-25403.

J. L. Green, S. Boardsen, S. Odenwald, J. Humble, and K. A. Pazamickas. Eyewitness reports of the great auroral storm of 1859. *Advances in Space Research*, 38(2):145–154, Jan. 2006. ISSN 02731177. doi: 10.1016/j.asr.2005.12.021. URL https://linkinghub.elsevier.com/retrieve/pii/S0273117706000160.

D. Greggio, B. W. Taylor, M. Bonaglia, V. Viotto, M. Bergomi, E. Pinna, G. Agapito, S. Ströbele, M. Aliverti, K. Radhakrishnan, C. Schwab, J. Cranney, I. Vaughn, L. Marafatto, D. Magrin, D. Brodrick, S. Chinellato, and F. Rigaut. MAVIS Adaptive Optics Module: optical configuration and expected performance. In D. Schmidt, L. Schreiber, and E. Vernet, editors, *Adaptive Optics Systems VIII*, page 254, Montréal, Canada, Aug. 2022. SPIE. ISBN 978-1-5106-5351-1 978-1-5106-5352-8. doi: 10.1117/12.2630017. URL https://www.spiedigitallibrary.org/conference-proceedings-of-spie/12185/2630017/MAVIS-Adaptive-Optics-Module-optical-configuration-and-expected-performance/10.1117/12.2630017.full.

R. Griffiths. *Continuous 24-hour Shack-Hartmann optical turbulence profiling on a small telescope*. PhD thesis, Durham University, Durham, UK, 2024. URL https://etheses.dur.ac.uk/15845/.

R. Griffiths, J. Osborn, O. Farley, T. Butterley, M. J. Townson, and R. Wilson. Demonstrating 24-hour continuous vertical monitoring of atmospheric optical turbulence. *Optics Express*, 31(4):6730, Feb. 2023. ISSN 1094-4087. doi: 10.1364/OE.479544. URL https://opg.optica.org/abstract.cfm?URI=oe-31-4-6730.

R. Griffiths, L. Bardou, T. Butterley, J. Osborn, R. Wilson, E. Bustos, A. Tokovinin, M. Le Louarn, and A. Otarola. A comparison of next-generation turbulence profiling instruments at Paranal. *Monthly Notices of the Royal Astronomical Society*, 529(1):320–330, Feb. 2024. ISSN 0035-8711, 1365-2966. doi: 10.1093/mnras/stae434. URL https://academic.oup.com/mnras/article/529/1/320/7606322.

J. Hardy. *Adaptive Optics for Astronomical Telescopes.* Oxford Univrsity Press, Inc., 198 Madiso n Avenue, New York, New York, 10016, USA, 1998. ISBN 0-19-509019-5. URL https://doi.org/10.1093/oso/9780195090192.001.0001.

C. T. Heritier, S. Esposito, T. Fusco, B. Neichel, S. Oberti, R. Briguglio, G. Agapito, A. Puglisi, E. Pinna, and P. Y. Madec. A new calibration strategy for adaptive telescopes with pyramid WFS. *Monthly Notices of the Royal Astronomical Society*, Sept. 2018. ISSN 0035-8711, 1365-2966. doi: 10.1093/mnras/sty2485. URL https://academic.oup.com/mnras/advance-article/doi/10.1093/mnras/sty2485/5094821.

C. T. Heritier, T. Fusco, S. Oberti, B. Neichel, S. Esposito, and P.-Y. Madec. SPRINT, system parameters recurrent invasive tracking: a fast and least-cost online calibration strategy for adaptive optics. *Monthly Notices of the Royal Astronomical Society*, 504(3): 4274–4290, May 2021. ISSN 0035-8711, 1365-2966. doi: 10.1093/mnras/stab1177. URL https://academic.oup.com/mnras/article/504/3/4274/6274481.

R. Hodgson. On a curious Appearance seen in the Sun. *Monthly Notices of the Royal Astronomical Society*, 20(1):15–16, Nov. 1859. ISSN 0035-8711, 1365-2966. doi: 10.1093/mnras/20.1.15a. URL https://academic.oup.com/mnras/article-lookup/doi/10.1093/mnras/20.1.15a.

C. K. Hoegemann, S. Chueca, J. M. Delgado, J. J. Fuensalida, B. Garcia-Lorenzo, E. G. Mendizabal, M. Reyes, M. Verde, and J. Vernin. Cute SCIDAR: presentation of the new Canarian instrument and first observational results. In *Advancements in Adaptive Optics*, page 774, USA, Oct. 2004. doi: 10.1117/12.551795. URL http://proceedings.spiedigitallibrary.org/proceeding.aspx?doi=10.1117/12.551795.

R. A. Horn and C. R. Johnson. *Matrix Analysis.* Cambridge University Press, 1 edition, Dec. 1985. ISBN 978-0-521-38632-6 978-0-521-30586-0 978-0-511-81081-7. doi: 10.1017/CBO9780511810817. URL https://www.cambridge.org/core/product/identifier/9780511810817/type/book.

H. L. Johnson and W. W. Morgan. Fundamental stellar photometry for standards of spectral type on the Revised System of the Yerkes Spectral Atlas. *Astrophysical Journal*, 117(3), May 1953. doi: 10.1086/145697. URL https://ui.adsabs.harvard.edu/abs/1953ApJ...117..313J/abstract.

A. Kellerer, N. Gorceix, J. Marino, W. Cao, and P. R. Goode. Profiles of the daytime atmospheric turbulence above Big Bear solar observatory. *Astronomy & Astrophysics*, 542: A2, June 2012. ISSN 0004-6361, 1432-0746. doi: 10.1051/0004-6361/201218844. URL http://www.aanda.org/10.1051/0004-6361/201218844.

A. N. Kolmogorov. The Local Structure of Turbulence in Incompressible Viscous Fluid for Very Large Reynolds Numbers. *Proceedings: Mathematical and Physical Sciences*, 434(1890): 9–13, 1991. ISSN 09628444. URL http://www.jstor.org/stable/51980. Publisher: The Royal Society.

P. Kongkaew. PhD-Codes, 2025a. URL https://github.com/gqmc62/PhD-Codes.

P. Kongkaew. soapy, 2025b. URL https://github.com/gqmc62/soapy.

P. Kongkaew, T. J. Morris, and J. Osborn. Distortion of visible daytime multi-conjugate adaptive optics control. In D. Schmidt, E. Vernet, and K. J. Jackson, editors, *Adaptive Optics Systems IX*, page 176, Yokohama, Japan, Aug. 2024. SPIE. ISBN 978-1-5106-7517-9 978-1-5106-7518-6. doi: 10.1117/12.3019648. URL https://www.spiedigitallibrary.org/conference-proceedings-of-spie/13097/3019648/Distortion-of-visible-daytime-multi-conjugate-adaptive-optics-control/10.1117/12.3019648.full.

V. Kornilov, A. A. Tokovinin, O. Vozyakova, A. Zaitsev, N. Shatsky, S. F. Potanin, and M. S. Sarazin. MASS: a monitor of the vertical turbulence distribution. In P. L. Wizinowich and D. Bonaccini, editors, *Proc. SPIE 4839, Adaptive Optical System Technologies II*, page 837, Waikoloa, Hawai'i, United States, Feb. 2003. doi: 10.1117/12.457982. URL http://proceedings.spiedigitallibrary.org/proceeding.aspx?doi=10.1117/12.457982.

O. Lai, M. Chun, R. Dungee, J. Lu, and M. Carbillet. DO-CRIME: dynamic on-sky covariance random interaction matrix evaluation, a novel method for calibrating adaptive optics systems. *Monthly Notices of the Royal Astronomical Society*, 501(3):3443–3456, Jan. 2021.

ISSN 0035-8711, 1365-2966. doi: 10.1093/mnras/staa3874. URL https://academic.oup.com/mnras/article/501/3/3443/6043240.

Lloyd's of London. Solar Storm Risk to the North American Electric Grid. Technical report, Lloyd's of London, 2013. URL https://www.lloyds.com/news-and-insights/risk-reports/library/solar-storm/.

M. G. Löfdahl. Evaluation of image-shift measurement algorithms for solar Shack-Hartmann wavefront sensors. *Astronomy & Astrophysics*, 524:A90, Dec. 2010. ISSN 0004-6361, 1432-0746. doi: 10.1051/0004-6361/201015331. URL http://arxiv.org/abs/1009.3401. arXiv:1009.3401 [astro-ph, physics:physics].

F. Mahmood, M. Toots, L.-G. Öfverstedt, and U. Skoglund. Algorithm and Architecture Optimization for 2D Discrete Fourier Transforms with Simultaneous Edge Artifact Removal. *International Journal of Reconfigurable Computing*, 2018:1–17, Aug. 2018. ISSN 1687-7195, 1687-7209. doi: 10.1155/2018/1403181. URL https://www.hindawi.com/journals/ijrc/2018/1403181/.

E. Marchetti, N. N. Hubin, E. Fedrigo, J. Brynnel, B. Delabre, R. Donaldson, F. Franza, R. Conan, M. Le Louarn, C. Cavadore, A. Balestra, D. Baade, J.-L. Lizon, R. Gilmozzi, G. J. Monnet, R. Ragazzoni, C. Arcidiacono, A. Baruffolo, E. Diolaiti, J. Farinato, E. Vernet-Viard, D. J. Butler, S. Hippler, and A. Amorin. MAD the ESO multi-conjugate adaptive optics demonstrator. In P. L. Wizinowich and D. Bonaccini, editors, *Astronomical Telescopes and Instrumentation*, page 317, Waikoloa, Hawai'i, United States, Feb. 2003. doi: 10.1117/12.458859. URL http://proceedings.spiedigitallibrary.org/proceeding.aspx?doi=10.1117/12.458859.

J. Marco De La Rosa, L. Montoya, M. Collados, I. Montilla, and N. Vega Reyes. Daytime turbulence profiling for EST and its impact in the solar MCAO system design. In E. Marchetti, L. M. Close, and J.-P. Véran, editors, *Proc. SPIE 9909, Adaptive Optics Systems V, 99096X*, page 99096X, Edinburgh, United Kingdom, July 2016. doi: 10.1117/12.2229471. URL http://proceedings.spiedigitallibrary.org/proceeding.aspx?doi=10.1117/12.2229471.

C. Max. Astronomy 289, Winter 2020, Adaptive Optics and its Applications, Jan. 2020.

Monthly Notices of the Royal Astronomical Society. Rev. Temple Chevallier. *Monthly Notices of the Royal Astronomical Society*, 34:137, Feb. 1874. doi: 10.1093/mnras/34.4.137. URL https://academic.oup.com/mnras/article/34/4/137/1044945.

Monthly Notices of the Royal Astronomical Society. Richard Christopher Carrington. *Monthly Notices of the Royal Astronomical Society*, 36(4):137–142, Feb. 1876. ISSN 0035-8711, 1365-2966. doi: 10.1093/mnras/36.4.137. URL https://academic.oup.com/mnras/article-lookup/doi/10.1093/mnras/36.4.137.

L. M. Montoya Martínez, S. Velasco Muñoz, J. Sánchez Capuchino, M. Collados Vera, L. F. Rodríguez-Ramos, A. Asensio Ramos, and F. J. De Cos Juez. The real time MCAO solar prototype for the EST. In D. Schmidt, L. Schreiber, and L. M. Close, editors, *Adaptive Optics Systems VI*, page 158, Austin, United States, July 2018. SPIE. ISBN 978-1-5106-1959-3 978-1-5106-1960-9. doi: 10.1117/12.2312445. URL https://www.spiedigitallibrary.org/conference-proceedings-of-spie/10703/2312445/The-real-time-MCAO-solar-prototype-for-the-EST/10.1117/12.2312445.full.

National Research Council (U.S.), editor. *Severe space weather events: understanding societal and economic impacts: a workshop report*. National Academies Press, Washington, D.C, 2008. ISBN 978-0-309-14153-6. URL https://doi.org/10.17226/12507. OCLC: ocn298513348.

National Solar Observatory. 2020: A New Era for Solar Astronomy, 2025a. URL https://nso.edu/telescopes/dkist/2020solarastronomy/.

National Solar Observatory. DKIST Science Overview, 2025b. URL https://nso.edu/research/dkist-science-overview/#more.

NHS. Sunscreen and sun safety, Dec. 2022. URL https://www.nhs.uk/live-well/seasonal-health/sunscreen-and-sun-safety/.

R. J. Noll. Zernike polynomials and atmospheric turbulence*. *Journal of the Optical Society of America*, 66(3):207, Mar. 1976. ISSN 0030-3941. doi: 10.1364/JOSA.66.000207. URL https://opg.optica.org/abstract.cfm?URI=josa-66-3-207.

NumPy Developers. numpy.fft.fftshift - NumPy v2.0 Manual, June 2024. URL https://numpy.org/doc/stable/reference/generated/numpy.fft.fftshift.html.

J. Osborn, D. Föhring, V. S. Dhillon, and R. W. Wilson. Atmospheric scintillation in astronomical photometry. *Monthly Notices of the Royal Astronomical Society*, 452(2): 1707–1716, Sept. 2015. ISSN 0035-8711, 1365-2966. doi: 10.1093/mnras/stv1400. URL `https://academic.oup.com/mnras/article-lookup/doi/10.1093/mnras/stv1400`.

R. Ragazzoni, E. Diolaiti, J. Farinato, E. Fedrigo, E. Marchetti, M. Tordi, and D. Kirkman. Multiple field of view layer-oriented adaptive optics: Nearly whole sky coverage on 8 m class telescopes and beyond. *Astronomy & Astrophysics*, 396(2):731–744, Dec. 2002. ISSN 0004-6361, 1432-0746. doi: 10.1051/0004-6361:20021406. URL `http://www.aanda.org/10.1051/0004-6361:20021406`.

A. Reeves. Soapy: an adaptive optics simulation written purely in Python for rapid concept development. In E. Marchetti, L. M. Close, and J.-P. Véran, editors, *Adaptive Optics Systems V*, page 99097F, Edinburgh, United Kingdom, July 2016. Society of Photo-Optical Instrumentation Engineers (SPIE). doi: 10.1117/12.2232438. URL `http://proceedings.spiedigitallibrary.org/proceeding.aspx?doi=10.1117/12.2232438`.

F. Rigaut, B. Neichel, M. Boccas, C. d'Orgeville, F. Vidal, M. A. van Dam, G. Arriagada, V. Fesquet, R. L. Galvez, G. Gausachs, C. Cavedoni, A. W. Ebbers, S. Karewicz, E. James, J. Lührs, V. Montes, G. Perez, W. N. Rambold, R. Rojas, S. Walker, M. Bec, G. Trancho, M. Sheehan, B. Irarrazaval, C. Boyer, B. L. Ellerbroek, R. Flicker, D. Gratadour, A. Garcia-Rissmann, and F. Daruich. Gemini multi-conjugate adaptive optics system review I: Design, trade-offs and integration. *Monthly Notices of the Royal Astronomical Society*, 437(3): 2361–2375, Jan. 2014. ISSN 0035-8711, 1365-2966. doi: 10.1093/mnras/stt2054. URL `http://arxiv.org/abs/1310.6199`.

T. R. Rimmele. Recent advances in solar adaptive optics. In *Advancements in Adaptive Optics*, page 34, USA, Oct. 2004. doi: 10.1117/12.551764. URL `http://proceedings.spiedigitallibrary.org/proceeding.aspx?doi=10.1117/12.551764`.

M. C. Roggemann and A. C. Koivunen. Wave-front sensing and deformable-mirror control in strong scintillation. *Journal of the Optical Society of America A*, 17(5):911, May 2000. ISSN 1084-7529, 1520-8532. doi: 10.1364/JOSAA.17.000911. URL `https://opg.optica.org/abstract.cfm?URI=josaa-17-5-911`.

G. Rousset. Wave-front sensors. In *Adaptive Optics in Astronomy*, page 115. Cambridge University Press, 1999. ISBN 978-0-511-52517-9. URL https://doi.org/10.1017/CBO9780511525179.

D. Saint-Jacques. *ASTRONOMICAL SEEING IN SPACE AND TIME.* PhD thesis, University of Cambridge, Cambridge, Dec. 1998. URL https://www.repository.cam.ac.uk/items/6279a25a-789f-464c-be81-c9156f749be5/full.

R. J. Sasiela. *Electromagnetic wave propagation in turbulence: evaluation and application of Mellin transforms.* Number 171 in SPIE PM. SPIE, Bellingham, Wash, 2. ed edition, 2007. ISBN 978-0-8194-6728-7. URL https://doi.org/10.1117/3.741372.

D. Schmidt, T. Berkefeld, B. Feger, and F. Heidecke. Latest achievements of the MCAO testbed for the GREGOR Solar Telescope. In B. L. Ellerbroek, M. Hart, N. Hubin, and P. L. Wizinowich, editors, *Adaptive Optics Systems II*, page 773607, San Diego, California, USA, July 2010. doi: 10.1117/12.857117. URL http://proceedings.spiedigitallibrary.org/proceeding.aspx?doi=10.1117/12.857117.

D. Schmidt, T. Berkefeld, and F. Heidecke. The 2012 status of the MCAO testbed for the GREGOR solar telescope. In B. L. Ellerbroek, E. Marchetti, and J.-P. Véran, editors, *Adaptive Optics Systems III*, pages 84473J–84473J–11, Amsterdam, , Netherlands, Sept. 2012. SPIE Press. doi: 10.1117/12.926902. URL http://proceedings.spiedigitallibrary.org/proceeding.aspx?articleid=1358976.

D. Schmidt, T. Berkefeld, F. Heidecke, A. Fischer, O. Von Der Lühe, and D. Soltau. GREGOR MCAO looking at the Sun. In E. Marchetti, L. M. Close, and J.-P. Véran, editors, *Adaptive Optics Systems IV*, page 91481T, Montréal, Quebec, Canada, July 2014. doi: 10.1117/12.2055154. URL http://proceedings.spiedigitallibrary.org/proceeding.aspx?doi=10.1117/12.2055154.

D. Schmidt, N. Gorceix, P. R. Goode, J. Marino, T. Rimmele, T. Berkefeld, F. Wöger, X. Zhang, F. Rigaut, and O. Von Der Lühe. *Clear* widens the field for observations of the Sun with multi-conjugate adaptive optics. *Astronomy & Astrophysics*, 597:L8, Jan. 2017. ISSN 0004-6361, 1432-0746. doi: 10.1051/0004-6361/201629970. URL http://www.aanda.org/10.1051/0004-6361/201629970.

D. Schmidt, A. Beard, A. Ferayorni, B. D. Goodrich, S. Gregory, L. C. Johnson, L. Rimmele, T. R. Rimmele, E. Starman, and F. Wöger. On the upgrade path to GLAO and MCAO on the Daniel K. Inouye Solar Telescope. In D. Schmidt, L. Schreiber, and E. Vernet, editors, *Adaptive Optics Systems VIII*, page 26, Montréal, Canada, Aug. 2022. SPIE. ISBN 978-1-5106-5351-1 978-1-5106-5352-8. doi: 10.1117/12.2631681. URL `https://www.spiedigitallibrary.org/conference-proceedings-of-spie/12185/2631681/On-the-upgrade-path-to-GLAO-and-MCAO-on-the/10.1117/12.2631681.full`.

J. D. Schmidt. *Numerical Simulation of Optical Wave Propagation with Examples in MATLAB.* SPIE, July 2010. ISBN 978-0-8194-8327-0. doi: 10.1117/3.866274. URL `https://spiedigitallibrary.org/ebooks/PM/Numerical-Simulation-of-Optical-Wave-Propagation-with-Examples-in-MATLAB/eISBN-9780819483270/10.1117/3.866274`.

G. Sliepen, A. P. L. Jägers, F. C. M. Bettonvil, and R. H. Hammerschlag. Seeing measurements with autonomous, short-baseline shadow band rangers. In L. M. Stepp, R. Gilmozzi, and H. J. Hall, editors, *Proc. SPIE 7733, Ground-based and Airborne Telescopes III, 77334L*, page 77334L, San Diego, California, USA, July 2010. doi: 10.1117/12.857643. URL `http://proceedings.spiedigitallibrary.org/proceeding.aspx?doi=10.1117/12.857643`.

T. Song, Z. Cai, Y. Liu, M. Zhao, Y. Fang, X. Zhang, J. Wang, X. Li, Q. Song, and Z. Du. Daytime optical turbulence profiling with a profiler of the differential solar limb. *Monthly Notices of the Royal Astronomical Society*, 499(2):1909–1917, Oct. 2020. ISSN 0035-8711, 1365-2966. doi: 10.1093/mnras/staa2729. URL `https://academic.oup.com/mnras/article/499/2/1909/5928239`.

F. R. Stephenson and D. M. Willis. The earliest drawing of sunspots. *Astronomy & Geophysics*, 40(6):6.21–6.22, Dec. 1999. ISSN 1366-8781, 1468-4004. doi: 10.1093/astrog/40.6.6.21. URL `https://academic.oup.com/astrogeo/article-lookup/doi/10.1093/astrog/40.6.6.21`.

P. Stoica and R. Moses. *Spectral Analysis of Signals.* Prentice Hall, 2005. ISBN 0-13-113956-8.

G. Strang. *Linear Algebra and Its Applications (Fourth Edition).* Wellesly-Cambridge Press, Wellesly, MA, USA, 4th edition edition, 2009. ISBN 978-0-9802327-1-4.

M. Tallon and R. Foy. Adaptive telescope with laser probe: isoplanatism and cone effect. *Astronomy and Astrophysics*, 235:549–557, Aug. 1990. ISSN 0004-6361. URL `https://ui.adsabs.harvard.edu/abs/1990A&A...235..549T`. ADS Bibcode: 1990A&A...235..549T.

V. I. Tartarskii. *The Effects of the Turbulent Atmosphere on Wave Propagation*. Israel Program for Scientific Translations Ltd., 1971. ISBN 0-7065-0680-4. URL `https://ntrl.ntis.gov/NTRL/dashboard/searchResults/titleDetail/TT6850464.xhtml`.

J. Taylor, R. Swanson, P. Levesque, M. P. Lamb, A. Vaz, M. Montoya, A. Gardner, K. M. Morzinski, and S. Sivanandam. ESCAPE: efficient synthesis of calibrations for adaptive optics through pseudo-synthetic and empirical methods. In D. Schmidt, E. Vernet, and K. J. Jackson, editors, *Adaptive Optics Systems IX*, page 31, Yokohama, Japan, Aug. 2024. SPIE. ISBN 978-1-5106-7517-9 978-1-5106-7518-6. doi: 10.1117/12.3020489. URL `https://www.spiedigitallibrary.org/conference-proceedings-of-spie/13097/3020489/ESCAPE--efficient-synthesis-of-calibrations-for-adaptive-optics-through/10.1117/12.3020489.full`.

R. K. G. Temple. The Chinese scientific genius. *The UNESCO Courier: a window open on the world*, XLI(10):9, Oct. 1988. URL `https://unesdoc.unesco.org/ark:/48223/pf0000081712`.

S. Thomas, T. Fusco, A. Tokovinin, M. Nicolle, V. Michau, and G. Rousset. Comparison of centroid computation algorithms in a Shack-Hartmann sensor: Comparison of centroid computation algorithms. *Monthly Notices of the Royal Astronomical Society*, 371(1):323–336, Aug. 2006. ISSN 00358711, 13652966. doi: 10.1111/j.1365-2966.2006.10661.x. URL `https://academic.oup.com/mnras/article-lookup/doi/10.1111/j.1365-2966.2006.10661.x`.

A. Tokovinin, J. Vernin, A. Ziad, and M. Chun. Optical Turbulence Profiles at Mauna Kea Measured by MASS and SCIDAR. *Publications of the Astronomical Society of the Pacific*, 117(830):395–400, Apr. 2005. ISSN 0004-6280, 1538-3873. doi: 10.1086/428930. URL `http://iopscience.iop.org/article/10.1086/428930`.

M. J. Townson, O. J. D. Farley, G. Orban De Xivry, J. Osborn, and A. P. Reeves. AOtools: a Python package for adaptive optics modelling and analysis. *Optics Express*, 27(22):31316, Oct. 2019. ISSN 1094-4087. doi: 10.1364/OE.27.031316. URL https://opg.optica.org/abstract.cfm?URI=oe-27-22-31316.

M. A. Van Dam, Y. Martin-Hernandez, M. A. Núñez Cagigal, and L. M. Montoya. Overcoming the effect of pupil distortion in multiconjugate adaptive optics. In D. Schmidt, L. Schreiber, and E. Vernet, editors, *Adaptive Optics Systems VII*, page 23, Online Only, United States, Dec. 2020. SPIE. ISBN 978-1-5106-3683-5 978-1-5106-3684-2. doi: 10.1117/12.2560873. URL https://www.spiedigitallibrary.org/conference-proceedings-of-spie/11448/2560873/Overcoming-the-effect-of-pupil-distortion-in-multiconjugate-adaptive-optics/10.1117/12.2560873.full.

M. A. Van Dam, B. Femenía Castellá, Y. Martín Hernando, M. Núñez Cagigal, L. M. Montoya, and D. Schmidt. Scintillation effects and the optimal sequence of deformable mirrors in multi-conjugate adaptive optics. *Journal of Astronomical Telescopes, Instruments, and Systems*, 7(04), Nov. 2021. ISSN 2329-4124. doi: 10.1117/1.JATIS.7.4.049002. URL https://www.spiedigitallibrary.org/journals/Journal-of-Astronomical-Telescopes-Instruments-and-Systems/volume-7/issue-04/049002/Scintillation-effects-and-the-optimal-sequence-of-deformable-mirrors-in/10.1117/1.JATIS.7.4.049002.full.

J. M. Vaquero. Sunspot observations by Theophrastus revisited. *Journal of the British Astronomical Association*, 117(6):346, Dec. 2007. URL https://ui.adsabs.harvard.edu/abs/2007JBAA..117..346V/abstract.

M. Vokhmyanin, R. Arlt, and N. Zolotova. Sunspot Positions and Areas from Observations by Thomas Harriot. *Solar Physics*, 295(3):39, Mar. 2020. ISSN 0038-0938, 1573-093X. doi: 10.1007/s11207-020-01604-4. URL http://link.springer.com/10.1007/s11207-020-01604-4.

O. F. H. Von Der Luhe. Photometric stability of multiconjugate adaptive optics. In *Advancements in Adaptive Optics*, page 617, USA, Oct. 2004. doi: 10.1117/12.553053. URL http://proceedings.spiedigitallibrary.org/proceeding.aspx?doi=10.1117/12.553053.

A. T. Young. Air mass and refraction. *Applied Optics*, 33(6):1108, Feb. 1994. ISSN 0003-6935, 1539-4522. doi: 10.1364/AO.33.001108. URL https://opg.optica.org/abstract.cfm?URI=ao-33-6-1108.

Colophon

This thesis is based on a template developed by Matthew Townson and Andrew Reeves. It was typeset with $\LaTeX\,2_{\varepsilon}$. It was created using the *memoir* package, maintained by Lars Madsen, with the *madsen* chapter style. The font used is Latin Modern, derived from fonts designed by Donald E. Kunith. This template was later adjusted by Puttiwat Kongkaew for desired parameters, considering text formats, margins, and spacing.